High-Pressure Phase Equilibria of Ionic Liquids and Compressed Gases for Applications in Reactions and Absorption Refrigeration

by

Wei Ren

Submitted to the graduate degree program in Chemical and Petroleum Engineering
and the Graduate Faculty of the University of Kansas
in partial fulfillment of the requirements for the degree of
Doctor of Philosophy

Committee Members: _____
Chairperson* Aaron M. Scurto

_____
Kyle V.Camarda

_____
Laurence R. Weatherley

_____
Jyun-Syung Tsau

_____
Brian B. Laird

Date defended: 11/23/2009

The Dissertation Committee for Wei Ren certifies that this is the approved version of the following dissertation:

High-Pressure Phase Equilibria of Ionic Liquids and Compressed Gases for Applications in Reactions and Absorption Refrigeration

Wei Ren

Committee Members:

_____
Chairperson* Aaron M. Scurto

_____
Kyle V. Camarda

_____
Laurence R. Weatherley

_____
Jyun-Syung Tsau

_____
Brian B. Laird

Date approved: _____

Abstract

High-Pressure Phase Equilibria of Ionic Liquids and Compressed Gases for Applications in Reactions and Absorption Refrigeration

by

Wei Ren

Environmental concerns using volatile organic compounds have attracted intensive research of replacing them with more sustainable ("greener") solvents. Ionic liquids have been promising alternatives due to their unique physical and chemical properties, especially their lack of volatility. However, using ionic liquids over common organic solvents has several challenges, i.e., higher viscosity (lower diffusivity) than common organic solvents; lower solubility of reaction gases and large number of high-melting solids not liquids at processing conditions. Coupling ionic liquids with compressed gases systems may overcome most of these difficulties for their applications in separations, reactions, materials processing and engineering applications. To further develop these processes, phase behavior and phase equilibrium knowledge are of essential significance. The main objective of this research is to investigate high pressure global phase behavior and measure phase equilibrium of ionic liquids and compressed gases for their applications as reaction media for hydrogenation and hydroformylation reaction and as working fluids for absorption air conditioning systems.

This research investigates imidazolium ionic liquids with various alkyl groups and anions and two compressed gases: carbon dioxide (CO_2) and 1,1,1,2-

Tetrafluoroethane (R-134a). The global phase behavior and phase equilibria are measured in the temperature range from approximately 0°C to 105°C and pressure up to 330 bar. Binary systems of R-134a with ionic liquids of [EMIm][Tf_2N], [HMIm][Tf_2N], [HMIm][PF_6], [HMIm][BF_4], and [BMIm][PF_6] indicate a Type V system according to the classification of Scott and van Konynenburg. Regions of multiphase equilibria exist, *viz*. vapor liquid equilibrium, vapor liquid liquid equilibrium, liquid liquid equilibrium; while Type III phase behavior for [HMIm][Br] and R-134a is observed, which provides a novel purification method to separate [HMIm][Tf_2N] from [HMIm][Br] after synthesis. The phase behavior of CO_2 and all ionic liquids indicate Type III systems. The effects of ionic liquid structures on the solubility, lower critical end-point (LCEP) and mixture critical points are also investigated.

Complete phase behavior study with the reactant, product, CO_2 and ionic liquids for hydrogenation and hydroformylation reactions are accomplished, and volume expansion and molar volume data of liquid phase with CO_2 pressure are measured simultaneously. Two regions of reaction rate with different primary phenomena can be explained by phase behavior knowledge: dilution effect and reactant partitioning. The unique phase properties of IL/CO_2 suggest an ease product purification process and make it a favorable biphasic solvent system. Detailed phase behavior and equilibrium help understand fully the kinetics results, determine the operating conditions, choose appropriate separation process and properly design an optimal reaction system.

The understanding and quantitative modeling of the high-pressure phase behavior and equilibria data are essential for process design and simulation. The Peng-Robinson equation of state model with van der Waals 2-parameter mixing rule is chosen to correlate the experimental data and predict phase equilibrium. Thermodynamic modeling of an absorption air conditioning system using ILs and compressed gases as working fluids is developed.

This work reveals that a biphasic reaction system with IL/CO_2 for homogeneously catalyzed reactions provides a highly tunable, flexible and economic platform for reactions and separations. However, without understanding the phase equilibrium, the kinetics results cannot be properly interpreted. This work also demonstrates that the absorption refrigeration system using ionic liquids and compressed gases in vehicles is feasible using just the waste heat from the engine and can provide comparable cooling capacity as vapor compression system. The common vapor compression system diverts work from the engine to power the air conditioning system and this adds to fuel consumption and pollution.

Acknowledgements

I want to express sincere gratitude to my advisor, Dr. Aaron M. Scurto, for his guidance, enthusiasm and encouragement throughout my graduate study at the University of Kansas. He inspired me to explore ideas and carry out research in the field of thermodynamics. I really appreciate his help and patience.

I am grateful to Professor Kyle Camarda, Dr. Jyun-Syung Tsau, Professor Jenn-Tai Liang, Professor Laurence Weatherley and Professor Brian B. Laird for their inspirational and valuable advice. I also want to thank Dr. Mark B. Shiflett and Dr. A. Yokozeki for their helpful discussions and rewarding collaborations. I would like to give my special thanks to Mr. Alan Walker and Mr. Scott Ramskill for their excellent work and help on setting up and maintaining experiment equipment.

I would like to thank the faculty and staff of the Department of Chemical and Petroleum Engineering, Center for Environmentally Beneficial Catalysis (CEBC) and Center of Tertiary Oil Recovery Project (TORP), especially Dr. Fenghui Niu, Dr. Claudia Bode, Mr. Ed Atchison, Mrs. Deanna Bieberly, Dr. Tie-pan Shi, Dr. Min Cheng, Dr. Chicheng Ma, and the friends I made during my graduate study for their encouragement and friendship.

I wish to thank my group mates, Jay Schleicher, Azita Ahosseini, Sylvia Ogechi Nwosu, for their support, discussion and cooperation.

Finally, I want to express my deepest appreciation to my family: my daughter, Katherine, son Kevin, husband Bao Lin and my parents: Lanting Ren and Minru Bao for their endless love and persistent support for me.

Dedicated to my loving family:

Katherine, Kevin, Bao Lin and my parents

List of Figures

List of Tables

Abbreviation

1234yf	2,3,3,3 tetrafluoropropene
APAM	N-acetyl-(S)-phenylalanine methyl ester
[BEIm]	1-n-Butyl-3-ethylimidazolium
[BF_4]	Tetrafluoroborate
CFC	chlorofluorocarbon
CFC-113	1,1,2-trichloro-1,2,2-trifluoroethane
CFC-113a	1,1,1-trichloro-2,2,2-trifluoroethane
CFC-114	1,2-dichloro-1,1,2,2-tetrafluoroethane
CFC-114a	1,1-dichloro-1,2,2,2-tetrafluoroethane
CHF_3	trifluoromethane
[Cl]	Chloride
[(Cn)mN]	tetraalkylammonium
[[(Cn)mP]	tetraalkylphosphonium
[CnPyr]+	n-alkylpyridinium
[Dca]	Dicyanoamide
[DMIm]	1-n-decyl-3-methyl-imidazolium bis(trifluoromethylsulfonyl)amide
[EMIm]	1-ethyl-3-ethylimidazolium bis(trifluoromethylsulfonyl)amide
[EMMIm]	1-ethyl-2,3-di-methylimidazolium
HFC	hydrofluocarbon
HCFC	hydrochlorofluorocarbon
HCFC-123	1,1-dichloro-2,2,2-trifluoroethane
HCFC-123a	1,2-dichloro-1,2,2-trifluoroethane
HCFC-124	1-chloro-1,2,2,2-tetrafluoroethane
HCFC-124a	1,2,2,2-tetrafluoroethane
HFC-134	1,1,2,2-tetrafluoroethane

HFC-134a	1,1,1,2-tetrafluoroethane
HFE	hydrofluoroether
HFO	Hydro-Fluoro-Olefin
[HFPS]	1,1,2,3,3,3-hexafluoropropanesulfonate
[HMIm]	1-n-Hexyl-3-methylimidazolium bis(trifluoromethylsulfonyl)amide
MAAC	methyl-(Z)-acetamidocinnamate
[PF_6]	hexaflurophosphate
[PMIm]	1-methyl-3-pentyl-imidazolium bis(trifluoromethylsulfonyl)amide
R-12	dichlorodifluoromethane
R125	pentafluoroethane
R-134a	1,1,1,2-tetrafluoroethane
R14	tetrafluoromethane
R152a	1,1-difluoroethane
R23	trifluoromethane
R32	difluoromethane
R143a	1,1,1-trifluoroethane
$scCO_2$	supercritical carbon dioxide
[Tf_2N]	bis(trifluoromethylsulfonyl)amide
TFE	2,2,2-trifloroethanol
[TFES]	1,1,2,2-tetrafluoroethanesulfonate
[TfO]	trifluoromethanesulfonate
[TPES]	1,1,2-trifluoro-2-(perfluoroethoxy)ethanesulfonate
[TTES]	1,1,2-trifluoro-2-(trifluoromethoxy)-ethanesulfonate

AARD	Average Absolute Relative Deviation
COP	Coefficient of Performance
CXL	CO_2 eXpanded Liquids
ECS	Extended Corresponding States
EoS	Equations of State
EPA	Environmental Protection Agency
GC	Gas Chromatography
GWP	Global Warming Potential
GXL	Gas eXpanded Liquids
HPLC	High-Pressure Liquid Chromatography
ICP	Inductively Covered Plasma
IL	Ionic Liquid
IR	Infrared Radiation
IUPAC	International Union of Pure and Applied Chemistry
LLE	Liquid-Liquid Equilibrium
LCEP	Lower Critical End Point
NIST	National Institute of Standard and Technology
NLP	NonLinear Programming
NMR	Nuclear Magnetic Resonance
NRTL	Non-Random Two-Liquid
PR EoS	Peng-Robinson Equations of State
PR-vdW2 EoS	Peng-Robinson EoS with van der Waals-2 mixing rule
QCM	Quartz Crystal Microbalance
RK EoS	Redlich-Kwong Equations of State
RTIL	Room Temperature Ionic Liquid
SAFT	Statistical Associating Fluid Theory
SILM	Supported Ionic Liquid Membrane

SLV	Solid-Liquid-Vapor Equilibrium
SRK EoS	Soave-Redlich-Kwong Equations of State
TSIL	Task-Specific Ionic Liquid
UCEP	Upper Critical End Point
UHP	Ultra High Purity
UNIQUAC	UNIversal QUAsi Chemical
VLE	Vapor-Liquid Equilibrium
VLLE	Vapor-Liquid-Liquid Equilibrium

Nomenclature

C_p	heat capacity
G	Gibbs free energy
M	molecular weight
N	number of experiment points
P	pressure
R	ideal gas constant
T	temperature
V	volume
a	the measure of the attraction strength between particles
b	the volume occupied by particles
f	fugacity
g	molar Gibbs free energy
l	binary interaction coefficient
k	binary interaction coefficient
m	mass
n	mole
v	molar volume
w	mass fraction
x	mole fraction of gas composition
y	mole fraction of liquid composition
z	solutions to the equifugacity conditions
$\tilde{g}$	dimensionless molar Gibbs energy
P	density
γ	activity coefficient

$\bar{\varphi}_i$	fugacity coefficient
μ	chemical potential
ω	acentric factor
[m]	molality
[M]	molarity
$\underline{V}$	molar volume
$\dot{W}$	work
$\hat{H}$	enthalpy
$\dot{m}$	mass flow rate
$\dot{Q}$	heat input

Superscript

0	reference state
F	fluid
L	liquid
S	solid
V	vapor
R	residual
IG	ideal gas
exp	experiment data
calc	calculated value

Subscript

1,2,…, 10	streams of refrigeration cycle
abs	absorber
C	critical property
cell	equilibrium cell
cond	condenser
evap	evaporator
G	gas phase
gen	generator
headspace	head space above the liquid
I	component *i* in the mixture
J	component *j* in the mixture
lines	line connecting the pump to the equilibrium cell
M	mixture
N	total number of phases
pump	gas pump
R	reduced property
S	strong solution
W	weak solution

Greek number

I, II, III,	index of phases

Table of Contents

Chapter 1 Introduction

With increasing environmental concerns, it becomes more and more important to decrease the use of volatile organic compounds. Thus, exploring alternatives of traditional solvents has become more critical. Ionic liquids (ILs) have been receiving more and more worldwide attention in academic research and commercial applications. Room-temperature ionic liquids (RTILs) are organic salts that form liquids at or near room temperature. Many of the properties of ILs make them environmental benign. For instance, ILs have non-measureable vapor pressure, which dramatically decreases the exposure for operator. ILs are nonflammable, non-explosive and stable as liquids in a wide temperature range. They have a wide window of electrochemical stability, good electrical conductivity, high ionic mobility and excellent chemical stabilities. ILs also are good absorbents for organic, inorganic, and gas components for a variety of applications in reactions, extractions, materials processing and engineering applications.

1.1 Ionic Liquids

1.1.1 Ionic liquids classification

The most commonly used ILs are quaternary ammonium, imidazolium, pyridinium, and phosphonium. As shown in Figure 1.1, ILs often have large organic cations. Other cations [1] (shown in Figure 1.2) are also reported such as sulfonium(1), oxazolium(2)[2] and pyrazolium(3)[3] lithium(4), pyrrolidinium(5),

thiazolium(6),[4] triazolium(7)[5]. The anions can be polynuclear anions, e.g. $[AlCl_4]$, $[Al_2Cl_7]$, $[Au_2C_{l7}]$, $[Fe_2C_{l7}]$, inorganic (halide, $[BF_4]$, $[PF_6]$), and organic anions $[C_4F_9SO_3]$, trifluoroacetic $[CF_3CO_2]$, triflate$[CF_3SO_3]$, amides $[Tf_2N]$, $[(C_2F_5SO_2)_2N]$, $[(FSO_2)_2N]$ and $[CF_3CONCF_3SO_2]$, methide $[(CF_3SO_2)_3C]$, $[(CF_3SO_2)_2N]$. Anions may also be based on cyano groups, such as $[Ag(CN)_2]$, $[C(CN)_3]$ and $[N(CN)_2]$ [1]. Several common ionic liquids with an abbreviation and chemical structures are given in Table 1.1.

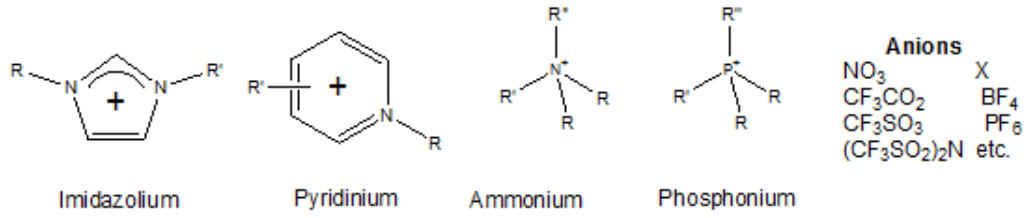

Figure 1.1 Illustrations of common cation classes and anions used with ionic liquids

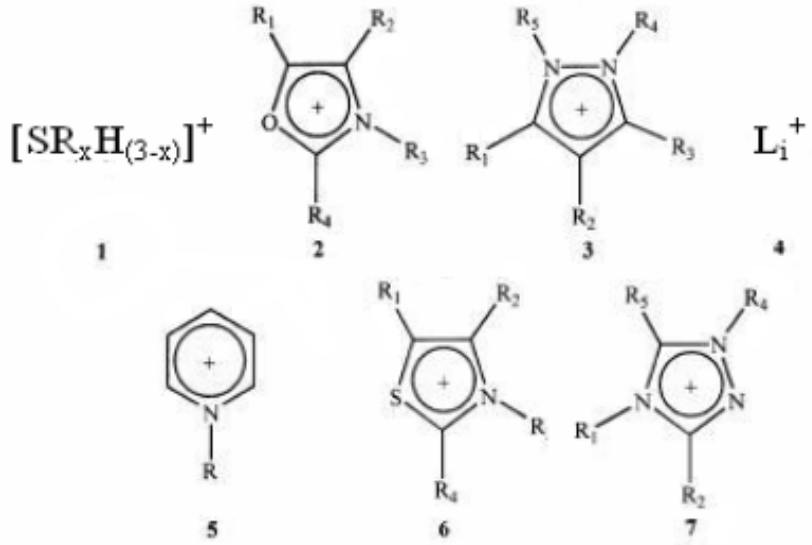

Figure 1.2 Other cations used in ionic liquids

Table 1.1 Common ionic liquids, abbreviation names and chemical structures

Name	Abbreviation	Chemical structure
1-Ethyl-3-ethylimidazolium chloride	[EMIm] [Cl]	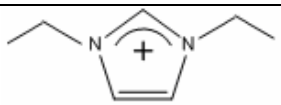
1-n-Butyl-3-ethylimidazolium tetrafluoroborate	[BMIm] [BF_4]	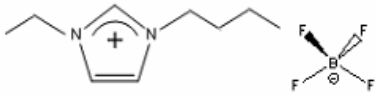
1-n-Hexyl-3-methylimidazolium hexaflurophosphate	[HMIm][PF_6]	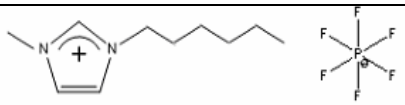
1-n-decyl-3-methyl-imidazolium bis(trifluoromethylsulfonyl)amide	[DMIm][Tf_2N]	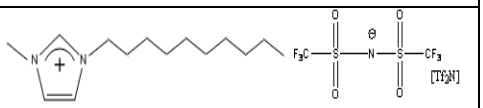

1.1.2 Ionic liquids nomenclature

Ionic liquids consist of cation and anion. Typically ILs are named as: [cation][anion]. Ionic liquids chosen in this research are 1-alkyl-3methylidazolium cations, which are abbreviated as [RMIm]. Regarding to different alkyl chain length, "R" is replaced by the first letter of alkyl chain. For instance, [EMIm] represents 1-Ethyl-3-methylimidazolium, and [BMIm] refers to 1-Butyl-3-methylimidazolium respectively. For imidazolium cations, if the C2 position (Figure 1.2) has been methylated, the cation is abbreviated as [RMMIm]. For example, [EMMIm] is abbreviation of 1-ethyl-2, 3-dimethylimidazolium. Pyridinium, ammonium and phosphonium cations have different abbreviation. [n-Alkylpyridinium] is abbreviated to $[C_nPyr]+$, where n is the number of carbons in the alkyl chain attached to the nitrogen of the pyridinium ring. $[(C_n)_mN]$ and $[[(C_n)_mP]$ are the abbreviations for

tetraalkylammonium and tetraalkylphosphonium, where *m* accounts for number of alkyl chain groups attached to nitrogen or phosphorus.

The anions are generally abbreviated as their molecular formulas. For example, hexafluorophosphates is abbreviated as [PF_6], tetrafluoroborates as [BF_4]. Triflate as Tf, Trifluoromethanesulfonyl, [CF_3SO_2] as [TfO], and bis(trifluoromethanesulfonyl)amide, [$(CF_3SO_2)_2N$] as [Tf_2N].

1.1.3 History of ionic liquids

Ionic liquids have been known for over a century. In 1888, Ethanolammonium nitrate with a melting point of 52-55 °C was reported by Gabriel [6]. In 1914, the room temperature ionic liquid, ethylammonium nitrate ([$EtNH_3$][NO_3]) with a melting point of 12 °C was first synthesized. However, little advancement occurred in the field for most of the 20th century. The development of chloroaluminate (Al_xCl_y) ionic liquids started from 1948. In 1951, Hurley and Weir [7] synthesized alkylpyridinium chloroaluminate salts. Because of alkylpyridinium cations are not satable, Hussey and Wilkes [8] used imidazolium cations. Despite the applications in catalysis and use as a solvent, chloroaluminate ILs suffer from extreme air and water sensitivity, which limit their applications as solvents in transition metal catalysis and mainly used in electrochemical process.

In 1972, the first use of an IL as a solvent for homogeneous transition metal catalysis reaction was described by Parshall [9]. Tetraethlylammonium trichlorostannate, with a melting point of 78 ºC was used in hydroformylation of ethylene with a platinum catalyst. 1-Ethyl-3-methylimidazolium [EMIm]

chloroaluminate ILs were discovered [8] in 1982, which provided acceleration for activity in the area of RTILs. The named salt was one of the most widely studied room-temperature melt systems until recently. It exists as liquid at room temperature for compositions between 33 and 67 mol% $AlCl_3$. The Diels-Alder reaction using 1-Ethyl-3-methylimidazolium chloride / chloroaluminate ([EMIm][Cl]/($AlCl_3$)x) has been reported [10]. The acidic/basic products are determined by the ratio of ([EMIm][Cl]/($AlCl_3$)x. The halogenoaluminate ILs can posses Lewis Acidity, which can be varied by controlling the molar ratio of the two components for various catalytic reactions. This kind of tuning makes these ILs attractive as nonaqueous reaction media [11]. A drawback of aluminum chloride-based ionic liquids is their moisture sensitivity.

In 1992, Wilkes and Zaworotko [12] reported the first air and moisture stable ionic liquids based on 1-Ethyl-3-methylimidazolium cation with either tetrafluoroborate or hexafluorophosphate as anions. Unlike the chloroaluminate ionic liquids, these ionic liquids could be prepared and safely stored outside of an inert atmosphere. In 2004, the first major industrial application of ILs was used by BASF in the *B*iphasic *A*cid *S*cavenging utilizing *I*onic *L*iquids (BASIL^{TM}) process [13]. This technology increases yield and capacities, and replaces the conventional process of forming solid salts when the acid is removed.

Now research and industrialization of ionic liquids are expanding dramatically as shown in Figure 1.3. All the data were given by Scifinder till September 2009. ILs have seen wider industrial applications [1, 14-20] in catalytic reactions, gas

separations, liquid-liquid extractions, electrochemistry, fuel cell, biotechnology especially for biocatalysis,[21-23] synthesis of RNA and DNA oligomers [24]. They have also been successfully used to dissolve and process cellulose, [25-27] for optoelectronic applications,[28] as well as in synthesizing novel polymers [29-30] and nanomaterials [31].

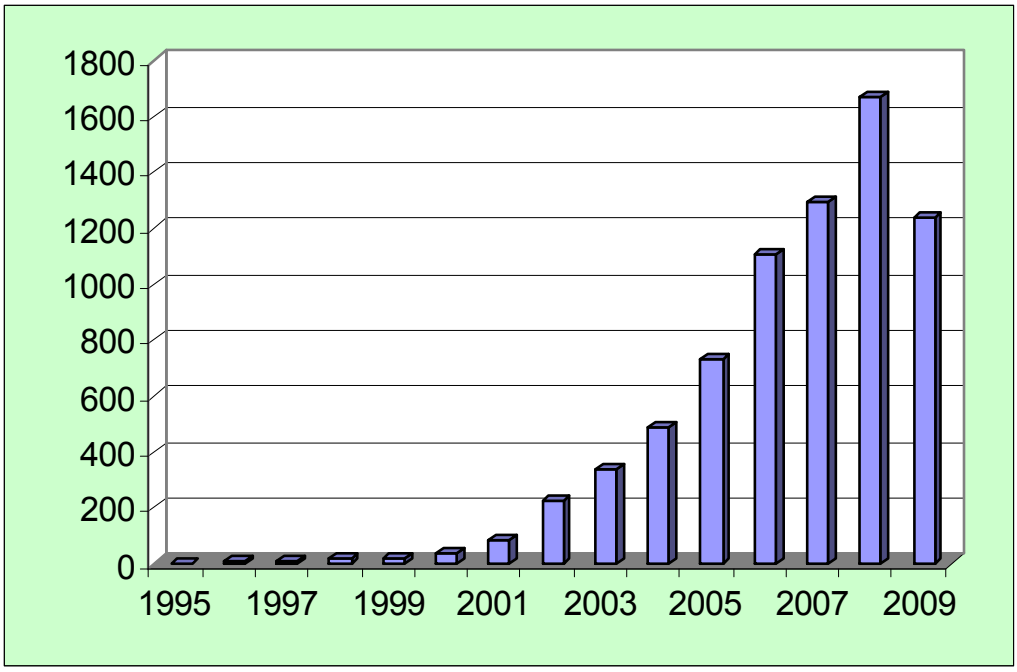

Figure 1.3 Literature survey on publications of ionic liquids. All data is until September, 2009

1.1.4 Physicochemical properties of ionic liquids

It is necessary to measure and understand the fundamental physical and chemical properties of ionic liquids in order to replace organic components as solvents for reactions or separation processes. Physical properties, such as melting point, density, viscosity, surface tension, are important for engineering design.

Chemical properties, such as co-ordination properties, Lewis acidity, polarity, hydrogen bonding ability of donating and accepting, play a key role in solubility, phase behavior, and reaction kinetic rates.

The most important feature of ILs is the ability to tune molecularly by the choice of functional groups on the cation and the anion [32-33]. It has been estimated that $\sim 10^{14}$ unique cation/anion combinations are possible [34]. Therefore, ionic liquids are "designer media", whose great flexibility allows for optimizing the solvent for any specific application. For example, replacing the $[PF_6]$ anion of the 1-alkyl-3-alkylimadazolium cation by $[BF_4]$ dramatically increases the miscibility of the ionic liquid in water; however, the replacement by $[Tf_2N]$ ion decreases the water miscibility. Changing the length of alkyl chain can tune the miscibility of ionic liquid in water [33].

For the properties of ionic liquid, there is a free web database available at National Institute of Standard and Technology (NIST)[35], which provides access to thermodynamic and transport properties of ionic liquids and contains information of more than 200 ions and 300 ionic liquids.

1.1.5 Structure of ionic liquids determines the properties

The relationships between properties and structures need to be understood before selecting and synthesizing the ionic liquids. Previous research demonstrated that the anion for any given cation class has the most significant effects on many of the properties. The alkyl chain length and functional alkyl chain added on cations are also important.

1.1.5.1 Melting point

Generally, ILs consisting of large and unsymmetrical ions have lower melting points [36]. Thus, relatively small and symmetrical ions, such as halide anion Cl often produce higher melting point salts, while larger amide anions, such as [Tf_2N], often produce room-temperature Pyridinium based ILs that generally have higher melting points than imidazolium ILs [37]. Table 1.1 lists the melting points for several 1-alkyl-3-methylimidazolium ionic liquids. The long alkyl chain IL causes a decrease in melting point initially, followed by an increase with longer alkyl chains. For a [PF_6] anion, the melting points decrease as [EMIm] > [BMIm] >[HMIm], however, if the alkyl chain length increased beyond a certain length, for instance, 8-10 carbons for 1-alkyl-3-methylimidazolium cations, the meting point increases instead of decreasing due to the difficulty of ion packing. Substituation at the C2-position of imidazolium ring (Figure 1.2) increases the melting point due to aromatic stacking or methyl-π stacking between cations. For the same cation, large, more asymmetrical anions have lower melting points, such as triflate ([TfO]) and [Tf_2N]. [Tf_2N] has relatively lower melting points probably due to the electron delocalization and the anion's inability to hydrogen bond [38]. The main factors affecting the melting points of ILs are the size, the symmetry of the ions, the distribution of charge on the ions, H-bonding ability and van der Waals interactions [39].

Table 1.2 Melting points of ionic liquids

Ionic liquids	Melting Points [°C]	Reference
[BMIm][Cl]	41	[41]
[BMIm][I]	-72	[41]
[BMIm][PF_6]	10	[41]
[BMIm][BF_4]	-81	[42]
[BMIm][$AlCl_4$]	65	[43]
[EMIm] [$AlCl_4$]	84	[43]
[EMIm] [PF_6]	58-60	[12]
[EMIm] [TfO]	9	[38]
[EMIm] [Tf_2N]	4	[38]
[HMIm] [PF_6]	-61	[42]

1.1.5.2 Density

ILs are usually denser than water. The densities of ionic liquids slightly decrease with increasing temperature. The effects of anions on the densities of 1-Butyl-3-methylimidazolium ionic liquids are shown in Table 1.2 [1]. For [BMIm] ILs, the density follows the order as: [methide] > [Tf_2N] > [PF_6] > [triflate] > [BF_4] > [dicyanamide(Dca)]. Therefore, the density of ILs increases with molecular weight of the anion. The larger anion has relatively higher density. With increasing alkyl chain length on cation, the density decreases. For example, the density of [EMIm][Tf_2N] is larger than [BMIm][Tf_2N]. Addition of methyl group on the C2 carbon reduces density, for instance, [EMIm][Tf_2N] > [EMMIm][Tf_2N]; [BMIm][BF_4]> [BMMIm][BF_4] [40].

Table 1.3 Densities of different anions for [BMIm] ionic liquids

Anion	Density (g cm^{-3})	references
$[BF_4]$	1.17 (30 °C)	[1]
$[PF_6]$	1.37 (30 °C)	[1]
$[CF_3SO_3]$	1.29 (20 °C)	[1]
$[CF_3CO_2]$	1.209 (21 °C)	[1]
$[Tf_2N]$	1.429 (19 °C)	[1]
[Triflate]	1.301 (22.6 °C)	[40]
[Dca]	1.058 (24.0 °C)	[40]
[Methide]	1.563 (24.5 °C)	[40]

1.1.5.3 Viscosity

Ionic liquids are often more viscous than conventional organic solvents. The viscosity data of a number of ionic liquids are shown in Table 1.4. It is shown that the viscosity of ionic liquids is several orders higher than water, which is 0.894 cP at 25 °C and acetone is 0.306 cP at 25 °C. As usual, the viscosity decreases with temperature, sometimes substantially. For $[HMIm][PF_6]$, the viscosity decreases by more than 50% when the temperature is only increased about 10 °C from 20 °C to 30 °C, which is observed with $[HMIm][BF_4]$ similarly.

For ILs with the same anion, the viscosity increases with alkyl chain length due to stronger van der Waals interactions [38]. As shown in Table 1.4, at 20 °C, for the $[BF_4]$ anion, the viscosity with an [HMIm] cation is 314 cP, for [BMIm] 154 cP and for [EMIm], 66.5 cP. The more asymmetrical cations have a lower viscosity. The viscosity of 1-alkyl-3-methylimidazolium salts can be decreased by using highly

branched and compact alkyl chains. Phosphonium ILs have higher viscosities than imidazolium ILs [46]. The effect of cation is not as important as changing the nature of the anion [46]. For the same cation, the viscosity decreases following the order:[Cl] > [PF_6] > [BF_4] ≈ [NO_3] >[Tf_2N] [1]. [EMIm] salts were reported to have the lowest viscosity with the combinated effects of sufficient side chain mobility and low molecular weight [38].

Table 1.4 Viscosity data for ionic liquids

Ionic liquids	Temperature [°C]	Viscosity [cP]	reference
[BMIm][I]	25	1110	[41]
[BMIm][BF_4]	25	219	[41]
[BMIm][PF_6]	25	450	[41]
[EMIm][Tf_2N]	25	28	[44]
[BMIm][Tf_2N]	25	69	[38]
[EMIm][BF_4]	20	66.5	[45]
[BMIm][BF_4]	20	154	[45]
[HMIm][BF_4]	20	314	[45]
[HMIm][BF_4]	30	177	[45]
[BMIm][PF_6]	20	371	[45]
[HMIm][PF_6]	20	680	[45]
[HMIm][PF_6]	30	363	[45]
[OMIm][PF_6]	20	866	[45]

Huddleston *et al*. [41] investigated a series of 1-alkyl-3-methylimidazolium cations. They reported that increasing the alkyl chain length from butyl to octyl increases the hydrophobicity and the viscosity of the ionic liquid; whereas densities and surface tension values decrease. It should be noted that changing the length of one or both alkyl chains on the cation does not necessarily result in a monotonous increase in the viscosity. For example, Bonhote *et al.* [47] reported that for $[Tf_2N]$ IL, replacing a butyl substituent by a methoxyethyl would decrease the viscosity by increasing the chain mobility, but no such effect could be observed.

1.1.5.4 Thermal stability and heat capacity

The thermal stability and heat capacity are important for ILs being used as both reaction media (especially for exothermic reactions) and as absorbents. For imidazolium ILs, the suggested order of relative stabilities for different anions are: $[PF_6] > [Tf_2N] \approx [BF_4] >$ [halides] [48]. The decomposition temperature on a series of [BMIm] ILs with various anions follows the order: $[Cl] < [Br] < [Dca] < [BF_4] < [CF_3SO_3] < [Tf_2N]$. For $[Tf_2N]$ ILs, the [BMIm] decomposes more easily than [BMMIm]. The thermal decomposition temperatures for several ionic liquids are listed in Table 1.5. Compared with anions, the alkyl chain length does not affect thermal stability significantly. For instance, for $[EMIm][BF_4]$, it is 412 °C and 403 °C for $[BMIm][BF_4]$. When the anion is changed to $[PF_6]$, it reduces to 349 °C.

Table 1.5 Thermal decomposition temperatures of ionic liquids

Ionic Liquid	Temperature onset for decomposition [°C]	References
[BMIm][I]	265	[41]
[BMIm][Cl]	254	[41]
[BMIm][BF_4]	403	[41]
[BMIm][PF_6]	349	[41]
[EMIm][Tf_2N]	455	[48]
[BMIm][Tf_2N]	439	[41]
[HMIm][PF_6]	417	[41]
[OMIm][PF_6]	376	[41]
[EMIm][BF_4]	412	[48]
[EMIm][CF_3SO_3]	~440	[38]

The effects of anions on heat capacity follow the order: [Br]<[Cl] <[BF_4]<[Dca] <[PF_6]<[TfO]<[Tf_2N]<[$C(CF_3SO_2)_3$] [40]. It is obvious that the larger the anion, the higher the heat capacity. For ILs with the same anion, alkyl substituent on the cation increases the heat capacity. Adding methyl group on the C2 carbon shows the same trend, except [Tf_2N] ILs.

1.1.5.5 Surface tension

Surface tension is a property of the surface of a liquid in contact with air, caused by the attraction of the liquid molecules due to various intermolecular forces. The surface tension plays an important role in the way liquids behave. Several ionic liquid surface tension data are given in Table 1.6. It is lower than water, which is 71.97 dyn/cm at 25 °C, but higher than some organic.

Table 1.6 Surface tension data of ionic liquids at 25 °C ([41])

Ionic Liquid	Surface tension [dyn/cm]
[BMIm][I]	54.7
[BMIm][BF_4]	46.6
[BMIm][PF_6]	48.8
[EMIm][Tf_2N]	455
[BMIm][Tf_2N]	37.5
[HMIm][PF_6]	43.4
[OMIm][PF_6]	36.5

1.1.5.6 Water miscibility

Seddon *et al*. [45] indicated that for imidazolium-based ionic liquids, halide (Cl, Br, I), ethanoate([AcO]), nitrate ([NO_3]) and trifluoroacetate ([CF_3CO_2]) salts were totally miscible with water, while [PF_6] and [Tf_2N] salts were immiscible. The miscibility of [BF_4] and [CF_3SO_3] salts depends essentially on the substituents on the cation [49]. Olivier-Bourbigou and Magna [1] pointed out that for [PF_6] based salts, the shorter symmetric substituted 1,3-dimethylimidazolium [PF_6] salt became water-soluble. Increasing the alkyl chain length of ILs decreased the water miscibility at room temperature. Huddleston *et al*. [41] reported that the solubility of [BF_4] salts in water varied with temperature. For example, at room temperature [BMIm][BF_4] was completely water-miscible, while the phase splits at 0 °C [26].

Jain *et al*. [32] reviewed new functionalized imidazolium ionic liquids. Some of them are miscible with water, such as 1-Methyl-3-ethoxyl imidazolium tetrafluoroborate ([C_2OHmim][BF_4], and 3-alkoxymethyl-1-methylimidazolium

tetrafluoroborates [C_4Omim] [BF_4]. In addition, they have relatively low viscosity (65 cP ~ 138 cP at 30°C) compared with other ILs. They also show that [C_2OHmim][PF_6] and [C_3Omim][PF_6] are totally miscible with water at room temperature, although imidazolium-based [PF_6] ionic liquids are usually water immiscible.

Zhang *et al*. [50] measured the density and viscosity of [EMIm][BF_4] and water. The densities and viscosities of mixtures declined sharply when the mole fraction of water increased to 50%. Rodriguez *et al*. [51] investigated the density and viscosity of binary mixtures of water with [EMIm][$EtSO_4$], [EMIm][TfO] and [EMIm][TFA]. It was shown that the ILs incorporating the fluorinated anions ([TfO] and [TFA]) had higher densities and lower viscosities than those with non-fluorinated anion ([$EtSO_4$]). The introduction of hydroxyl groups on the alkyl chain considerably modifies the miscibility of water in ILs.

In general, the melting point, thermal stability, heat capacity, viscosity and density mainly depend on the size and symmetry of ions. The larger and more unsymmetrical ions the lower melting points, the higher decomposition temperature, the larger heat capacity and the lower water miscibility. The effects of the alkyl chain length and substituents on cations should also be considered for their specific applications.

1.1.5.7 Purity effect

All of properties shown here are affected by the impurities of ionic liquids significantly. For example, at 20 °C, a 1.8 molal solution of [Cl] in [EMIm][BF_4]

will increase viscosity to 92.4 $mPas^{-1}$ from 66.5 $mPas^{-1}$ [45]. Water content is another important factor for changing physical properties. Dry [DMIm][Tf_2N] decomposes at 439 °C, but the water equilibrated [DMIm][Tf_2N] will decompose at 394 °C [41]. Therefore, during the synthesis process and storage, the ILs have to be purified and kept dry, otherwise, the properties, such as density, viscosity, surface tension, solubility, etc. will be changed considerably.

1.1.5.8 Challenges

Using ionic liquids only face several challenges. Firstly, the cost of making ILs is relatively higher than conventional solvents, which makes large-scale solvent replacement difficult. The Scurto laboratory is involved in the understanding and development of sustainable methods to make ionic liquids in large-scale. Secondly, higher viscosity of ionic liquids often lowers mass transfer rates; lower diffusivity generally leads to lower reaction rates in a mass transfer limit reactions. Thirdly, a lower solubility of reaction gases, such as H_2, CO, O_2, makes it hard to apply ILs into gas reactions. Fourthly, despite the huge theoretical number of ionic liquids are liquids, (e.g. $\sim 10^{14}$)[34], the vast majority are actually solids having melting points above 100°C. Finally, the limited information and data are available on structural variations, chemical and physical properties, corrosion and toxicity, etc. All of these challenges will limit their applications. These challenges must be overcome for further process development.

1.2 Compressed Gases

1.2.1 Carbon dioxide

Using carbon dioxide (CO_2) as green reaction media has gained more and more research interests due to environmental and nontoxic properties. Carbon dioxide is nonflammable, nontoxic and inexpensive. The most important aspect of CO_2 is its tunable properties, which can change significantly with temperature and pressure. CO_2 has a relatively low critical temperature (31.1 °C) and moderate critical pressure (73.8 bar). By changing the operating conditions, the properties of CO_2 can be adjusted between liquid-like and gas-like.

Besides of being a green solvent, CO_2, also known as R744, is a natural refrigerant, which had already been known for more than a century. A Global Warming Potential (GWP) with CO_2 is 1,300 times less than with the most used refrigerant R-134a [52]. As a refrigerant, carbon dioxide has a number of advantages: low cost, non-combustible, a high cooling capacity, available worldwide in the required qualities. Numerous tests on vehicles with CO_2 A/C systems have shown that CO_2 does provide cooling performance comparable to R-134a [53-54].

However, compared to 20 to 30 bar pressure on the high side for R-134a, CO_2 requires extremely high operating pressures, 25 to 30 bar on the low side and up to 125 bar on the high side, because CO_2 remains in the gaseous state and does not condense in the refrigeration cycle. As a result, the front heat exchanger is called a "cooler" rather than a condenser.

1.2.2 Gas expanded liquids (GXLs) / CO_2 expanded liquids (CXLs)

In recent years, Gas-Expanded liquids (GXLs) , more specifically CO_2-Expanded liquids (CXLs) have been applied to separations, extractions, reactions and other applications successfully. Jessop and Subramaniam [55] calssified CXLs into three types: Type I liquids are not able to dissolve sufficient CO_2 to induce a large expansion of the solvent volume, for instance water. Type II are liquids having ability to dissolve large amount of CO_2, such as methanol, acetone, etc. Type III are liquids dissolving relatively large amounts of CO_2, such as ionic liquids, liquid polymers, crude oil, etc., but whose volume does not expand much. Some physical properties of CXLs are changed compared with the pure liquid, such as density, viscosities, etc. But some of them change very little over certain pressure/compositions, such as polarity.

Scurto *et al.* [56] reviewed the science, technologies, fundamentals and applications of GXLs and CXLs, and showed GXLs/CXLs have many benefits with combination of dense CO_2 and liquids. It has been found that CO_2 can increase the solubility of reaction gases in GXLs/CXLs up to two orders of magnitude relative to organic solvents even in ambient conditions.

The presence of CO_2 in the liquid phase can significantly affect the transport properties. As more CO_2 dissolves in the liquid state, the viscosity decreases accordingly. Sih *et al.* [57] reported the viscosity of methanol with CO_2 pressure at 40°C. The viscosity decreases nearly 80% from pure methanol to CXL methanol at 77 bar. This viscosity reduction is especially striking for ionic liquids, which is generally more viscous than organic solvents. The Scurto group has measured the

viscosity of a number of ILs. The viscosity of [HMIm][Tf_2N] decreases approximately 80+% with up to 60 bar of CO_2 at 40°C. As the viscosity decreases, the diffusivity correspondingly increases. Eckert *et al.* [58] reported the diffusivity of benzene in methanol and CO_2 mixtures at 40°C and 150 bar. The diffusivity of benzene increases by over 200%. These enhanced transport properties allow enhancement in mass transfer during reactions.

Furthermore, Gas expanded liquids/CO_2 expanded liquids (GXLs/CXLs)[55, 59-65] show reaction benefits, such as enhanced solubility of gaseous reactants and catalyst miscibility compared to supercritical CO_2, higher turnover frequencies, milder operating pressure (tens of bars) compared to hundreds of bar with $scCO_2$, potential for catalyst recovery and comparable or better product selectivity than in neat organic solvent or $scCO_2$ [63-65].

However, even operating in supercritical conditions, CO_2 is still a poor solvent for polar and low volatile components. Moreover, despite its high solubility in organic substrate, many homogeneous catalysts are not very soluble in CO_2, which limits the application of CO_2 as solvent, especially for catalytic reactions.

1.2.3 Refrigerant: 1,1,1,2-tetrafluoroethane

The most common refrigerant gas used in automobile air conditioners today is 1,1,1,2-Tetrafluoroethane (R-134a), which replaced dichlorodifluoromethane (R-12) in the early 1990s. R-12 has ozone depleting properties, while R-134a does not. However, both have significant global warming potential (GWP = 1300 for R-134a, compared to 1 for carbon dioxide) [52]. R-134a is non-toxic, non-flammable and non-corrosive and it is safe for normal handling. The manufacturing industries use it in plastic foam blowing. Pharmaceuticals industry uses it as a propellant for

aerosolized delivery systems. It exists in gas form when expose to the environment as the boiling temperature is -26.1°C. It has critical points as 101.5° C and 40.6 bar.

However, the European Community has recently decided to phase out R-134a in new vehicles starting in 2011, with a complete phase-out by 2017. The European rules require any new refrigerants must have a global warming potential of less than 150. CO_2 is a promising alternative refrigerant as replacement of R-134a. However, R-134a use will continue in much of the rest of the world for the foreseeable future. Both R-134a and CO_2 were investigated here as refrigerants in automobile absorption air conditioners.

1.3 Combination of ILs and Compressed Gases

1.3.1 Benefits

There are several challenges by using ionic liquids only, including higher viscosity, existing as solids for most of them, limited solubility for reaction gases, etc. Combining ionic liquids and compressed gases has a number of advantages. Both CO_2 and R-134 have a high solubility in ionic liquids, which results in dramatic decrease of the viscosity of the liquid mixture [66]. For CO_2 and ionic liquids, the phase behavior of IL with CO_2 is unique. CO_2 is very soluble in the ionic liquids and in contrast, the ionic liquids are immeasurably insoluble in the pure CO_2 phase. Therefore, IL and CO_2 mixture does not become miscible (critical) even at elevated pressures, which makes them advantageous for be reaction media of biphasic systems.

Moreover, compressed CO_2 can increase the solubility of reaction gases (H_2 and O_2) in ILs [67-68], and dramatically decreases the melting point of many ionic solids, even inducing melting over 100°C below some ionic solids' normal melting points, which was demonstrated by Scurto *et al*. [69-70] Concurrent studies in the Scurto laboratory reveal that the viscosity of the IL/CO_2 mixture decreases approximately 80+% with up to 60 bar of CO_2 at 40°C compared with pure IL. This decrease in viscosity results in an increase of diffusivity. The diffusivity predicted by the viscosity in the ionic liquid has approximately a 3 fold improvement over the same pressure range. Thus, the combination of ILs and compressed gases may overcome many of the limitations of pure ionic liquids and expand its applications widely.

1.3.2 Applications of ILs and compressed gases

1.3.2.1 Reaction media

There are a number of reactions using IL-CO_2 biphasic system as reaction media: hydrogenation, hydroformylation, oxidation, C-C coupling reactions, metathesis, dimerisation- polymerization, etc. Dyson and Geldbach [71] reviewed the reactions in ionic liquids in book *metal catalyzed reactions in ionic liquids* and covered the literature till early 2005. Recently, Keskin et.al [72] reviewed the applications of the solvent systems composed of IL and supercritical fluids with an emphasis on supercritical carbon dioxide ($scCO_2$). More recently, the Scurto group used IL-CO_2 for hydrogenation, hydroformylation reactions, the detailed phase behavior for these two reactions and literature survey are given in Chapter 7.

1.3.2.2 Solute recovery and solvent regeneration from ILs using $scCO_2$

The negligible vapor pressure of ILs and the insolubility in CO_2 also facilitate efficient extraction of products from ILs. The advantages of using supercritical CO_2 to recovery solute from the solvent are: nontoxic, low cost, no cross contaminations, ease of separation from the products with minimal pollution, etc. Blanchard and Brennecke [73] reported a wide variety of solutes can be extracted from [BMIm][PF_6] with scCO_2, with recovery rates greater than 95%. Scurto *et al.* [74] demonstrated that the addition of CO_2 can induce phase split in [BMIm][PF_6]–methanol system and phase separation in IL–water systems [75]. Aki *et al.* [76] measured vapor–liquid–liquid equilibrium on eight different IL–CO_2–organic solvent systems at 25 °C and 40 °C. Mellein and Brennecke [77] investigated the ability of compressed CO_2 to induce liquid/liquid phase separation in mixtures of ILs and organic solvents, such as Acetonitrile, 2-butanone, and 2,2,2-trifluoroethanol. [HMIm][Tf_2N], 1-n-hexyl-2,3-dimethylimidazolium bis(trifluoromethylsulfonyl)amide ([HMMIm][Tf_2N]), 1-n-hexyl-3-methylimidazolium triflate ([HMIm][TfO]), and ethyl-dimethyl-propylammonium bis (trifluoromethylsulfonyl)amide ([NMe_2EtPr][Tf_2N]), were chosen to vary hydrogen-bond-donating and -accepting abilities of the ionic liquids. Strong hydrogen bonding between the ionic liquid and the organic component was found to make it more difficult for CO_2 to induce a liquid/liquid-phase separation. Saurer *et al.* [78] showed compressed CO_2 at 25ºC can be used to remove ammonium bromide (NH_4Br), ammonium chloride (NH_4Cl), and zinc acetate ($Zn(CH_3COO)_2$) from [HMIm][Tf_2N] with dimethylsulfoxide or acetonitrile mixtures.

Zhang *et al.* [79] studied the phase behavior of CO_2–water–1-n-Butyl-3-methyl-imidazolium tetrafluoroborate ([BMIm][BF_4]) system in the temperature range of 5 to 25 °C and pressures up to 160 bar. The distribution coefficients of the IL, water, and CO_2 in the IL-rich phase and water rich phase are discussed in detail. Increase of pressure and decrease of temperature are favorable to the separation of the IL and water. Zhang *et al.* [80] investigated the effect of CO_2 on the phase behavior of the reaction system and equilibrium conversion for esterification of acetic acid and ethanol in ionic liquid (1-Butyl-3-methylimidazolium hydrogen sulfate, [BMIm][HSO_4]) at 60.0 °C and up to 150 bar. It was demonstrated that there was only one phase in the reaction system in the absence of CO_2. The reaction system underwent two-phase→three-phase→two-phase transitions with increasing CO_2 pressure. The pressure of CO_2 or the phase behavior of the system affected the equilibrium conversion of the reaction markedly. Zhang, Han and *et al.* [80] studied CO_2/acetone/1-n-Butyl-3-methyl-imidazolium hexafluorophosphate ([BMIm][PF_6]) system at 313.15 K and at pressures up to 150 bar. The ternary system forms two phases at most conditions. At pressures from 4.9 to 8.1 MPa, a three-phase region appeared in the system.

Najdanovic-Visak *et al.* [81] showed phase changes in ionic liquid + water systems, induced by addition of ethanol and supercritical carbon dioxide, which allows reaction cycles to proceed as depicted. They also demonstrated that the surprisingly varied phase behavior of [BMIm][PF_6]–ethanol–water–CO_2 mixtures,

ranging from total miscibility through partial miscibility to nearly complete phase separation, can be very useful in reaction/separation cycles.

Bortolini *et al.* [82] used $scCO_2$ to recovery the epoxides in several ILs [BMIm][X] (X = BF_4, PF_6, TfO and Tf_2N) from the epoxidation reaction of several electron-deficient olefins (2-cyclohexen-1-one and its derivatives). Kroon *et al.* [83] recovered N-acetyl-(S)-phenylalanine methyl ester (APAM), the product of asymmetric hydrogenation of methyl-(Z)-acetamidocinnamate (MAAC) from [BMIm][BF_4] by using $scCO_2$. In addition, the product APAM can also be precipitated out of the ionic liquid phase using $scCO_2$ as an anti-solvent, because the solubility of APAM in [BMIm][BF_4]–$scCO_2$ mixture was lower than the solubility of APAM in pure [BMIm][BF_4] at ambient conditions. Yoon *et al.* [84] employed $scCO_2$ to extract the products of Heck reaction (C-C coupling reaction) between iodobenzene and olefins using [BMIm][PF_6] as solvent. It is possible to recycle the catalyst four times without loss of activity.

1.3.2.3 Gas sensing materials

ILs with their distinctive properties are potential new materials for gas detections. Liang *et al.* [85] developed a Quartz Crystal Microbalance (QCM) device of using ionic liquids as the sensing materials for organic vapors. The sensing mechanism is based on the fact that the viscosity of the ionic liquid membrane decreases rapidly due to solubilization of analytes in the ionic liquids. The QCM sensor demonstrated a rapid response (average response time of < 2 s) to organic vapors with an excellent reversibility because of the fast diffusion of analytes in ionic

liquids. Jin *et al.* [86] investigated a novel sensor array using seven room-temperature ionic liquids (ILs) as sensing materials and a quartz crystal microbalance (QCM) as a transducer to detect of organic vapors, such as Ethanol, dichloromethane, benzene, and heptane at ambient and elevated temperatures. Selected organic components were taken as representative gas analytes for various kinds of environmental pollutants and common industrial solvents.

Recently, supercritical carbon dioxide ($scCO_2$) was used to recover contaminants from IL extracts to clean contaminated soils [87]. ILs are used to dissolve soil contaminants at ambient conditions and then $scCO_2$ extraction is chosen to contaminants. Naphthalene was used as the model component to represent a group of soil contaminants, and 1-*n*-Butyl-3-methylimidazolium hexafluorophosphate ([BMIm][PF_6]) was used as the IL. The results demonstrated the amount of naphthalene remaining in the soil after extraction was below the allowable contamination limit.

1.3.2.4 Gas separation

Anthony *et al.* [88] measured the selective solubility of gases in ionic liquids, which leads to the possibility for gas separations using absorbers, liquid-supported membranes, scrubbers, etc. Carbon dioxide exhibits relatively high solubility in imidazolium-based ionic liquids; while oxygen, nitrogen, hydrogen, carbon monoxide, argon have lower solubility, Brennecke and Maginn [89] studied natural gas treatment by removing of acid gases using ionic liquids.

Bates *et al.* [90] synthesized "Task-specific" Ionic Liquids (TSILs) for selective gas solubilities. The structure of an imidizolium-based cation was modified by appending an amine substitutent, yielding an IL with elevated carbon dioxide capture ability from gas mixtures. Noble group has been using ionic liquids to separate the gases. Bara *et al.* [91] investigated CO_2, O_2, N_2 and CH_4 using a four imidazolium supported ionic liquid membrane (SILM) configuration. These fluoroalkyl-functionalized room-temperature ionic liquids were found to exhibit ideal selectivities for CO_2/N_2 separation that were lower than their alkyl-functionalized analogues, but higher ideal selectivity for CO_2/CH_4 separation. Bara *et al.* [91] also reviewed RTILs as media for CO_2 separation appears especially promising with imidazolium-based salts. They found the solubilities of gases, particularly CO_2, N_2, and CH_4, have been studied in a number of RTILs. Process temperature and the chemical structures of the cation and anion have significant impacts on gas solubility and gas pair selectivity. Koval *et al.* [92] studied properties of imidazolium-based room temperature ionic liquids that effect CO_2 solubility and selectivity for CO_2/N_2 and CO_2/CH_4 gas separations. Koval *et al.* [93] also used ionic liquids for membrane-based and electrochemically - driven gas separations.

Bara *et al.* [94] studied the effect of "Free" cation substituent on gas separation performance of polymer-room-temperature ionic liquid composite membranes. Functional groups attached to the imidazolium cation include alkyl, ether, nitrile, fluoroalkyl, and siloxane functionalities. The poly(RTIL)-RTIL composites were homogeneous, optically transparent solids and exhibited high

stability. The presence of 20 mol% "free" RTIL within the poly(RTIL) matrix was shown to increase CO_2 permeability by approximate 100-250% compared with the pure poly(RTIL) membranes, which were utilized as gas separation membranes and tested for their permeabilities to CO_2, N_2, and CH_4.

1.3.2.5 Extract metal chelates from ILs

Supercritical CO_2 can also be used to extract metal chelates from ILs. Mekki *et al.* [95] extracted Cu(II) from [BMIm][Tf_2N] using the trifluoroacetonate or hexafluoroacetonate chelating agents with a contingent addition of tributylphosphate as a CO_2-philic synergist agent to stabilize the metal chelates. The extraction efficiencies varied somewhat with the experimental arrangement (static/dynamic extraction, with/without tributylphosphate) but generally exceeded 95%. Mekki *et al.* [96] also used fluorinated-diketones, hexafluoroacetylacetonate and 4,4,4-trifluoro-1-(2- thienyl)-1,3-butanedione, to extract Eu(III) and Ln(III) from [BMIm][Tf_2N] or from aqueous solution via [BMIm][Tf_2N]. In some experiments, tributylphosphate was added to stabilise the metal chelates, and extraction efficiencies exceeding 87% were achieved.

1.3.2.6 CO_2 storage and sequestration

Chinn *et al.* [97] reported a process and method for separation of CO_2 from a gaseous stream such as natural gas. The ionic liquids, [BMIm][BF_4] and [BMIm][acetate], were used as adsorbents to selectively extract the CO_2 yielding a gaseous stream with a greatly reduced CO_2 content. The ionic liquid can then be easily regenerated and recycled. Sharma *et al.* [98] discovered a cost-effective carbon

dioxide absorbing ionic liquid, tri-(2-hydroxyethyl) ammonium acetate in Knoevenagel condensation.

Palgunadi *et al.* [99] measured solubilities of carbon dioxide in a series of fluorine-free room temperature ionic liquids (RTILs), dialkylimidazolium dialkylphosphates and dialkylimidazolium alkylphosphites at 40 ~60 °C and pressures up to 50 bar. The CO_2 solubility in a phosphorus-containing RTIL was found to increase with the increasing molar volume of the RTIL. In general, dialkylimidazolium dialkylphosphate exhibited higher absorption capacity than dialkylimidazolium alkylphosphite with an same cation. Among RTILs tested, 1-butyl-3-methylimidazolium dibutylphosphate [BMIM][Bu_2PO_4] and 1-Butyl-3-methylimidazolium butylphosphite [BMIM][$BuHPO_3$] exhibited similar Henry's law coefficients to 1-butyl-3-methylimidazolium bis (trifluoromethylsulfonyl)amide ([BMIm][Tf_2N]) and 1-butyl-3-methylimidazolium tetrafluoroborate ([BMIm][BF_4]), respectively.

Lee *et al.* [100] investigated using ionic liquids as SO_2 absorbents to separate SO_2 in SO_2/O_2 gaseous mixtures from the sulfuric acid decomposer. SO_2 absorption rate in ILs was mainly influenced by anions of ILs. [BMIm][Cl] and [BMIm][OAc] showed the highest SO_2 solubility in the tested ILs at 50 °C and 0.67 atm SO_2 . Interestingly, [BMIm][OAc] showed irreversibility in the cycle of absorption and desorption. [BMIm][$MeSO_4$] showed moderate SO_2 solubility and good reversible cycles of absorption and desorption. Huang *et al.* [101] demonstrated that ionic

liquids can reversibly absorb large amounts of molecular SO_2 gas at under ambient conditions, which is useful for SO_2 removal in pollution control.

Kulkarni *et al.* [102] proposed a new, simple, and efficient approach for the absorption of dioxins from gaseous streams using thermally stable ionic liquids. Dioxins are highly toxic compounds from incineration and combustion sources. The absorption process of non-chlorinated and chlorinated dibenzo-p-dioxin compounds was studied in the temperature range 100 ~ 200 °C. Imidazolium-, ammonium-, and guanidinium-based ionic liquids were designed for this specific purpose. It was observed that imidazolium cations having long alkyl side chains exhibit the highest absorption capacities, whereas the anion [Dca] possesses higher absorption capacity than other anions studied. Kulkarni *et al.* [103] also did a comparative study on absorption and selectivity of organic vapors by a series of imidazolium, ammonium, and guanidinium-based ILs containing several types of anions. Organic solutes were chosen for the absorption studies include 1,4-benzodioxane, biphenyl, xanthene, and menthol. Absorption of water vapor was also studied along with the organic solutes. Absorption values of more than 25 000 ppm were observed in some ionic liquids. Desorption of organic vapors from ionic liquids was successfully carried out by applying a vacuum. Further, it was observed that the same ionic liquid can be repeatedly reused several times for absorption.

Zhang *et al.* [104] synthesized a new type of "task specific ionic liquid", tetrabutylphosphonium amino acid $[P(C_4)_4][AA]$ by the reaction of tetrabutylphosphonium hydroxide $[P(C_4)_4][OH]$ with amino acids, including glycine,

L-alanine, L-beta-alanine, L-serine, and L-lysine. The $[P(C_4)_4][AA]$ supported on porous silica gel effected fast and reversible CO_2 absorption when compared with bubbling CO_2 into the bulk of the ionic liquid. The CO_2 absorption capacity at equilibrium was 50 mol % of the ionic liquids. The CO_2 absorption mechanisms of the ionic liquids were affected by water content.

ILs are also used for storage and delivery of hazardous specialty gases such as phosphine (PH_3), arsine (AsH_3) and stibine (SbH_3)[74]. The mechanism of absorption is that the desired gases (BF_3 and PH_3) are chemically bonded to ILs, then high purity gas is released by pulling the vacuum on the IL–gas complex.

1.3.2.7 Working fluids

Refrigerants are very soluble in ionic liquids. The refrigerant/ionic liquid pairs are useful as working fluids in absorption cooling and heating systems. Shiflett and Yokozeki [105] invented an absorption refrigeration cycle utilizing ionic liquid as working fluid, where the IL absorbs the refrigerant gas in absorber and releases the high pressure gas in the generator with heat. The invention also provides the execution of absorption cycles utilizing refrigerant/ionic liquid pairs. Currently, the Scurto group was also considering the use of ILs and compressed gases for absorption refrigeration applications. The detailed feasibility studies are presented in Chapter 6.

1.4 Overall Objectives

The objectives of this research are to investigate high pressure global phase behavior and measure phase equilibrium of ionic liquids and compressed gases for

their applications as reaction media for hydrogenation and hydroformylation reaction and as working fluids for absorption air conditioning systems through both experimental and thermodynamic modeling studies.

This research investigates imidazolium ionic liquids with various alkyl groups and anions and two compressed gases: carbon dioxide (CO_2) and 1,1,1,2-tetrafluoroethane (R-134a). The global phase behavior needs to be investigated to determine the operating conditions and phase transitions in equilibria, such as vapor-liquid, vapor-liquid-liquid, liquid-liquid, etc. Phase equilibria data are also needed to quantify the solubility of each component in each phase at equilibria. The experimental data along with literature data allow comparison of the effects of both the anion and the alkyl-chain length of the cation on the phase behavior and equilibrium. For further process design for current and other IL/compressed gases applications, to develop a thermodynamic model of the high-pressure phase behavior and equilibria is essential. Moreover, the feasibility of using ionic liquids and CO_2/R-134a as working fluids in novel absorption refrigeration systems for vehicles needs to be evaluated based on a thermodynamic model. The hydrogenation and hydroformylation reactions kinetics and results need to be fully understood by the phase behavior and equilibrium results and knowledge.

The technologies used in IL/compressed gases investigations are not only be limited to reactions or absorption refrigeration, but also can be extended to other general applications.

1.5 Outlines of Chapters

Chapter 2 introduces all of equipments and detailed experimental procedures used to measure all of properties in this work. Which include the high pressure vapor-liquid equilibrium set up to measure the solubility and critical points of compressed gases in ionic liquids, high pressure autoclaves to measure the global phase behavior, high pressure UV-Vis cell to measure polarities of compressed gases and different ILs, GC and ICP to measure the liquid-liquid extraction by using ILs. Chapter 2 also describes the ionic liquid synthesis, analysis method and lists all of materials used in investigations.

Chapter 3 reviews the equation of state models to correlate the VLE and other equilibria data of ionic liquids and compressed gases. Different mixing rules are also included. The phase equilibrium software, PE2000, is introduced as well.

Chapter 4 presents a global phase behavior study for ionic liquids and compressed gases. Most of ionic liquid and R-134a belong to type V, ionic liquid and CO_2 belong to type III, according to van Konynenburg and Scott classification indicating regions of multi-phase behavior. The effects of alkyl chain length and anion on local end critical point are studied. The global phase behavior prediction using GPEC are also presented.

Chapter 5 reports the phase equilibrium (solubility) of compressed gases and ionic liquids. Both experimental data and modeling results are presented at three isotherm runs for R-134a and CO_2. Peng-Robinson model with van der Waals 2 mixing rule is employed. The model predicts the vapor liquid equilibrium very well. But for mixture critical points, the prediction is much lower than experimental value due to the limits of equation of state.

Chapter 6 presents the feasibility study of using ILs as absorbents for CO_2 and R-134a in an absorption refrigeration system. The performance between adsorption cycle and conventional vapor compression cycle is compared by the cycle thermodynamic modeling.

Chapter 7 presents the results of phase behavior study of IL/CO_2 as reaction media for hydrogenation and hydroformylation reactions. The phase behavior with conversion is completely studied to determine the operating condition and explain the reaction results. The solubility and volume expansion data are used to help calculate the molarity of reactants to understand explain the apparent kinetics results with CO_2 pressure. The unique phase behavior of CO_2 and ILs help to develop a product separation technology by using supercritical gas extraction.

Chapter 8 shows the results of using CO_2 expanded liquid as reaction media for hydroformylation reaction. The phase behavior of reactant, product, CO_2 with/without syngas pressure are studied to define a boundary of reaction happened in one phase or biphasic. The solubility, volume expansion, molar volume in pure octane, pure nonanal, and mixture with conversion of 25%, 50%, 75% are measured. Peng-Robison equation of state is employed to correlate the VLE data and shows excellent regression. The binary interaction parameters are used to correlate the ternary system, which gives the good correlation in higher pressure and reasonable regression in lower pressure.

Chapter 9 completes the work with conclusions and gives recommendation for future research activities.

1.6 References

1. Olivier-Bourbigou, H. and L. Magna, *Ionic liquids: perspectives for organic and catalytic reactions.* Journal of Molecular Catalysis A: Chemical, 2002. **182**(183): p. 419-437.
2. Tomoharu and N. Sanyo, C.I. Ltd., Editor. 1999: JP
3. Mamantov, G., J. Caja, and T.D.J. Dunstan, *Low-temperature molten salt compositions containing fluoropyrazolium salts for battery electrolytes.* 1996: U.S. p. 5552241.
4. Davis, J.H., Jr and K.J. Forrester, *Thiazolium-ion based organic ionic liquids (OILs). Novel OILs which promote the benzoin condensation.* Tetrahedron Letters, 1999. **40**(9): p. 1621-1622.
5. Vestergaard, B., N.J. Bjerrum, I. Petrushina, H.A. Hjuler, R.W. Berg, and M. Begtrup, *Molten triazolium chloride systems as new aluminum battery electrolytes.* Journal of the Electrochemical Society, 1993. **140**(11): p. 3108-13.
6. Gabriel, S. and J. Weiner, *Ueber einige Abkömmlinge des Propylamins.* Ber., 1888. **21**(2): p. 2669-2679.
7. Hurley, F.H. and T.P. Wier, *Electrodeposition of metals from fused quaternary ammonium salts.* Journal of the Electrochemical Society, 1951. **98**: p. 203-6.
8. Wilkes, J.S., J.A. Leviskey, R.A. Wilson, and C.L. Hussey, *Dialkylimidazolium chloroaluminate melts: a new class of room-temperature*

ionic liquids for electrochemistry, spectroscopy and synthesis. lnorg. Chem., 1982. **21**: p. 1263-1264.

9. Parshall, G.W., *Catalysis in molten salt media.* J. Am. Chem. Soc. , 1972. **94**: p. 8716-8719.

10. Lee, C.W., *Diels-Alder reactions in chloroaluminate ionic liquids: acceleration and selectivity enhancement.* . Tetrahedron Letters, 1999. **40**(13): p. 2461-2464.

11. Tait, S. and R.A. Osteryoung, *Infrared study of ambienttemperature chloroaluminates as a function of melt acidity.* Inorg. Chem., 1984. **23**: p. 4352 - 4360.

12. Wilkes, J.S. and M.J. Zaworotko, *Air and Water Stable 1-Ethyl-3-methylimidazolium Based Ionic Liquids.* J. Chem. Soc.-Chem. Commun., 1992. **13**(S.): p. 965-967.

13. BASF. *BASILTM: Higher yield thanks to new acid scavengers*. 2004 [cited 2009 September 27]; Available from: http://www.basf.com/group/corporate/en/innovations/innovative-olutions/basil.

14. Brennecke, J.F. and E.J. Maginn, *Ionic liquids: innovative fluids for chemical processing.* . AIChE Journal 2001. **47**(11): p. 2384-2389.

15. Seddon, K.R. and A. Stark, *Selective catalytic oxidation of benzyl alcohol and alkylbenzenes in ionic liquids.* Green Chemistry 2002. **4**(2): p. 119-123.

16. Forsyth, S.G., J.; MacFarlane, D. R.; Forsyth, M. , *N-methyl-N-alkylpyrrolidinium tetrafluoroborate salts: ionic solvents and solid electrolytes.* Electrochimica Acta 2001. **46**(10-11): p. 1753-1757.

17. Buijsman, R.C., E. van Vuuren, and J.G. Sterrenburg, *Ruthenium-catalyzed olefin metathesis in ionic liquids.* Organic Letters 2001. **3**(23): p. 3785-3787.

18. Gordon, C.M., *New developments in catalysis using ionic liquids.* . Applied Catalysis, A: General, 2001. **222**(1-2): p. 101-117.

19. Rogers, R.D. and K.R. Seddon, *Ionic Liquids as Green Solvents*. ACS symposium series 856. 2003, Washington,DC: American Chemical Society.

20. Rogers, R.D. and K.R. Seddon, *Ionic Liquids: Industrial Application to Green Chemistry*. ACS symposium series 856. 2002, Washington,DC: American Chemical Society.

21. Kaar, J.L., A.M. Jesionowski, J.A. Berberich, R. Moulton, and A.J. Russell, *Impact of Ionic Liquid Physical Properties on Lipase Activity and Stability.* Journal of the American Chemical Society, 2003. **125**(14): p. 4125-4131. .

22. Walker, A.J. and N.C. Bruce, *Cofactor-dependent enzyme catalysis in functionalized ionic solvents.* Chemical communications (Cambridge, England), 2004. **22**: p. 2570-1.

23. Park, S. and R.J. Kazlauskas, *Improved preparation and use of room-temperature ionic liquids in lipase-catalyzed enantio- and regioselective acylations.* The Journal of organic chemistry, 2001. **66**(25): p. 8395-401.

24. Hayakawa, Y., R. Kawai, A. Hirata, J.-i. Sugimoto, M. Kataoka, A. Sakakura, M. Hirose, and R. Noyori, *Acid/Azole Complexes as Highly Effective Promoters in the Synthesis of DNA and RNA Oligomers via the Phosphoramidite Method* J. Am. Chem. Soc., , 2001. **123** (34): p. 8165 -8176.

25. Swatloski, R.P., S.K. Spear, J.D. Holbrey, and R.D. Rogers, *Dissolution of cellulose [correction of cellose] with ionic liquids*. Journal of the American Chemical Society, 2002. **124**(18): p. 4974-5. .

26. Swatloski, R.P.R., Robin Don; Holbrey, John David. *Dissolution and processing of cellulose using ionic liquids, cellulose solution, and regenerating cellulose*. 2003: PCT Int. Appl. p. 59pp.

27. Zhang, H., J. Wu, J. Zhang, and J. He, *1-Allyl-3-methylimidazolium chloride room temperature ionic liquid: A new and powerful nonderivatizing solvent for cellulose.* Macromolecules, 2005. **38**(20): p. 8272-8277. .

28. Haristoy, D. and D. Tsiourvas, *Novel Ionic Liquid-Crystalline Compounds Bearing Oxadiazole and Pyridinium Moieties as Prospective Materials for Optoelectronic Applications.* Chemistry of Materials 2003. **15**(10): p. 2079-2083.

29. Zhao, D.C., H.T. Xu, P. Xu, F.Q. Liu, and G. Gao, *Advances of polymerization in room temperature ionic liquids.* Prog. Chem. , 2005. **17**(4): p. 700-705.

30. Lu, W., A.G. Fadeev, B.H. Qi, and B.R. Mattes, *Fabricating conducting polymer electrochromic devices using ionic liquids.* J. Electrochem. Soc., 2004. **151**(2): p. H33-H39.

31. Cao, J.M., B.Q. Fang, J. Wang, M.B. Zheng, S.G. Deng, and X.J. Ma, *Ionic liquids for the convenient synthesis of functional inorganic nanomaterials.* Prog. Chem., 2005. **17**(6): p. 1028-1033.

32. Jain, N., A. Kumar, S. Chauhan, and S.M.S. Chauhan, *Chemical and biochemical transformations in ionic liquids.* Tetrahedron Letters, 2005. **61**(5): p. 1015-1060.

33. Marsh, K.N., J.A. Boxall, and R. Lichtenthaler, *Room temperature ionic liquids and their mixtures-a review.* Fluid Phase Equilibria, 2004. **219**(1): p. 93-98.

34. Holbrey, J.D. and K.R. Seddon, *Ionic Liquids.* Clean Prod. Proc., 1999. **1**(4): p. 223-236.

35. NIST. *Ionic Liquids Database- (ILThermo)*. 2009, Available from: http://ilthermo.boulder.nist.gov/ILThermo/mainmenu.uix.

36. Galinski, M., A. Lewandowski, and I. Stepniak, *Ionic liquids as electrolytes.* Electrochimica Acta, , 2006. **51**(26): p. 5567-5580. .

37. Gordon, C.M., J.D. Holbrey, A.R. Kennedya, and K.R. Seddon, *Ionic liquid crystals: hexafluorophosphate salts.* J. Mater. Chem., 1998. **8**: p. 2627–2636.

38. Bonhote, P., A.-P. Dias, N. Papageorgiou, K. Kalyanasundaram, and M. Gratzel, *Hydrophobic, Highly Conductive Ambient-Temperature Molten Salts.* Inorg. Chem., 1996. **35**(5): p. 1168-78.

39. Wasserscheid, P. and T.E. Welton, *Ionic Liquids in Synthesis*, ed. Germany. 2003: Wiley-VCH Verlag GmbH & Co. KGaA, Weinheim, Germany.

40. Fredlake, C.P., J.M. Crosthwaite, D.G. Hert, S.N.V.K. Aki, and J.F. Brennecke, *Thermophysical properties of imidazolium-based ionic liquids.* Journal of Chemical and Engineering Data, 2004. **49**(4): p. 954-964.

41. Huddleston, J.G., A.E. Visser, W.M. Reichert, H.D. Willauer, G.A. Broker, and R.D. Rogers, *Characterization and comparison of hydrophilic and hydrophobic room temperature ionic liquids incorporating the imidazolium cation.* Green Chemistry, 2001. **3**: p. 156–164.

42. Suarez, P.A.Z., S. Einloft, J.E.L. Dullius, R.F. De Souza, and J. Dupont, *Synthesis and physical-chemical properties of ionic liquids based on 1-n-butyl-3-methylimidazolium cation.* J. Chim. Phys., 1998. **95**: p. 1626-1639.

43. Fannin, A.A., Jr., D.A. Floreani, L.A. King, J.S. Landers, B.J. Piersma, D.J. Stech, R.L. Vaughn, J.S. Wilkes, and J.L. Williams, *Properties of 1,3-dialkylimidazolium chloride-aluminum chloride ionic liquids. 2. Phase transitions, densities, electrical conductivities, and viscosities.* J. Phys. Chem., 1984. **88**: p. 2614-21.

44. McEwen, A.B., E.L. Ngo, K. LeCompte, and J.L. Goldman, *Electrochemical properties of imidazolium salt electrolytes for electrochemical capacitor applications.* J. Electrochem. Soc., 1999. **146**: p. 1687-95.

45. Seddon, K.R., A. Stark, and M.-J. Torres, *Influence of chloride, water, and organic solvents on the physical properties of ionic liquids.* Pure Appl. Chem., 2000. **72**: p. 2275-87.

46. Swartling, D., L. Ray, S. Compton, and D. Ensor, *Preliminary investigation into modification of ionic liquids to improve extraction parameters.* SAAS Bulletin Biochemistry and Biotechnology 2000. **13**: p. 1-7.

47. Bonhote, P., A.-P. Dias, N. Papageorgiou, K. Kalyanasundaram, and M. Graetzel, *Hydrophobic, Highly Conductive Ambient-Temperature Molten Salts.* Inorganic Chemistry, 1996. **35** (5): p. 1168-78.

48. Ngo, H.L., K. LeCompte, L. Hargens, and A.B. McEwen, *Thermal properties of imidazolium ionic liquids.* Thermochimica Acta, 2000. **357**(358): p. 97-102.

49. Anthony, J.L., E.J. Maginn, and J.F. Brennecke, *Solution Thermodynamics of Imidazolium-Based Ionic Liquids and Water.* Journal of Physical Chemistry B 2001. **105**(44): p. 10942-10949.

50. Zhang, S., X. Li, H. Chen, J. Wang, J. Zhang, and M. Zhang, *Determination of Physical Properties for the Binary System of 1-Ethyl-3-methylimidazolium Tetrafluoroborate + H_2O.* Journal of Chemical and Engineering Data 2004. **49**(4): p. 760-764.

51. Rodriguez, H. and J.F. Brennecke, *Temperature and composition dependence of the density and viscosity of binary mixtures of water + ionic liquid.* Journal of Chemical & Engineering Data 2006. **51**(6): p. 2145-2155.

52. Intergovernmental panel on climate change *Direct GWPs* 2009; Available from: http://www.ipcc.ch/ipccreports/tar/wg1/248.htm#tab67.

53. Preissner, M., B. Cutler, S. Singanamalla, Y. Hwang, and R. Radermacher, *Comparison of automotive air-conditioning systems operating with CO2 and R134a.*, in *Final Proceedings of the IIR-Gustav Lorentzen Conference on Natural Working Fluids*. 2000: Purdue, West Lafayette, IN, United States,. p. 191-198.

54. Steven Brown, J., S.F. Yana-Motta, and P.A. Domanski, *Comparative analysis of automotive air conditioning systems operating with CO_2 and R134a.* International Journal of Refrigeration, 2002. **25**(1): p. 19-32.

55. Jessop, P.G. and B. Subramaniam, *Gas-Expanded Liquids.* Chemical Reviews, 2007. **107**(6): p. 2666-2694.

56. Hutchenson, K.W., A.M. Scurto, and B. Subramaniam, *Gas-Expanded Liquids and Near-Critical Media: Green Chemistry and Engineering*. ACS Symp. Ser., ed. P.P.a.t.t.A.C.S.N. Meeting. 2009, Boston, MA ACS.

57. Sih, R., F. Dehghani, and N.R. Foster, *Viscosity measurements on gas-expanded liquid systems—methanol and carbon dioxide.* J. Supercrit. Fluids, 2007. **41**: p. 148-157.

58. Eckert, C.A., C.L. Liotta, D. Bush, J.S. Brown, and J.P. Hallett, *Sustainable reactions in tunable solvents.* J. Phys. Chem. B, 2004. **108**: p. 18108-18118.

59. Chamblee, T.S., R.R. Weikel, S.A. Nolen, C.L. Liotta, and C.A. Eckert, *Reversible in situ acid formation for b-pinene hydrolysis using CO_2 expanded liquid and hot water.* Green Chemistry, 2004. **6**(8): p. 382-386.

60. Combes, G., E. Coen, F. Dehghani, and N. Foster, *Dense CO_2 expanded methanol solvent system for synthesis of naproxen via enantioselective hydrogenation.* Journal of Supercritical Fluids 2005. **36**(2): p. 127-136.

61. Heldebrant, D.J. and P.G. Jessop, *Liquid Poly(ethylene glycol) and Supercritical Carbon Dioxide: A Benign Biphasic Solvent System for Use and Recycling of Homogeneous Catalysts.* . Journal of the American Chemical Society 2003. **125**(19): p. 5600-5601.

62. Jessop, P.G., *Homogeneous catalysis using supercritical fluids: Recent trends and systems studied.* Journal of Supercritical Fluids, 2006. **38**(2): p. 211-231.

63. Jin, H. and B. Subramaniam, *Homogeneous catalytic hydroformylation of 1-octene in CO_2-expanded solvent media.* Chemical Engineering Science, 2004. **59**(22-23): p. 4887-4893.

64. Jin, H., B. Subramaniam, A. Ghosh, and J. Tunge, *Intensification of catalytic olefin hydroformylation in CO_2-expanded media.* AIChE Journal, 2006. **52**(7): p. 2575-2581.

65. Wei, M., G.T. Musie, D.H. Busch, and B. Subramaniam, *Autoxidation of 2,6-di-tert-butylphenol with cobalt Schiff base catalysts by oxygen in CO_2-expanded liquids.* Green Chemistry, 2004. **6**(8): p. 387-393.

66. Ahosseini, A., E. Ortega, B. Sensenich, and A.M. Scurto, *Viscosity of n-alkyl-3-methyl-imidazolium bis(trifluoromethylsulfonyl)amide ionic liquids saturated with compressed CO_2.* Fluid Phase Equilibria, 2009. **286**(1): p. 62-68.

67. Solinas, M., A. Pfaltz, P.G. Cozzi, and W. Leitner, *Enantioselective Hydrogenation of Imines in Ionic Liquid / Carbon Dioxide Media.* Journal of the American Chemical Society, 2004. **126**: p. 16142-16147.

68. Hert, D.G., J.L. Anderson, S.N.V.K. Aki, and J.F. Brennecke, *Enhancement of oxygen and methane solubility in 1-hexyl-3-methylimidaxolium bis(trifluoromethylsulfonyl)imide using carbon dioxide.* Chem. Comm., 2005.

69. Scurto, A.M. and W. Leitner, *Expanding the useful range of ionic liquids: melting point depression of organic salts with carbon dioxide for biphasic catalytic reactions.* Chem. Comm., 2006(35): p. 3681-3683.

70. Scurto, A.M., E. Newton, R.R. Weikel, L. Draucker, J. Hallett, C.L. Liotta, W. Leitner, and C.A. Eckert, *Melting Point Depression of Ionic Liquids with CO_2: Phase Equilibria.* Ind. Eng. Chem. Res., 2008. **47** (3): p. 493-501.

71. Dyson, P.J. and T.J. Geldbach, *Metal Catalysed Reactions in Ionic Liquids*. 2005: Springer. 246.

72. Keskin, S., D. Kayrak-Talay, U. Akman, and O. Hortacsu, *A review of ionic liquids towards supercritical fluid applications.* Journal of Supercritical Fluids, 2007. **43**(1): p. 150-180.

73. Blanchard, L.A. and J.F. Brennecke, *Recovery of organic products from ionic liquids using supercritical carbon dioxide.* Ind. Eng. Chem. Res. , 2001. **40**: p. 287-292.

74. Scurto, A.M., S.N.V.K. Aki, and J.F. Brennecke, *CO_2 as a separation switch for ionic liquid/organic mixtures.* J. Am. Chem. Soc., 2002. **124**: p. 10276.

75. Scurto, A.M., S.N.V.K. Aki, and J.F. Brennecke, *Carbon dioxide induced separation of ionic liquids and water.* Chem. Commun. , 2003. **5**: p. 572-573.

76. Aki, S.N.V.K., A.M. Scurto, and J.F. Brennecke, *Ternary phase behavior of ionic liquid (IL)–organic–CO_2 systems.* Ind. Eng. Chem. Res., 2006. **45**: p. 5574.

77. Mellein, B.R. and J.F. Brennecke, *Characterization of the ability of CO_2 to act as an antisolvent for ionic liquid/organic mixtures.* J Phys Chem B. , 2007. **111**: p. 4837-43.

78. Saurer, E.M., S.N.V.K. Aki, and J.F. Brennecke, *Removal of Ammonium Bromide, Ammonium Chloride, and Zinc Acetate from Ionic Liquid/Organic Mixtures Using Carbon Dioxide.* Green Chem. , 2006. **8**: p. 141-143.

79. Zhang, Z., W. Wu, H. Gao, B. Han, B. Wang, and Y. Huang, *Tri-phase behavior of ionic liquid-water-CO_2 system at elevated pressures.* Phys. Chem. Chem. Phys., 2004. **6**: p. 5051-5.

80. Zhang, Z., W. Wu, B. Han, T. Jiang, B. Wang, and Z. Liu, *Phase Separation of the Reaction System Induced by CO_2 and Conversion Enhancement for the Esterification of Acetic Acid with Ethanol in Ionic Liquid* J. Phys. Chem. B, 2005. **109**: p. 16176–16179.

81. Najdanovic-Visak, V., A. Serbanovic, J.M.S.S. Esperanc, H.J.R.G. a, L.P.N. Rebelo, and M.N.d. Ponte, *Supercritical carbon dioxide-induced phase changes in (ionic liquid, water and ethanol mixture) solutions: application to biphasic catalysis.* Chem. Phys. Chem. , 2003. **4**: p. 520-522.

82. O. Bortolini, S., V. Campestrini, G. Conte, M. Fantin, S. Fogagnolo, and E. Maietti, *Sustainable Epoxidation of Electron-Poor Olefins with Hydrogen Peroxide in Ionic Liquids and Recovery of the Products with Supercritical CO_2* Eur. J. Org. Chem., 2003: p. 4804 - 4809.

83. Kroon, M.C., J.v. Spronsen, C.J. Peters, R.A. Sheldon, and G.-J. Witkamp, *Recovery of pure products from ionic liquids using supercritical carbon dioxide as a co-solvent in extractions or as an anti-solvent in precipitations.* Green Chem. , 2006. **8**: p. 246-249.

84. Yoon, B., C.H. Yen, S. Mekki, S. Wherland, and C.M. Wai, *Effect of Water on the Heck Reactions Catalyzed by Recyclable Palladium Chloride in Ionic Liquids Coupled with Supercritical CO_2 Extraction.* Ind. Eng. Chem. Res., 2006. **45**(12): p. 4433–4435.

85. Liang, C., C.-Y. Yuan, R.J. Warmack, C.E. Barnes, and S. Dai, *Ionic Liquids: A New Class of Sensing Materials for Detection of Organic Vapors Based on*

the Use of a Quartz Crystal Microbalance. Analytical Chemistry, 2002. **74**: p. 2172-6.

86. Xiaoxia, J., Y. Lei, G. Diego, R.R. X, and Z. Xiangqun, *Ionic liquid high-temperature gas sensor array.* Analytical Chemistry, 2006. **78**: p. 6980-9.

87. Fu, D., X. Sun, Y. Qiu, X. Jiang, and S. Zhao, *High-pressure phase behavior of the ternary system CO_2 + ionic liquid [bmim][PF_6] + naphthalene* Fluid Phase Equilib., 2007. **251**: p. 114-120.

88. Anthony, J.L., E.J. Maginn, and J.F. Brennecke, *Thermodynamic Properties and Solubilities of Gases in 1-n-butyl-3-methylimidazolium hexafluorophosphate.* Journal of Physical Chemistry B, 2002. **106**: p. 7315-7320.

89. Brennecke, J.F. and E.J. Maginn, *Purification of gas with liquid ionic compounds*. 2003: US.

90. Bates, E.D., R.D. Mayton, I. Ntai, and J.H. Davis, *CO_2 capture by a task-specific ionic liquid.* J. Am. Chem. Soc., 2002. **124**: p. 926.

91. Bara, J.E., T.K. Carlisle, C.J. Gabriel, D. Camper, A. Finotello, D.L. Gin, and R.D. Noble, *Guide to CO_2 Separations in Imidazolium-Based Room-Temperature Ionic Liquids.* Ind. Eng. Chem. Res., 2009. **48**: p. 2739-2751.

92. Koval, C., D. Camper, A. Finotello, and R. Noble, *Properties of imidazolium-based room temperature ionic liquids that affect CO_2 solubility and selectivity for CO_2/N_2 and CO_2/CH_4 gas separations.* PMSE Preprints, 2006. **95**(266).

93. Koval, C.A., C.R. Becker, D.E. Camper, J.H. Davis, Jr., R.D. Noble, C. Oral, and P. Scovazzo. *Use of ionic liquids for membrane-based and electrochemically - driven gas separations*. in *Molten salts XIV*. 2006. Honolulu, Hawaii.

94. Bara, J.E., R.D. Noble, and D.L. Gin, *Effect of "Free" Cation Substituent on Gas Separation Performance of Polymer-Room-Temperature Ionic Liquid Composite Membranes.* Ind. Eng. Chem. Res., 2009. **48**(9): p. 4607-4610.

95. Mekki, S., C.M. Wai, I. Billard, G. Moutiers, C.H. Yen, J.S. Wang, A. Ouadi, C.Gaillard, and P. Hesemann, *Cu(2+) extraction by supercritical fluid carbon dioxide from a room temperature ionic liquid using fluorinated .beta.-diketones.* Green Chem., 2005. **7**: p. 421-3.

96. Mekki, S., C.M.Wai, I. Billard, G. Moutiers, J. Burt, B. Yoon, J.S.Wang, C. Gaillard, A. Ouadi, and P. Hesemann, *Extraction of lanthanides from aqueous solution by using room-temperature ionic liquid and supercritical carbon dioxide in conjunction.* Chem. Eur. J., 2006. **12**: p. 1760-6.

97. Chinn, D., D.Q. Vu, M.S. Driver, and L.C. Boudreau, *CO_2 removal from gas using ionic liquid absorbents*. 2009: USA.

98. Sharma, Y.O. and M.S. Degani, *CO_2 absorbing cost-effective ionic liquid for synthesis of commercially important alpha cyanoacrylic acids: A safe process for activation of cyanoacetic acid.* Green Chemistry, 2009. **11**: p. 526-530.

99. Palgunadi, J., J.E. Kang, M. Cheong, H. Kim, H. Lee, and H.S. Kim, *Fluorine-free imidazolium-based ionic liquids with a phosphorous-containing*

anion as potential CO_2 absorbents. Bulletin of the Korean Chemical Society, 2009. **30**: p. 1749-1754.

100. Lee, K.Y., G.T. Gong, K.H. Song, H. Kim, K.-D. Jung, and C.S. Kim, *Use of ionic liquids as absorbents to separate SO_2 in SO_2/O_2 in thermochemical processes to produce hydrogen.* International Journal of Hydrogen Energy, 2008. **33**: p. 6031-6036.

101. Jun, H., R. Anders, W. Peter, and F. Rasmus, *Reversible physical absorption of SO_2 by ionic liquids.* Chem. Commun., 2006. **38**: p. 4027-9.

102. Kulkarni, P.S., L.C. Branco, J.G. Crespo, and C.A.M. Afonso, *Capture of dioxins by ionic liquids.* Environmental Science & Technology, 2008. **42**: p. 2570-4.

103. Kulkarni, P.S., L.C. Branco, J.G. Crespo, and C.A.M. Afonso, *A comparative study on absorption and selectivity of organic vapors by using ionic liquids based on imidazolium, quaternary ammonium, and guanidinium cations.* Chemistry, 2007. **13**: p. 8470-7.

104. Jianmin, Z., Z. Suojiang, D. Kun, Z. Yanqiang, S. Youqing, and L. Xingmei, *Supported absorption of CO_2 by tetrabutylphosphonium amino acid ionic liquids.* Chemistry, 2006. **12**: p. 4021-6.

105. Shiflett, M. B.; Yokozeki, A. Absorption Cycle utilizing Ionic Liquids as Working Fluid. WO /08426 2006A1, 2006

Chapter 2 Experimental Technology

Several apparatus have been used in the study of global phase behavior, vapor-liquid equilibrium (VLE), liquid-liquid equilibrium (LLE), vapor-liquid-liquid equilibrium (VLLE), and polarity measurement of mixtures of ILs/compressed gases. The details are described in the following sections.

2.1 An Apparatus to Measure Vapor-Liquid Equilibrium

2.1.1 Literature overview

Several experimental methods can be used to measure high-pressure phase equilibria. These methods are generally divided into two categories: analytical and synthetic approaches [3]. For analytical methods, samples are typically taken from each phase and analyzed using various detection methods, such as gas chromatography (GC), high-pressure liquid chromatography (HPLC), nuclear magnetic resonance (NMR), infrared radiation (IR), etc. The synthetic method is a direct approach in a closed system. A certain concentration of mixture is loaded and the points of phase transition (temperature, pressure, etc.) are observed.

The apparatus introduced in this chapter belongs to the category of the synthetic method, based on a material balance. This apparatus is capable of measuring vapor-liquid (VLE), liquid-liquid (LLE), vapor-liquid-liquid (VLLE), and solid-liquid-vapor (SLV) equilibria, in addition to viewing general high-pressure phase behavior (pressure and temperature of transitions). The apparatus is most commonly used to determine the vapor-liquid equilibrium (gas solubility) of

compressed gases, such as carbon dioxide, in single component or multicomponent liquids. Many properties may be obtained including concentration (mass fraction, mole fraction, molarity, molality, etc.) of gases in liquids, liquid molar volume and density, the induced volume expansion of the gas-expanded liquids, etc. SLV data and VLLE data can also be obtained by slightly different procedures. Quantitative solubility measurements are limited to single component gases, and liquids or liquid mixtures with lower volatilities than the compressed gas. This chapter describes the design in detail of the setup, phototypesets the method of building the apparatus, and illuminates the operation of the apparatus. Phase equilibrium data of ionic liquids, organic components and compressed gases measured by this apparatus will be given in Chapters 5, 7 and 8. In addition, a rigorous error analysis has been performed to quantify the inherit error at any condition (T, P, volume, composition, etc.). The details are given in Appendices B and D.

2.1.2 Overview of apparatus and the principle of operation

This apparatus mainly consists of a high-pressure view cell (equilibrium cell), high-pressure and precision syringe pump filled with desired gas, a water bath and accessories to measure the temperature and pressure (see Figure 2.1). [6] The detailed mechanic draw and the whole setup picture are given in Appendix A. A spreadsheet is developed to calculate the solubility, density of the liquid solution, molar volume, volume expansion and molarity. The spreadsheet sample is given in Appendix D for [HMIm][Tf_2N] and R-134a at 50 ºC. These calculations are based on the mass balance by determining the amount of gas delivered from the pump, the moles/mass

of gas in the headspace above the liquid and in the tubing/lines to the equilibrium cell. This method can yield high resolution of solubility data (often better than ±0.001), pressure with accuracy of ±0.2 bar, temperature of ±0.01°C, density up to ±0.4 %, and volume expansion to ±0.05%. In addition, there is no need for analytical methods, nor calibration for each system of interest.

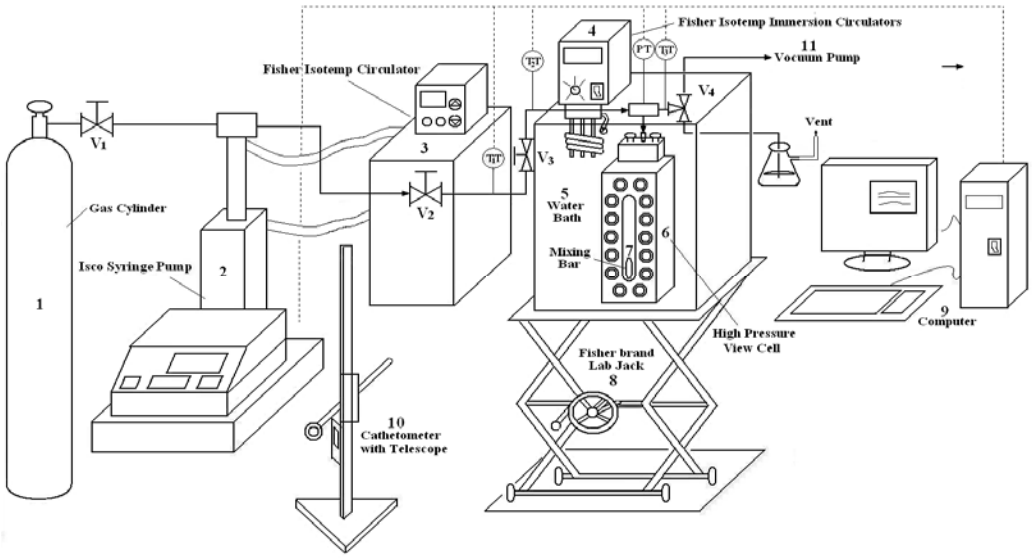

Figure 2.1 Diagram of experimental apparatus. (1) Gas Cylinder; (2) Syringe Pump; (3) Heater/Circulator; (4) Immersion Heater/Circulator; (5) Water Bath; (6) High pressure view cell; (7) Mixing Bar; (8) Lab Jack; (9) Computer; (10) Cathetometer with Telescope (11) Vacuum Pump

Some of the initial concepts of this apparatus were devised by Kurata and Kohn, here at the University of Kansas, over fifty years ago [7]. Some modifications were introduced by Kohn and Huie [8] and Brennecke and Scurto [9] at the University of Notre Dame. Luks [10] at the University of Tulsa used a similar

apparatus as Kohn's . However, these devices utilize mercury for pressure transfer to the gas and in volume reduction in the pressure gauges. The Cailletet apparatus [11-12] also uses mercury as a pressure intermediate to measure vapor liquid equilibrium. The present apparatus uses a similar mass balance concept, but simplifies the initial design, eliminates the use of mercury, provides a robust equilibrium cell and improves the accuracy, operability, and ease of data acquisition. Procedures for the measurement of other types of phase equilibria are introduced in sequel.

2.1.3 Experimental principles

The phase equilibria data are obtained based on a mass balance. The main assumption asserts that the pressure of the compressed gas is much greater than the vapor pressure of the liquid; and/or the vapor phase composition of the liquid component is much less (<<10% mole) than the compressed gas. The mass of gas in the liquid phase is calculated by subtracting the mass of gas in the lines and headspace above the liquid from the total mass of gas injected into the system. The mass balance equation of the gas is:

$$m_g = m_{pump} - m_{lines} - m_{headspace} + m_{lines}^{\,0} + m_{headspace}^{\,0} \tag{2.1}$$

$$m_{pump} = \Delta V_{pump} \times \rho\left(T_{pump}\,,\, P_{pump}\right) \tag{2.2}$$

$$m_{lines} = \; V_{lines} \times \rho\left(T_{lines}\,,\, P\right) \tag{2.3}$$

$$m_{headspace} = (V_{cell} - V_l) \times \rho\left(T\,,\, P\right) \tag{2.4}$$

$$m_{lines}^{\,0} = V_{lines} \times \rho\left(T_{lines}\,,\, P^0\right) \tag{2.5}$$

$$m_{headspace}^{\,0} = V_{headspace} \times \rho\left(T\,,\, P^0\right) \tag{2.6}$$

where, m_g is the mass of the gaseous component in the liquid. m_{pump} is the mass of the gas injected into the system, which is the product of the volume of the gas

displaced by the metering pump (ΔV_{pump}) that is at constant temperature and pressure, and the density of the gas in the pump ($\rho(T_{pump}, P_{pump})$). m_{lines} is the mass of the gas in the lines connecting the pump to the equilibrium cell. It is calculated as the product of the volume of the lines (V_{lines}) and the density of the gas in the lines ($\rho(T_{lines}, P)$) at the system equilibrium pressure, P, and at a relatively high temperature. The temperature is usually set higher than the critical point of the gas to eliminate gas condensing in the lines which could decrease the accuracy of the liquid solubility data (see error analysis in Appendix D). $m_{headspace}$ is the mass of the gas in the headspace, which is calculated in the same way as m_{lines} except at the system temperature, T. The volume of the headspace is the difference between the liquid volume (V_l) and the total cell volume (V_{cell}). Since the liquid volume generally expands with the gas pressure, the headspace volume also decreases with the pressure/composition. As the apparatus is purged with the compressed gas of interest to remove any air or other capping gases, some of the gas is initially in the lines and headspace. M_{line}^{0} is the mass of the gas in the lines before after venting the system. $m_{headspace}^{0}$ is the mass of the gas in the headspace initially in the system after venting. For work at moderate to high pressures (>10bar), the initial solubility of the gas in the liquid at atmospheric pressure, P^0, will be negligible compared to higher pressures, e.g. for CO_2. However, for gases that are highly soluble in liquids at atmospheric pressure (for instance, hydrofluorocarbons, etc.), a vacuum pump may be applied to establish initial conditions with low solubility in the liquid.

The mole fraction of the gas in the liquid, x_g, then becomes:

$$x_g = \frac{n_g}{n_l + n_g} = \frac{m_g / M_g}{m_l / M_l + m_g / M_g} \tag{2.7}$$

where n_g is the moles of the gaseous component; n_l is the moles of the liquid component; M_g is the molecular weight of the gas; m_l is the mass of the liquid sample; M_l is the molecular weight of the liquid. The mass fraction of the gas, *i*, in the liquid, w_g, is:

$$\omega_g = \frac{m_g}{m_g + m_l} \tag{2.8}$$

Molar volume of the liquid mixture, $\underline{V}$, is computed from the liquid volume and the moles of the gas and liquid mixture:

$$\underline{V} = \frac{V_l}{(n_g + n_l)} \tag{2.9}$$

where V_l is the volume of the liquid (usually in ml/cm^3); volume expansion accounts for the volume change before and after dissolving the gas in the liquid:

$$\frac{\Delta V}{V_0} = \frac{V_l - V_0}{V_0} \tag{2.10}$$

where, ΔV is the volume difference between pure liquid volume and expanded liquid volume; V_o is the initial liquid volume at the system temperature. Molality, [*m*] (braces to distinguish from mass, *m*), can be calculated from the definition:

$$[m] = \frac{1000 \times n_g}{m_l} \tag{2.11}$$

Molarity, [*M*], is expressed as:

$$[M] = \frac{1000 \times n_g}{V_l} \tag{2.12}$$

where, the unit of m_l is in grams, V_l is in milliliters.

Density calculations

Density calculations of the pure gas must have a high accuracy. While experimental data may be used or interpolated, ultra-accurate equations of state are highly useful. Here, densities are determined from REFPROP database (version 8.0)[13] from the National Institute of Standards and Technology (NIST). REFPROP includes three models to calculate the thermodynamic properties of pure fluids: equations of state explicit in Helmholtz energy, the modified Benedict-Webb-Rubin equation of state, and an extended corresponding states (ECS) model. As an example, the database uses the ultra-accurate Span-Wagner Equation of state [13-14]. For gases, such as CO_2, R134a, H_2, CO, REFPROP provides a dynamic link library (".dll") that allows incorporation in a broad variety of software applications, such as Excel, Visual Basic & C, Matlab, Labview, etc. The database of REFPROP includes 83 pure fluids and 54 mixtures.

2.1.4 Apparatus details

This setup mainly includes an Isco, Inc. 100 DM syringe pump with a 5000 psi externally mounted pressure transducer of 0.1% full scale accuracy, a high pressure view cell and a computer data acquisition system. The pump has a volume resolution of 9nl. The accessories include a Fisher, Inc. Isotemp circulator, model 3016 with 0.01° C resolution, to maintain the temperature of the pump; a water bath and an immersion circulator (Haake DC30/DL3) to maintain the water bath temperature with temperature stability greater than ±0.1 K. A platform jack (Fisher Lab-Jack) allows the bath to be lowered away from the equilibrium cell which is

mounted from above. An Eberbach 5160 cathetometer with telescope is used to read the height of the liquid level to a resolution of 0.01mm and accuracy of ± (0.02 + 0.00005L), where, L represents the length from the starting point of the measurement to the given position (mm). The gas lines are heated using fiberglass covered heating tape, controlled by two variable AC transformers, STACO ENERGY® Model 3PN1010B. The line temperatures are usually maintained above the critical point of the gas; for instance with CO_2 (Tc = 31.1°C) ~60°C. In order to prevent the heat from dissipating to the surroundings, a fiberglass cloth tape insulation is used. The line temperatures are measured by T-type thermocouples with an accuracy of ±0.5°C. A MEASUREMENT COMPUTING, Inc. USB–TC is used to interface the thermocouples to the data acquisition system. The pump temperature is measured by an ERTCO-EUTECHNIC 5 digital thermister, Model 4400, with an accuracy of at least ±0.01 °C in the range of 0-100°C. The pressure of the cell is measured by a 5000 psi Heise DXD Series #3711 precision digital pressure transducer which has an accuracy of ±0.02% full scale (F.S.) with ranges of 10°-30°C , ±0.04% F.S. 0°-50°C, and ±0.05% F.S. –10°-70°C. The pressure transducer interfaces with the data acquisition system by a serial port converter. LabView 8.2 software is used for the data acquisition. The temperature of the lines, the pressure of the cell and the lines, the pump information including volume, flow rate, and pressure are monitored and logged at 60 second intervals. The data sampling rate is adjustable from 30 to 240 seconds. The gas line tubing uses small diameter (1/16” OD, 0.006”ID) HIP tubing to minimize the volume of the lines. The tubing connections use HIP 1/16” taper seal

fittings (AF1) and HIP 15-24AF1 316SS tee. All valves are HIP 15-11AF1 316SS type except the output valve, which uses the three way Swagelok® valve (SS-41XS1), and is connected from the output line to a vacuum pump and to a 125 ml PYREX vent filtering flask with a #4 rubber stopper to remove any organic compounds from the venting gas. The vent filtering flask uses 1/16 inch Nalgene 180 PVC non-toxic autoclavable 3/8" ID tubing to vent the gas directly to an exhaust hood.

2.1.4.1 Equilibrium view cell

The high pressure equilibrium cell is one of the key components of the apparatus (see Figure 2.2).

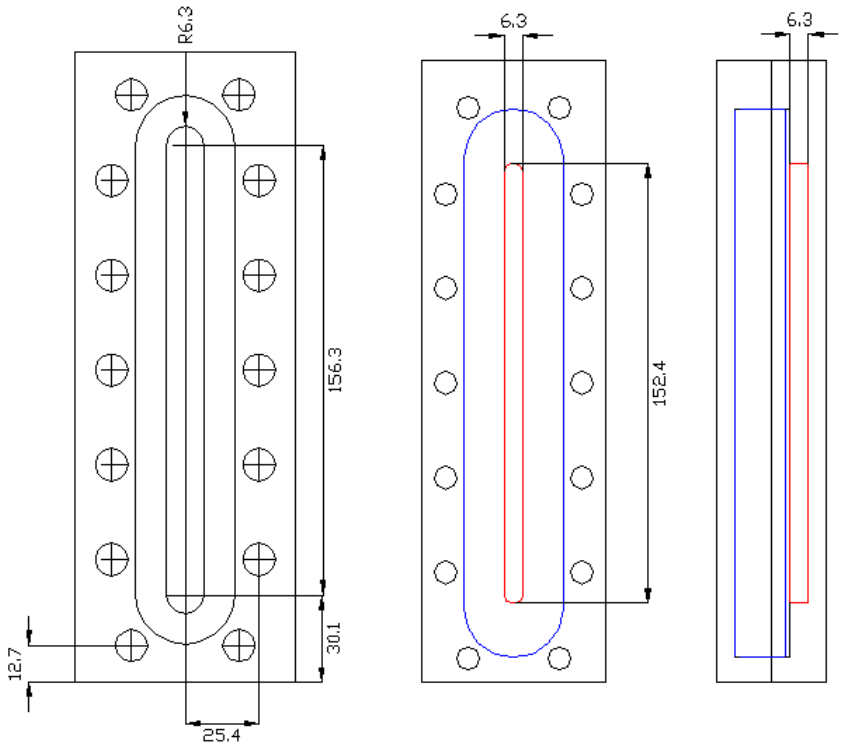

Figure 2.2 High- pressure equilibrium view-cell

The equilibrium cell is equipped with a high pressure gauge glass window so that the interface between vapor and liquid phases can be observed. The gauge glass is from L.J. Star Inc. Ilmadur® Borosilicate Glass I-420 brand with maximum pressure of 4000 psi and temperature of 280 °C. The equilibrium cell consists of a rectangular vessel, which is fabricated out of stainless steel and pressure tested for 24 hours at 4000 psi without leakage. The Gore-Tex® GR PTFE gasket is used for sealing; other gasket materials are possible for use at higher temperatures. A small PTFE coated stirring bar (3.2mm diameter x 12.7mm) is placed inside of the cell. An external rare-earth magnet in a slot behind the cell is raised and lowered by a pulley system and allows precision mixing throughout the cell.

2.1.4.2 Volume calibration

In order to measure the phase equilibrium data based on the mass balance, precision calibration of the volume of the cell and the lines is necessary. Calibration of both the lines and equilibrium cell was performed by the high-precision metering pump using high purity nitrogen. Nitrogen was used to calibrate due to its relatively low compressibility. Nitrogen was added to the lines or cell at the same temperature (usually room temperature). The volume needed to return the pump and lines/cell to the original pressure is the volume of the lines/cell. The calibration was repeated three times at different pressures. Our line volume was measured as 0.846 ml and the volume of the cell is 5.716 ml. In order to minimize the volume of the lines, a short feed line with small inside diameter tubing, 0.006”ID and 20” long, is used.

The liquid volume of the cell is calibrated by correlating the height in the cell (height difference between a permanent fixed reference and the liquid height). The liquid volume was calibrated by using a 5 ml Kimax Brand microburet with subdivision of 0.01ml, tolerance ±0.01ml. n-Tetradecane (99%) was used as a calibration liquid because of its low vapor pressure and surface tension. The liquid was injected into the cell, 0.05ml each time, using a 12 inch long needle. The height (difference) was read from the cathetometer with the telescope. The relationship between the height and the volume of the liquid is determined by a linear regression. With a 3.2 diameter x 12.7mm PTFE stir-bar installed, the minimum sample size to just cover the bar to allow accurate height measurement is approximately 0.60 ml. Thus, only a small amount of sample is needed for the measurements.

2.1.5 Experimental procedure

2.1.5.1 Vapor-liquid equilibria

The Isco pump is filled with the desired gas, such as CO_2 or R-134a. For a typical isothermal run, the apparatus is preheated and thermally equilibrated for about one hour to the desired temperature. The pump pressure is generally set constant at just above the maximum anticipated pressure and a temperature above the critical temperature, e.g. 150 bar and 60 °C for the CO_2 run; this may be changed during the run. In the constant-pressure mode, the pump automatically adjusts the volume to achieve the desired pressure. The delivery lines are set above the critical temperature as well. The water bath is set at the desired temperature and the cell is put in the water bath to be preheated. The atmospheric pressure is read from a barometer, since the pump pressure transducer yields the gauge pressure.

A syringe with liquid sample is weighed before and after injection with a long needle (12 inches) on a precision balance (±0.01mg). The sample is carefully injected into the cell to avoid leaving droplets on the wall, which would alter the initial volume obtained from the liquid height. After injection, the cell is attached to the lines. The water bath is physically raised to immerse the entire cell in water. It generally takes approximately 30 minutes for the sample and cell to reach thermal equilibrium as confirmed in a separate experiment.

The cathetometer with telescope is set to zero on the reference line (marked on the lower portion of the cell), then the initial liquid height is measured. The initial liquid volume is calculated based on the calibration of the height with volume. The cell is quickly flushed several times with gas at low pressure to remove any residual air or other gases. For lower pressure runs with highly soluble gases, such as R-134a, the vacuum pump is connected to the cell by the three way valve in order to reduce the gas pressure to a minimal solubility level. The apparatus is ready to collect data after recording the initial liquid height, the initial cell pressure, temperature, each line temperature, and the pump conditions (pressure, temperature, and initial volume), as well as creating the log file to save the data in the computer.

Valve 3 (see Figure 2.1), between the pump and the cell, is opened slowly to increase the cell pressure until the first desired value. The flowrate of the pump to maintain a constant pressure while the main valve is open is kept at less than 0.20 ml/min to prevent any large PVT disturbances in temperature. After valve 3 is closed, the pump is given time to equilibrate until the flowrate reads zero, then the final

volume of the pump is recorded. The difference of the volume is used to compute the mass of CO_2 injected into the cell by the computed density of the gas. During the pressurization, the stir bar inside of the cell is used to mix the vapor phase and liquid phase by stirring the interface to accelerate the mass transfer process into the liquid sample. With vigorous mixing, equilibrium is often reached after approximately 30 minutes; longer times are needed with more viscous liquids. When equilibrium is reached, all variables are recorded and then entered into the spreadsheet (Excel) to compute the properties and associated error analysis.

2.1.5.2 Mixture critical points

The mixture critical points can be determined by careful observation of the liquid-vapor interface. As the vapor-liquid critical point usually occurs in organic liquids that have expanded several hundred percent of the initial volume, lower sample volumes/mass are loaded; here ~0.6mL. The gas is injected into the system while mixing until near the critical point in pressure. The gas is then very slowly injected (<0.1bar/min.) while stirring until the disappearance of the interface which is often preceded by "critical opalescence" [15]. In order to see the phenomena clearly (not near the top of the cell), it may take several runs to find an appropriate initial loading. As the critical mixture is in one phase, the mole fraction is simply the total pump amount delivered to the cell and the initial mass of liquid.

2.1.5.3 Solid-liquid-vapor equilibrium

For binary systems, the pressure and temperature in which a solid, liquid and vapor coexist in equilibrium may be determined. First, solid is loaded into the cell;

this may require dissolution into a volatile solvent, injection into the cell, followed by sufficient vacuum. The system is pressurized and heated until the solid completely melts. The temperature is then reduced until the first appearance of a crystal. This procedure is called the method of "first freezing". The composition at this point is often difficult to measure as the mass balance procedure requires accurate measures of initial volume; the compound of interest in the case is a solid until it is induced to melt with compressed gas.

For ternary systems, the point at which a solid is precipitated from a liquid solution using the compressed gas as an anti-solvent is the solid-liquid-vapor equilibrium. The knowledge of this point is very important for particle production methods that are beginning to be used by the pharmaceutical industry [16]. The procedure is similar to the VLE experiments, except that the initial liquid has a certain concentration of a solid component. For an isotherm run, the gas, such as CO_2, is continuously injected into the cell with the liquid solution, until the first appearance of a solid particle, which is assumed to have negligible mass compared with the total solution. The concentration of all components can then be measured. The pressure and composition will change with different initial concentrations of the solid in the liquid.

2.1.5.4 Dew points

This apparatus can also be used for measuring dew points. However, it is often difficult to perform the measurements at constant temperature. First the gas is added into the cell and mixed with a small amount of the liquid to make a solution of

known overall concentration. The temperature is raised until one phase is formed and then cooled until the first drop of liquid appears in the cell. The drop is assumed to have negligible mass, thus the composition is determined from the initial loading of gas and liquid. More gas can be added to the cell and the procedure is repeated.

2.1.5.5 Vapor-liquid-liquid equilibrium

Vapor-liquid-liquid equilibrium (VLLE) can occur near the vapor pressure of the pure gas and even extend to temperatures above the critical point of the pure gas. At this point, a liquid phase rich in the organic liquid L_1, a liquid phase rich in the compressed gas L_2, and a vapor phase rich in the compressed gas can exist. VLLE data can terminate at an upper critical end point (UCEP) at higher temperatures. In addition, type IV systems according to the classification of Scott and van Konynenburg [17-18] can have a break in the VLLE line at a lower temperature upper critical endpoint. The VLLE composition for each of the liquid phases is determined by two individual runs with different initial loadings of the organic liquid. If the phase of the organic liquid of interest, here labeled L_1, is to be studied, the cell is injected with a large amount by volume of the liquid sample, and the gas, e.g., CO_2 is continuously added to the system just until a droplet or very thin film of the L_2 layer appears; the phase is assumed to have negligible mass, and the composition of the mostly organic liquid can be determined. To determine the composition of the L_2 layer, a small amount of the liquid sample, L_1, is added into the cell. Gas is added until a large amount of the L_2 phase forms and the L_1 phase just dissolves completely into the L_2 phase or only a small fraction of the original L_1 phase remains. The

composition of the L_2 phase can then be determined assuming all of the loaded L_1 phase dissolved into the L_2 phase, the density of the L_2 to be that of the pure saturated liquid at the system temperature, and knowing the volume of the L_2 phase. It should be noted that for many binary systems, the L_2 phase is often mostly the gaseous species 95+% and errors in the organic liquid component in L_2 will often have larger errors. When the three phase equilibrium is reached, the upper and lower critical endpoints (UCEP and LCEP respectively) can be determined by increasing or decreasing the temperature until one of the liquid phase disappears.

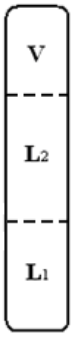

Figure 2.3 Liquid-liquid-vapor equilibria

The phase equilibrium data of carbon dioxide in n-Decane at 71.1°C is given in Table 2.1.

Figure 2.4 illustrates the Pressure (P) – mole fraction (x) phase equilibrium of CO_2 (99.99% purity) and n-Decane (with purity of 99.9%) binary system. As shown in the figure, the experimental data of this setup are in excellent agreement with literature data of Gasem and coworkers [2] and Robinson and coworkers [5], which were measured by an analytical method. They sampled the liquid phase from the equilibrium cell and analyzed using a gas chromatograph (GC) for composition.

Table 2.1 The phase equilibrium data of Carbon Dioxide + n-Decane at 71.1 °C

Pressure [Bar]	Mole fraction of CO_2 in Decane	Density [g/cc]	Volume Expansion	Molarity [mol/l]
17.26	0.1284±0.0010	0.6758±0.0007	0.0401±0.0005	0.669±0.006
33.68	0.2669±0.0009	0.6861±0.0008	0.0902±0.0005	1.578±0.008
56.24	0.4127±0.0011	0.6888±0.0009	0.1881±0.0005	2.794±0.012
73.26	0.5246±0.0012	0.6948±0.0011	0.2978±0.0005	4.017±0.019
87.43	0.6209±0.0016	0.7069±0.0017	0.4329±0.0005	5.401±0.036
101.15	0.7023±0.0023	0.7064±0.0034	0.6459±0.0006	6.771±0.075

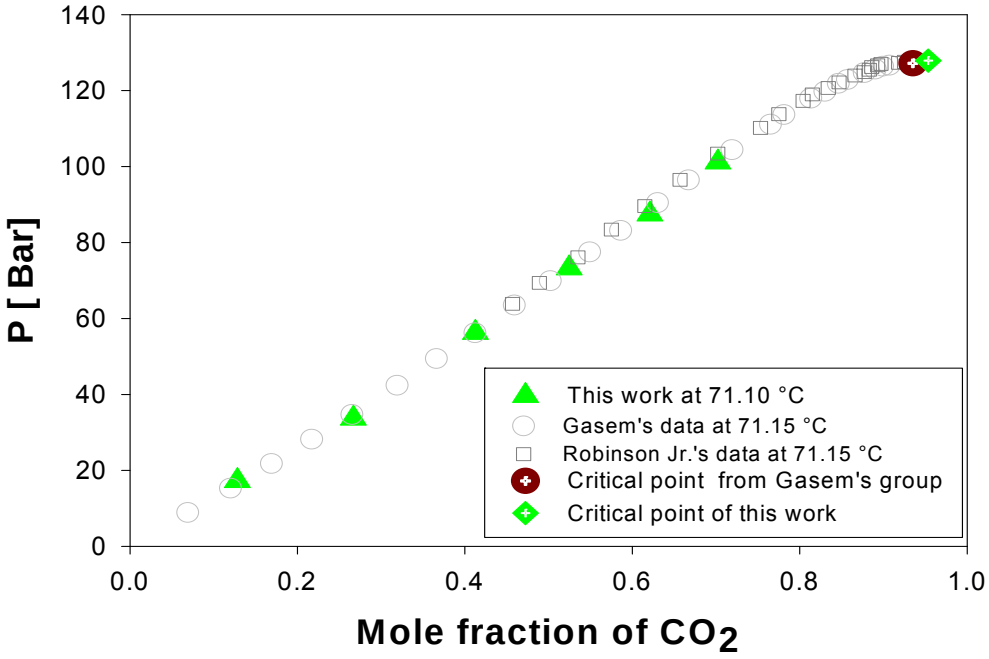

Figure 2.4 Phase equilibrium data of Decane/CO_2 71°C with literature data of Gasem's group[2] and Robinson Jr.'s group[5]**.**

Figure 2.5 gives the comparison between our work, Sage and coworkers [1] and Schucker and coworkers[4], which used the synthetic method; again, our data agree very well. Sage and coworkers [1] used a gravimetric method by weighing the CO_2 and determined n-decane from volumetric measurements. Schucker and coworkers [4] used a variable-volume cell apparatus and a flow apparatus. They weighed the n-decane and CO_2, and then computed the solubility.

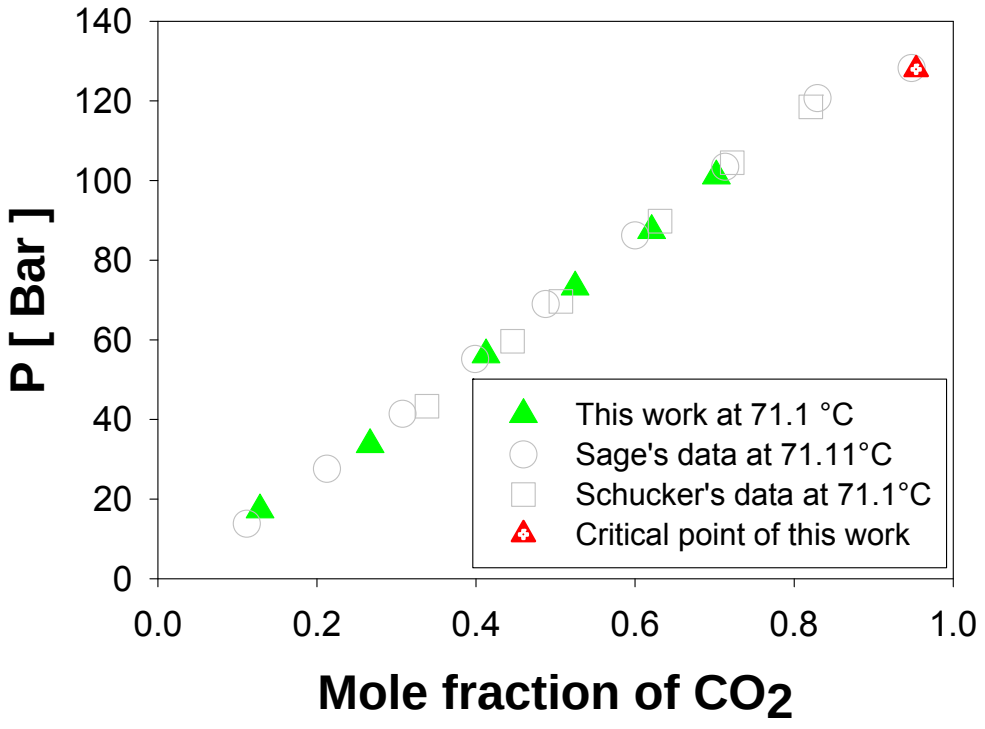

Figure 2.5 Phase equilibrium data of Decane/CO_2 at 71°C with literature data of Sage's group[1], Schucker's group[4]

Figure 2.6 illustrates the density data of n-decane and CO_2 in the liquid phase. The experimental data has a very good correlation to the literature data of Gasem and coworkers [2] and Robinson and coworkers [5]. Their density data were obtained by using a densitometer. The mixture critical point for n-decane and CO_2 at 71.1 °C is 127.9 bar and the mole fraction of CO_2 is 95.34%, compared to the literature data (127.2 bar and 93.5%CO_2) at 71.15°C [2]. The difference of CO_2 composition is less than 2%, and the critical pressure difference is less than 1 bar.

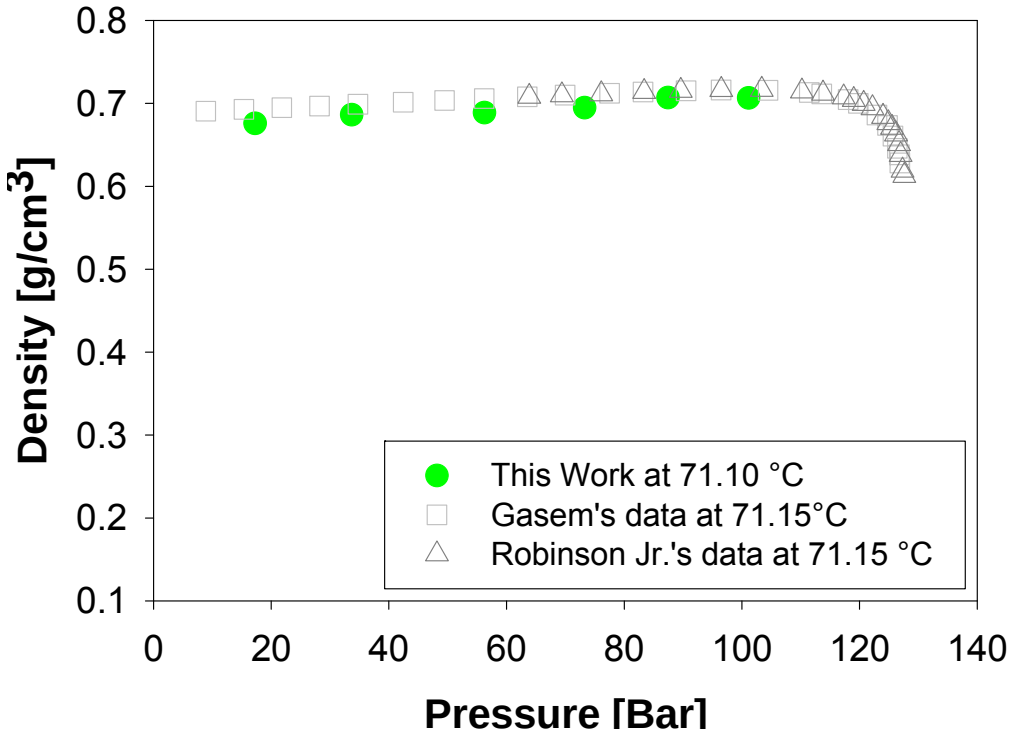

Figure 2.6 The mixture density data of Decane/CO_2 at 71°C with literature data of Gasem's group [2] and Robinson Jr.'s group[5]

For the determination of gas solubility, this apparatus is based on an assumption of little or no liquid dissolution in the vapor phase. Comparison with literature data does not allude to any meaningful difference. However, the veracity of this assertion deserves further discussion. By using the dew point data for CO_2/n-decane from literature sources [5], an estimate of the mass transferred from the liquid phase to the vapor phase may be computed and is illustrated in Table 2.2. For instance, at 103.34 bar and 71.15°C, the dew point composition is 0.008 mole fraction n-decane. By computing the molarity with the vapor density and using the typical volumes of the vapor phase found in our experiments, only ~0.13% of the original (loaded moles) of n-decane would be removed from the liquid phase to the vapor phase. Thus, the loss can be considered negligible. From simulation of the more volatile systems, the reported accuracies can be maintained with dew point compositions less than 10%.

2.1.6 Summary

A new apparatus is set up for measuring the high pressure phase equilibrium up to 300 bar and 150 °C. The construction and operation of the apparatus is described in detail and uses no mercury. The apparatus is capable of a large variety of experiments for different equilibria and properties, e.g. VLE, SLE, VLLE, mixture critical points, etc. It is easy to use, very accurate, does not need any system-specific calibration. Data from this apparatus is in excellent agreement with literature reports using two very different substrates: an n-alkane and an ionic liquid.

Table 2.2 Estimate of the amount of n-Decane transferred to the CO_2 phase at 71.1°C

Pressure [Bar]	Mole fraction of Decane in CO_2 [a]	Molarity [mM]	Moles of Decane * 10^5	Percentage of loaded Decane in CO2 phase [%]
35.06	0.006	8.19	1.8	0.12
46.04	0.005	9.39	1.9	0.13
71.83	0.004	13.29	2.2	0.14
71.97	0.005	16.62	2.7	0.18
83.54	0.005	20.61	2.7	0.18
90.57	0.006	27.95	2.9	0.19
103.45	0.008	46.26	2.0	0.13

[a] The dew points data are from Nagarajan and Robinson Jr. [5]

2.2 Setup to Measure the Critical Points and Global Phase Behavior

2.2.1 Instrument setup

The phase behavior and the temperature and pressure of the transitions were observed in a windowed high-pressure autoclave similar to a design by Koch and Leitner [19] and modified in our group; for further details see Schleicher [20]. The whole set up is shown in Figure 2.7. The ~10mL viewcell has a temperature limit of 150 °C and a pressure limit of 400 bar. Agitation is performed with a stirbar within the vessel. The temperature was maintained by a heating plate (Ika Werke, GmbH, PN: RET Basic C) with electronic temperature control (Ika Werke, GmbH, PN:

IKATRON ETS-d4-fuzzy) using a Pt-1000 RTD placed through the wall of the autoclave; the temperature precision is ±0.1°C. Pressures were measured with a high precision digital pressure gauge, Omega DPG7000 with an error band of ± 0.05% of full scale (FS=3000psi). For the runs of pressure higher than 3000 psi, the Omega DPG5000 digital pressure gauges with an accuracy of ± 0.25% of full scale (FS = 5000psi) was used. The autoclaves of these two set ups are shown in Figure 2.8.

Figure 2.7 Setup to measure the global phase behavior

Figure 2.8 Setup of autoclaves

2.2.2 Experimental procedure

Three different types of phase behavior transitions were observed: vapor-liquid (VLE) to vapor-liquid-liquid (VLLE); VLLE to liquid-liquid (LLE); and VLE, VLLE or LLE to critical transitions including upper-critical (UCEP) and lower-critical endpoints (LCEP). Approximately 1.5 ml (see below) ionic liquid was loaded into the cell and heated to the desired temperature. The compressed gases, R-134a or CO_2, was slowly introduced by a high-pressure syringe pump (Teledyne-Isco, Inc. model 100DM) and vented to remove any argon or air. Gas was slowly added to the vessel to the desired pressure, stirred and allowed to reach equilibrium (approximately 30 minutes). The pressure was slowly raised, stirred, and raised again until the first sign of the phase transition. The vessel was partially vented to a pressure just below the transition, and allowed to re-equilibrate. The process was

repeated until the transition was reproduced within ±0.5 bar. In addition, the temperature of the system was changed at constant pressure. These temperatures were reproducible to approximately ±0.5°C. The amount of initial ionic liquid is also important as the liquid phase will expand significantly with increases pressure/solubility of the gases and the transition may occur above the window of the vessel. This is especially important for the mixture critical points. The amount of IL was varied so as to render the transition approximately at a height of 70% of the total window height.

2.3 Liquid Liquid Equilibrium Measurement

2.3.1 Cloud point method

The liquid-liquid equilibrium envelope at ambient pressure of three components, such as 1-octene, n-nonanal and ionic liquids was measured by a cloud point method, where one component is continuously added to the other component (for binary mixtures) or a mixture at a certain ratio (ternary mixtures), until the mixture becomes cloud. Take a two-component mixture as an example, such as 1-octene and [HMIm][Tf_2N], the two components are immiscible when the mixture becomes cloud.

The detailed procedure of the cloud point method consists of the following steps. First, a clean vial is weighed with cover and the stirring bar. Second, the amount of 1-octene to be added is weighed (NOTE: the amount of 1-octene is fixed at the beginning), and the balance is reset to zero. Third, [HMIm][Tf_2N] is continuously

added into the vial with 1-octene until the mixture becomes cloud (NOTE, a relatively large dosage of [HMIm][Tf_2N], i.e., 3-5 drops, can be added in the beginning, then reduce the dosage to a single drop when the mixture approaches the immiscible status). Then fixing the amount of IL, and adding 1-octene until the mixture becomes clear. After that, adding IL in small dosage until the mixture becomes cloud again. An iterative procedure is necessary to measure the solubility of [HMIm][Tf_2N] in 1-octene, i.e., the ratio of the mole fractions of the two components switching between the miscible and immiscible statuses is sufficiently small (< 0.1%).

After determining the solubility of [HMIm][Tf_2N] in 1-octene, continuously adding IL to 1-octene to obtain the solubility of 1-octene in [HMIm][Tf_2N] by following similar iterative steps. However, it is recommended to start a new run with a small amount of IL in the vial and add 1-octene into it. This is an economical way since [HMIm][Tf_2N] is more expensive than 1-octene.

The amount of each component is measured with a Mettler Toledo XS205 Dual Range Balance. Its accuracy is 0.01 mg for the range of 81g and 0.1 mg for the range of 220g. A Branson Model 2510 Ultrasonic cleaner was used to mix the solutions. When the Ultrasonic cleaner is used, extra cares must be taken. Firstly, it is necessary to make sure that the vial is above the liquid content of the tank and the cover is tight enough to prevent the water from entering the vial. Secondly, the water has to be wiped completely. Otherwise, it will be counted in the weight of the sample. Thirdly, the Ultrasonic cleaner generally increases the temperature of the sample. The

vial should not be kept in the water longer than 3 minutes, in order to avoid the influence of the temperature on the measured solubility.

2.3.2 Gas chromatograph

For liquid-liquid equilibrium measurement, e.g. ethanol/butanol/acetone extraction study, Varian Star CP-3800 Gas Chromatograph (GC) was used to measure the concentration of organic components in aqueous solutions. Varian Star Workstation Version 6.30 software was chosen to collect and record data. The column of Varian CP-SIL-5CB, 25m,.32 mm, 1.2 micrometer CP7760 Chrompack Capillary Column was used. The detector was FID detector.

The 2%, 4%, 6%, 8%, 10%, 20% molar organic solvent calibration standards were made for each organic component. Except butanol, water was used as the solvent for ethanol and acetone, since for butanol, there is a miscibility gap with water, then ethanol was used as the solvent instead. To make the GC samples for the calibration standards, a 20-200uL Finnpipette® was used to draw 100uL from one of the standards, then add ~900 uL solvent to dilute the samples, ethanol was chosen as solvent for the acetone/butanol standards and acetone was chosen for the ethanol standards. The samples follow the same procedures. All standards and samples are weighted before and after dilutions.

In order to prevent of vaporization from affecting the accuracy of experiments, all of standards and samples are sealed with Parafilm, and they are made immediately before running through the GC. The methods used in the GC were listed in Tables 2.3 and 2.4.

Table 2.3 GC parameters for acetone/ethanol analysis

First Clean:	CH_2Cl_2	Sample depth:	90%
Second Clean:	Ethanol /Acetone	Solvent depth:	90%
Prep ahead delay:	1.00 minutes	Injector Oven:	250°C
Coolant:	Enabled at 50°C	Detector:	300° C
Coolant timeout:	20.00 minutes	Time constant:	Fast
Stabilization time:	0.20 minutes	Make-up flow:	25ml/min
Column Oven:	50°	H_2 flow:	30ml/min
Oven duration:	4.00 minutes	Air flow:	300ml/min

Table 2.4 GC parameters for butanol analysis

First Clean:	CH_2Cl_2	Sample depth:	95%
Second Clean:	Ethanol	Solvent depth:	90%
Prep ahead delay:	2.23 minutes	Injector Oven:	250°C
Coolant:	Enabled at 50°C	Detector:	300° C
Coolant timeout:	20.00 minutes	Time constant:	Fast
Stabilization time:	0.20 minutes	Make-up flow:	25ml/min
Column Oven:	100°	H_2 flow:	30ml/min
Oven duration:	5.00 minutes	Air flow:	300ml/min

By using these methods, an ethanol peak was formed at ~1.95 minutes, an acetone peak was formed at ~2.12 minutes, and a butanol peak was formed at ~2.01 minutes. After calibration, the numerical results for each calibration standard were input into Excel and used to develop a calibration curve to determine the sample concentrations of the ternary system study.

2.3.3 Inductively covered plasma (ICP) spectroscopy

For Ethanol/ Butanol/ Acetone extraction experiments, HORIBA Jobin Yvon 2000 Inductively Covered Plasma (ICP) Spectroscopy as shown in Figure 2.9 is used to determine the ionic liquid concentration in both the aqueous phase and IL phase, which is an analytical technique used for trace and measure the element in aqueous or organic sample. ICP is to measure characteristic wavelength specific light emitted by the elements. It typically includes a sample introduction system (nebulizer), torch, high frequency generator, transfer optics and spectrometer and interface with computer. In a typical run, the sample was prepared in an aqueous or organic solution. Then it is pumped into the nebulizer, which transforms the solution into an aerosol. It is lighted at the torch. The light emitted by the atoms of an element is converted to an electrical signal by resolving the light into its component radiation, and then the light intensity is measured by a photomultiplier tube at the specific wavelength for each element line. The intensity of the electron signal is compared to previously measured intensities of known standard concentration of the element and a concentration is computed. Each element will have many specific wavelengths

available in the spectrum for analysis. Thus, the selection of the best requires considerable experience of ICP wavelengths.

ICP was used here to find the concentration of sulfur in the solutions. For JY2000, typical detection limit can be down to ppb level on radial view plasma. Radial view minimizes interferences. Continuous wavelength coverage is from 180 to 400nm.

Figure 2.9 Inductively Covered Plasma (ICP) Spectroscopy

The ICP acts by nebulizing the sample and then passing it through a plasma torch, which results in the compounds being transformed into their atomic elements. Each element emits certain wavelengths and intensities of light, which correspond to the specific elements in the solution and their concentrations. The detailed setup of ICP is shown in Figure 2.10.

Figure 2.10 Set up of ICP

When the samples were tested, firstly the ICP was ignited and given at least twenty minutes to warm up and stabilize. After that, it should run through a zero-order function and reference search in order to ensure that the device was functioning correctly. The calibration method should be set up, i.e., choosing the element of analyzing, unites, concentrations of all standards, and the wavelengths used to measure. The wavelength is generally chosen by detection limit, the lower, the better. But one can definitely select multiple wavelengths and after calibrations, compared

the peaks and choose the best one. Then the analysis sequence could be built, starting with a peak search and auto-attenuate (to calibrate the device to the lines being analyzed), followed by the calibration samples and then the analysis of all of samples. The lines used for this analysis were S 180.676 and S 181.978, due to their low limit of detection (0.0108 mg/ml).

The ICP parameters for aqueous solution and organic solutions are listed in Tables 2.5 and 2.6.

Table 2.5 ICP parameters for aqueous solutions

Power	1000 watts	Sheath stabilization time	10 s
Pump Speed	20 rpm	Nebulization flowrate	0.02 L/min
Plasma gas flowrate	12.0 L/min	Nebulization pressure	2.4 bar
Sheath gas flowrate	0.2 L/min	Transfer time	15 s, high speed
Aux gas flowrate	0.0 L/min	Rinse time	10 s, high speed
Concentration units	mg/ml	Stabilization time	10 s

Table 2.6 ICP parameters for organic solutions

Power	1350 watts	Sheath stabilization time	15 s
Pump Speed	5 rpm	Nebulization flowrate	0.35 L/min
Plasma gas flowrate	18.0 L/min	Nebulization pressure	1.2 bar
Sheath gas flowrate	0.5 L/min	Transfer time	40 s, normal speed
Aux gas flowrate	0.8 L/min	Rinse time	20 s, normal speed
Concentration units	mg/ml	Stabilization time	20 s

2.4 Polarity Measurements

In order to find out the reasons that ionic liquids and compressed gases, especially refrigerant, R134a, show different phase behaviors with temperature and pressure, the polarity of ionic liquids, R134a and mixtures of them were measured by Cary 300 Bio UV-visible Spectrophotometer. Since the usual Uv-vis vials only can handle atmosphere pressure, a steel high pressure Uv-vis cell is set up for this specific task. The whole set up is shown in Figure 2.11. The detailes of the high pressure cell are given in the following.

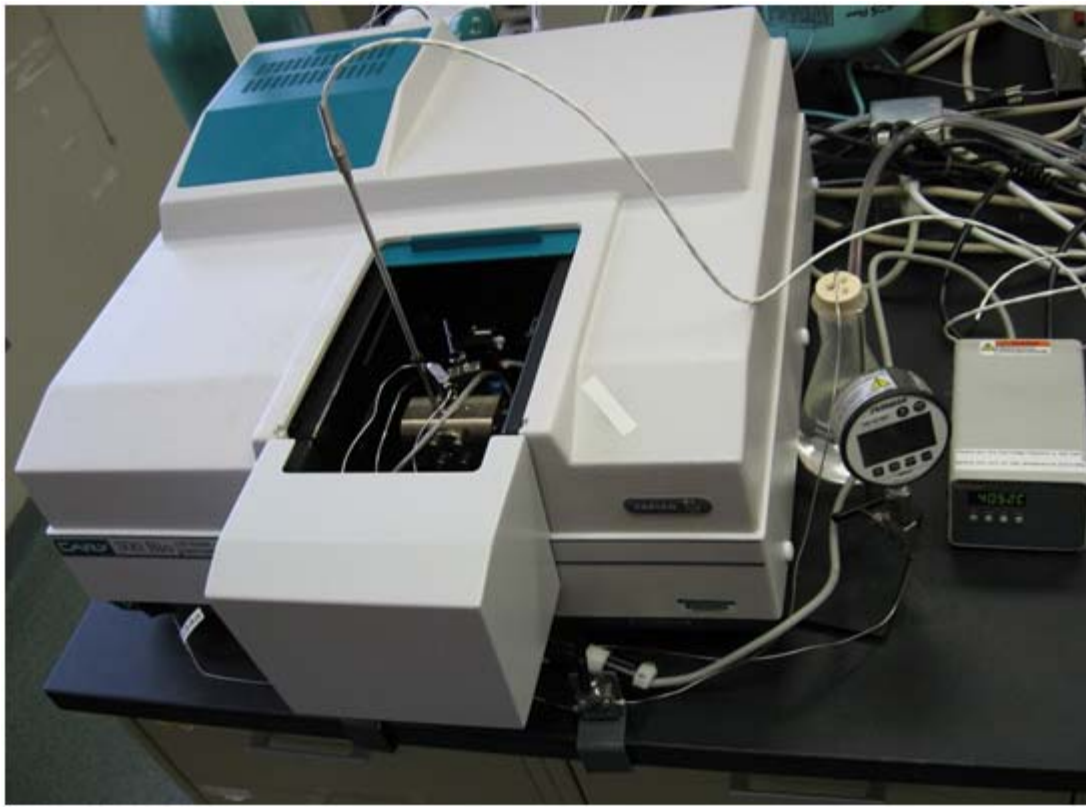

Figure 2.11 The whole set up of UV-vis high pressure polarity measurement

2.4.1 Setup of high pressure UV-vis cell

A stainless steel high pressure cell was built with three sapphire windows. The details are shown in Figures 2.12 and 2.13. The mechanical drawings of the high pressure cell are given in Appendix B. The side window was designed for monitor the liquid level when measure the gas/ liquid mixture. All of sapphire windows were sealed with PTFE 'O'-ring from McMaster Carr, which are 9560K38 – size 012 for main windows and 9560K36 – size 010 for the side window. This high pressure cell can be operated up to 150 ºC and 250 bar. The light path length is designed as 19.98 mm. The internal maximum volume of the cell is 2.5 ml. Three steel plugs were used to adjust the internal volume to be 1.9 ml, 1.6 ml and 1.3 ml. A Teflon stirring bar was used to agitate the contents to help to reach equilibrium. The cell is heated by a heating cartridges inserted into the cell body. The temperature controller 2200 is from Hart Scientific® with a resolution of 0.01 ºC or ºF and an accuracy of ±1.0 ºC. The pressure was monitored by two high accuracy digital test gauge, the DPG7000 series, with 0.05% Full Scale Total Error Band. At low pressure range, DPG 7000-1K was chosen with measuring range as 0-1000 psi. At high pressure range, DPG7000-3K was chosen with measuring range as 0-3000 psi. The solvatochromic measurement was measured by Cary 300 Bio UV-visible Spectrophotometer (Varian).

Figure 2.12 Picture of the high pressure UV-vis Cell

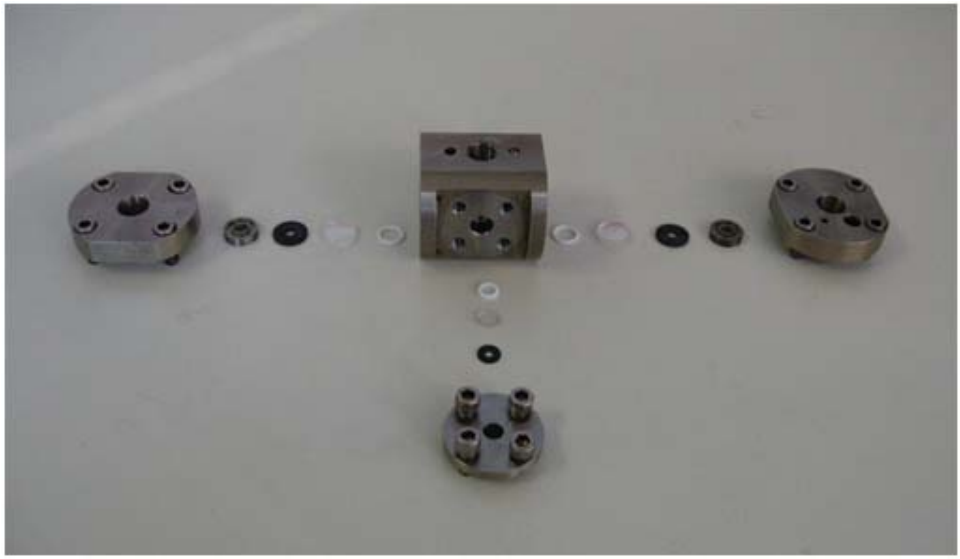

Figure 2.13 The detailed set up of the high pressure UV-vis Cell

2.4.2 Experimental procedure

The ILs will be dried under vacuum at given temperature at least 24 hours before using. The experimental procedure is as follows:

(1) The empty cell is scanned to check if there is solvent or any impurity left inside of the cell. If any impurity is found, the cell has to be washed for several time and dried until the background is clear.

(2) The pure ionic liquids are added into the cell with enough amount to cover the monitor window. Then the background was collected without dyes.

(3) The dye is added into the cell and a quick scan is done to check if the concentration of dye is appropriate. If the absorption (concentration) is too high, the pure ionic liquid is added to dilute. If the concentration is low, more dye is needed. Around 0.8 or 0.9 absorbance is corresponding to the right amount of dye to start with.

(4) The cell is closed and heated to desired temperature. It takes about 30-40 minutes to reach thermal equilibrium.

(5) After achieving thermal equilibrium, the gas is added into the cell. The pressure is controlled by injection of gases using syringe pumps (ISCO model 260 for CO_2 and ISCO model 100DM for R134a),

(6) The mixtures is mixed very well until there was no pressure drop, and the system is at phase equilibrium.

(7) The scan is done at all the wavelength range, and then narrowed to small rage according to the peak position.

(8) Gases were carefully vented and injected for several times to check if the measurement is repeatable.

(9) The pressure is increased to next desired value and repeat procedure given above.

(10) All the solvatochromic spectra were corrected by subtraction of the spectrum without dye.

2.4.3. Verifications

At room temperature (22 °C), the solvatochromic parameters of ethanol, 1-butanol and [HMIm][Tf_2N] with dyes were measured and the results are shown in Table 2.7. N,N-diethyl-4-nitroaniline was chosen to determine π^*, 4-nitroaniline was used to determine β, Reichardt's Dye was selected to determine α. The E_{T30} and E_{TN} were calculated accordingly.

Table 2.7 Verification of polarity measurements of Uv-vis cell

Component		π^*	β	α	E_{T30}	E_{TN}
Ethanol	This work	0.52	0.89	0.85	51.98	0.657
	Literature([21])	0.54	(0.77)	0.83		
	Diff (%)	3.85	13.48	2.35		
1-Butanol	This work	0.49	1	0.75	49.83	0.59
	Literature([21])	0.47	(0.88)	0.79		
	Diff (%)	4.08	12.00	5.33		
[HMIm][Tf_2N]	This work	0.8	0.45	0.61	52.04	0.659
	Literature ([22])				51.9	0.654
	Diff (%)				0.27	0.76
	Literature([23])	0.98	0.25	0.65	51.8	
	Diff (%)	22.50	44.44	6.56	0.19	

Note: The data in () are not certain by Authors

Diff= (this work-literature)/this work *100%

2.5 Ionic Liquid Synthesis and Analysis

1-n-Alkyl-3-methylimidazolium ionic liquids were prepared by anion exchange from the corresponding bromide salt of the imidazolium cation ([R-MIm][Br]) with corresponding anion in deionized water as described in the literature [24-25].

Elemental analysis was performed for all of ionic liquids used by Desert Analytics Transwest Geochem. ^{1}H-NMR spectra were recorded on a Bruker 400 NMR Spectrometer. The water content was determined by a Mettler Toledo DL32 Karl Fisher Coulometer and the Br content was measured by a Cole Parmer Bromide Electrode (27502-05) read with an Oakton Ion 510 series meter.

1-Ethyl-3-methylimidazolium bis(trifluoromethylsulfonyl)amide ([EMIm][Tf_2N]) was synthesized by anion exchange from 1-Ethyl-3-methyl-imidazolium bromide ([EMIm][Br]). [EMIm][Br] was synthesized by a quaternization reaction of 1-methyl-imidazole and bromoethane in acetonitrile at 40°C. Cation: *this reaction is highly exothermic and adequate amounts of solvent or cooling should be used.* To purify 1-Ethyl-3-methyl-imidazolium bromide, acetonitrile is added to dissolve the solid and then passed through a plug of celite (l=3cm) and passed through a short column of acidic alumina. The solvent was removed on a rotavap under reduced pressure and 40°C. [EMIm][Tf_2N] was prepared from the anion exchange of [EMIm][Br] with lithium bis(trifluoromethanesulfonyl)amide (Li[Tf_2N]) in deionized water as described in the literature [25]. The denser hydrophobic IL phase is decanted and washed with twice amount of water for 8-10 times. The IL is then dried under vacuum for at least 48 hours and stored in Schlenk tubes under dry argon.

HNMR chemical shifts (relative to TMS internal standard) and coupling constants J/Hz: δ=8.59 (s, 1H), 7.42(d, 2H, J=10.3), 4.24 (q, 2H, J=7.36), 3.93(s, 3H), 1.54(t, 3H, J=7.4). Analysis calculated for C8H11N3F6S2O4: C, 24.55; H, 2.83; N, 10.74; S, 16.39. Found: C, 24.62; H, 2.84; N, 10.71; S, 15.88, Water content is 63 ppm.

1-Hexyl-3-methylimidazolium bis(trifluoromethylsulfonyl) amide ([HMIm][Tf_2N]) was prepared in a similar manner synthesized by anion exchange from 1-hexyl-3-methyl-imidazolium bromide ([HMIm][Br]) [25]. An anion exchange of [HMIm][Br] with lithium bis(trifluoromethylsulfonyl)amide (Li[Tf_2N]) was performed in deionized water [24, 26]. The analysis results are as follows: ^{1}H NMR chemical shifts (relative to TMS internal standard) and coupling constants J/Hz: δ=8.65 (s, 1H), 7.39 (d, 2H, J=4.19), 4.17 (q, 2H, J=7.4), 3.93(s, 3H), 1.87(m, 4H), 1.32(6H, m) 0.87(t, 3H, J=6.53). Analysis calculated for $C_{12}H_{19}N_3F_6S_2O_4$: C, 32.21; H, 4.28; N, 9.39; S, 14.33. Found: C, 32.21; H, 4.27; N, 9.25; S, 14.19. The purity is estimated from elemental analysis and NMR to be 99+%. The water content is less than 100 ppm and the bromide content is 23 ppm.

1-n-Decyl-3-methyl-imidazolium bis(trifluoromethylsulfonyl)amide([DMIm][Tf_2N]): was prepared in a similar manner synthesized by anion exchange from 1-Decyl-3-methyl-imidazolium bromide ([DMIm][Br]) with lithium bis(trifluoromethylsulfonyl)amide (Li[Tf_2N]) ^{1}H NMR chemical shifts (relative to TMS internal standard) and coupling constants J/Hz: δ=8.66 (s, 1H), 7.36 (s, 1H), 7.36 (s, 1H), 4.15 (t, 2H, J=7.5), 3.92(s, 3H), 1.86(m, 4H), 1.26 (14H, m), 0.87 (t, 3H, J=6.7). Analysis calculated for $C_{16}H_{27}N_3F_6S_2O_4$: C,

38.17; H, 5.4; N, 8.34; S, 12.73. Found: C, 38.55; H, 5.3; N, 8.15; S, 12.29. The purity is estimated from elemental analysis and NMR to be 99+%. Bromide content was 46 ppm. The water content is 56 ppm.

1-Hexyl-3-Methylimidazolium Hexafluorophosphate ([HMIm][PF_6]): [HMIm][PF6] was prepared in a similar manner as [HMIm][Tf_2N], but from the anion exchange of [HMIm][Br] with ammonium hexafluorophosphate in deionized water [27-28]. ^{1}HNMR chemical shifts (relative to TMS internal standard) and coupling constants J/Hz: δ=8.43 (s, 1H), 7.33(brs, 2H), 4.12 (t, 2H, J=7.22), 3.87(s, 3H), 1.85(m, 4H), 1.28(6H, m), 0.84 (t,3H,J=6.96). Analysis calculated for $C_{10}H_{19}N_2PF_6$: C, 38.47; H, 6.13; N, 8.97; P, 9.92. Found: C, 38.64; H, 6.01; N, 9.01; P, 9.62. The purity is estimated from elemental analysis and NMR to be 99+%. The water content is 62 ppm and the bromide content is <8ppm.

1-Butyl-3-Methylimidazolium Hexafluorophosphate ([BMIm][PF_6]): [BMIm][PF6] was prepared in a similar manner as [HMIm][PF_6], but from the anion exchange of [BMIm][Br] with ammonium hexafluorophosphate in deionized water. ^{1}HNMR chemical shifts (relative to TMS internal standard) and coupling constants J/Hz: δ=8.35 (s, 1H), 7.31(brs, 1H), 7.28(brs, 1H), 4.09 (t, 2H, J=7.4), 3.83(s, 3H), 1.79(quint, 2H, J=7.4), 1.29(hex,2H, J=7.4), 0.85 (t,3H,J=7.4). Analysis calculated for $C_8H_{15}N_2PF_6$: C, 33.81; H, 5.32;N,9.86; P, 10.90; F,40.11. Found: C, 33.69; H, 5.21; N, 9.63; P, 10.40; F: 41.70. The purity is estimated from elemental analysis and NMR to be 99+%. The water content is 62 ppm and the bromide content is <8 ppm.

1-Hexyl-3-Methylimidazolium Tetrafluoroborate ([HMIm][BF_4]): [HMIm][BF4] was prepared from the anion exchange of [HMIm][Br] with ammonium tetrafluoroborate in deionized water. HNMR chemical shifts (relative to TMS internal standard) and coupling constants J/Hz: δ=8.72 (s, 1H), 7.52(d, 2H, J=3.6), 4.22 (t, 2H, J=7.23), 3.96(s, 3H), 1.89(m, 4H), 1.32(6H,m) 0.86(t,3H,J=6.54). Analysis calculated for $C_{10}H_{19}N_2BF_4$: C, 47.27; H, 7.54; N, 11.02; B, 4.25. Found: C, 46.99; H, 7.21; N, 10.88; B, 4.39. The purity is estimated from elemental analysis and NMR to be 99+%. The water content is less than 64 ppm and the bromide content is 123 ppm.

2.6 Materials

2.6.1 Synthesis ionic liquids

The materials used in ionic liquid synthesis are listed as follows: 1-Methylimidazole, (CAS 616-47-7) 99+%, lithium bis(trifluoromethylsulfonyl)amide (CAS 90076-65-6) 99.95%, acetonitrile, ≥99.9%; ammonium hexafluorophosphate (CAS 16941-11-0) 99.99%, ammonium tetrafluoroborate (CAS 13826-83-0) 99.99%, were purchased from Sigma-Aldrich. 1-Bromoethane (CAS 74-96-4) 99+%, bromobutane (CAS 109-65-9) 99%, bromohexane (CAS 111-25-1) 99+%, bromodecane (CAS112-29-8) 98%, and aluminium oxide (activated, acidic, for column chromatography; 100-500 micron) were obtained from Acros. Compressed argon (CAS 7440-37-1) (Ultra High Purity (UHP) grade) was obtained from Airgas,

Inc. 1-Methylimidazole, 1-bromo bromo-alkanes (ethane, butane, hexane, decane) were distilled immediately before the synthesis.

2.6.2 Compressed gases

1,1,1,2-Tetrafluoroethane (R-134a , 99.99%) was purchased from Linweld, Inc and used as received. Coleman Instrument grade CO_2 (99.99% purity) and Compressed argon (CAS 7440-37-1) (Ultra High Purity (UHP) grade) were obtained from Airgas, Inc.

2.6.3 Other components used

1-octene (CAS 111-66-0) 98% and nonanal (CAS 124-19-6) 95+% were purchased from Sigma-Aldrich. Coleman Instrument grade CO_2 (99.99% purity), syngas (H_2/CO (1:1): H_2: 99.99%, CO: 99.5%, certified standard) were obtained from Airgas, Inc. 1-octene and nonanal were used as received. Acetone (CAS: 67-64-1, ≥99.9%) 1-butanol (CAS: 71-36-3, ≥99%), ethanol (CAS: 64-17-5, ≥99.5%) were purchased from Sigma-Aldrich and used as received.

2.7 References

1. Reamer, H.H. and B.H. Sage, *Phase equilibriums in hydrocarbon systems. Volumetric and phase behavior of the n-decane-CO_2 system.* Journal of Chemical and Engineering Data, 1963. **8**(4): p. 508-13.
2. Shaver, R.D., R.L. Robinson, and K.A.M. Gasem, *An automated apparatus for equilibrium phase compositions, densities, and interfacial tensions: data for carbon dioxide +decane.* Fluid Phase Equilibria 2001. **179**(1-2): p. 43-66.

3. Dohrn, R. and G. Brunner, *High-pressure fluid-phase equilibria: experimental methods and systems investigated (1988-1993).* Fluid Phase Equilibria, 1995. **106**(1-2): p. 213-82.

4. Jennings, D.W. and R.C. Schucker, *Comparison of High-Pressure Vapor-Liquid Equilibria of Mixtures of CO_2 or Propane with Nonane and C9 Alkylbenzenes.* Journal of Chemical and Engineering Data 1996. **41**(4): p. 831-838.

5. Nagarajan, N. and R.L. Robinson, Jr., *Equilibrium phase compositions, phase densities, and interfacial tensions for carbon dioxide + hydrocarbon systems. 2. Carbon dioxide + n-decane.* Journal of Chemical and Engineering Data, 1986. **31**(2): p. 168-71.

6. Ren, W. and A.M. Scurto, *High-pressure phase equilibria with compressed gases.* . The Review of scientific instruments, 2007. **78**(12).

7. Kohn, J.P., *THE HETEROGENEOUS PHASE AND VOLUMETRIC BEHAVIOR OF THE METHANE-HYDROGEN SULFIDE SYSTEM*, in *Department of chemical engineering*. 1956, Uinversity of Kansas: Lawrence, Kansas. p. 238.

8. Huie, N.C., *THE HETEROGENEOUS PHASE EQUILIBRIA OF CARBON DIOXIDE-NORMAL PARAFFIN SYSTEMS*, in *Department of Chemical Engineering*. 1972, University of Notre Dame: Notre Dame, Indiana.

9. Scurto, A.M., *HIGH-PRESSURE PHASE AND CHEMICAL EQUILIBRIA OF β–DIKETONE LIGANDS AND CHELATES WITH CARBON DIOXIDE*, in

Department of Chemical Engineering. 2002, University of Notre Dame: Notre Dame, Inidiana. p. 323.

10. Fall, D.J. and K.D. Luks, *Phase equilibria behavior of the systems carbon dioxide + n-dotriacontane and carbon dioxide + n-docosane.* Journal of Chemical and Engineering Data, 1984. **29**(4): p. 413-17.
11. De Loos, T.W., H.J. Van der Kooi, and P.L. Ott, *Vapor-liquid critical curve of the system ethane + 2-methylpropane.* . Journal of Chemical and Engineering Data, 1986. **31**(2): p. 166-8.
12. Kuehne, E., C.J. Peters, J. van Spronsen, and G.-J. Witkamp, *Solubility of carbon dioxide in systems with [BMIm][BF_4] and some selected organic compounds of interest for the pharmaceutical industry.* Green Chemistry 2006. **8**(3): p. 287-291.
13. Lemmon, E.W., M.L. Huber, and M.O. McLinden, *NIST Reference Fluid Thermodynamic and Transport Properties - REFPROP*, in *Version 8.0*. 2007: Gaithersburg, Maryland.
14. Span, R. and W. Wagner, *A New Equation of State for Carbon Dioxide Covering the Fluid Region from the Triple-Point Temperature to 1100 K at Pressures up to 800 MPa.* J. Phys. Chem. Ref. Data, 1996. **25**(6): p. 1509-1596.
15. Hicks, C.P. and C.L. Young, *Gas-liquid critical properties of binary mixtures.* Chemical Reviews, 1975. **75**(2): p. 119-75.

16. Sacha, G.A., W.J. Schmitt, and S.L. Nail, *Identification of critical process variables affecting particle size following precipitation using a supercritical fluid.* Pharmaceutical Development and Technology, 2006. **11**(2): p. 187-194.

17. Konynenburg, P.H.V. and R.L. Scott, *Critical Lines and Phase Equilibria in Binary Van Der Waals Mixtures*, in *Philos. Trans. R. Soc. Ser. A* 1980: London. p. 495-540.

18. Scott, R.L. and P.H. Van Konynenburg, *Static properties of solutions. 2. Van der Waals and related models for hydrocarbon mixtures.* Discussions of the Faraday Society, 1970. **No. 49**: p. 87-97.

19. Koch, D. and W. Leitner, *Rhodium-Catalyzed Hydroformylation in Supercritical Carbon Dioxide.* Journal of the American Chemical Society, 1998. **120**(51): p. 13398-13404.

20. Schleicher, J., *Kinetics and Solvent Effects in the Synthesis of Ionic Liquids*, in *Chemical & Petroleum Engineering*. 2007, University of Kansas: Lawrence.

21. Kamlet, M., J. Abboud, M. Abraham, and R. Taft., *Linear solvation energy relationships.* J. Org. Chem., 1983. **48**: p. 2877-2887.

22. Reichardt, C., *Polarity of ionic liquids determined empirically by means of solvatochromic pyridinium N-phenolate betaine dyes.* Green Chem., 2004. **7**: p. 339-351.

23. Mellein, B.R., S.N.V.K. Aki, R.L. Ladewski, and J.F. Brennecke, *Solvatochromic Studies of Ionic Liquid/Organic Mixtures.* Journal of Physical Chemistry B, 2007. **111**: p. 131-138.

24. Bonhôte, P., A.P. Dias, N. Papageorgiou, K. Kalyanasundaram, and M. Gratzel, *Hydrophobic, highly conductive ambient-temperature molten salts.* Inorg. Chem, 1996. **35**(5): p. 1168-1178.

25. Nockemann, P., K. Binnemans, and K. Driesen, *Purification of imidazolium ionic liquids for spectroscopic applications.* Chemical Physics Letters, 2005. **415**(1-3): p. 131-136.

26. Burrell, A.K., R.E.D. Sesto, S.N. Baker, T.M. McCleskey, and G.A. Baker, *The large scale synthesis of pure imidazolium and pyrrolidinium ionic liquids.* Green Chem., 2007. **9**(5): p. 449-454.

27. Maruyama, T., S. Nagasawa, and M. Goto, *Poly (ethylene glycol)-lipase complex that is catalytically active for alcoholysis reactions in ionic liquids.* Biotechnology Letters, 2002. **24**(16): p. 1341-1345.

28. Wang, B., Y.R. Kang, L.M. Yang, and J.S. Suo, *Epoxidation of a, ß-unsaturated carbonyl compounds in ionic liquid/water biphasic system under mild conditions.* Journal of Molecular Catalysis A: Chemical, 2003. **203**(1-2): p. 29-36.

Chapter 3 Thermodynamic Modeling

The measurement of vapor liquid equilibrium is described in Chapter 2. In order to evaluate and design the systems using ionic liquids and compressed gases, a large amount of data need to be collected, such as P-T-x, H-T, H-x, etc. However, experiments are time-consuming, expensive and usually difficult at high temperature and pressure. Therefore, a thermodynamic model is necessary to be developed to predict phase equilibria over a wide range of conditions.

This chapter focuses on the thermodynamic models that have been developed to correlate and predict phase equilibria. A thermodynamic phase is defined as a part of system that is uniform in chemical and chemical properties. Two phases tend to exchange constituents when they are brought into contact until the composition of each phase attains a constant value as determined by thermodynamics. In vapor liquid equilibrium (VLE), the overall system is heterogeneous, but each phase itself is homogenous.

3.1 Criteria for Phase Equilibrium

In this work, phase equilibria calculations include the mixture critical points and binodal equlibrium. The criteria to evaluate the phase equilibria are the basis for thermodynamic calculations.

3.1.1 Criteria of phase equilibrium for pure component

If a pure component reaches phase equilibrium between vapor and liquid phases, the temperature, pressure and chemical potential in two phases are identical. The same for other phase equilibria, such as liquid-solid and vapor-solid.

$$T^{I} = T^{II} \tag{3.1a}$$

$$P^{I} = P^{II} \tag{3.1b}$$

$$\mu^{I} = \mu^{II} \tag{3.1c}$$

The equivalent conditions can also be expressed as Gibbs function and fugacity:

$$G^{I} = G^{II} \tag{3.2a}$$

$$f^{I} = f^{II} \tag{3.2b}$$

3.1.2 Criteria of phase equilibrium for binary or multiple mixtures

For binary mixture and multiple component systems, the thermodynamic criteria for phase equilibria can be extended from pure component as:

$$T^{I} = T^{II} = T^{III} = \cdots\cdots = T \tag{3.3a}$$

$$P^{I} = P^{II} = P^{III} = \cdots\cdots = P \tag{3.3b}$$

$$\hat{\mu}_i^{I} = \hat{\mu}_i^{II} = \hat{\mu}_i^{III} = \cdots\cdots = \hat{\mu}_i \tag{3.3c}$$

The chemical potential is often difficult to use for phase equilibrium calculations as it becomes negative infinity at low pressures and dilute concentrations. However, fugacity is directly related to the chemical potential but does not have the same numerical problems. Fugacity is also called as “corrected pressure” and helps

to bridge between theory and pure thermodynamics. At equilibrium, the fugacities must be identical in all phases,

$$\bar{f}_i^I = \bar{f}_i^{II} = \bar{f}_i^{II} = \cdots\cdots = \bar{f}_i \tag{3.4}$$

The relation between chemical potential and fugacity is:[1]

$$\begin{aligned} &\mu_i - \mu_i^o = RT \ln \frac{\bar{f}_i}{\bar{f}_i^o} \\ &\bar{f}_i \to P y_i \qquad as \qquad P \to 0 \end{aligned} \tag{3.5}$$

The fugacity with hat represents the mixture fugacity. The superscript "o" is defined as standard state. For an ideal gas mixture, fugacity is equal to partial pressure.

The fugacity coefficient is defined as the ratio of the fugacity of a gas to its pressure.

$$\hat{\phi}_i = \frac{\bar{f}_i}{P} \tag{3.6}$$

For vapor-liquid equilibrium, two thermodynamic methods are generally used to calculate the phase equilibrium: equations of state (Φ-Φ method) and activity coefficient models (γ- Φ method). These two models will be discussed in the following sections.

3.1.3 Stability analysis

For a fluid-fluid equilibrium problem at constant temperature and pressure, the conventional algorithm is the fugacity-equality criteria, but it is only a necessary condition for stable state. The global minimum of Gibbs free energy needs to be located in order to obtain the thermodynamically stable state. Many false solutions

have been found in liquid-liquid and vapor-liquid-liquid equilibria by only solving the fugacity-equality criteria. Reported approaches to solve global phase stability can be classified into two groups:

(1) examine the magnitude and sign of the appropriate determinants of partial derivatives

(2) tangent plane analysis.

The tangent-line analysis satisfies the following equations at overall composition:

$$\left(\frac{\partial \tilde{g}_m}{\partial x_i} - \frac{\partial \tilde{g}_m}{\partial x_n}\right) - \left(\frac{\partial \tilde{g}_m}{\partial x_i} - \frac{\partial \tilde{g}_m}{\partial x_n}\right)_{x=z} = 0 \tag{3.7}$$

which can be also rewritten by

$$D(x,z) = \tilde{g}_m(x) - \tilde{g}_m(z) - \sum_{i=1}^{n}\left(\frac{\partial \tilde{g}_m}{\partial x_i}\right)_{x=z}\left(x_i - z_i\right) \tag{3.8}$$

where, $\tilde{g}_m$ is the dimensionless molar Gibbs energy of mixing, x_i means the mole fraction of component *i* in the mixture, and z_i is the solutions to the equifugacity conditions for solid-fluid equilibrium.

If *D* is negative for any value of *x*, the Gibbs energy surface is below the tangent plane. Thus, the phase of composition *z* being tested is not stable.

Based on the Peng-Robinson equation of state, the dimensionless molar Gibbs energy of mixing at certain Pressure and temperature is:

$$\tilde{g}_m(x) = \frac{P\underline{V}}{RT} + \ln\frac{RT}{\underline{V} - b_m} + \frac{a_m}{b_m \times 2\sqrt{2} \times RT}\ln\left(\frac{\underline{V} + (1-\sqrt{2})b_m}{\underline{V} + (1+\sqrt{2})b_m}\right) + \sum_{i=1}^{n} x_i \ln x_i - \sum_{i=1}^{n} x_i \tilde{g}_i^0 \tag{3.9}$$

3.1.4 Criteria of vapor-liquid, liquid-liquid, vapor-liquid-liquid phase equilibrium

3.1.4.1 Criteria of vapor-liquid phase equilibrium

When system reaches vapor liquid equilibrium, the fugacity for each component in liquid phase (f_i^L) is equivalent to the fugacity in vapor phase (f_i^V):

$$\bar{f}_i^L = \bar{f}_i^V \qquad i = 1,2,\cdots \tag{3.10}$$

For Φ-Φ method, the fugacity for each phase can be expressed as fugacity coefficient Φ_i, mole fraction (x or y), and pressure (P).

$$\hat{\phi}_i^L x_i P = \hat{\phi}_i^V y_i P \quad i = 1,2,\cdots \tag{3.11}$$

where, the fugacity for both the liquid phase and vapor phase can be calculated from an equation of state.

For γ - Φ method, the fugacity of liquid and vapor phase can be expressed as:

$$\bar{f}_i^L = \gamma_i x_i \bar{f}_i^0 = \bar{f}_i^V = \hat{\phi}_i^V y_i P \quad i = 1,2,\cdots \tag{3.12}$$

Although the vapor phase fugacity can be calculated from equation of state, the liquid phase fugacity is calculated from activity coefficient model.

3.1.4.2 Criteria of liquid-liquid phase equilibrium

The system can reach liquid-liquid equilibrium at certain pressure and temperature. For instance, ionic liquids and compressed gases, when pressure is higher than vapor pressure and temperature lower than critical temperature, the

systems exist at liquid-liquid equilibrium. The fugacity for each component in one liquid phase (f_i^{L1}) is equivalent to the fugacity in the other liquid phase (f_i^{L2}).

$$\bar{f}_i^{L_1} = \bar{f}_i^{L_2} \qquad i = 1,2,\cdots \tag{3.13}$$

If the equation of state is used for calculation, the fugacity equivalence can be related by:

$$\hat{\phi}_i^{L_1} x_i^{L_1} P = \hat{\phi}_i^{L_2} x_i^{L_2} P \tag{3.14a}$$

or

$$\hat{\phi}_i^{L_1} x_i^{L_1} = \hat{\phi}_i^{L_2} x_i^{L_2} \tag{3.14b}$$

If the activity coefficient model is chosen here for calculation, the fugacity equivalence can be related by:

$$\gamma_i^{L_1} x_i^{L_1} \bar{f}_i^0 = \gamma_i^{L_2} x_i^{L_2} \bar{f}_i^0 \tag{3.15}$$

or

$$\gamma_i^{L_1} x_i^{L_1} = \gamma_i^{L_2} x_i^{L_2} \tag{3.16}$$

3.1.4.3 Criteria of vapor-liquid-liquid phase equilibrium

When a system reaches vapor-liquid-liquid equilibrium, there are three phases coexist. For an ionic liquid and R-134a system, when the temperature is at between lower critical end point (LCEP) and upper critical end point (UCEP), the pressure is close to pure R-134a vapor pressure, vapor-liquid-liquid equilibrium exists in the system. The fugacities for each component are equal in each phase.

$$\bar{f}_i^{L_1} = \bar{f}_i^{L_2} = \bar{f}_i^{V} \qquad i = 1,2,\cdots \tag{3.17}$$

For Φ-Φ method, the equivalent can be rewritten as

$$\hat{\phi}_i^{L_1} x_i^{L_1} P = \hat{\phi}_i^{L_2} x_i^{L_2} P = \hat{\phi}_i^{V} y_i P \quad i = 1,2,\cdots \tag{3.18}$$

For γ- Φ method, it can be obtained by

$$\gamma_i^{L_1} x_i^{L_1} \bar{f}_i^{0} = \gamma_i^{L_2} x_i^{L_2} \bar{f}_i^{0} = \hat{\phi}_i^{V} y_i P \tag{3.19}$$

Equilibrium of phases requires the fugacity (or chemical potential) of a given component to be the same in every phase. Temperature, pressure, concentration, etc are equal too. In addition, the fugacity (or chemical potential) of a given component is the same in every phase. In principle, formulation VLE in terms of fugacity and chemical potential are equivalent.

3.2 Equation of State

Equations of state (EoS) are thermodynamic functions that mathematically describe the state of a matter under a given set of physical conditions, i.e., the temperature, pressure and volume (or molar volume). EoS have been an important tool to study phase equilibria of fluid or fluid mixtures. EoS offer several advantages to calculate phase equilibria [2]. First, EoS is a proven tool of describing mixtures of diverse components. Extensive researches have been carried out on the application of EoS to various phase equilibria studies, such as vapor-liquid, liquid-liquid, etc. Second, EoS can be applicable over a wide range of physical conditions, i.e., temperature and pressure. EoS have also been reported to calculate phase equilibria in the region of critical condition and systems involving supercritical fluids.

The ideal gas law states that the state of an amount of hypothetical ideal gas is determined by its pressure, volume, and temperature according to the equation:

$$P\underline{V} = RT \tag{3.20}$$

where

P – the pressure

T – the temperature

$\underline{V}$ – the molar volume

R – the gas constant

The ideal gas law assumes that an imaginary gas satisfies the following conditions: (1) interactions between the molecules are negligible; (2) molecules occupy no volume; (3) collisions between molecules are perfectly elastic. Therefore the ideal gas EoS describes the PVT behaviors inaccurately, both quantitatively and qualitatively. Various EoS have been developed that radically improved predictive capability over ideal gas EoS.

3.2.1 Cubic EoS

In 1873, van der Waals proposed the following EoS to predict the coexistence of vapor and liquid:

$$\left(P + \frac{a}{\underline{V}^2}\right)(\underline{V} - b) = RT \tag{3.21}$$

where

a – the measure of the attraction strength between particles

b - the volume occupied by particles

The constants can be calculated from the critical properties of the matter (P_c, T_c and v_c):

$$a = \frac{27R^2T_c^2}{64P_c}$$
$$b = \frac{RT_c}{8P_c} \tag{3.22}$$

Redlich and Kwong [3] reported the RK EoS in 1949:

$$P = \frac{RT}{\underline{V} - b} - \frac{a}{T^{1/2}\underline{V}(\underline{V} + b)} \tag{3.23}$$

where

$$a = \frac{0.42748R^2T_c^{2.5}}{P_c} \quad , \quad b = \frac{0.08664RT_c}{P_c} \tag{3.24}$$

RK EoS is superior to the van der Waals EoS through the introduction of the temperature dependence for the attractive term. Soave [4] improved the RK EoS by introducing temperature dependence to the 2nd term (SRK EoS):

$$P = \frac{RT}{\underline{V} - b} - \frac{a\alpha}{\underline{V}(\underline{V} + b)} \tag{3.25}$$

where

$$\alpha = (1 + k(1 - \sqrt{T_r}))^2$$
$$k = 0.480 + 1.574\omega - 0.176\omega^2 \tag{3.26}$$
$$T_r = T / T_c$$

w- acentric factor

In 1976, Peng and Robinson [5] proposed additional modifications to obtain more accurate prediction of the liquid density:

$$P = \frac{RT}{\underline{V} - b} - \frac{a}{\underline{V}(\underline{V} + b) + b(\underline{V} - b)} \tag{3.27}$$

where

$$\begin{aligned} a &= a_c(1 + \kappa(1 - \sqrt{T_r}))^2 \\ a_c &= \frac{0.45724 R^2 T_c^2}{P_c} \\ \kappa &= 0.37464 + 1.54226\omega - 0.26992\omega^2 \\ b &= \frac{0.07780 R T_c}{P_c} \end{aligned} \tag{3.28}$$

These EoS mentioned above belong to the family of the cubic EoS, which can be expressed in a general form of five parameters:

$$P = \frac{RT}{\underline{V} - b} - \frac{\Theta(\underline{V} - \eta)}{(\underline{V} - b)(\underline{V}^2 + \delta\underline{V} + \varepsilon)} \tag{3.29}$$

Relations and values for parameters in several common cubic EoS are shown in Table 3.1. Parameter *b*, in all cases listed, is a positive constant and $\eta = b$. The temperature dependence is included in the parameter $\Theta = a\alpha(T_r, w)$.

Table 3.1 Parameters for cubic EoS

EoS	δ	ε	Θ
van der Waals	0	0	a
RK	0	0	$aT_r^{-0.5}$
SRK	b	0	$a\left[1 + (0.48 + 1.574\omega - 0.176\omega^2)(1 - T_r^{0.5})\right]^2$
PR	2b	$-b^2$	$a\left[1 + (0.3744 + 1.54226\omega - 0.2699\omega^2)(1 - T_r^{0.5})\right]^2$

3.2.2 Non cubic equation of state

Cubic EoS are based on van der Waals equation. Modifications have been made to the treatment of the hard sphere repulsive term and/or the mean field attractive term. Parameter values are obtained by fitting experimental data such that the phase behavior of simple fluids and their mixtures can be accurately predicted. However, modeling complex systems, such as polymers and associating systems demands EoS derived from a more theoretical basis that accommodates the complexities of molecular shape and molecular association. [6]

Substantial progress has been made in the molecular theory based EoS, such as those derived from Statistical Associating Fluid Theory (SAFT) approach [7]. Since the effects of molecular shape and interactions on the thermodynamic properties are separated and quantified, the SAFT EoS is able to accurately model both simple spherical molecules and chain fluids. Furthermore, SAFT EoS has the potential advantage of being capable of modeling polar systems by including an association contribution to the Helmholtz free energy of the system [8].

SAFT was originally developed to model associating fluids as Lennard–Jones chains with short-range association sites. Recent years, the original expression has been extended to describe chain molecules formed from hard-core segments with attractive potentials of variable range (SAFT-VR) which provides significant improvement and predictive capability over the earlier formulations [6].

3.3 Mixing Rules

When EoS are extended to model mixtures, the inherent assumption is that the form of EoS remains the same as pure fluid, but with modified attractive and volume parameters, *a* and *b*. EoS parameters of the mixture are assembled using the mole fraction concentrations and can be density dependent. Mixing rules incorporate compositional dependence into the mixture parameters.

The van del Waals mixing rule is mostly commonly used:

$$a_m = \sum_i \sum_j x_i x_j a_{ij} \tag{3.30}$$

$$b_m = \sum_i \sum_j x_i x_j b_{ij} \tag{3.31}$$

where a_m is the attractive parameter and b_m is the mixture co-volume parameter; a_{ii} and a_{jj} are the constants of pure components; a_{ij} and b_{ij} are the cross parameters.

van der Waals mixing rule assumes that the radial distribution function of the component molecules are identical and they both explicitly contain a contribution from interactions between dissimilar molecules. Extensive investigations have shown that the van del Waals mixing rule is adequate for modeling phase behavior of mixtures of nonpolar and slightly polar compounds, however it may fail to model strongly nonideal mixtures [2].

For binary systems, the mixture attractive and co-volume parameters, a_m and b_m, can be defined with one binary parameter (vdW-1 parameter mixing rule).

$$a_{12} = (1 - k_{12}) a_1^{0.5} a_2^{0.5} \tag{3.32}$$

$$b_{12} = \frac{b_1 + b_2}{2} \tag{3.33}$$

where k_{12} measures the deviation from geometric intermolecular interactions a_m. Alternatively, a second parameter can be included that measures the deviation from arithmetic intermolecular interactions repulsions (vdW-2 parameter mixing rule). Then,

$$b_{12} = \frac{b_1 + b_2}{2}(1 - l_{12}) \tag{3.34}$$

These binary interaction parameters (k_{ij}, l_{ij}) are a measure of the deviation from the geometric mean of parameter *a* and the arithmetic mean of the parameter *b*, which can be positive, negative, or zero. While some have seen physical meaning in the size and sign of the parameters, they are mostly to correct the assumptions of the model. For instance, sometimes a k_{12} less than zero may indicate the presence of specific chemical interaction such as hydrogen bonding in the mixture. However, this observation does not always hold.

Research efforts have been taken to improve the van der Waals mixing rule in order to accurately represent phase equilibria in highly polar mixtures, associated mixtures, and other very complex systems [9]. Reported approaches include non-quadratic mixing rules, multiple interaction parameters in the quadratic mixing rules, the introduction of the local-composition concept, the combination of excess Gibbs free energy models and EoS. Adachi and Sugie [10] proposed the following nonquadratic mixing rule that includes the composition dependent binary interaction parameters to *a* and keeps *b* unchanged:

$$a_{ij} = a_{ii}^{0.5} a_{jj}^{0.5} \left[1 - l_{ij} - m_{ij}(x_i - x_j)\right] \tag{3.35}$$

where

$$l_{ij} = l_{ji} \text{ and } m_{ij} = -m_{ji}$$

Wong and Sandler [11] proposed a mixing rule (WS mixing rule) for two-parameter cubic EoS that is consistent with statistical mechanical requirements. Particularly, the second virial coefficient depends quadratically on the concentration. The parameters *a* and *b* are obtained from:

$$b - \frac{a}{RT} = \sum_i \sum_j x_i x_j \left(b - \frac{a}{RT}\right)_{ij} \tag{3.36}$$

and

$$\frac{A_\infty^{ex}}{CRT} = \frac{a}{bRT} - \sum_i x_i \frac{a_i}{b_i RT} \tag{3.37}$$

where *C* is a constant. For PR EoS,

$$C = \frac{\ln(\sqrt{2} - 1)}{\sqrt{2}} = -0.62323 \tag{3.38}$$

The cross term is calculated as:

$$\left(b - \frac{a}{RT}\right)_{ij} = \frac{1}{2}\left[\left(b_i - \frac{a_i}{RT}\right) + \left(b_j - \frac{a_j}{RT}\right)\right]\left(1 - k_{ij}\right) \tag{3.39}$$

WS mixing rule provides a simple method to accurately extend low-pressure prediction models to high temperature and pressure.

Binary interaction parameters are of significant importance for cubic EoS model to predict the correct phase behavior. The parameter can be estimated by

fitting experimental data. Therefore, the binary interaction parameters can be obtained by minimizing the difference between the experimental data and the calculated values with cubic EoS models. The approach of determine the binary interaction parameters with solubility data is described in sequel.

3.4 Activity Coefficient Models

At lower pressures, activity coefficient models may be used to account for non-idealities of the liquid phase. Several activity coefficient models (also called the excess Gibbs free energy models) have been developed, such as Wilson model [12], NRTL model (Non-Random Two-Liquid [13], Universal Quasi Chemical (UNIQUAC) [14], etc. The Wilson model [12] only requires binary parameters even for multi-component systems. It can apply to a variety of miscible mixtures containing polar or association components, but it is invalid to LLE systems. The NRTL model [13] can provide a good representation of experimental data for strongly nonideal mixtures, especially for partially immiscible systems. For a binary system, the NRTL model involves 3 parameters. One is related to the nonrandomness in the mixture and the other two are energy parameters characteristic of the interaction. The NRTL parameters are fitted to activity coefficients derived from experimental data. Temperature dependent parameters can be introduced, if activity coefficients are available over a large temperature range. NRTL model fits for both miscible and partially miscible systems.

The UNIQUAC model [14] represents the excess Gibbs free energy as two terms, a combinatorial part and a residual part. The combinatorial part is calculated exclusively from chemical parameters and attempts to describe the dominant entropic contribution. The residual contains an empirical parameter and accounts for intermolecular forces. The main advantages of the UNIQUAC model are its relative simplicity and wide range of applications. The UNIQUAC equation has been extended to the development of the UNIFAC model [15], which uses the functional groups to calculate activity coefficients and eliminates the calculation of UNIQUAC parameters from experimental data. The UNIFAC model, a predictive version of UNIQUAC, has been successfully applied to semi-quantitatively predict VLE for a wide variety of mixtures. It is good for both miscible and partially miscible systems.

3.5 Phase Equilibria Calculations

The section describes how to calculate the phase equilibria in this work and the approach to optimally determine the binary interaction parameters with the PR EoS model. PR EoS is selected in this study due to its simplicity and accuracy for the prediction of volumetric and thermodynamics properties.

3.5.1 Parameter regression

For a binary liquid mixture in equilibrium with a vapor, the fugacity coefficient of each component in the vapor phase, $\hat{\varphi}_i^V$, is calculated as:

$$\ln \hat{\varphi}_i^V = \frac{1}{RT}\int_{V^V}^{\infty}\left[\left(\frac{\partial P}{\partial n_i}\right)_{T,V,n_j} - \frac{RT}{\underline{V}}\right]dV - \ln\frac{P\underline{V}^V}{n_T RT} \tag{3.41}$$

Where n_i is the number of moles of component i and n_T is the total number of moles in the vapor phase.

Similarly, $\hat{\varphi}_i^L$, is calculated as:

$$\ln \hat{\varphi}_i^L = \frac{1}{RT}\int_{V^L}^{\infty}\left[\left(\frac{\partial P}{\partial n_i}\right)_{T,V,n_j} - \frac{RT}{\underline{V}}\right]dV - \ln\frac{P\underline{V}^L}{n_T RT} \tag{3.42}$$

Using the Peng-Robinson EoS for mixture,

$$P = \frac{RT}{\underline{V} - b_m} - \frac{a_m}{\underline{V}(\underline{V}+b_m)+b_m(\underline{V}-b_m)} \tag{3.43}$$

and the vdW-1 parameter mixing rule, the fugacity coefficient, the fugacity coefficients of vapor and liquid are calculated as:

$$\ln \hat{\varphi}_i^v = \frac{b_i}{b}\left(\frac{P\underline{V}^V}{RT}-1\right) - \ln\frac{P\left(\underline{V}^V - b\right)}{RT} - \frac{a}{2\sqrt{2}bRT}\left(\frac{2\sum_k y_k a_{ki}}{a} - \frac{b_i}{b}\right)\ln\frac{\underline{V}^V + \left(1+\sqrt{2}\right)b}{\underline{V}^V + \left(1-\sqrt{2}\right)b} \tag{3.44}$$

$$\ln \hat{\varphi}_i^L = \frac{b_i}{b}\left(\frac{P\underline{V}^L}{RT}-1\right) - \ln\frac{P\left(\underline{V}^L - b\right)}{RT} - \frac{a}{2\sqrt{2}bRT}\left(\frac{2\sum_k x_k a_{ki}}{a} - \frac{b_i}{b}\right)\ln\frac{\underline{V}^L + \left(1+\sqrt{2}\right)b}{\underline{V}^L + \left(1-\sqrt{2}\right)b} \tag{3.45}$$

In summary, the problem is formulated as a nonlinear programming (NLP) problem. Given the VLE data of a binary system that consists of sets of temperature (T), pressure (P), and liquid (x) and vapor phase mole fractions (y) for one of the components, it is obvious that the independent variables of the optimization problem are binary interaction parameters. Therefore, the determination of binary interaction coefficients is an optimization problem of a small number of dimensions, and various

optimization methods can be employed determine the optimal value of binary interaction parameters.

3.5.2 Regression VLE parameters with PE2000

The software, Phase Equilibrium 2000 (PE2000) developed by Brunner *et al.* [16] was employed here to regress VLE parameters. The software package has been reported to be a powerful tool to correlate and predict phase equilibria [17-20]. PE2000 optimizes the binary interaction parameters by minizing one of four types of objective functions, such as absolute, absolute square, relative and relative square. PE2000 offers the possibility to calculate phase equilibria and densities at any conditions using optimum interaction parameters.

PE2000 offers more than 40 different equations of state (EoS) with up to 7 different mixing rules for correlating and predicting phase equilibria. Users can also supply source code with the own EoS to be implemented in PE2000.

Given EoS, mixing rule and objective functions, PE 2000 optimizes the binary interaction parameters by minizing the deviation between experiment data and calculated values. Moreover, PE2000 offers the possibility to calculate phase equilibria and densities at any conditions using optimum interaction parameters. Graphical output routines then plot the miscibility gaps in binary and ternary systems.

The binary interaction parameters are determined by minimizing the differences between experimental and calculated data. The objective function chosen here is the average absolute relative deviation (%AARD):

$$\%AARD = \frac{1}{N}\sum_{i=1}^{N}\left|\frac{x_2^{\exp} - x_2^{calc}}{x_2^{\exp}}\right| \times 100\% \tag{3.46}$$

where, x_2^{exp} is the experimental data; x_2^{calc} is the calculated thermodynamic property with PR EoS model; N is the number of experimental data. Solubility data are used to determine the optimal binary interaction parameters.

3.5.2.1 Binary systems

If both k_{12} and l_{12} are used in the mixing rule, the optimal values can be determined by solving a 2 dimensional optimization problem. PE2000 provides two ways to optimize interaction parameters: the Grid method and the Simplex-Nelder-Mead algorithm [21]. The Grid method calculates the deviation on a user-defined rectangular grid, while the Simplex-Nelder-Mead algorithm is a direct search algorithm that requires initial guesses for the interaction parameters and locates the optimum based on the concept of a simplex. A simplex is a polytope of N + 1 vertices in N dimensions (a triangle in this case). The approach starts with an initial simplex. At each iteration, a new point will be generated using operators such as reflect, contract, expand and shrink. Normally, the worst point of the simplex is replaced with the new point. The steps continue till the diameter of the simplex is less than a predefined threshold. It should be noted that the Nelder-Mead method is a local search algorithm that does not guarantee the global optimality of the solution. Therefore, the final result depends on the initial solution.

In this work, the deviation calculated by PE2000 is based on the mole fractions of the coexisting phases at certain temperature and pressure. The objective function

is the absolute average relative deviation (AARD) of liquid phase mole fraction, and the Simplex Nelder–Mead algorithm is used to optimize the binary parameter.

3.5.2.2 Ternary systems

Reaction systems and separation processes generally involve multiple components. Accurate prediction of multiple phase equilibria is an important aspect for industrial applications. Ternary phase equilibrium calculation was performed.

Generally, the phase equilibrium and phase behavior for ternary system can be assumed as extension of binary system. The binary interaction parameters can be obtained from the analysis of the three binary sub-systems. Thus, to construct a ternary diagram, it is necessary to know the three binary systems interaction parameters for the three components. As discussed in Chapter 8, for CO_2, 1-octene, nonanal system, one should consider the phase behavior of the binary CO_2 +1-octene, CO_2 + nonanal, and 1-octene + nonanal three sub-system.

In order to predict the ternary equilibrium, 3 binary interaction parameters are needed. All of the parameters need to fit the ternary data. However, regression of one or more of the interaction parameters is difficult if the equilibria of two of the components are unavailable. For CO_2 +1-octene + nonanal system, one is between 1-octene and CO_2, the other is between nonanal and CO_2, another is between 1-octene and nonanal. The first two can be obtained from correlating the experimental data. However, there is no literature data can be found for VLE data between 1-octene and nonanal, so that the last one is tentatively set to zero. Then the ternary equilibrium was predicted only based on the interaction of 1-octene and CO_2, nonanal and CO_2.

3.5.3 PE2000 calculation procedure

A general procedure of using PE2000 is summarized as follows:

1. Input data

   Phase equilibrium calculation requires the data of pure components and experimental data. Pure component data is saved in a so-called .PCFILE file, which includes component name, the molecular weight, the critical temperature and pressure, the acentric factor, etc. A new PCFILE is generated by selecting File/New/Pure Component Data.

   Experimental data of mixture are stored in an EXFILES file. An EXFILE consists of a header, pure-component data, pure-component EOS parameters, phase equilibrium data of mixtures, and optional binary EOS interaction parameters. It can be generated by selecting File/New/Mixture Data from the main menu. An EXFILES can be edited by Selecting File/Add/Equilibrium Data from the main menu or using text editor, such as notepad.

2. Calculate interaction coefficients

   To calculate interactive coefficients, first open an EXFILES containing the experimental data. Then, select an EoS (Peng-Robinson, in this study), mixing rule (Quadratic in this study), and a data set. PE2000 offers two approaches to calculate interaction coefficients, grid and optimization (used in this study). The optimization approach finds the optimal binary interaction parameters by correlating with experimental data. An objective

function needs to be defined, including the selection of calculating deviation and average mole fractions. In this study, the choices are “L1 and L2 only” for calculation deviation and “Relative” for average mole fraction. The process of locating the optimal binary coefficients can by shown in a separate window by selecting the checkbox of “visualization”. The process of finding the binary interaction coefficients can be saved in a text file.

3. Calculate phase equilibrium

   After obtaining the binary interaction coefficients, the phase equilibrium can be calculated by selecting Mixture/Calculate. The checkbox “Additional Box” enables PE2000 to calculate at the first equilibrium of the current block in the EXFILE then try to use this equilibrium as starting point for subsequent additional calculations in order to generate a complete Pxy-diagram or similar. The results can be saved in text file and plotted in a separate window, which can then be exported as a “windows metafile”.

3.6 Summary

This chapter reviews the thermodynamic phase equilibrium calculation approaches. Key EoS models and activity coefficient models are summarized, with the focus on cubic EoS. Several mixing rules are presented that involve a number of binary interaction parameters. The regression of the binary interaction parameters in this work is formulated as an NLP problem. The software package, PE2000, used to regress interaction parameters.

3.7 References

1. Smith, J.M. and H.C.V. Ness, *Introduction to chemical engineering thermodynamics*. Fourth ed. 1916, New York: McGraw-Hill Inc.
2. Wei, Y.S. and R.J. Sadus, *Equations of state for the calculation of fluid-phase equilibria.* AIChE Journal, 2000. **46**: p. 169-191.
3. Redlich, O. and J.N.S. Kwong, *On the Thermodynamics of Solutions. An Equation of State. Fugacities of Gaseous Solutions.* Chemical Review, 1949. **44**: p. 233-244.
4. Soave, G., *Equilibrium Constants from a Modified Redlich-Kwong Equation of State.* Chem. Eng. Science, 1972. **27**: p. 1197-1203.
5. Peng, D.Y. and D.B. Robinson, *A New Two-Constant Equation of State.* Industrial and Engineering Chemistry: Fundamentals, 1976. **15**: p. 59-64.
6. McCabe, C. and S.B. Kiselev, *A crossover SAFT-VR equation of state for pure fluids: preliminary results for light hydrocarbons.* Fluid Phase Equilibria, 2004. **219**: p. 3–9.
7. Chapman, W.G., K.E. Gubbins, G. Jackson, and M. Radosz, *New Reference Equation of State for Associating Liquids.* Ind. Eng. Chem. Res., 1990. **29**: p. 1709-1721.
8. Twu, C.H., B. Tilton, and D. Bluck *The Strengths and Limitations of Equation of State Models and Mixing Rules*.
9. Valderrama, J.O., *The State of the Cubic Equations of State.* Ind. Eng. Chem. Res., 2003. **42**: p. 1603-1618.

10. Adachi, Y. and H. Sugie, *A New Mixing Rule - Modified Conventional Mixing Rule.* Fluid Phase Equilibria, 1986. **28**: p. 103-118.

11. Wong, D.S.H. and S.I. Sandler, *A theoretically correct mixing rule for cubic equations of state.* AIChE J., 1992. **38**: p. 671-680.

12. Wilson, G.M., *Vapor-Liquid Equilibria. XI. A New Expression for the Excess Free Energy of Mixing.* J. Am. Chem. Soc., 1964. **86**: p. 127-130.

13. Renon, H. and J.M. Prausnitz, *Local Compositions in Thermodynamic Excess Functions for Liquid Mixtures.* AIChE J., 1968. **14**: p. 135-144.

14. Abrams, D.S. and J.M. Prausnitz, *Statistical Thermodynamics of Liquid Mixtures: A New Expression for the Excess Gibbs Energy of Partly or Completely Miscible Systems.* AIChE J., 1975. **21**: p. 116-128.

15. Fredenslund, A., R.L. Jones, and J.M. Prausnitz, *Group Contribution Estimation of Activity Coefficients in Nonideal Solutions.* AIChE J., 1975. **21**: p. 1086-1099.

16. Pfohl, O., S. Petkov, and G. Brunner, *PE 2000 – A Powerful Tool to Correlate Phase Equilibria*. 2000, München: Herbert Utz Verlag.

17. Petkov, S., O. Pfohl, and G. Brunner, *Calculating Fluid-Phase Equilibria with PE 2000*, in *FOMMS 2000: Foundations of Molecular Modeling and Simulation;*. 2000: Keystone Resort, CO.

18. Schwarz, C.E. and I. Nieuwoudt, *Phase equilibrium of propane and alkanes. Part I. Experimental procedures, dotriacontane equilibrium and EOS modelling.* Journal of Supercritical Fluids 2003. **27**(2): p. 133-144.

19. Schwarz, C.E. and I. Nieuwoudt, *Phase equilibrium of propane and alkanes. Part II: Hexatriacontane through hexacontane.* Journal of Supercritical Fluids 2003. **27**(2): p. 145-156.

20. Teodorescu, M., L. Lugo, and J. Fernandez, *Modeling of Gas Solubility Data for HFCs-Lubricant Oil Binary Systems by Means of the SRK Equation of State.* . International Journal of Thermophysics 2003. **24**(4): p. 1043-1060.

21. Nelder, J.A. and R. Mead, *A Simplex Method for Function Minimization.* Comput. J. , 1965. **7**: p. 308-313.

Chapter 4 Global Phase Behavior of Imidazolium Ionic Liquids and Compressed gases: 1,1,1,2-Tetrafluoroethane (R-134a) and carbon dioxide (CO_2)

4.1 Introduction

Knowledge of the global phase behavior is practically important for reaction engineering, process design, separation technology, etc. Global phase behavior indicates the conditions (temperature and pressure) of the different equilibria and transitions, i.e., vapor-liquid, liquid-liquid, vapor-liquid-liquid, etc. Therefore, for new applications with ionic liquids and compressed gases, the high-pressure phase behavior and equilibria are very important data. For instance, regions in which an ionic liquid and refrigerant are miscible would not be conducive to separations or absorption refrigeration. CO_2 and IL have unique phase behavior as there is no measurable amount of ionic liquid existing in the CO_2 phase. This chapter will give insight into the fundamentals of phase behavior of mixtures consisting of ionic liquids and compressed gases: 1,1,1,2-tetrafluoroethane (R-134a) and carbon dioxide (CO_2). The temperature range is from approximately 0°C to 105°C and pressure up to 330 bar. 1-Alkyl-3-methyl imidazolium ionic liquids with various alkyl groups and anions and the common refrigerant R-134a are investigated.

4.2 Global Phase Behavior

A rich variety of phase behavior is possible with liquids and gases. For the process design of any system with a compressed gas, the global phase behavior must be characterized. The Gibbs Phase Rule indicates that even for binary systems, up to 4 phases may coexist in equilibrium. Thus, two phase and three phase regions are likely to exist at various temperatures, pressures and compositions. Van Konynenburg and Scott [1] were the first to provide a uniform classification scheme for binary phase behavior of liquids and gases. In their scheme, all binary systems fall within one of 6 phase behavior types as illustrated in Figure 4.1.

Each phase behavior type has characteristic phase transitions. For Type I, the two critical points of each pure component are connected by a vapor liquid mixture critical line. Type II adds one more line on Type I. The extra liquid-liquid line starts at upper critical end-point (UCEP) and extends to high pressure. Below UCEP, it connects to a vapor liquid-liquid equilibrium line. For type III, the mixture has two distinct critical curves. The first one starts from pure component critical points and extends to UCEP connected with vapor-liquid-liquid critical line. The second one also starts with the critical point of the other pure component but with higher temperature and extends to higher pressure. For Type IV, two critical point lines start from the pure component. One ends at UCEP and the other ends at a lower critical end-point (LCEP). A vapor-liquid-liquid equilibrium line connects between LCEP and UCEP. There is also a critical line ends at another UCEP. Type V is similar to Type IV but without a lower temperature critical line ending at UCEP. For type VI,

one liquid-liquid critical line is added to Type I. It starts from LCEP and ends at UCEP, between which is the vapor-liquid-liquid equilibrium.

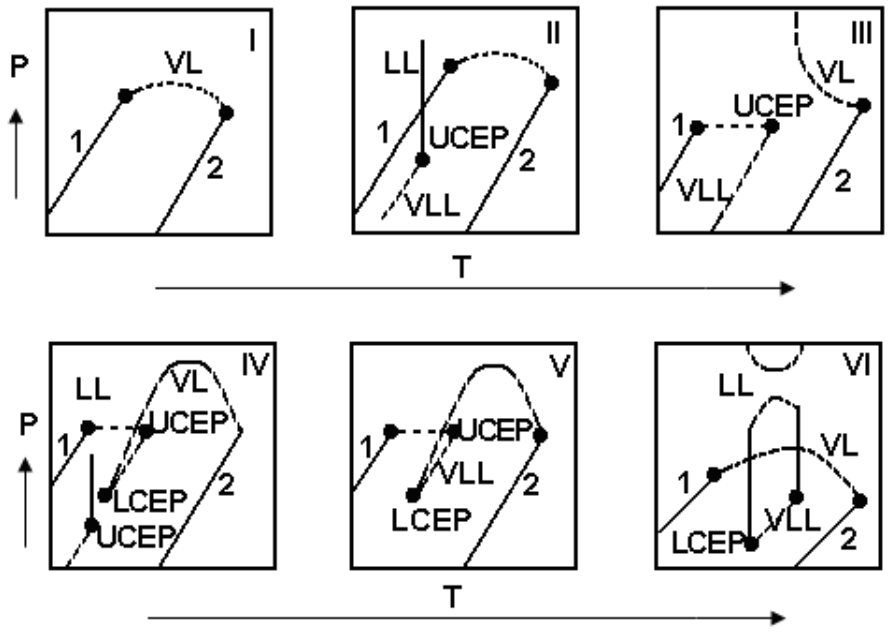

Figure 4.1 Common types of global phase diagrams according to their Scott and van Konynenburg [1] and Bolz *et al*. [3].

As will be discussed, R-134a and most ILs systems are believed to be a Type V system (possibly Type IV), while CO_2 and ILs are Type III systems. Detailed descriptions of the phase behavior and equilibria of Type III and V systems will be found below. Yokozeki and Shiflett [2] predicted that the system of trifluoromethane and [BMIm][PF_6] is a Type V system using an equation of state. Recently, Bolz *et al.* [3] have proposed a new nomenclature system for the International Union of Pure and Applied Chemistry (IUPAC) in which a more descriptive nomenclature is presented. The new designation conveys the topology and connectivity of critical curves.

4.3 Global Phase Behavior of Ionic Liquids/Refrigerants Mixture

The main advantage of combining ionic liquids and refrigerants is that most refrigerant gases have a high solubility in ionic liquids [4]. One of the challenges of ionic liquids is that their viscosity is often higher than conventional solvents,[5] which leads to slower mass transport rates. The Scurto group has recently reported that the viscosity of the IL, [HMIm][Tf_2N] decreases approximately 80+% with up to 6 bar of R-134a at 25°C [6]. The diffusivity in the ionic liquid is predicted to improve approximately 5-fold over the same pressure range based on the decrease in the mixture viscosity. Moreover, this dramatic increase in the mass transport properties will demand less capital intensity as processes with smaller equipment (e.g. heat exchangers, contactors, etc.) can be used.

Only a limited number of groups have reported phase equilibria data for ionic liquids and refrigerant gases: Shiflett, Yokozeki and coworkers, Cor J. Peters, Ziegler, and Maurer. The complete literature review for phase equilibria will be presented in Chapter 5. For the global phase behavior, it has been only reported by Shariati and Peters [7-8] and Shiflett and Yokozeki [9]. Shariati and Peters [7-8] believe that trifluoromethane (CHF_3) in [EMIm][PF_6] belongs to type III. However, Shiflett and Yokozeki [9] indicates Type V behavior of IL and refrigerant system by equation of state predictions. In this chapter, the global phase behavior of 1-alkyl-3-methyl imidazolium ionic liquids with various alkyl groups and anions and R-134a were measured experimentally for the first time.

1-Ethyl-3-methylimidazolium bis(trifluoromethylsulfonyl)amide ([EMIm][Tf_2N]), 1-Hexyl-3-methylimidazolium bis(trifluoromethylsulfonyl)amide ([HMIm][Tf_2N]), 1-Hexyl-3-methylimidazolium hexafluorophosphate ([HMIm][PF_6]), 1-Butyl-3-methylimidazolium hexafluorophosphate ([BMIm][PF_6]), 1-Hexyl-3-methylimidazolium tetrafluoroborate ([HMIm][BF_4]), 1-Hexyl-3-methylimidazolium bromide ([HMIm][Br]), were used for the global phase behavior study in this chapter. The structure of ILs used in this chapter is shown in Figure 4.2. The synthesis methods and analysis results are shown in Chapter 2.

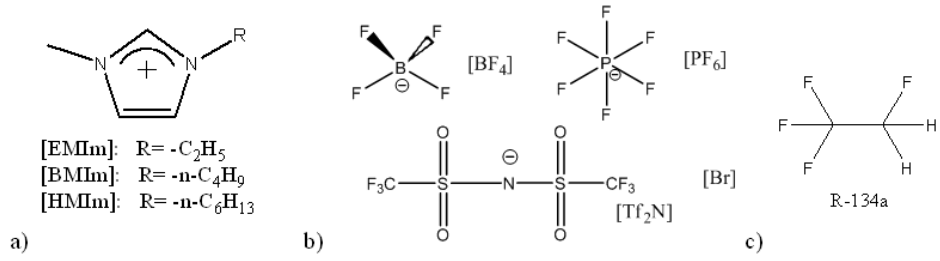

Figure 4.1 Ionic liquid cations and anions and refrigerant used in this study: a) cation structures; b) anion structures; c) refrigerant gas: 1,1,1,2-tetrafluoroethane

4.3.1 Global phase behavior

The global phase behavior must be characterized for process design of any systems with a compressed gas. As will be discussed below, refrigerant gases and ionic liquids are believed to be mostly of type V behavior, which is shown qualitatively with exaggerated features (for clarity) in Figure 4.3. Type V behavior of the Scott-van Konynenburg scheme is characterized by vapor-liquid equilibrium at

low temperatures, followed by a LCEP where another liquid phase forms (thus, vapor-liquid-liquid equilibrium), followed by an UCEP at higher temperatures in which the liquid phases merge. The mixture critical point extends from the LCEP to the pure component critical point of the less volatile component.

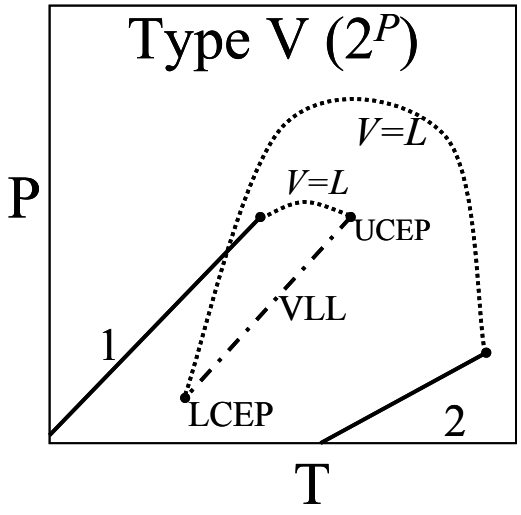

Figure 4.3 Global phase diagram of a Type V system according to Scott and van Konynenburg [1] and Bolz et al. [3].

Figure 4.4 illustrates the qualitative pressure-composition behavior of a Type V system at three different isotherms. The temperature of the global phase behavior (PT) is shown in the inset. At each isotherm, when pressure is increased, the system shows different phase behavior. The vapor-liquid equilibrium for an isotherm at temperatures below the LCEP (T_a) is shown in Figure 4.4a, where liquid 2 (L_2, ionic liquid here), is primarily composed of the less-volatile (liquid) component, while component 1, which is R-134a here, is the more volatile component (gas). At pressures above the vapor pressure of pure component 1, component 1 exists as pure

liquid, and the two liquids are completely miscible. At a temperature above the LCEP and below the pure component 1 critical temperature designated T_b, several different equilibria are possible depending on the pressure and loading (ratio) of the components as shown in Figure 4.4b. At lower pressures, VLE exists until the pressure of transition to vapor-liquid-liquid equilibrium (VLLE) which has compositions symbolized by the solid squares in the figure. These compositions as exaggerated for clarity and the L_1 and V compositions are more often at higher concentrations of the compressed gas. The newly formed liquid 1 phase is rich in or mostly composed of component 1. Beyond the VLLE pressure, two different equilibria are possible depending on the overall mole fraction composition. If an overall composition exists between the L_1 and V compositions of the VLLE (x^{L1} and x^{V} in the figure), then an increase in pressure will create VLE of the vapor and the L_1 phase. At pressures above the vapor pressure of component 1, then the L_1 phase and the pure liquid of component 1 are completely miscible. However, if the overall composition is between the L_2 and L_1 compositions of the VLLE (x^{L1} and x^{L2} in the figure), increasing pressure produces liquid-liquid equilibrium (LLE) of the L_1 and L_2 phases. At higher pressures, the mixture critical point is obtained and the two phases become critical to one another, thus the mixture is completely miscible and the whole system is one phase. At a temperature above the UCEP (T_c in Figure 4.4c), then VLE exists to the mixture critical pressure, where the vapor becomes critical with L_2. Type IV is similar to type V, except a low temperature region of LLE, VLLE and a second UCEP exist (see Figure 4.1).

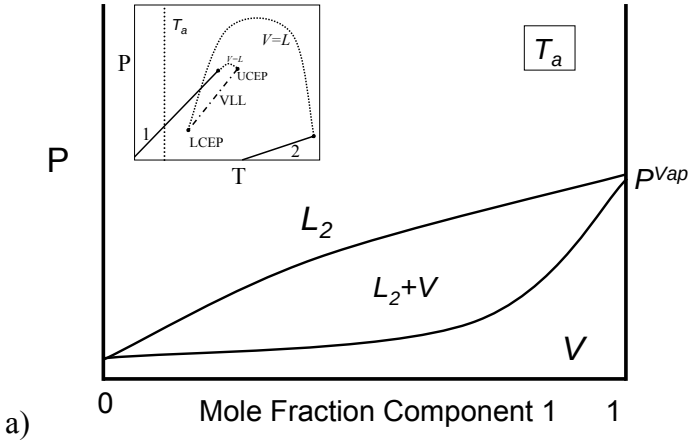

a)

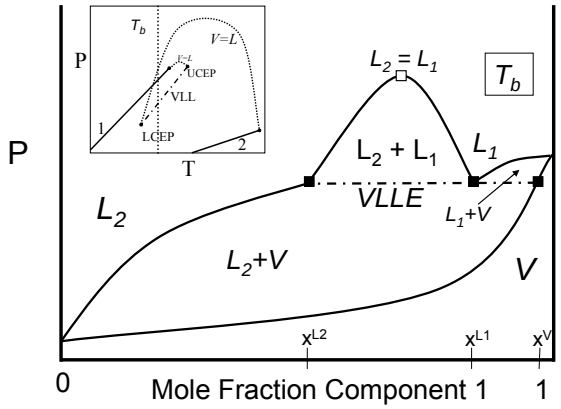

b)

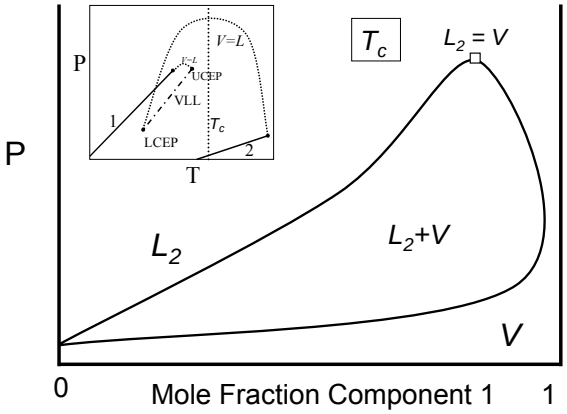

c)

Figure 4.4 Qualitative pressure-composition diagrams of isotherms from Type V systems as shown in the inset. a) an isotherm below the LCEP; b) an isotherm between the LCEP and critical temperature of component 1; c) an isotherm above the UCEP.

4.3.2 Results and discussions

The global phase behavior of binary mixture between R-134a and [EMIm][Tf_2N], [HMIm][Tf_2N], [HMIm][PF_6], [HMIm][BF_4], and [BMIm][PF_6] were studied between approximately 0°C to 105ºC and pressures to 330 bar. These data represent some of the first complete global phase diagrams for compressed gases and ionic liquids.

Table 4.1 Global phase behavior data for ILs studied and R-134a

Transitions	Mixture critical points		LCEP		UCEP		VLE[a]		VLLE	
	T	*P*	*T*	*P*	*T*	*P*	*T*	*P*	*T*	*P*
ILs	[ºC]	[bar]	[ºC]	[bar]	[ºC]	[bar]	[ºC]	[bar]	[ºC]	[bar]
[EMIm][Tf_2N]	60.0	35.0	55.0	15.0	101	40.8	28.2	7.3	60.0	16.6
	75.0	92.3					32.2	8.2	82.0	27.4
	80.0	108.0					38.2	9.7	92.0	33.0
	101	164.0					44.2	11.3		
							48.2	12.6		
[HMIm][Tf_2N]	75.0	43.2	62.6	19.0	101	40.5	24.0	5.9	80.0	26.8
	85.0	76.1					33.6	7.9	90.1	33.2
	101	123.5					42.0	10.2	100	40.2
[HMIm][BF_4]	50.0	46.4	37.9	10.0	101	40.5	21.9	5.7	40.7	10.6
	75.0	143.3					23.0	6.7	60.5	17.8
	90.0	204.3					33.7	8.4	79.6	27.3
	105	254.7					35.6	8.7	94.1	37.2
[HMIm][PF_6]	50.0	27.7	48.3	12.5	101	40.5	5.0	3.4	50.0	13.0
	60.0	69.8					15.0	4.7	54.0	14.4
	75.0	128.8					25.1	6.3	60.0	16.7
	90.0	175.9					30.0	6.9	75.0	24.0
	105	225.2					40.0	9.9	90.0	32.6
[BMIm][PF_6]	50.0	111.9	27.8	7.3	101	40.5	10.0	4.2	40.0	9.8
	75.0	215.4					15.0	4.9	60.0	15.8
	90.0	277.7					20.0	5.7	80.2	26.1
	105	327.6					24.0	6.4	95.0	35.9
a) confirmed points of VLE miscibility at the vapor pressure of R-134a										

4.3.2.1 [EMIm][Tf_2N] and R134a

The global phase behavior for [EMIm][Tf_2N] and R-134a was measured and presented in Figures 4.5 and 4.7. This contribution is one of the first complete global phase diagrams for a compressed gas and an ionic liquid. As shown various regions of single phase and multi-phase equilibria exist. One of the interesting aspects of this behavior is the presence of single miscible or critical regions. This is opposed to the majority of the high-pressure equilibria data in the literature for ionic liquids and various gases [10-12]. Shariati and Peters [7] have reported a vapor-liquid mixture critical pressure and composition for [EMIm][PF_6] and high-pressure CHF_3. The three phase vapor-liquid-liquid (VLLE) equilibrium exists between the lower and upper critical endpoints (LCEP and UCEP) and is equal to the pure component vapor pressure of R-134a within the experimental accuracy of this study. When the pressure of the VLLE and pure vapor pressure are so similar, this often indicates that the second liquid phase is almost pure R-134a ($x_{R\text{-}134a}$<0.01) as confirmed by Shiflett and Yokezeki [2, 9] for this and other ionic liquids. As the R-134a-rich phase is nearly pure, its UCEP is nearly indentical (within experimental accuracy) to the pure component critical point. Below the LCEP temperature, the system is in vapor-liquid equilibrium until the pressure is raised to the vapor pressure of the pure R-134a, at which point, the system becomes miscible. These points of miscibility have been confirmed experimentally and are shown on the plot Figure 4.5. For CO_2, only VLE and then LLE are possible for temperatures below the pure CO_2 critical point (see below). For [EMIm][Tf_2N] and R-134a above the LCEP but below the UCEP, four different equilibria are possible. VLE exists at the lower pressures and VLLE exists

near or at the pure R-134a vapor pressure. Above the VLLE, LLE exists until mixture critical point and the system becomes critical/miscible. Above the UCEP, VLE exists and terminates at the mixture critical point.

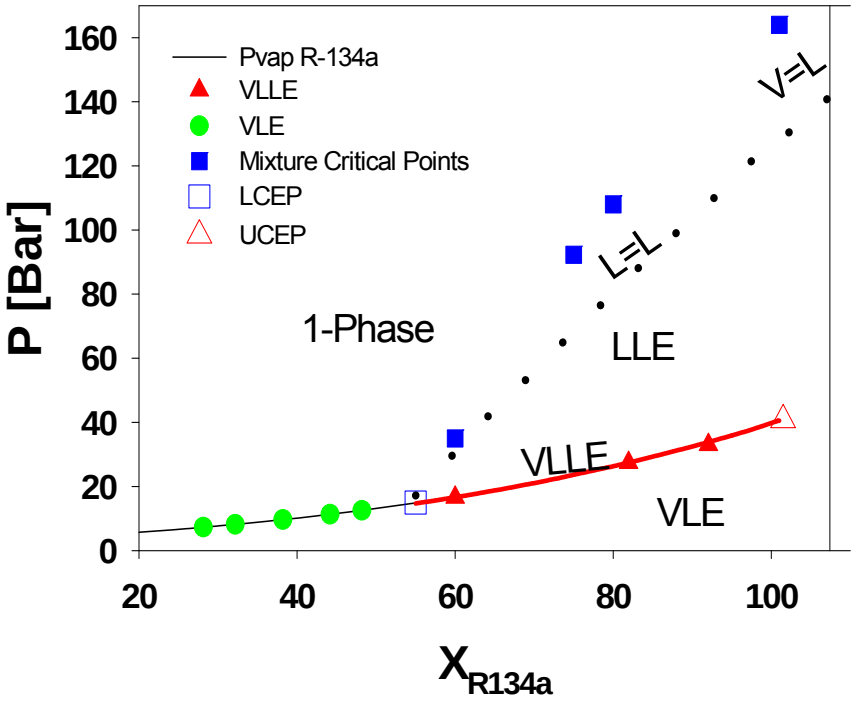

Figure 4.5 Global phase behavior for [EMIm][Tf_2N] and R-134a. Pressure-temperature diagram with experimental data and model predictions from lower pressure VLE data.

Legend: ●: VLE, ▲: VLLE; ■: mixture critical points.▼: vapor-liquid-liquid equilibrium (VLLE) for [EMIm][Tf_2N]; □: lower critical endpoint (LCEP) of R-134a with [EMIm][Tf_2N] ; Δ: upper critical endpoint (UCEP) with [EMIm][Tf_2N] (also R-134a critical point). Dash line is the predicted mixture critical point from the EoS model. Solid line through VLE, VLLE, and UCEP is the vapor pressure of pure R-134a from [14].

The global phase behavior was predicted using an equation of state model by collaboration with Dr. Mark Shiflett and Dr. Amichi Yokezeki at DuPont Central Research & Developement. A modified Redlich-Kwong type of cubic equations of state (EoS) is employed in this study to model global phase behavior of [EMIm][Tf_2N] and R134a with parameters regressed with only the low pressure VLE data (P<3.5 bar). For model details, please refer to Yokezeki's work [9]. In the modified model, there are a maximum of four binary interaction parameters: l_{ij}, l_{ji}, m_{ij}, τ_{ij} for each binary pair. However, two or three parameters are sufficient for most of the cases. The optimal binary interaction parameters are listed in Table 4.2 and determined from the low-pressure VLE data of Shiflett and Yokezeki [9].

Table 4.2 Equation of state parameters and binary interaction parameters[a]

Compound	T_c [K]	P_c [bar]	β_0	β_1	β_2	β_3
[EMIm][Tf_2N]	808.82	20.28	1.0	1.35500	0	*0*
R-134a	374.21	40.59	1.0025	0.50532	-0.04983	*0*
	l_{12}	l_{21}	$m_{12} = m_{21}$	$\tau_{12} = \tau_{21}$ [/K]		
R-134a/ [EMIm][Tf_2N]	-0.03084	-0.00416	0.00726	17.50		

[a] *From Shiflett and Yokezeki [9]*

As shown in Figure 4.5, VLE and VLLE data are nearly equal to the pure R-134a vapor pressure line. The model underpredicts the mixture critical points, especially at higher temperatures. From convergence of the critical point and VLLE predictions, the lower critical endpoint (LCEP) is approximated as 54°C and 14.5 bar. This is very close to the experimental point of 55°C and 15 bar, despite the fact that the prediction is from lower pressure data. The predicted UCEP is approximately 101°C and 40.5 bar and the experimental point is 101 °C and 40.8 bar. The model provides an adequate correlation of the mixture critical pressure at 60°C. However, for the critical points at higher pressure, the model significantly underpredicts the critical pressure. The data used to correlate the interaction parameters are nearly 30 times lower than the mixture critical point. Even with data close to the mixture critical point, researchers have described difficulty predicting both the critical composition and pressure at a given temperature [13-14]. Often, one must fit the interaction parameters directly to the critical point data to get quantitatively agreement for pressure and composition.

From the experimental data and the modeling predictions, the system of [EMIm][Tf_2N] and R-134a are believed to be classified as a Type V system (see Figure 4.7). The Type IV system is similar, but exhibits another lower temperature region of liquid-liquid immiscibility and VLLE ending at another UCEP. For reference, phenyloctane and R-134a are a Type IV system and the difference between the lower-branch of the UCEP and the LCEP is 29°C [15]. Experimentally, the VLE region for [EMIm][Tf_2N] and R-134a was investigated down to 0°C with no

occurrence of liquid immiscibility. The phase behavior at cryogenic temperatures is beyond the capabilities of the experimental equipment. However, from EoS predictions and the experimental data set here, Type V behavior is believed to exist for this system.

4.3.2.2 [HMIm][Tf_2N] and R-134a

The global phase behavior for [HMIm][Tf_2N] and R-134a is presented in Figure 4.7 with pictures, illustrating the regions of 1-, 2- and 3-phases. As shown in each picture, the global phase behavior was measured in a windowed autoclave reactor with a stir bar in center; IL phase is at the bottom. IL was loaded to autoclave at the beginning, then R-134a was injected into the system, the system exists as different phases with increasing temperature and pressure. Similar to Figure 4.4a, vapor liquid equilibrium exists at lower temperatures below the LCEP with complete liquid miscibility above the vapor pressure of R-134a. This point of miscibility at the vapor pressure has been confirmed experimentally for several temperatures as shown in Figure 4.7. This is different from the behavior of most gases (CO_2, ethane, etc.) with ILs, which have liquid-liquid immiscibility above the vapor pressure. The results of [EMIm][Tf_2N] and R-134a are also shown here for comparison.

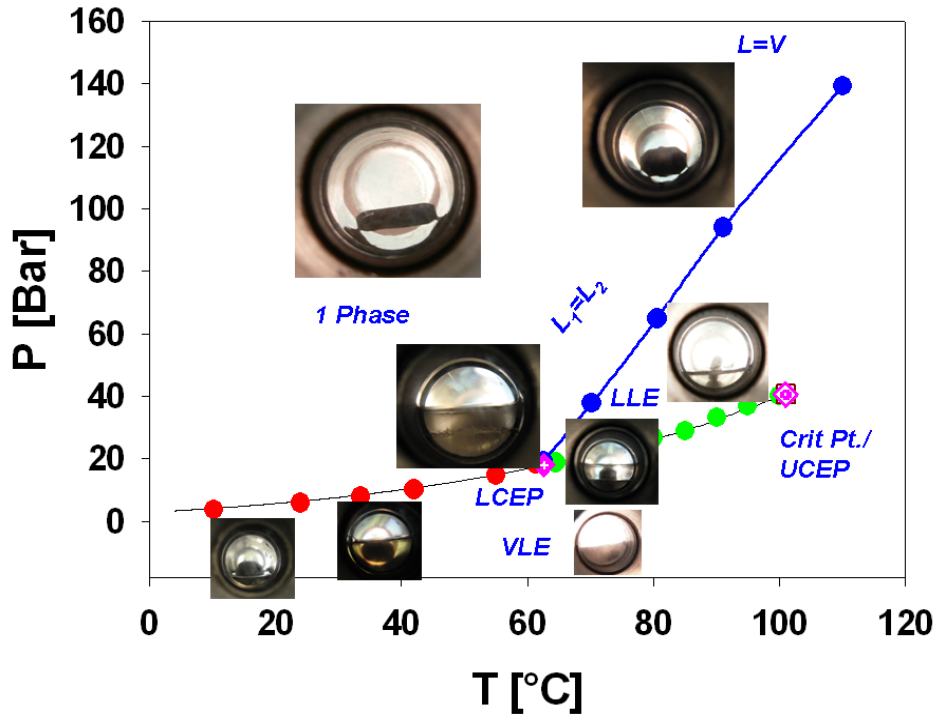

Figure 4.6 Experimental global phase behavior pictures for [HMIm][Tf_2N] and R-134a.

Vapor-liquid-liquid (VLLE) equilibrium exists between LCEP and UCEP. The pressure-temperature profile of the VLLE data is equal, within experimental accuracy, to the pure component vapor pressure of R-134a as calculated from the REFPROP database version 8.0 [16]. This often indicates that the second liquid phase is nearly pure R-134a ($x_{R\text{-}134a}$<0.01), as confirmed experimentally by Shiflett and Yokozeki [9] for systems with refrigerant gases and [EMIm][Tf_2N], [HMIm][Tf_2N], [BMIm][PF_6], [HMIm][PF_6] and [HMIm][BF_4]. The LCEP is the start of both the VLLE line and the mixture critical points. At temperatures above the LCEP, but below the UCEP, four different equilibria are possible depending on the pressure. VLE exists at the

lowest pressures and VLLE exists near or at the pure R-134a vapor pressure. At pressures above VLLE, liquid-liquid (LLE) equilibria exists until the mixture critical point, beyond which the system become critical/miscible. At very high loadings of R-134a, VLE would exist above the VLLE pressure; see Figure 4.4b. However, this region is estimated to be between a mole fraction of R-134a of 0.99 to 1.00 and was not explored experimentally. Above the UCEP, VLE exists and terminates at the mixture critical point (see Figure 4.4c). For [HMIm][Tf_2N]/R-134a, the LCEP was measured at 62.6°C and 19 bar. Mixture critical points technically extend from the LCEP to the critical point of the less-volatile component (see Figure 4.1–Type V). But, no known critical points of ILs are known to exist, due to decomposition.

The UCEP of the [HMIm][Tf_2N]/R-134a was measured at 101°C and 40.6 bar. As the R-134a-rich liquid phase is nearly pure, its UCEP is nearly identical (within experimental accuracy) to the pure component critical point of 101°C and 40.6 bar. Below the LCEP temperature, the system is in vapor-liquid equilibrium until the pressure is raised to the vapor pressure of the pure R-134a, at which point the two liquids becomes miscible. These points of miscibility at the R-134a vapor pressure have been confirmed experimentally and are shown in Figure 4.7.

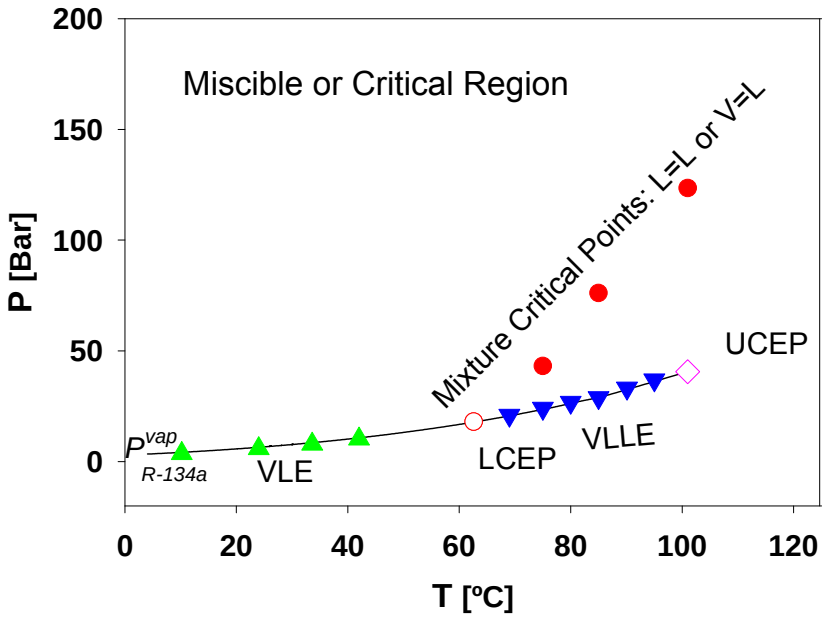

Figure 4.7 Experimental global phase behavior for [HMIm][Tf_2N] and R-134a Legend: ▲: VLE with confirmed miscibility at the vapor pressure of R-134a; ▼: vapor-liquid-liquid equilibrium (VLLE) for [HMIm][Tf_2N]; ○: lower critical endpoint (LCEP) of R-134a with [HMIm][Tf_2N]; ◊: upper critical endpoint (UCEP) with [HMIm][Tf_2N] (also R-134a critical point); ●:mixture critical points of [HMIm][Tf_2N]. Solid line through VLE, VLLE, and UCEP is the vapor pressure of pure R-134a from [16].

4.3.2.3 Alkyl chain effects

Figure 4.8 displays the LCEP and mixture critical points for [EMIm][Tf_2N] and [HMIm][Tf_2N]. As shown, the LCEP is lower and the slope of the mixture critical line is steeper for [EMIm][Tf_2N] than [HMIm][Tf_2N]. For instance at 80°C, the mixture critical pressure of the [EMIm][Tf_2N]/R-134a system is 108 bar, while that

for [HMIm][Tf_2N] is 65.4 bar. Thus, an increase in the alkyl chain length of the cation increases the area (T and P) in which R-134a is 1-phase (miscible/critical) with imidazolium ionic liquids. ILs with longer alkyl chain do not have phase split with R134a until higher temperature and pressure. Thus, with longer alkyl- groups the LCEP temperature (and pressure) increases. This is the same trend for the solubility of refrigerant gases in ILs, *viz.* longer alkyl groups result in higher solubility at a given temperature and pressure. The added dispersion forces of the longer alkyl group and induced dipole forces with the polar compressed or liquefied gas provide more favorable interactions, and, thus, miscibility (or increased solubility) at lower temperatures and pressures. If a process requires no miscibility of the IL in the compressed gas phase, then shorter alkyl-chains are needed as the LCEP is lower in temperature and the critical points are higher but at the expense of slightly lower gas solubility. The presence of a single miscible phase or critical regions is somewhat unique to hydrofluorocarbon refrigerant gases and ionic liquids, as the majority of the high-pressure equilibria data for ILs and various compressed gases have no reported miscibility [10-12].

The effect of the alkyl group was also investigated with the [PF_6] anion and the 1-Butyl- and 1-Hexyl-3-methylimidazolium cations ([BMIm] and [HMIm] respectively). Figure 4.9 illustrates the LCEP and mixture critical points of [BMIm][PF_6] and [HMIm][PF_6]. As the majority of the VLLE data and the UCEPs are nearly equal to the pure R-134a vapor pressure and critical point, respectively, most of the individual systems data have been omitted from the plot for clarity Figure

4.9. As shown, the addition of the two methylene (-CH_2-) groups changes the LCEP by 20°C. The mixture critical points for [HMIm] are less than that for [BMIm]. Again, the added length of the alkyl chain increases the area where the two components are miscible.

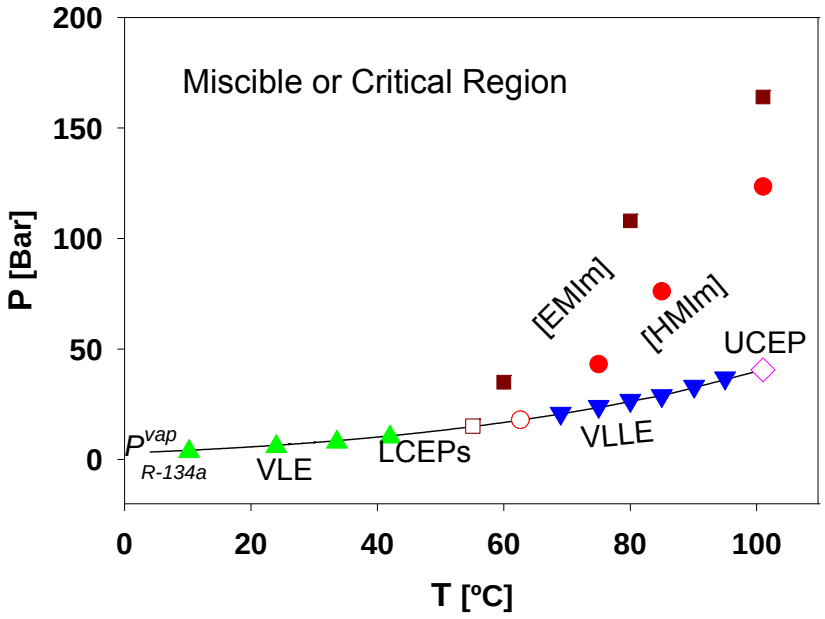

Figure 4.8 Experimental global phase behavior for [R-MIm][Tf_2N] and R-134a for R- = ethyl ([EMIm]), and n-hexyl ([HMIm]). Legend: ▲: VLE with confirmed miscibility at the vapor pressure of R-134a; ▼: vapor-liquid-liquid equilibrium (VLLE) for [HMIm][Tf_2N]; lower critical endpoint (LCEP) of R-134a with [HMIm][Tf_2N] (○) and [EMIm][Tf_2N] (□); ◊: upper critical endpoint (UCEP) with [HMIm][Tf_2N] (also R-134a critical point); mixture critical points of [HMIm][Tf_2N] (●) and [EMIm][Tf_2N] (■). Solid line through VLE, VLLE, and UCEP is the vapor pressure of pure R-134a from [14].

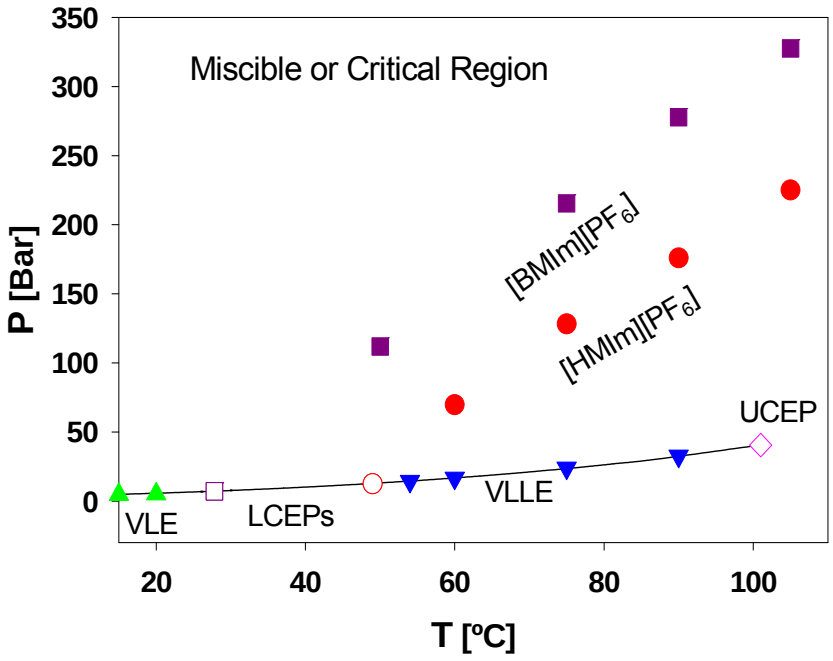

Figure 4.9 Experimental global phase behavior for [BMIm] and [HMIm][PF_6] and R-134a. Mixture critical points of [HMIm][PF_6] (●) and [BMIm][PF_6] (■).

4.3.2.4 Anion effects

Based on the cation 1-Hexyl-3-metyl-imidazolium ([HMIm]), three anions were chosen here to determine the effect of the anion, which are the fluorinated anions [BF_4], [PF_6], and the aforementioned [Tf_2N] as shown in Figure 4.10. The mixture of R-134a and [Tf_2N] anion has lowest critical points among these three ionic liquids. Compared with the [Tf_2N] anion, the mixture critical pressures for [PF_6] and [BF_4] dramatically increase. [17] For instance, at 75°C, the mixture critical pressure for [HMIm][BF_4] is 143.3 bar and 128.8 bar for [HMIm][PF_6]; the critical point for [HMIm][Tf_2N] is nearly a hundred bar less at 43.2 bar. Thus, the anion plays a key

role on determining the ultimate global phase behavior. The LCEP of these three ILs shows a inverse trend with mixture critical points. It decreases in the order of [HMIm][Tf_2N] at 62.6 ºC, [HMIm][PF_6] at 48.3 ºC and [HMIm][BF_4] at 37.9 ºC. However, this is the same trend for the solubility of refrigerant gases in ILs, *viz.* solubility at a given temperature and pressure follows in the order [Tf_2N] > [PF_6] > [BF_4]. This trend scales with the diameter of the anion or charge density because larger anions can have more disperse negative charge. Ions with more disperse charge can more readily be solvated by the polar compressed hydrofluorocarbon, the polarity of R-134a decreases with temperature and increases with pressure. Thus, [Tf_2N] anion ILs with R-134a have a wide rage of temperature to be miscible, but for [PF_6] and [BF_4] having less negative charge, they even have phase split at lower temperature. As a result, as the temperature of the LCEP increases, the regions of temperature and pressure of miscibility increase. For certain processes, the anion can be designed to suit the needed property.

From the experimental data, the systems of 1-n-alkyl-3-methyl-imidazolium ionic liquids and R-134a are believed to be classified as a Type V system (see Figure 4.1) The Type IV system is similar, but exhibits another lower temperature region of liquid-liquid immiscibility and VLLE ending at another UCEP. Phenyloctane and R-134a are a Type IV system (see Figure 4.1) and the difference between the lower-branch of the UCEP and the LCEP is 29°C[15]. The VLE region for the ionic liquids and R-134a was confirmed experimentally to 0°C with no occurrence of liquid immiscibility; this about 38° to 60°C below the LCEP of all ILs tested. While

cryogenic temperatures are beyond the capabilities of the experimental equipment, the current data and equation of state predictions for similar systems indicate solely Type V behavior. [18]

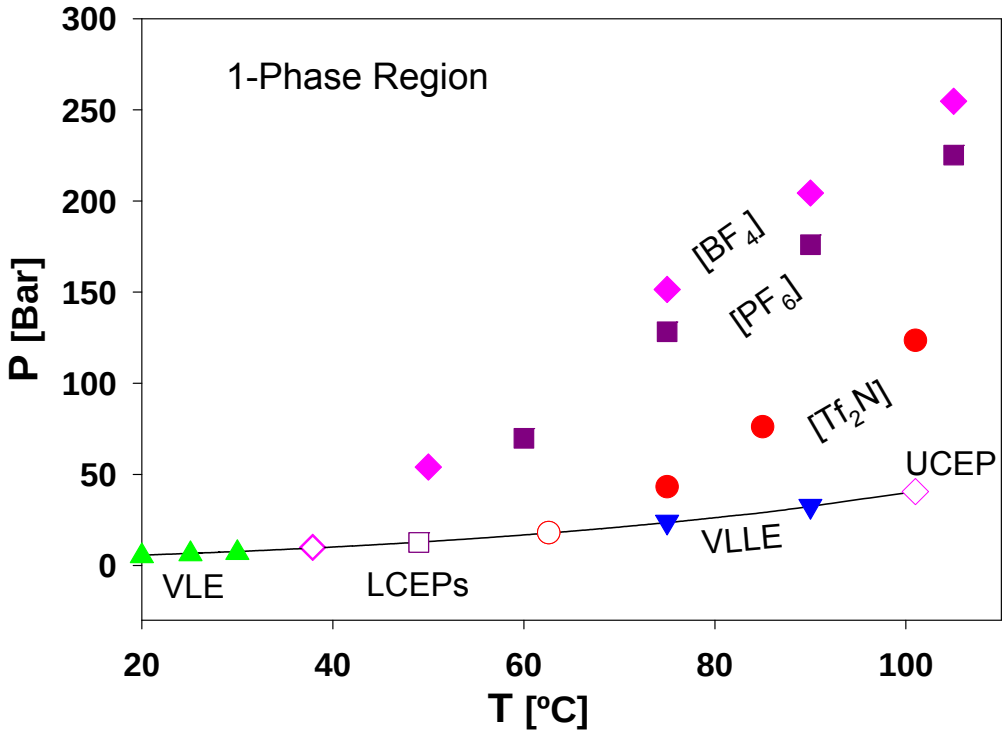

Figure 4.10 Experimental global phase behavior for [HMIm][An] for [An]= $[BF_4]$ (♦), $[PF_6]$ (■), and $[Tf_2N]$ (●) with R-134a. See caption of Figure 4.7 for more details.

4.3.2.5 [HMIm][Br] and R134a

The global phase behavior of [HMIm][Br] and R134a was also measured at temperatures up to 141°C and pressure up to 345 bar. The data is listed in Table 4.3 and shown in Figure 4.11. As we can see from the figure, vapor-liquid-liquid equilibrium (VLLE) exists at the temperatures below the UCEP and pressures nearly

identical to the vapor pressure of R-134a. The UCEP is at 101 °C, which is almost same as the critical temperature for pure R-134a. When the temperature is higher than the UCEP, two-phase vapor-liquid equilibrium was found in the region to 141°C and pressures up to 344 bar. This behavior is significantly different from the ionic liquids discussed above, [HMIm][Br] and R134a shows what is believed to be Type III phase behavior. The [Br] anion does not have fluorine, has a relatively small molar volume, and higher charge density so that there is less dispersion force between the anion and hydrofluorcarbon to dissolve each other. Thus, there is no miscibility even to higher pressure.

Table 4.3 Global phase behavior data for [HMIm][Br] and R-134a

Transitions	UCEP		VLLE		LLE	
	T	*P*	*T*	*P*	*T*	*P*
ILs	[ºC]	[bar]	[ºC]	[bar]	[ºC]	[bar]
[HMIm][Br]	101	40.6	13.2	4.3	110.0	343.6
			20.3	5.2	122.0	343.2
			25.5	6.4	127.0	343.0
			32.6	7.5	141.0	343.8
			40.9	9.9		
			52.4	12.3		
			61.5	17.1		
			70.0	20.3		
			80.0	25.3		
			90.0	31.7		
			100.0	40.3		

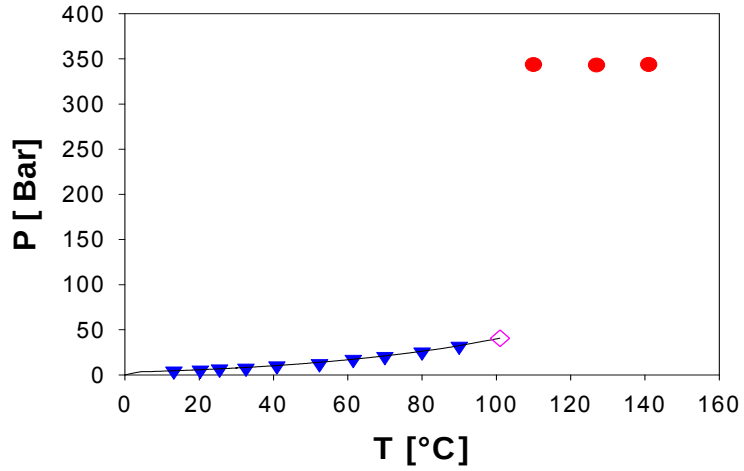

Figure 4.11 Experimental global phase behavior for [HMIm][Br] with R-134a. ▼: vapor-liquid-liquid equilibrium (VLLE); ●: Fluid-liquid equilibrium (FLE) ◊: upper critical endpoint (UCEP) with [HMIm][Br] (also R-134a critical point); Solid line through VLLE is the vapor pressure of pure R-134a from [16]

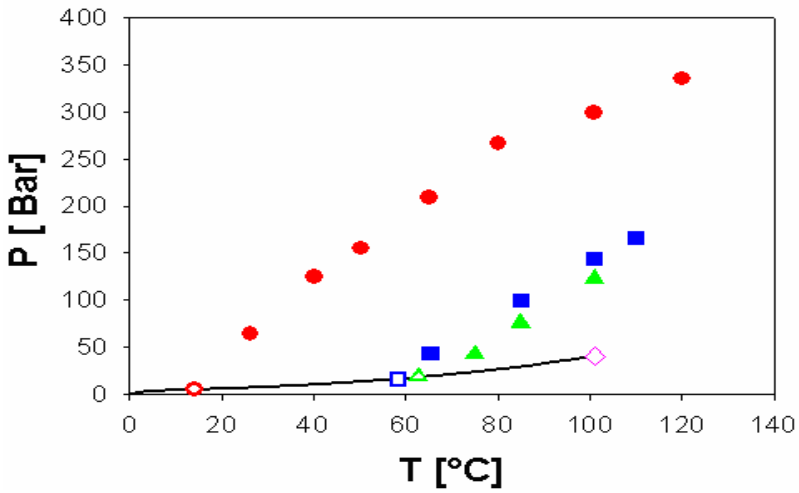

Figure 4.12 Experimental mixture critical points of [HMIm][Tf_2N], [HMIm][Tf_2N] and [HMIm][Br] mixture with R-134a Legend: ▲: [HMIm][Tf_2N], ■: mixture of [HMIm][Tf_2N] : [HMIm][Br] =10.11:1, ●: mixture of [HMIm][Tf_2N] : [HMIm][Br] =1.73:1. See Figure 4.6 for more details.

The ternary global phase behavior of R-134a with [HMIm][Tf_2N], and [HMIm][Br] at different initial ratios of the ILs (1.17:1 and 10.11:1, respectively) were measured and listed in Table 4.4. Since the VLE data and VLLE data are really similar to pure [HMIm][Tf_2N] and close to vapor pressure of R-134a, only LCEP and mixture critical points are reported here. The pure component and mixture behaviors are given in Figure 4.12. When [HMIm][Br] is added into [HMIm][Tf_2N], the LCEP is decreased and mixture critical points are increased. If 8% of [HMIm][Br] is in the mixture(ratio of [Tf_2N]:[Br] as 10.11:1), the LCEP drops about 7.2% from 62.6 ºC to 58.1 ºC. At 85 ºC, the mixture critical point increases about 30.5% from 76.1 bar to 99.3 bar. If 46% mole of [HMIm][Br] is in the mixture (ratio of [Tf_2N]:[Br] as 1.17:1), the LCEP drops about 77% from 62.6 ºC to 14.2 ºC. At 101 ºC, the mixture critical point increases dramatically about 142 % from 123.5 bar to 298.9 bar. Again, the anion seems to play a significant role on the miscibility due to different intermolecular forces.

4.3.2.6 IL purification using supercritical fluids

[HMIm][Tf_2N] is synthesized by anion exchange of [HMIm][Br] and Li[Tf_2N]. After reaction, it is difficult to separate [HMIm][Tf_2N] from the reactant mixture since they are miscible. To prevent the [HMIm][Br] from being impurity of [HMIm][Tf_2N], traditional method is to use excessive Li[Tf_2N] about 10 ~ 15% mole fraction. Because Li[Tf_2N] is miscible with water, it can be removed after reaction. However, Li[Tf_2N] is much more expensive than [HMIm][Br]. Therefore, the traditional approach of synthesizing [HMIm][Tf_2N] is not cost-effective.

Table 4.4 LCEP and mixture critical points of [HMIm][Br], [HMIm][Tf_2N] with R-134a

System	[HMIm]			
	[Tf_2N]:[Br]=1.17:1		[Tf_2N]:[Br]=10.11:1	
	T [ºC]	*P [bar]*	*T [ºC]*	*P [bar]*
LCEP	14.2	5.1	58.1	16.3
Mixture critical points	26.3	64.5	65.3	43.0
	40.1	124.9	85.1	99.3
	50.2	155.3	101.0	144.3
	65.1	208.7	110.0	166.1
	80.1	266.2		
	101.0	298.9		
	120.0	335.4		

Based this phase behavior study, the miscibility difference between [HMIm][Tf_2N], [HMIm][Br] and R-134a indicates an alternative purification method. These ionic liquid mixtures have phase split with R-134a pressure. Thus R-134a can extract [HMIm][Tf_2N] from [HMIm][Tf_2N] and [HMIm][Br] mixture, since [HMIm][Tf_2N] and R-134a can be totally miscible as reach the mixture critical point, but [HMIm][Br] does not. It is thus not necessary to use excessive Li[Tf_2N] for the synthesis of [HMIm][Tf_2N]. Therefore, separations of these two different ILs can use a compressed or supercritical fluid, which is not limited to R-134a. Other compressed gases with lower critical points can also be used. Similar methods can be used to synthesize other types of ILs if reactant and product show different miscibility with compressed gases.

4.4 Global Phase Behavior of IL and CO_2

The phase behaviors of ionic liquids and CO_2 have been investigated here to approximately 250 bar. Figure 4.13 illustrates the global phase behavior of [HMIm][Tf_2N] and CO_2. As shown, only VLE, VLLE and then LLE are possible for temperatures below the pure CO_2 critical point. For instance, at 25 ºC, binary mixture starts from VLE at lower pressure. With increasing pressure, VLLE is observed near vapor pressure of CO_2. The difference between VLLE pressure and vapor pressure of CO_2 is in experimental error range, the data will be given in Chapter 5. Then the LLE will be reached after the pressure is increased higher than vapor pressure. The upper critical end point (UCEP) is almost same as critical point of pure CO_2, which is very similar to R-134a case. When the system temperature is higher than the UCEP, VLE exists until very high pressure. The other critical line (not shown in the Figure 4.13) theoretically starts with pure IL critical point with higher temperature and extends to very high pressure.

Carvalho *et al.* [19] studied the the phase equilibrium of [EMIm][Tf_2N] and CO_2, which can not reach the critical at 70°C until 435.8 bar pressure. They also investigate 1- Pentyl - 3 - methyl imidazolium bis(trifluoromethylsulfonyl)imide ([PMIm][Tf_2N]) and CO_2 system, VLE exists at 80 °C and 561.1 bar pressure. Brennecke and coworkers[20] report that [BMIm][PF_6] and CO_2 represent a two-phase system even beyond 3100 bar at 40°C, see Figure 4.14. As shown, ionic liquids have unique phase behavior with CO_2. CO_2 is very soluble in the ionic liquid, but the ionic liquid is immeasurably insoluble in the CO_2 phase.

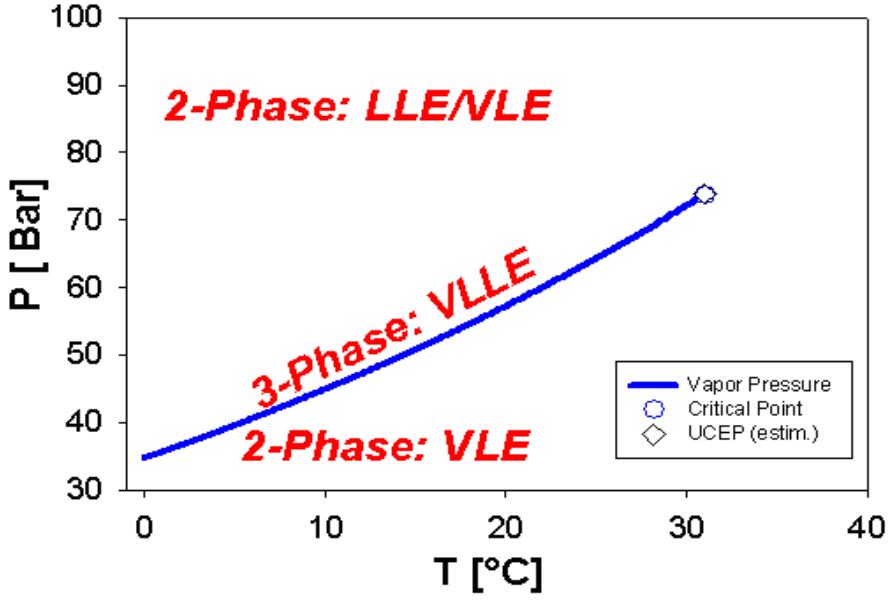

Figure 4.13 Global phase behavior of CO_2 and [HMIm][Tf_2N]

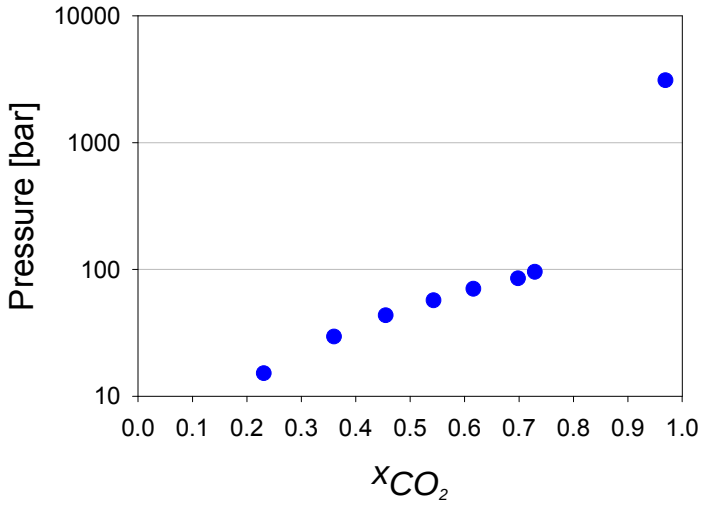

Figure 4.14 Phase behavior of the IL, [BMIm][PF_6] with CO_2 at 40°C to ultra-high pressures from Blanchard et al. [20]

The ionic liquid and CO_2 system has only regions of VLE, VLLE, a UCEP and no measurable critical points. This phase behavior for binary systems implies that CO_2/IL systems probably belong to Type III (see Figure 4.15) of the van Konynenburg and Scott classification. The figures are taken from the book of McHugh and Krukonis [21]. This indicates that CO_2 with this ionic liquid forms a Type III system with a critical locus that approaches hyperbaric to infinite pressure. Therefore, we may not be able to measure it experimentally. At higher temperatures, the critical point should be at a lower pressure, but the ionic liquids may begin to decompose before this temperature-pressure point is found. Shariati *et al.* [22] report that systems with [BMIm][PF_6] and CO_2 (or trifluoromethane) have a type III phase behavior, however, this has been questioned by Shiflett and Yokozeki [2]. The vapor liquid, vapor- liquid-liquid, liquid-liquid equilibrium of CO_2 and [Tf_2N] ionic liquids will be presented in Chapter 5.

Type III systems (Figure 4.16) have two distinct critical lines: one critical curve connect between pure component critical point of the more volatile component, and a critical end point on the end of a vapor-liquid-liquid line. The other critical line starts from the pure component with high critical temperature and extends to high pressure, technically infinite pressure. This line may have a variety shapes depending on the interactions of the components, as shown in Figure 4.15. For case 1, the mixture critical curve extends to temperatures lower than pure component critical point. It also shows one pressure maximum and one pressure minimum. For case 2, the mixture critical curve shows one pressure extreme and temperature minimum. For

case 3, it has a negative slope of $(dP/dT)_c$ at the critical point of component having higher critical temperature. For case 4, it only has a temperature minimum. For case 5, it has a positive slope of $(dP/dT)_c$ at the critical point of less volatile component.

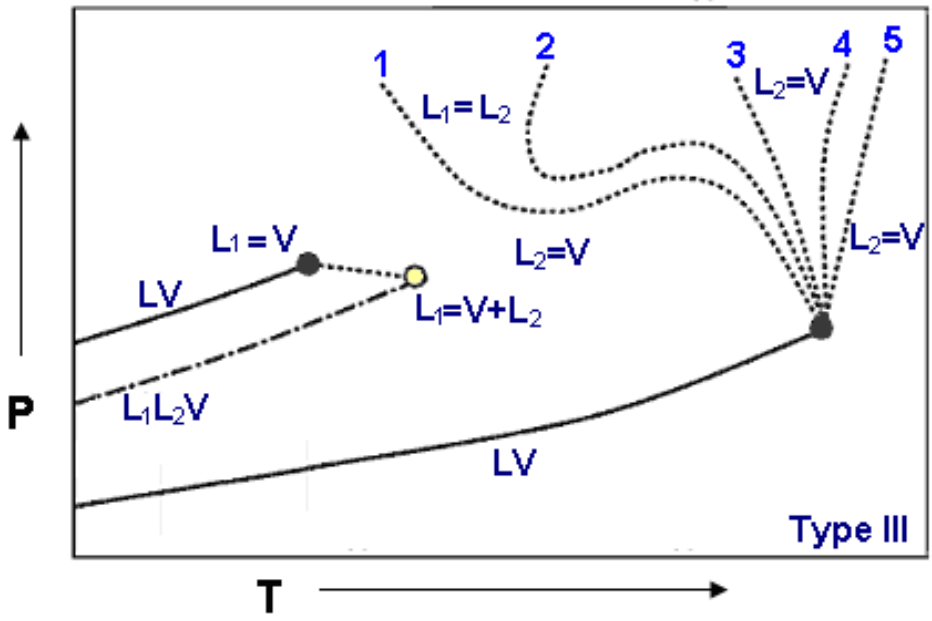

Figure 4.15 Diagram of type III Phase behavior with different shape of critical curve. [20]

To better understand and explain the type III phase behavior, case 2 is taken as an example. Here, four isothermal intersections are chosen for different scenarios, as shown in Figure 4.16. For case b, the temperature (T_1) is lower than critical temperature of more volatile component. At lower pressure, only vapor phase exists. When pressure is increased, the system intercrosses the dew point line, and then vapor liquid equilibrium exists. LLV three - phase line is reached. When pressure continues to increase, the system may go to liquid-liquid envelop based on the

composition x_1, if x_1 is less than x', LLE exists, and then it diverges at high pressure, otherwise, VLE exists, until it cross the vapor pressure line of more volatile component.

Temkin [23] proposed two simple criteria to predict "gas-gas" immiscibility for case b based on the relative magnitude of the van der Waals equation of state parameters. In terms of the critical volume (V_c) and critical temperature (T_c) of the components, the criteria are:

$$V_1^c \geq 0.42 V_2^c \tag{4.1}$$

$$T_1^c V_1^c < 0.052 T_2^c V_2^c \tag{4.2}$$

where component 2 is the component having the higher critical temperature.

For case c, the temperature (T_2) is increased. The phenomenon is similar to case b except the system reaches a mixture critical point at higher pressures for the region with a large amount of the more volatile component.

For case d, the temperature (T_3) is raised to higher than UCEP. The VLE exists when the pressure is increased due to no intersections with mixture critical curve.

For case e, the temperature (T_4) is increased but lower than critical temperature of less volatile component. With increasing pressure, vapor-liquid envelope ends up at one critical point when it first intercrosses the mixture critical curve. However, when pressure is higher than mixture critical pressure, the system splits into two phases. At higher pressure, the system reaches the other mixture critical point at minimum pressure of fluid-liquid envelope.

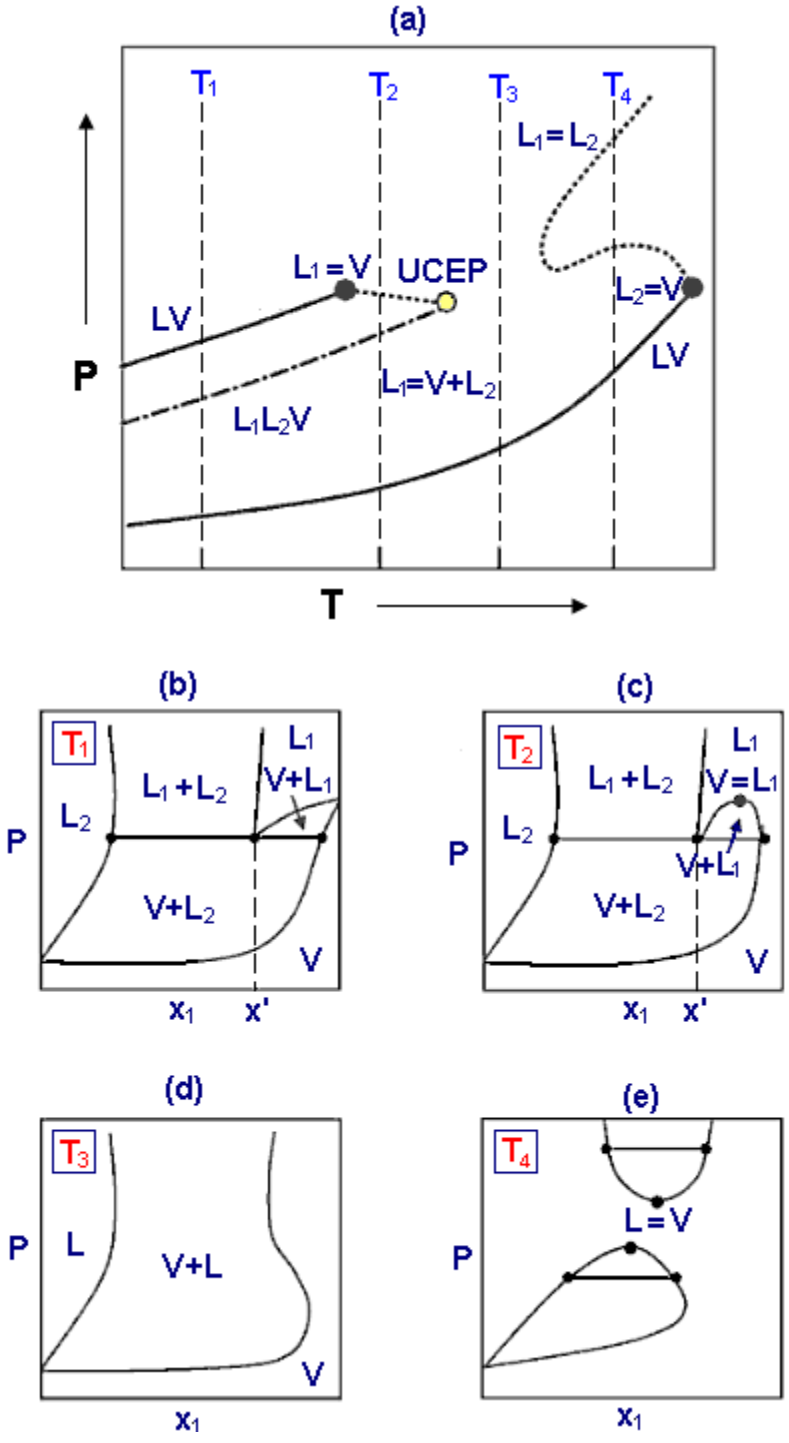

Figure 4.16 P-T and P-x diagrams of Type III Phase behavior. [20]

4.5 Global Phase Behavior Modeling

The global phase behavior can be calculated using equation of state models and mixing rules. A software package, GPEC facilitates these predictions. GPEC was developed by the group of process thermodynamics (GTP) of Planta Piloto de Ingeniería Química (PLAPIQUI) / Universidad Nacional del Sur (UNS). GPEC allows phase diagrams and other thermodynamic plots to be computed for binary systems with different equations of state. The diagrams you can calculate with GPEC are: global phase equilibrium diagrams in different projections, P-x-y diagrams for constant temperature and T-x-y diagrams for constant pressure. In the present version of GPEC, there are six different equations of state available to use: Soave-Redlich-Kwong EOS, Peng-Robinson EOS, RK-PR EOS, Simplified Perturbed Hard Chain Theory EOS, Perturbed Chain Statistical Associating Fluid Theory, and Group Contribution EOS.

For a given binary system, a global phase equilibrium diagram is a collection of critical lines, pure compound vapor pressure lines, vapor liquid liquid equilibrium lines, and in some cases also LLV and/or azeotropic lines in the P-T-x-ρ space. All these lines can be calculated by GPEC [24] with the computational strategy and methods proposed by Cismondi *et al.* [25].

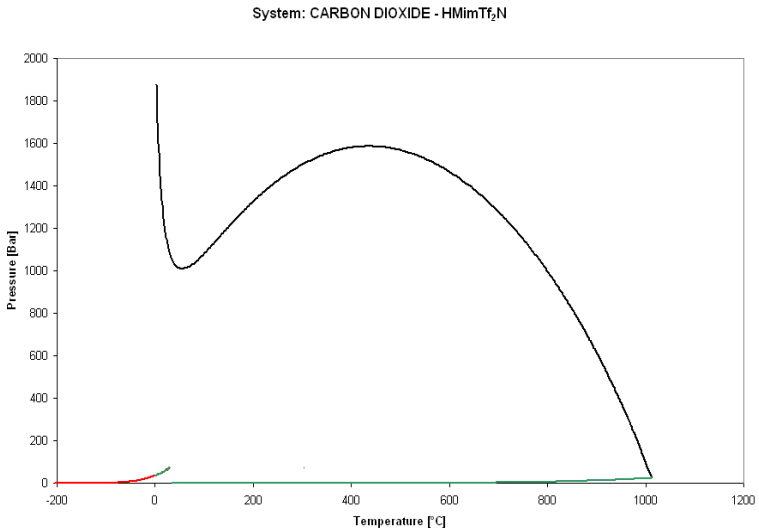

Figure 4.17 Global phase behavior of [HMIm][Tf_2N] and CO_2 calculated with GPEC**.**

4.5.1 [HMIm][Tf_2N] and CO_2

The global phase behavior of [HMIm][Tf_2N] and CO_2 are given in Figure 4.17. Peng-Robinson EOS with van der Waals-2 mixing rule (PR-vdW2 EoS) was chosen here to calculate the phase diagram. The binary interaction parameters were obtained by correlating VLE data from Chapter 5 at 25°C, k_{12} used here was 0.0579, l_{12} used here was 0.0826. The details for VLE calculation are given in Chapter 5. The predicted global phase behavior indicates that [HMIm][Tf_2N] and CO_2 binary system belongs to type III system. The UCEP calculated here is 31.07 ºC and 73.84 bar, which is very close to the critical points of pure CO_2 as 31.1 ºC and 73.8 bar. The VLLE line is almost overlapping with the vapor pressure line of CO_2. The mixture critical curve starts from pure ionic liquid critical point, passes through a pressure

maximum and a minimum, runs to the direction of CO_2 critical point, and finally goes to very high pressure. Ethane + methanol [26] shows similar phase behavior, which has a pressure maximum and minimum on its critical curve going to infinite pressure.

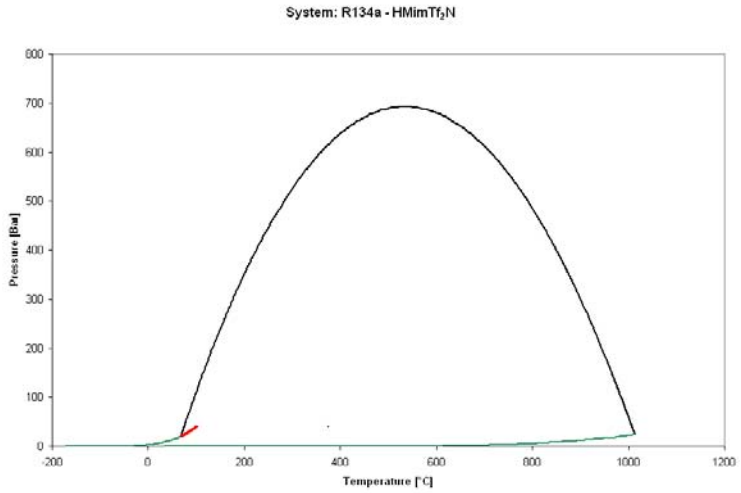

Figure 4.18 Global phase behavior of [HMIm][Tf_2N] and R-134a calculated with GPEC.

4.5.2 [HMIm][Tf_2N] and R-134a

The global phase behavior of [HMIm][Tf_2N] and R-134a were predicted and are shown in Figure 4.18. Similarly PR-vdW2 EOS was chosen with the binary interaction parameters correlated to VLE data at 75°C. k_{12} is -0.0224, l_{12} is 0.0057. It verifies that [HMIm][Tf_2N] and R-134a binary system belongs to Type V system, which is consistent with experimental data. Compared with the measured LCEP as 62.6 °C and 19.0 bar, the calculated LCEP is 68.5 °C and 20.25 bar, where the temperature is about 9.4% higher and pressure is about 6.6% higher. UCEP was

predicted very well. UCEP is 101.3 ºC and 40.7 bar, which is 0.3% higher than experimental temperature and 0.5% higher than that of pressure. The VLLE line is overlapping with the vapor pressure line of R-134a, which is consistent with experimental data. The comparison between experimental and calculated data is given in Table 4.5. The PR-vdW2 EoS model under-predicts of mixture critical points due to the limitation of EoS that will be discussed in Chapter 5.

Table 4.5 Mixture critical points of [HMIm][Tf_2N] mixture with R-134a

System	Mixture critical points			
	Experimental data		Predicted data	
[HMIm][Tf_2N] + R-134a	Temperature [°C]	Pressure [bar]	Temperature [°C]	Pressure [bar]
	75.0	43.2	75.5	41.0
	85.0	76.1	85.4	69.6
	101	123.5	100.8	112.6

4.6 Conclusions

The global phase behavior and equilibrium of ionic liquids and compressed gases were investigated and discussed in this Chapter. For refrigerant gas, R-134a, experiment data of [EMIm][Tf_2N], [HMIm][Tf_2N], [HMIm][PF_6], [HMIm][BF_4], and [BMIm][PF_6] were measured. Regions of multiphase equilibria exist, viz. VLE, LLE,

and VLLE. This phase behavior indicates that this is a Type V system according to the classification of Scott and van Konynenburg. The LCEP temperature increases and the mixture critical pressures decrease with increasing the alkyl group on the cation. The anion has a more pronounced effect on LCEP temperature and mixture critical pressure: the LCEP temperature increases and the mixture critical pressures decrease in the order of [BF_4], [PF_6], and [Tf_2N]. The global phase behavior and equilibria of [EMim][Tf_2N] with the refrigerant gas, R-134a were modeled with a modified RK cubic EoS. The cubic EoS using parameters regressed at the low pressure VLE data was able to predict the higher pressure VLE, VLLE and the LCEP. However, the model under predicts the high pressure mixture critical points. The global phase behavior of [HMIm][Br] and R-134a, [HMIm][Br], [HMIm][Tf_2N] and R-134a mixture were also measured, which shows Type III phase behavior. The phase behavior of CO_2 and ionic liquids are also discussed here, the phase behavior indicates Type III system. GPEC was chosen to calculate the global phase behavior and predict the right type phase behavior. These data will allow the proper design of various processes that utilize ionic liquids with compressed gases.

4.7 References

1. Van Konynenburg, P.H. and R.L. Scott, *Critical lines and phase equilibriums in binary Van der Waals mixtures.* Philos. Trans. R. Soc. London, Ser. A, 1980. **298**(1442): p. 495-540.

2. Yokozeki, A. and M.B. Shiflett, *Global Phase Behaviors of Trifluoromethane in Room-Temperature Ionic Liquid [BMIm][PF_6]*. AIChE J., 2006. **52**(11): p. 3952-3957.

3. Bolz, A., U.K. Deiters, C.J. Peters, and T.W. De Loos, *Nomenclature for phase diagrams with particular reference to vapour-liquid and liquid-liquid equilibria.* Pure Appl. Chem., 1998. **70**(11): p. 2233-2257.

4. Shiflett, M.B. and A. Yokozeki, *Solubility and Diffusivity of Hydrofluorocarbons in Room-Temperature Ionic Liquids.* AIChE J. , 2006. **52**(3): p. 1205-1219.

5. Crosthwaite, J.M., M.J. Muldoon, J.K. Dixon, J.L. Anderson, and J.F. Brennecke, *Phase transition and decomposition temperatures, heat capacities and viscosities of pyridinium ionic liquids.* J Chem Thermodyn, 2005. **37**(6): p. 559–568.

6. Ahosseini, A., W. Ren, and A.M. Scurto, *Viscosity and Diffusivity of Imidazolium Ionic Liquids with Compressed 1,1,1,2-Tetrafluoroethane (R-134a).* Manuscript in Preparation, 2009.

7. Shariati, A. and C.J. Peters, *High-pressure phase behavior of systems with ionic liquids: measurements and modeling of the binary system fluoroform/1-ethyl-3-methylimidazolium hexafluorophosphate.* J. Supercrit. Fluids, 2003. **25**: p. 109-117.

8. Shariati, A. and C.J. Peters, *High-pressure phase equilibria of systems with ionic liquids* J. Supercrit. Fluids, 2005. **34**(2): p. 171-176.

9. Shiflett, M.B. and A. Yokozeki, *Solubility Differences of Halocarbon Isomers in Ionic Liquid [EMIm][Tf_2N]*. J. Chem. Eng. Data, 2007. **52**: p. 2007-2015.

10. Aki, S.N.V.K., B.R. Mellein, E.M. Saurer, and J.F. Brennecke, *High-Pressure Phase Behavior of Carbon Dioxide with Imidazolium-Based Ionic Liquids.* Journal of Physical Chemistry B 2004. **108**(52): p. 20355-20365.

11. Kumelan, J., A. Perez-SaladoKamps, D. Tuma, and G. Maurer, *Solubility of H_2 in the Ionic Liquid [HMIm][Tf_2N]*. J. Chem. Eng. Data, 2006. **51**(4): p. 1364-1367.

12. Kumelan, J., A. Perez-SaladoKamps, D. Tuma, and G. Maurer, *Solubility of the Single Gases Methane and Xenon in the Ionic Liquid [HMIm][Tf_2N]*. Ind. Eng. Chem. Res., 2007. **46**(24): p. 8236-8240.

13. Castier, M. and S.I. Sandler, *Critical points with the Wong-Sandler mixing rule--II. Calculations with a modified Peng-Robinson equation of state.* Chemical Engineering Science, 1997. **52**(20): p. 3579-3588.

14. Scurto, A.M., C.M. Lubbers, G. Xu, and J.F. Brennecke, *Experimental measurement and modeling of the vapor-liquid equilibrium of carbon dioxide + chloroform.* Fluid Phase Equilibria, 2001. **190**(1-2): p. 135-147.

15. Proot, W. and T.W. de Loos, *High pressure phase behaviour of binary systems of refrigerants and phenylalkanes: the system 1,1,1,2-tetrafluorethane + phenyloctane.* Fluid Phase Equilibria, 2004. **222-223**: p. 255-259.

16. Lemmon, E.W., M.L. Huber, and M.O. McLinden, *NIST Reference Fluid Thermodynamic and Transport Properties - REFPROP Version 8.0*. 2007: Gaithersburg, Maryland.

17. Ren, W. and A.M. Scurto, *Global Phase Behavior of Imidazolium Ionic Liquids and Compressed 1,1,1,2-Tetrafluoroethane (R-134a).* AIChE J. , 2009. **55**: p. 486-493.

18. Ren, W., A.M. Scurto, M.B. Shiflett, and A. Yokozeki, *Phase Behavior and Equilibria of Ionic Liquids and Refrigerants: 1-Ethyl-3-methyl-imidazolium bis(trifluoromethylsulfonyl)imide ([EMIm][Tf_2N]) and R-134a*, in *Green Chemistry and Engineering with Gas Expanded Liquids and Near-Critical Media*, K.W. Hutchenson, A.M. Scurto, and B. Subramaniam, Editors. 2008, ACS Symposium Series: Washington, D.C. p. 112-128.

19. Carvalho, P.J., V.H. Álvarez, J.J.B. Machado, J. Pauly, J.-L. Daridon, I.M. Marrucho, M. Aznar, and J.A.P. Coutinho, *High pressure phase behavior of carbon dioxide in 1-alkyl-3-methylimidazolium bis(trifluoromethylsulfonyl)imide ionic liquids* J. Supercrit. Fluids, 2008. **48**(2): p. 99-107.

20. Blanchard, L., Z. Gu, and J. Brennecke, *High-pressure phase behavior of ionic liquid/CO_2 systems.* J. Phys. Chem. B, 2001. **105**(12): p. 2437-2444.

21. McHugh, M.A. and V.J. Krukonis, *Supercritical Fluid Extraction: Principles and practice*. 2nd ed. Butterworth-Heinemann series in chemical engineering. 1994, toneham, MA: Butterworth-Heinemann.

22. Shariati, A., K. Gutkowski, and C.J. Peters, *Comparison of the phase behavior of some selected binary systems with ionic liquids* AIChE J., 2005. **51**(5): p. 1532-1540.

23. Temkin, M.I., *Conditions Governing the Coexistence of Gaseous Phases.* Russ. J. Phys. Chem., 1959. **33**(275-277).

24. *GPEC (Global Phase Equilibrium Calculations)*. Available from: http://gpec.efn.uncor.edu/.

25. Cismondi, M., D.N. Nuñez, M.S. Zabaloy, E.A. Brignole, M.L. Michelsen, and J.M. Mollerup. *GPEC: A Program for Global Phase Equilibrium Calculations in Binary Systems*. in *EQUIFASE 2006: VII Conferencia Iberoamericana sobre Equilibrio entre Fases para el Diseño de Procesos*. 2006. Michoacán, México.

26. Brunner, E., *Fluid Mixtures at High Pressures II. Phase Separations and Critical Phenomena of (ethane + an n-alkanol) and of (ethane + methanol) and of (propane + methanol).* J. Chem. Thermodyn., 1985. **17**: p. 871-885.

Chapter 5 Phase Equilibria of Imidazolium Ionic Liquids and Compressed gases: Refrigerant Gas, 1,1,1,2-Tetrafluoroethane (R-134a) and carbon dioxide

5.1 Introduction

Ionic liquids (ILs) and compressed gases including hydrofluorocarbon gases and carbon dioxide have gained increasing attention in absorption refrigerant processes, extractions, reactions, materials process, etc. Detailed phase equilibria and modeling on these systems are highly needed for the process design and further development. Chapter 4 reports the global phase behavior of ionic liquid and compressed gases. This chapter presents the phase equilibrium of the binary system. For the hydrofluorocarbon refrigerant gas, 1,1,1,2-tetrafluorethane (R-134a), the vapor-liquid equilibrium, vapor-liquid-liquid equilibrium, liquid-liquid equilibrium, and mixture critical points with imidazolium ionic liquids were measured at temperatures of 25°C, 50°C, 75°C and pressure up to 143 bar. For CO_2 and n-alkyl-3-methyl-imidazolium bis(trifluoromethylsulfonyl)amide ionic liquids, the vapor-liquid equilibrium, vapor-liquid-liquid equilibrium and liquid-liquid equilibrium were also measured at temperatures of 25°C, 50°C, 70°C and pressure up to 250 bar. The effects of the anion and cation on the solubility were investigated with the anion having the greatest impact. The volume expansion and molar volume were also measured for R-134a, CO_2 and the ILs simultaneously. The Peng-Robinson Equation of State with van der Waals 2-parameter mixing rule with estimated IL critical points was chosen to model and correlate the experimental data.

5.2 Literature Survey: Phase Equilibrium of Imidazolium Ionic Liquids and Refrigerant Gases

There are only a few groups who have studied phase equilibria data for ionic liquids and refrigerant gases. Shiflett, Yokozeki and coworkers [2-14] have reported the majority of known low-pressure equilibria data. They investigated the solubility of a series of hydrofluocarbons (HFCs) in ionic liquids. In [BMIm][PF_6] , difluoromethane (R32) shows highest solubility and HFCs solubility follows an order as difluoromethane(R32) > 1,1-difluoroethane (R152a) > trifluoromethane(R23) > 1,1,1,2-tetrafluoroethane(R134a) > pentafluoroethane(R125) > 1,1,1-trifluoroethane(R143a). It is found that the trend in solubility does not correlate with the HFCs dipole moment as expected; however, the unique H-bonding capability (H-F- H) of HFCs is believed to be involved.

They also investigated the solubility and diffusivity of R-32 in 19 room temperature ionic liquids in order to gain further insight into these molecular interactions. A comparison between five sulfonate anions with a common [BMIm] cation reveals that the decreasing order is 1,1,2,3,3,3-hexafluoropropanesulfonate [HFPS] > 1,1,2-trifluoro-2-(perfluoroethoxy)ethanesulfonate [TPES] > 1,1,2-trifluoro-2-(trifluoromethoxy)-ethanesulfonate [TTES] > 2-(1,2,2,2-tetrafluoroethoxy)-1,1,2,2-tetrafluoroethanesulfonate [FS] > 1,1,2,2-tetrafluoroethanesulfonate [TFES]. For [TFES] anion ionic liquids, the order of

attraction between R-32 and the cations was [HMIm] > [DMIm] > [BMIm] > [EMIm]. R-32 has higher solubility with fluorinated anions than nonfluorinated anions.

Shiflett and Yokozeki [6] reported the solubilities of three classes of halocarbons, chlorofluorocarbons (CFCs), hydrochlorofluorocarbons (HCFCs), and hydrofluorocarbons (HFCs). In room temperature ionic liquid of [EMIm][Tf_2N], solubilities of five isomer pairs have been studied: 1,1,2-trichloro-1,2,2-trifluoroethane (CFC-113) and 1,1,1-trichloro-2,2,2-trifluoroethane(CFC-113a); 1,2-dichloro-1,1,2,2-tetrafluoroethane(CFC-114) and 1,1-dichloro-1,2,2,2-Tetrafluoroethane (CFC-114a); 1,1-dichloro-2,2,2-trifluoroethane (HCFC-123) and 1,2-dichloro-1,2,2-trifluoroethane (HCFC-123a); 1-chloro-1,2,2,2-tetrafluoroethane(HCFC-124) and 1,2,2,2-tetrafluoroethane (HCFC-124a); 1,1,2,2-tetrafluoroethane (HFC-134) and 1,2,2,2-tetrafluoroethane (HFC-134a). The hydrogen substitution (Cl →H) significantly increased the solubility in [EMIm][Tf_2N]: for CFCs to HCFCs, CFC-113($CFCl_2$-CF_2Cl) → HCFC-123a ($CHClF$-CF_2Cl), CFC-113a(CCl_3-CF_3) → HCFC-123 ($CHCl_2$-CF_3), CFC-114 (CF_2Cl-CF_2Cl) → HCFC-124a (CHF_2-CF_2Cl), CFC-114a ($CFCl_2$-CF_3) → HCFC-124 ($CHFCl$-CF_3), and for HCFCs to HFCs, HCFC-124a (CHF_2-CF_2Cl) → HFC-134 (CHF_2-CHF_2), HCFC-124 ($CHFCl$-CF_3) → HFC-134a (CH_2F-CF_3). Hydrogen substitution effect was also found in [BMIm][PF_6]. The hydrogen-substitution for perhalogenated methane ($CFCl_3$ → $CHCl_3$) and ethane ($CFCl_2$ → CF_2Cl → $CHCl_2$-CF_3) increases the solubility significantly in [BMIm][PF_6].

Ammonia solubilities in four RTILs [16] were investigated: 1-Butyl-3-methylimidazolium hexafluorophosphate ([BMIm][PF_6]), 1-Hexyl-3-methylimidazolium chloride ([HMIm][Cl]), 1-Ethyl-3-methylimidazolium bis(trifluoromethylsulfonyl)amide ([EMIm][Tf_2N]), and 1-Butyl-3-methylimidazolium tetrafluoroborate ([BMIm][BF_4]). Amazingly high solubilities of ammonia in these RTILs have been observed and almost comparable to the case of ammonia-water mixtures, which is high due to reversible chemical reaction.

For R-134a, Shiflett and Yokozeki [2] measured and modeled the solubility and diffusivity in seven RTILs at the low-pressure (<3.5 bar). R-134a solubility follows the order as: [BMIm][TPES] > [BMIm][TTES] 1-Ethyl-3-methylimidazolium bis(pentafluoroethylsulfony)amide([EMIM][BEI]) > [4,4,4,14-P][TPES] > 1,1,2-trifluoro-2-(perfluoroethoxy)ethanesilfonate([6,6,6,14-P][TPES]) > 1-Butyl-3-methy-limidazolium hexafluorophophate([BMIm][PF_6]) > [BMIm][HFPS]. The preliminary molecular simulations indicate that H-bonding (H-F) between anion, cation and R-134a contributes to attractions and results in high solubility.

Shiflett and Yokozeki also measured vapor-liquid-liquid equilibria (VLLE) of seven hydrofluorocarbons (including R-134a) with 1-butyl-3-methylimidazolium hexafluorophosphate ([BMIm][PF_6]) [2-3]. Using a modified Redlich-Kwong equation of state, Shiflett and Yokozeki [6] modeled the low-pressure vapor-liquid equilibrium of R-134a and [EMIm][Tf_2N]. They used the regressed parameters from the low-pressure data and predicted that this system was a Type V of Scott-van Konynenburg (see Chapter 4). In Chapter 4, we have also measured the high-

pressure phase behavior and equilibria of this system and have confirmed the Type V behavior [3, 17-18]. Shariati and Peters measured the high-pressure phase behavior of fluoroform (trifluoromethane (CHF_3)) in [EMIm][PF_6] and [BMIm][PF_6] [19]. Kim *et al.* [20] have studied the refractive index, heat capacity, and vapor pressure of mixtures of [BMIm][BF_4] and [BMIm][Br] with 2,2,2-trifloroethanol (TFE) and water [21]. To model these ionic liquid-hydrofluorocarbon gas systems, both activity coefficient models and equation of state models have been reported. Shiflett and Yokozeki used the Non Randon Two Liquid (NRTL) solution model [2], and Redlich-Kwong EoS model [4] to correlate the phase equilibrium data. Karakatsani, *et al.* [22] and Kroon *et al.* [23] applied a model, called tPc-PSAFT to predict the solubility of gases in ILs.

Kumelan *et .al.* measured the solubility of tetrafluoromethane (R14) in [HMIm][Tf_2N] and correlated the data with extended Henry's Law [24]. Shiflett and Yokozeki [25] measured the LLE in the mixture of five hydrofluoroethers and [EMIm][Tf_2N], and LLE were well correlated by using NRTL model. All binary systems show large immiscibility gaps. [EMIm][Tf_2N] is more soluble in hydrofluoroether (HFE) with lower boiling point. The excess molar volumes of the mixture are small and similar to ordinary binary mixtures, which are opposite to the mixtures of hydroflurocarbons and ionic liquids. The VLE and VLLE between hydrofluorocarbons (pentafluoroethane: HFC-125 and 1,1,1-trifluoroethane: HFC-143a) and hydrofluoroethers (trifluoromethane: HFE-125 and trifluoromethoxy methane: HFE-143a) in [EMIm][Tf_2N] were measured, compared and correlated with

NRTL model [12]. They all exhibit partial miscibility, the immiscibility gap of HFC-125 binary system is smaller than that of HFE-125 system, while HFC-143a binary system is larger than that of HFE-143a system. Compared with [BMIm][PF_6], HFC-125 is more soluble in [EMIm][Tf_2N]. The solubility of *threo*- and *erythro*-diastereomers of HFC-4310mee, including their deuterated isomers, with [BMIm][PF_6], [BMIm][BF_4] and [BMIm][BF_4] were reported [13] and all system exhibited liquid-liquid separations. The threo-isomers are more miscible than the erythro-isomers in the studied ILs The deuterated threo-isomer systems show slightly better solubility than the nondeuterated system.

Shiflett, Yokozeki and coworkers [10-11, 17] measured liquid-liquid equilibrium of halogenrated benzene, fluorinated benzenes, and substituted benzenes in [EMIm][Tf_2N] and correlated by NRTL model. The fluorinated benzenes having a larger dipole moments (1,2-difluorobenzene 2.4 D, 1,2,3,4-tetrafluorobenzene 2.4 D, and 1,2,3-trifluorobenzene 2.8 D) were completely miscible over the temperature range studied (283 to 413 K), while the other fluorinated benzenes with a dipole moment of 1.4 D (1,2,4-trifluorobenzene, fluorobenzene, 1,3- difluorobenzene, pentafluorobenzene, and 1,2,3,5-tetrafluorobenzene) and 0 D (1,4-difluorobenzene, benzene, 1,2,4,5-tetrafluorobenzene, hexafluorobenzene, and 1,3,5-trifluorobenzene) were only partially miscible in [EMIm][Tf_2N]. A trend between the dipole moment and the miscibility was discovered, but other intermolecular interactions (higher-order moments, π-electron effects, and hydrogen bonding) are also believed to play a role in controlling the degree of miscibility. The binary mixtures with the largest

immiscibility gaps (1,3,5-trifluorobenzene, 1,2,3,5-tetrafluorobenzene, and pentafluorobenzene) show the largest negative excess molar volumes. For binary systems of halgogenranted benzene and IL, a general trend between the molecular size of the solute and the immiscibility gap was discovered. As the solute molecular size increases (fluorobenzene < chlorobenzene < bromobenzene < iodobenzene), less of the solute can exist in these cavities, resulting in a larger immiscibility region. There is no trend between the dipole moment and the miscibility was discovered, other intermolecular interactions may play a role. For substituted benzenes system, the immiscibility gap decreases as the polarity increased and the molecular size decreased. The nonalkyl-substituted benzenes containing functional groups (-NH_2, -NO_2, -OH, and -CHO) were completely soluble in [EMIm][Tf_2N] from 20 ºC to 100 ºC .

Shiflett and Yokozeki [9] measured the solubility of benzene + [EMIm][Tf_2N], and hexafluorobenzene + [EMIm][Tf_2N] systems at 10 ºC, 25 ºC and 45 ºC. Both binary systems show immiscibility gaps with concentration ranges from about 77 to 100 mol % for benzene and from about 66 to 100 mol % for hexafluorobenzene, respectively. Ternary phase diagrams for the present three components were constructed using the binary interaction parameters correlated by Redlich-Kwong cubic equation equation-of-state (EOS) model.

5.3 Results and Discussions

The ionic liquids include 1-Ethyl-3-methyl-imidazolium bis(trifluoromethylsulfonyl)amide ([EMIm][Tf_2N]), 1-Hexyl-3-methyl-imidazolium bis(trifluoromethylsulfonyl)amide ([HMIm][Tf_2N]), 1-Hexyl-3-methyl-imidazolium hexafluorophosphate ([HMIm][PF_6]), and 1-Hexyl-3-methyl-imidazolium tetrafluoroborate ([HMIm][BF_4]). The structures are given in Figure 5.1. The details of ionic liquid synthesis procedure and analysis results are given in Chapter 2.

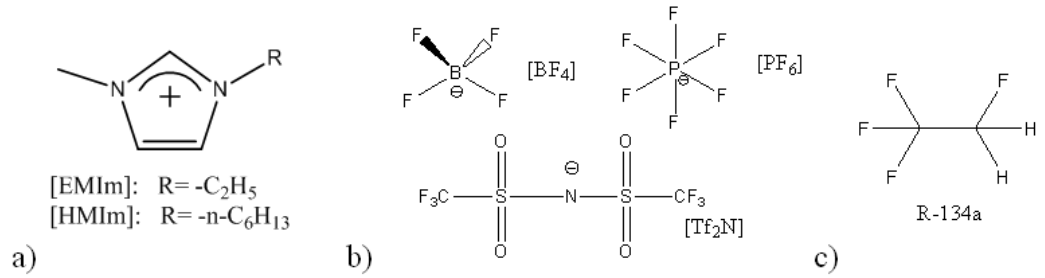

Figure 5.2 Ionic liquid cations (a), anions (b) and the refrigerant gas (c): 1,1,1,2-tetrafluoroethane (R-134a).

The VLE, VLLE and mixture critical points of 1,1,1,2-tetrafluoroethane (R-134a) and the ILs, [EMIm][Tf_2N], [HMIm][Tf_2N], [HMIm][BF_4], and [HMIm][PF_6] were measured at 25°C, 50°C, and 75°C and pressures up to 143 bar. In addition, the volume expansion and the liquid molar volume were measured for each IL at each isotherm. A quantitative model of the high-pressure phase behavior and equilibria data is essential to design IL/refrigerant applications. The phase behavior determines the conditions (temperature and pressure) of the transitions in equilibria, i.e., whether

they are VLE, LLE, etc. Phase equilibria data quantify the solubility of each component in each phase. The experimental data of IL/R-134a data were correlated by the Peng-Robinson EoS with van der Waals 2-parameter mixing rule (PR-vdW2) to predict the VLE, VLLE, and mixture critical points. The details are given in Chapter 3. Predicted critical point properties of the ILs used in model are given in Table 5.1. Since the ILs will decompose at high temperature, the physical critical points can not be obtained experimentally. The physical properties of ILs used here are calculated from group contribution methods[26-27]. The property data of R-134a are from the PE2000 database [28].

Table 5.1 The physical properties of ILs and R-134a

Component	Formula	Molecular Weight [g/mol]	Critical Temp. [K]	Critical Pressure [bar]	ω Acentric Factor
[EMIm][Tf_2N]	$C_8H_{11}N_3F_6S_2O_4$	391.30	1244.9	32.6	0.1818
[HMIm][Tf_2N]	$C_{12}H_{19}N_3F_6S_2O_4$	447.41	1287.3	23.9	0.3539
[HMIm][BF_4]	$C_{10}H_{19}N_2BF_4$	254.08	679.1	17.9	0.9258
[HMIm][PF_6]	$C_{10}H_{19}N_2PF_6$	312.24	754.3	15.5	0.8352
R-134a	$C_2H_2F_4$	102.03	374.3	40.6	0.3268
Note: ILs data from the literature [26]; The property data of R-134a from the PE2000 database [28].					

5.3.1 Phase equilibria of [HMIm][Tf_2N]/R-134a

Chapter 4 presents the global phase behavior (pressure-temperature projection) of binary mixtures of R-134a and [EMIm][Tf_2N], [HMIm][Tf_2N], [BMIm][PF_6], [HMIm][PF_6], and [HMIm][BF_4] between approximately 0°C to 105ºC and pressures

to 330 bar [18-19]. In all cases, the phase behavior is classified with reasonable certainty as Type V according to the classification of Scott and van Konynenburg [29]. This single phase behavior is quite unique for hydrofluorocarbon refrigerant gases and ionic liquids, as most compressed gases (CO_2, CO, etc.) have no reported miscibility with ILs [30-33].

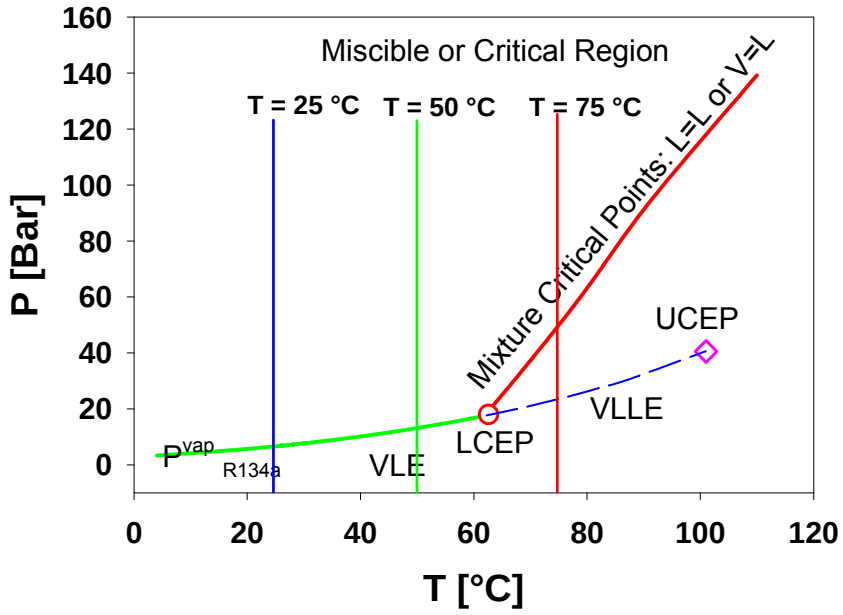

Figure 5.2 Smoothed experimental global phase behavior for [HMIm][Tf_2N] and R-134a adapted from data and vapor pressure of R-134a by Lemmon *et al.* [36] .

Figure 5.2 illustrates the global phase behavior of [HMIm][Tf_2N] and R-134a. As shown, there are the regions of 1-, 2-, and 3-phase equilibrium. At lower temperatures, such as 25 °C and 50 °C below the LCEP at approximately 62.6 ºC, vapor-liquid equilibrium exists with complete liquid miscibility above the vapor pressure of R-134a. Vapor-liquid-liquid (VLLE) equilibrium exists between the

lower and upper critical endpoints (LCEP and UCEP) and pressure of this 3-phase equilibrium is nearly equal to the vapor pressure of pure R-134a. The UCEP is equal within experimental accuracy to the critical point of pure R-134a. At temperatures above the LCEP, but below the UCEP, for instance, at 75°C, four different equilibria are possible depending on the pressure. VLE exists at the lowest pressures and VLLE exists near or at the pure R-134a vapor pressure. At pressures above VLLE, liquid-liquid (LLE) equilibria exist until the mixture critical point, beyond which the system becomes critical/miscible. The global phase behavior study helps to determine the physical conditions or limitations for any potential application of ILs with compressed refrigerant gases.

The phase equilibria for [HMIm][Tf_2N]/R-134a at the three isotherms are plotted in Figure 5.3. The experimental data are given in Table 5.2. As expected, the R-134a solubility increases with pressure and decreases with temperature. As shown from the global phase behavior in Figure 5.2, the lower-critical endpoint is at approximately 62°C. Thus, VLE will exist for the system at 25°C and 50°C until the vapor pressure of R-134a where the mixture becomes completely miscible. However, for 75°C, there are regions of VLE, VLLE, and LLE until the mixture critical point is reached where the mixture becomes miscible/critical. The experimental mixture critical point of 75°C is at 43.2 bar and 96% mole fraction R-134a. This indicates that 4% of the IL is soluble in the compressed gas. This phenomenon is largely different from all other reported studies with compressed gases and ionic liquids, where the IL is usually insoluble in the vapor phase.

Table 5.2 Vapor liquid equilibrium experimental data and mixture critical points of R-134a and [HMIm][Tf_2N]

T [° C]	P [bar]	$x_{R\text{-}134a}$	$\Delta V/V_0$ a	V_L [cm^3/mol]
[HMIm][Tf_2N]				
25	0.42	0.0247±0.0019	0.0007±0.0006	335.48±0.14
	0.75	0.0761±0.0017	0.0085±0.0006	320.28±0.13
	1.17	0.1442±0.0015	0.0273±0.0006	302.21±0.12
	1.81	0.2360±0.0012	0.0569±0.0006	277.58±0.11
	2.51	0.3416±0.0009	0.1060±0.0006	250.29±0.09
	3.46	0.4609±0.0006	0.1812±0.0006	218.88±0.08
	4.02	0.5264±0.0005	0.2414±0.0007	202.09±0.07
	4.55	0.5893±0.0004	0.3219±0.0007	186.60±0.06
	5.23	0.6724±0.0002	0.4668±0.0007	165.19±0.05
	5.86	0.7578±0.0001	0.7304±0.0008	144.08±0.03
50	0.53	0.0282±0.0014	0.0015±0.0005	336.77±0.12
	1.04	0.0652±0.0013	0.0093±0.0005	326.46±0.12
	1.55	0.1100±0.0012	0.0194±0.0005	313.96±0.11
	2.13	0.1604±0.0011	0.0346±0.0005	300.56±0.11
	2.86	0.2123±0.0010	0.0537±0.0005	287.21±0.10
	3.92	0.2860±0.0008	0.0839±0.0005	267.80±0.09
	5.06	0.3577±0.0007	0.1225±0.0006	249.48±0.08
	6.12	0.4223±0.0006	0.1649±0.0006	232.85±0.07
	7.48	0.5019±0.0005	0.2329±0.0006	212.50±0.06
	8.66	0.5702±0.0004	0.3109±0.0006	194.98±0.06
	9.72	0.6267±0.0003	0.3981±0.0006	180.57±0.05
	10.62	0.6807±0.0003	0.5119±0.0007	167.04±0.04

	11.43	0.7334±0.0002	0.6685±0.0007	153.94±0.03
	11.92	0.7642±0.0002	0.7894±0.0008	146.01±0.03
75	5.02	0.2429±0.0044	0.050±0.002	293.7±0.3
	8.74	0.3916±0.0033	0.113±0.002	250.1±0.2
	12.11	0.5145±0.0025	0.189±0.002	213.3±0.2
	15.59	0.6205±0.0019	0.310±0.002	183.7±0.2
	18.78	0.7157±0.0013	0.498±0.002	157.3±0.1
	22.92[vll]	0.9107±0.0010		
	43.2[cp]	0.9600±0.0010		

[a] $\frac{\Delta V}{V_0} = \frac{V_m(T,P,x_i) - V_{IL}(T,P=1bar)}{V_{IL}(T,P=1bar)}$;

[cp]= mixture critical point;

[vll]= vapor-liquid-liquid equilibrium points for the IL-rich phase.

Table 5.3 The parameters and results of EoS modeling

ILs + R-134a	Temperature [° C]	Exp. Data Points	Interaction Parameters		AARD%
			k_{12}	l_{12}	
[HMIm][Tf_2N]	25	10	0.0062	0.0025	6.75
	50	14	0.0029	0.0070	3.37
	75	5	-0.0224	0.0057	0.39
[HMIm][BF_4]	25	5	0.0631	-0.0037	5.30
	50	7	0.0894	0.0155	5.36
	75	5	0.0972	0.0280	1.90
[HMIm][PF_6]	25	6	0.0218	-0.0040	2.74
	50	10	0.0875	0.0154	5.97
	75	5	0.0873	0.0145	2.05

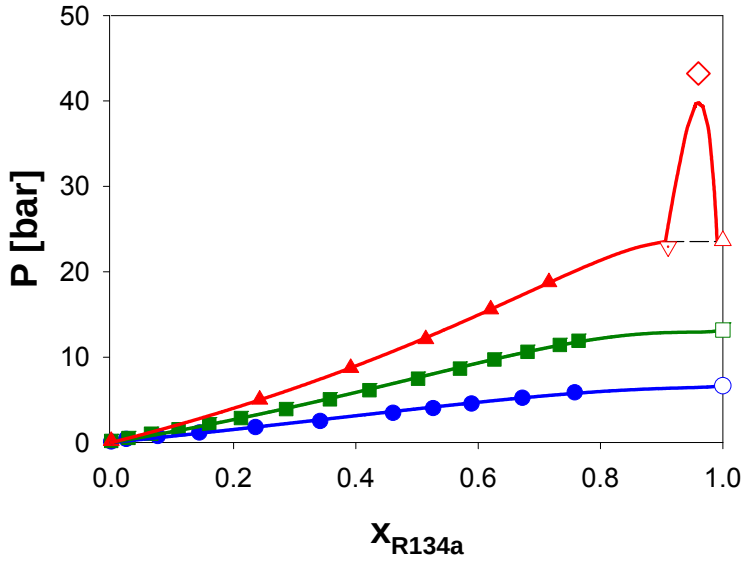

Figure 5.3 Experimental Vapor liquid Equilibrium data and modeling results for [HMIm][Tf_2N] and R-134a. Legend: ●:25°C; ■:50°C ▲:75°C Inverted open triangle: experimental VLLE point; diamond: experimental critical points at 75°C; all points at a mole fraction of 1 are the vapor pressure of R-134a by Lemmon *et al.* [36] Solid lines are modeling VLE and LLE. VLE, dash line is VLLE.

The experimental data of [HMIm][Tf_2N]/R-134a were correlated by the PR-vdW2 model. For the model details, refer to Chapter 3. The binary interaction parameters with deviations between the predicted and experimental data are listed in Table 5.3. As shown in Figure 5.3 and Table 5.3, a good agreement is observed between the model and the experimental data. The VLE data at 25°C and 50°C are well correlated throughout the pressure-composition range. At 75°C, the model predicts VLLE at 23.5 bar with compositions of 90.6% mole R-134a in the IL-rich

phase, 0.9% mole of the IL in the R-134a-rich phase and 2 $\times 10^{-8}$ mole fraction in the vapor phase. Only the composition in the IL-rich phase was measured here and the predicted pressure is 2.7% higher than the experiment and the mole fraction composition prediction is 0.5% lower. However, the model prediction of the mixture critical point is approximately 3.5 bar lower than the experimental pressure and a difference of 1% mole. It should be noted that the interaction parameters were regressed solely to the VLE data and did not include the mixture critical point. The poor prediction of mixture critical points by cubic EoS models with parameters regressed from VLE data has also been reported [26, 34].

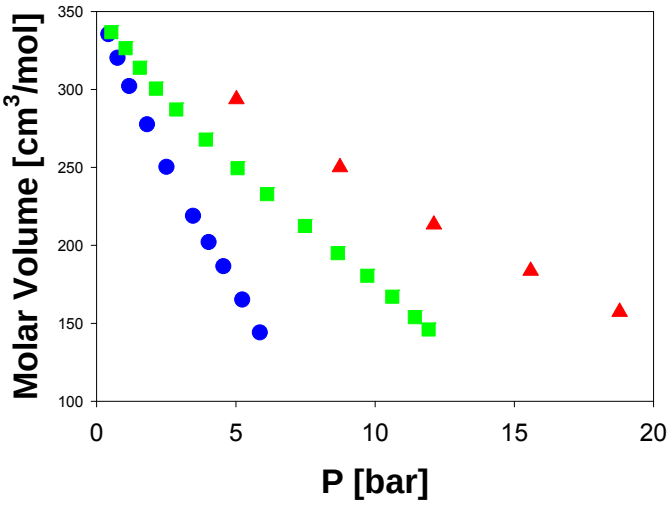

Figure 5.4 Experimental molar volume data for [HMIm][Tf_2N] and R-134a. Legend: ●:25°C; ■:50°C ▲:75°C.

The molar volume data of [HMIm][Tf_2N] and R-134a are listed in Table 5.3. As shown in Figure 5.4, the liquid mixture molar volume decreases linearly with R-134a pressure due to the increased solubility of R-134a. The slope of liquid molar

volume with pressure increases when temperature decreases. The inverse of molar volume is the molar density. That means the molar density increases with R-134a solubility. Figure 5.5 indicates that the molar volume of liquid mixture is independent of temperature and decreases linearly with mole fraction of R-134a. This trend is similar to ionic liquid and hydrofluorocarbons demonstrated by Shiflett and Yokozeki [2]. The volume expansion data of [HMIm][Tf_2N] and R-134a are listed in Table 5.3 and shown in Figure 5.6. The volume of liquid mixture is expanded with the pressure at all three isotherms. At the same pressure, volume is expanded more at lower temperature due to higher R-134a solubility.

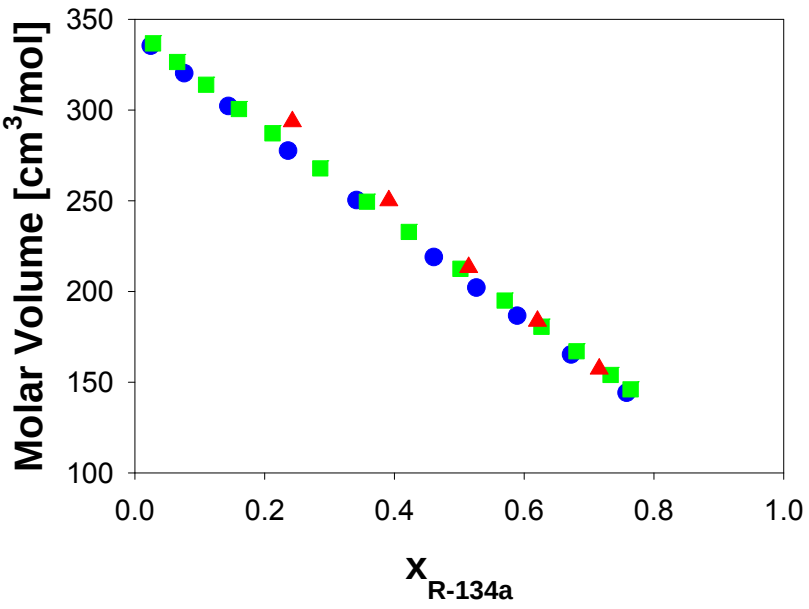

Figure 5.5 Experimental molar volume data for [HMIm][Tf_2N] and R-134a. Legend: ●:25°C; ■:50°C ▲:75°C.

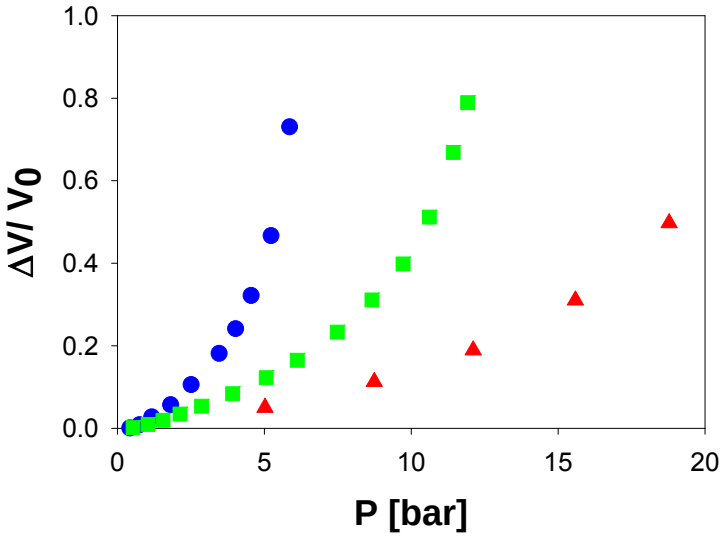

Figure 5.6 Experimental volume expansion data for [HMIm][Tf_2N] and R-134a. Legend: ●:25°C; ■:50°C ▲:75°C.

5.3.2 Phase equilibria of [EMIm][Tf_2N]/R-134a

Figure 5.7 shows the phase equilibrium data of [EMIm][Tf_2N] and R-134a at 25°C, 50°C, and 75°C, and the experimental data are listed in Table 5.4. Shiflett and Yokezeki [6] studied the vapor-liquid equilibrium of [EMIm][Tf_2N] and R-134a at 10°C, 25°C, 50°C, and 75°C, but only until approximately 3.5 bar due to experimental limitations. Here, the high-pressure VLE data at 25°C, 50°C, and 75°C has been extended to just below the vapor pressure of the pure R-134a or the pressure of VLLE. As shown in the Figure 5.7, the data from this work matches Shiflett and Yokezeki's data very well. The higher pressure data smoothly continue to just below the pure R-134a vapor pressure or VLLE.

Here, we have correlated the experimental data with the PR-vdW2 model. Only VLE data is used to regress the binary interaction parameters. The binary interaction parameters and modeling results of [EMIm][Tf_2N] and R-134a are given in Table 5.5. The VLE data is correlated very well. The modeling result line goes through all of experimental data points. AARD% decreases with temperature. The k_{12} and l_{12} decrease with temperature. The modeling results show that the model predicts VLE very well. However, significant differences are observed for the VLLE composition and mixture critical pressure and composition. For VLLE at 75°C, only the mole fraction of R-134a in ionic liquid rich phase was measured. The experimental pressure is 22.91 bar and 88.04% mole fraction of R-134a in ionic liquid rich phase. The model predicted as 22.36 bar and 83.09% mole fraction, which is 0.45 bar (1.98%) higher on pressure and 5.61% lower on R-134a mole fraction than experimental data. The model also predicted 1.7% mole of the IL in the R-134a-rich phase and 2×10^{-7} mole fraction in the vapor phase. Only the composition in the IL-rich phase was measured here. Shiflett and Yokozeki [6] measured the VLLE of a similar system R-134a and [EMIm][Tf_2N] at 76°C and determined that the composition of the IL in R-134a-rich liquid phase was very low (<0.5%mole). At the mixture critical point, the prediction of the pressure is 44.4 bar lower and the mole fraction of R134a is 4% mole less than the experimental data.

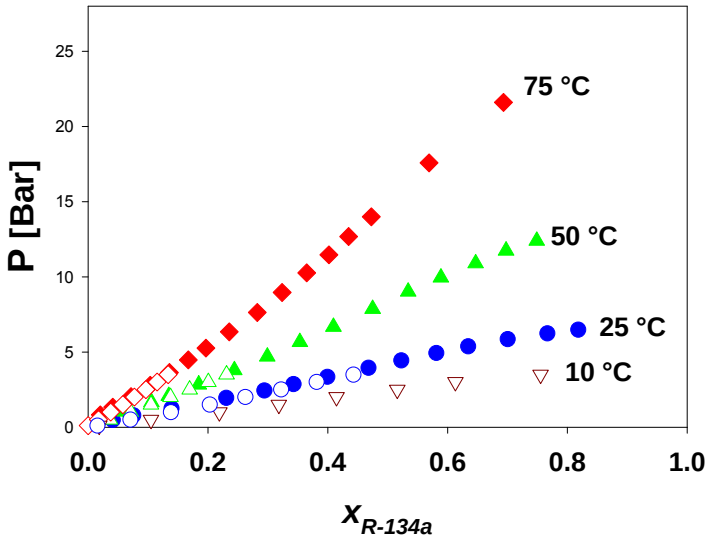

Figure 5.7 Vapor-liquid equilibrium data for [EMIm][Tf_2N] and R-134a. Closed symbols: experimental data in this study; Open symbols are the data of Shiflett and Yokezeki [1] for VLE and VLLE respectively.

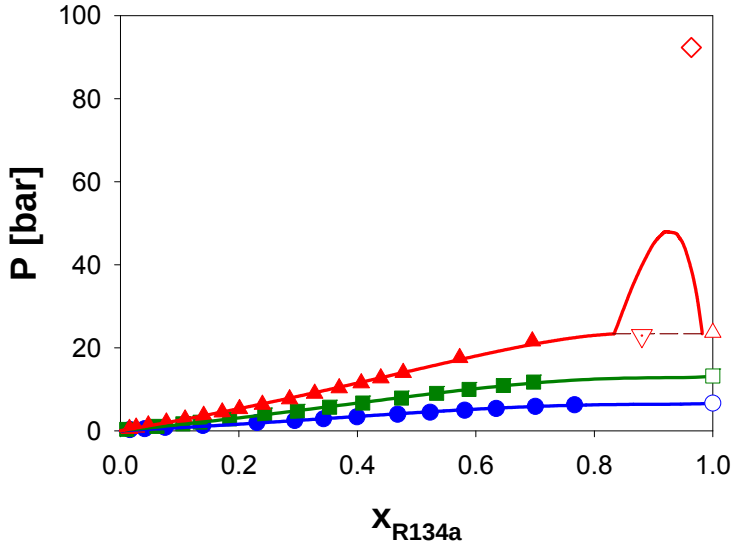

Figure 5.8 Experimental Vapor liquid Equilibrium data and modeling results for [EMIm][Tf_2N] and R-134a. Legend: ●:25°C; ■:50°C ▲:75°C Inverted open triangle: experimental VLLE point; diamond: experimental critical points at 75°C; all points at mole fraction of 1 are vapor pressure of R-134a by Lemmon *et al.* [38]

Table 5.4 Vapor liquid equilibrium experimental data and mixture critical points of R-134a and [EMIm][Tf_2N]

T [° C]	P [bar]	x_{R-134a}	$\Delta V/V^{0}$ [a]	V_L[cm^3/mol]
[EMIm][Tf_2N]				
25	0.28	0.0161±0.0020	0.0012±0.0007	266.26±0.14
	0.48	0.0411±0.0019	0.0040±0.0007	260.21±0.13
	0.79	0.0754±0.0018	0.0137±0.0007	253.34±0.13
	1.25	0.1392±0.0016	0.0348±0.0007	240.75±0.12
	1.95	0.2304±0.0013	0.0754±0.0007	223.70±0.11
	2.44	0.2943±0.0011	0.1093±0.0008	211.58±0.10
	2.86	0.3428±0.0009	0.1372±0.0008	201.99±0.09
	3.35	0.3992±0.0008	0.1792±0.0008	191.50±0.08
	3.95	0.4681±0.0006	0.2417±0.0008	178.49±0.07
	4.44	0.5228±0.0005	0.3033±0.0008	168.10±0.07
	4.93	0.5812±0.0004	0.3906±0.0009	157.42±0.06
	5.37	0.6344±0.0004	0.4923±0.0009	147.46±0.05
	5.85	0.7004±0.0003	0.6759±0.0010	135.69±0.04
	6.24	0.7667±0.0002	0.9675±0.0011	124.08±0.03
	6.48	0.8183±0.0001	1.3474±0.0013	115.26±0.02
50	0.34	0.0105±0.0012	0.0018±0.0005	267.83±0.10
	1.04	0.0616±0.0011	0.0097±0.0005	256.00±0.10
	1.66	0.1055±0.0010	0.0238±0.0006	247.44±0.09
	2.08	0.1345±0.0010	0.0335±0.0006	241.68±0.09
	2.84	0.1844±0.0009	0.0538±0.0006	232.23±0.09
	3.79	0.2437±0.0008	0.0823±0.0006	221.16±0.08
	4.69	0.2986±0.0007	0.1110±0.0006	210.54±0.07
	5.66	0.3531±0.0006	0.1461±0.0006	200.32±0.07

	6.67	0.4090±0.0006	0.1930±0.0006	190.47±0.06
	7.86	0.4745±0.0005	0.2597±0.0006	178.85±0.05
	9.01	0.4662±0.0004	0.3350±0.0006	168.16±0.05
	9.95	0.5884±0.0004	0.4253±0.0007	158.50±0.04
	10.89	0.6465±0.0003	0.5532±0.0007	148.35±0.04
	11.74	0.6974±0.0003	0.7022±0.0008	139.18±0.03
	12.40	0.7486±0.0002	0.9161±0.0008	130.16±0.03
75	0.51	0.0087±0.0008	0.0027±0.0004	273.83±0.08
	0.82	0.0203±0.0008	0.0038±0.0004	270.95±0.08
	1.33	0.0409±0.0007	0.0082±0.0004	266.43±0.08
	2.04	0.0715±0.0007	0.0185±0.0004	260.61±0.08
	2.79	0.1035±0.0006	0.0290±0.0004	254.29±0.08
	3.64	0.1355±0.0006	0.0411±0.0004	248.15±0.07
	4.48	0.1670±0.0006	0.0540±0.0005	242.11±0.07
	5.26	0.1963±0.0005	0.0671±0.0005	236.54±0.07
	6.34	0.2354±0.0005	0.0829±0.0005	228.44±0.07
	7.63	0.2818±0.0004	0.1101±0.0005	220.03±0.06
	8.96	0.3235±0.0004	0.1350±0.0005	211.68±0.06
	10.26	0.3644±0.0005	0.1634±0.0005	203.65±0.05
	11.46	0.4014±0.0005	0.1963±0.0005	197.06±0.05
	12.68	0.4345±0.0005	0.2300±0.0005	191.28±0.05
	13.99	0.4722±0.0005	0.2679±0.0005	183.92±0.05
	17.57	0.5687±0.0003	0.3962±0.0005	165.64±0.04
	21.60	0.6928±0.0002	0.6374±0.0006	138.58±0.03
	22.91[vLL]	0.8804±0.0002		
	92.29[cp]	0.9628±0.0001		

[a] $\frac{\Delta V}{V_0} = \frac{V_m(T,P,x_i) - V_{IL}(T,P=1bar)}{V_{IL}(T,P=1bar)}$;

cp= mixture critical point;

[vLL]= vapor-liquid-liquid equilibrium points for the IL-rich phase.

Table 5.5 The parameters and results of EoS modeling

ILs + R-134a	Temperature [° C]	Exp. Data Points	Interaction Parameters		AARD%
			k_{12}	l_{12}	
[EMIm][Tf_2N]	25	14	0.0201	0.0140	7.41
	50	14	0.0074	0.0089	3.95
	75	17	-0.0058	0.0054	3.11

The molar volume data of [EMIm][Tf_2N] and R-134a are listed in Table 5.4. Figures 5.9 and 5.10 present the molar volume data of [EMIm][Tf_2N] and R-134a with pressure and mole fraction. The liquid mixture molar volume decreases linearly with R-134a pressure due to the increased solubility of R-134a and it is independent of temperature. The slope of liquid molar volume with pressure increases when temperature decreases. However, the relation between the molar volume and the mole fraction is linear and independent of temperature as shown in Figure 5.6. This trend has also been demonstrated by Shiflett and Yokozeki [2] for a given ionic liquid and hydrofluorocarbons. The volume expansion data of [EMIm][Tf_2N] and R-134a are listed in Table 5.4 and shown in Figure 5.11, which shows similar trend as [HMIm][Tf_2N] and R-134a.

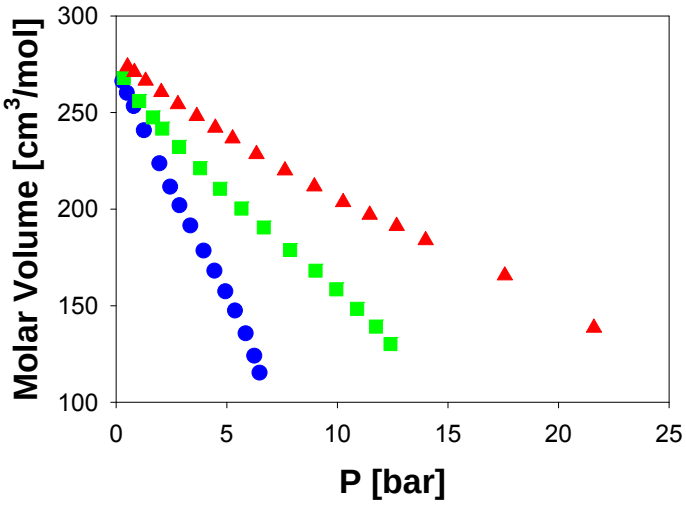

Figure 5.9 Experimental molar volume data for [EMIm][Tf_2N] and R-134a. Legend: ●:25°C; ■:50°C ▲:75°C.

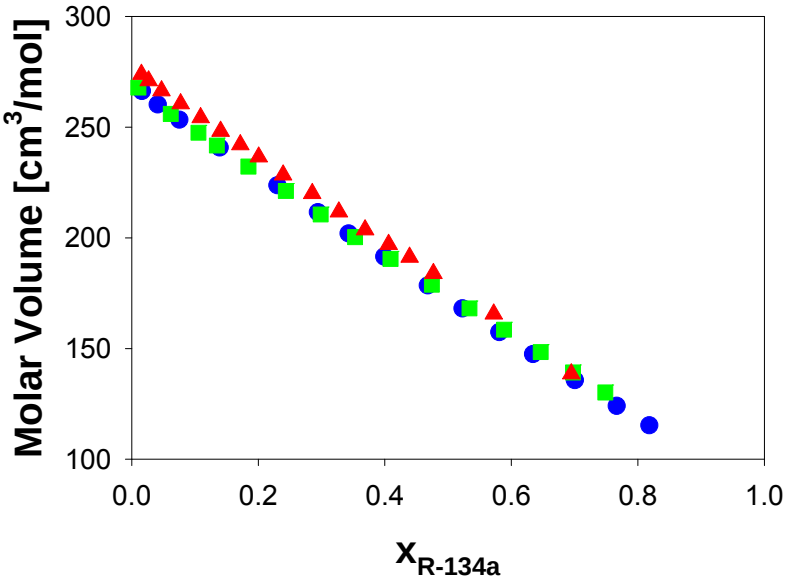

Figure 5.10 Experimental molar volume data for [EMIm][Tf_2N] and R-134a. Legend: ●:25°C; ■:50°C ▲:75°C.

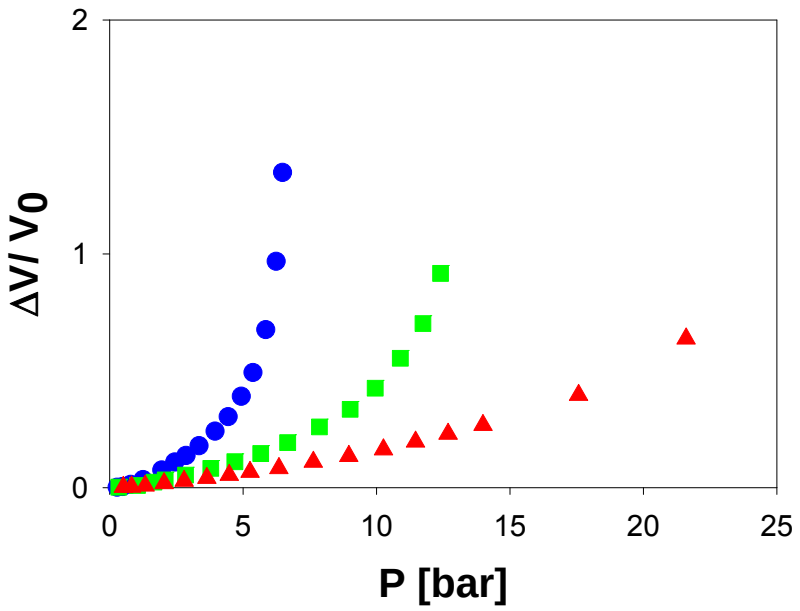

Figure 5.11 Experimental volume expansion data for [EMIm][Tf_2N] and R-134a. Legend: ●:25°C; ■:50°C ▲:75°C.

5.3.3 The cation alkyl- length effect on R-134a solubility in imidazolium ILs

The effect of the length of the cation alkyl- group on the R-134a solubility is investigated for the same anion: [Tf_2N]. As shown in Figure 5.12, if the alkyl length is increased from [EMIm] to [HMIm], the solubility of R-134a is only slightly increased. The hexyl- group increases the dispersion forces of the cation for better interaction with R-134a. Shiflett and Yokozeki [3] measured difluoromethane(R-32) solubility in a series ILs, and for the case where the novel [TFES] anion remains the same, the order of solubility R-32 and the cations was [HMIm] ~ [DMIm] > [BMIm] > [EMIm]. Aki *et al.* [30] compared the solubility of CO_2 in [BMIm][Tf_2N],

[HMIm][Tf_2N], and [OMIm][Tf_2N] at 25 °C, 40 °C, and 60 °C. They reported that the CO_2 solubility in ILs can be increased by increasing alkyl chain length.

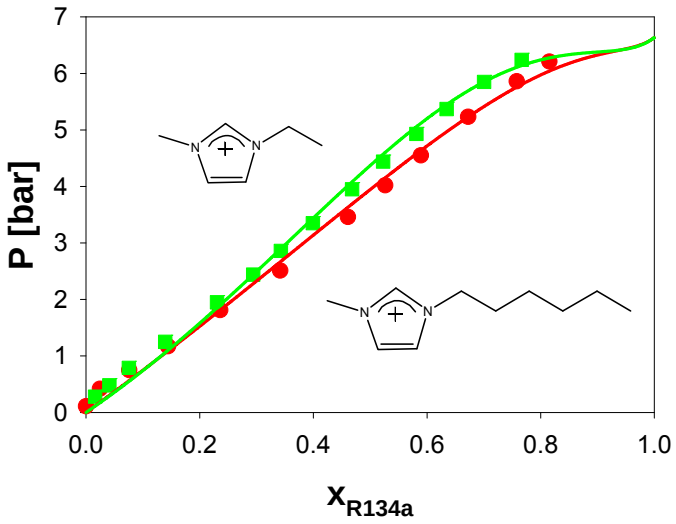

Figure 5.12 Alkyl chain effect of experimental vapor liquid equilibrium data and modeling results for [HMIm][Tf_2N] /[EMIm][Tf_2N] and R-134a at 25°C. Legend: ●:[HMIm][Tf_2N]; ■:[EMIm][Tf_2N]; Solid lines are modeling VLE

5.3.4 Phase equilibria of [HMIm][BF_4]/R-134a & [HMIm][PF_6]/R-134a

The phase equilibrium data and modeling results for [HMIm][BF_4]/R-134a and [HMIm][PF_6]/R-134a at 25 °C, 50 °C and 75 °C are shown in Table 5.6, Figures 5.13 and 5.14 respectively.

Table 5.6 Vapor liquid equilibrium experimental data and mixture critical points of R-134a and ILs

T [° C]	P [bar]	$x_{R\text{-}134a}$	$\Delta V/V^0$ a	V_L [cm^3/mol]
[HMIm][BF_4]				
25	0.81	0.0438±0.0024	0.0169±0.0009	226.05±0.14
	1.56	0.1305±0.0020	0.0444±0.0009	211.09±0.13
	2.42	0.2236±0.0016	0.0846±0.0010	195.75±0.12
	4.22	0.4156±0.0010	0.2026±0.0010	163.38±0.09
	5.12	0.5222±0.0007	0.3362±0.0011	148.44±0.07
50	0.86	0.0308±0.0023	0.0021±0.0009	227.35±0.15
	1.70	0.0761±0.0022	0.0055±0.0009	217.45±0.14
	3.50	0.1768±0.0018	0.0467±0.0010	201.70±0.13
	f5.30	0.2734±0.0015	0.1024±0.0010	187.48±0.11
	7.68	0.3953±0.0012	0.2009±0.0010	169.98±0.09
	10.60	0.5737±0.0007	0.4459±0.0012	144.27±0.07
	12.27	0.7071±0.0003	0.8315±0.0014	125.57±0.05
	12.75^{vll}	0.7766±0.0002		
	46.4^{cp}	0.8904±0.0002		
75	6.12	0.0000±0.0049	0.012±0.002	209.3±0.3
	9.86	0.2006±0.0043	0.062±0.002	188.1±0.3
	13.44	0.3155±0.0036	0.124±0.002	166.0±0.2
	16.62	0.4292±0.0030	0.213±0.002	149.5±0.2
	19.70	0.5235±0.0025	0.333±0.002	136.7±0.1
	23.24^{vLL}	0.8291±0.0015		
	143.30^{cp}	0.9631±0.0003		

[HMIm][PF_6]				
25	0.81	0.0594±0.0000	0.010±0.001	244.03±0.23
	1.33	0.1242±0.0042	0.023±0.001	230.31±0.22
	2.2	0.2116±0.0037	0.060±0.001	214.82±0.19
	3.04	0.3093±0.0031	0.081±0.001	191.84±0.17
	4.29	0.4529±0.0024	0.179±0.001	165.74±0.13
	5.76	0.6507±0.0016	0.508±0.001	135.42±0.09
50	0.89	0.0295±0.0027	0.003±0.001	257.07±0.17
	1.77	0.0739±0.0025	0.009±0.001	246.77±0.16
	3.40	0.1659±0.0021	0.032±0.001	227.48±0.15
	5.12	0.2723±0.0017	0.079±0.001	207.45±0.13
	6.65	0.3544±0.0015	0.115±0.001	190.15±0.11
	8.10	0.4238±0.0013	0.170±0.001	178.12±0.10
	9.21	0.4809±0.0011	0.226±0.001	168.13±0.09
	10.77	0.5856±0.0008	0.370±0.001	150.00±0.07
	11.93	0.6683±0.0005	0.559±0.001	136.66±0.06
	12.83	0.7677±0.0002	0.978±0.001	121.40±0.04
75	6.23	0.1997±0.0045	0.005±0.002	238.9±0.3
	10.11	0.3231±0.0038	0.059±0.002	212.8±0.2
	13.48	0.4330±0.0032	0.119±0.002	188.4±0.2
	17.13	0.5437±0.0025	0.210±0.002	164.0±0.2
	20.57	0.6368±0.0020	0.360±0.002	146.6±0.1
	23.22[vll]	0.8262±0.0012		
	128.8[cp]	0.9572±0.0015		

a $\frac{\Delta V}{V_0} = \frac{V_m(T,P,x_i) - V_{IL}(T,P=1bar)}{V_{IL}(T,P=1bar)}$;

[cp]= mixture critical point;

[vLL] = vapor-liquid-liquid equilibrium points for the IL-rich phase.

Table 5.7 The parameters and results of EoS modeling

ILs + R-134a	Temperature [° C]	Exp. Data Points	Interaction Parameters		AARD%
			k_{12}	l_{12}	
[HMIm][BF_4]	25	5	0.0631	-0.0037	5.30
	50	7	0.0894	0.0155	5.36
	75	5	0.0972	0.0280	1.90
[HMIm][PF_6]	25	6	0.0218	-0.0040	2.74
	50	10	0.0875	0.0154	5.97
	75	5	0.0873	0.0145	2.05

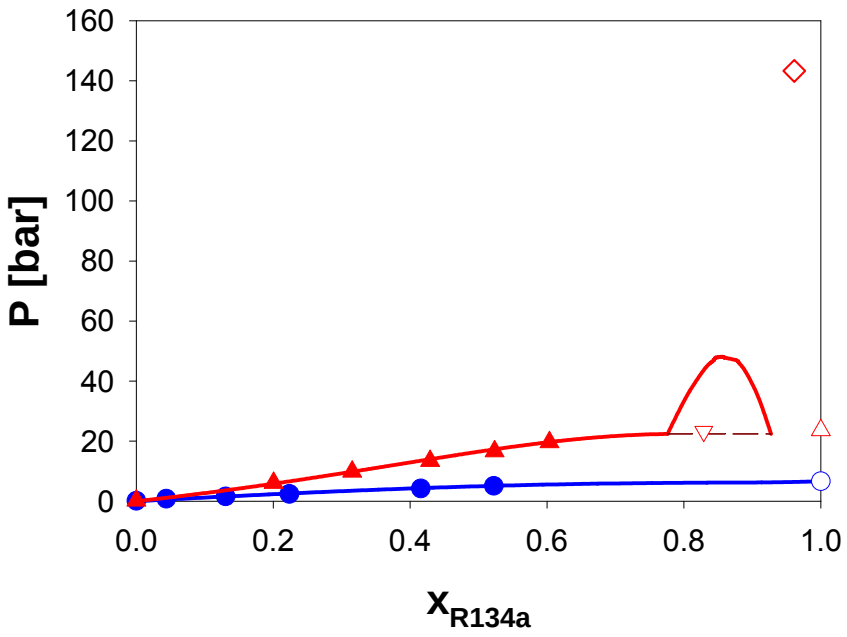

Figure 5.13 Experimental vapor liquid equilibrium data and modeling results for [HMIm][BF_4] and R-134a. See caption of Figure 5.3 for description of symbols.

For [HMIm][BF_4], the lower-critical endpoint is at approximately 37.8°C. Therefore, VLE exists for the system at 25°C till the vapor pressure of R-134a where the mixture becomes completely miscible. However, the isotherms of 50 °C and 75°C are above the LCEP and below the UCEP for this system and multiple phases can exist, such as VLE, VLLE, LLE, and mixture critical points. Only the data and modeling results at 25° and 75 °C are shown in the plot for clarity. The experimental mixture critical point for [HMIm][BF_4]/R-134a system at 75°C is at 143.3 bar and 96.1% mole R-134a. The critical pressure is about 100 bar higher than that of [HMIm][Tf_2N]. For [HMIm][PF_6], the lower-critical endpoint is at 48.3°C, and the isotherms at 50°C and 75°C have regions of multi-phase phenomena. The experimental mixture critical point for [HMIm][PF_6]/R-134a system at 75°C is at 128.8 bar and 95.7% mole R-134a.

The binary interaction parameters and modeling results of [HMIm][BF_4]/R-134a and [HMIm][PF_6]/R-134a are given in Table 5.7, Figures 5.13 and 5.14. Results reveal a good agreement between the model and the vapor-liquid equilibrium data at 25°C and 75°C for both [HMIm][BF_4]/R-134a and [HMIm][PF_6]/R-134a. However, the predicted compositions at the VLLE pressure for the IL-rich phase are lower than experimental data for both ILs. For [HMIm][BF_4]/R-134a system at 75°C, the model predicts the VLLE at 22.4 bar with R-134a compositions of 77.6%, but the experimental data is 23.2 bar with compositions of 82.9% mole R-134a. For [HMIm][PF_6]/R-134a system at 75°C, the experimental data in IL-rich phase is 23.2 bar with compositions of 82.6%mole R-134a, while the model prediction is about

22.8 bar and 76.6% mole percent of R-134a. The predicted compositions of the R-134a-rich liquid phase shows significant and unrealistic quantities of the IL (5+% mole of the IL) for both the [HMIm][BF_4] and [HMIm][PF_6]. The measurement of the IL in the R-134a rich liquid phase and the subsequent liquid-liquid equilibrium would allow better EoS parameter regression to improve the model performance over more pressure-composition regions.

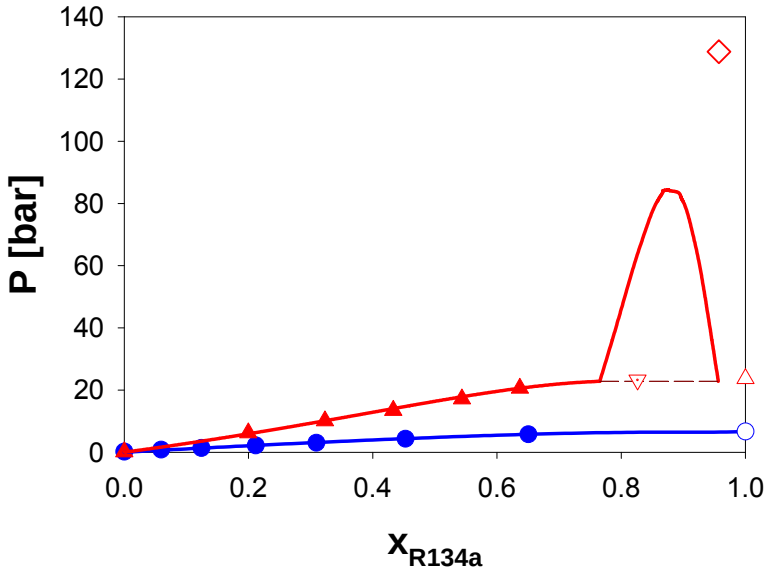

Figure 5.14 Experimental vapor liquid equilibrium data and modeling results for [HMIm][PF_6] and R-134a. See caption to Figure 5.3 for description of symbols.

Using the parameters regressed from the VLE data, the model under-predicts the mixture critical points compared to the experimental data. For the [HMIm][BF_4]/R-134a system, the experimental data is 143.3 bar and 96.1 % model fraction of R-134a, which is about 95.2 bar higher on pressure and 10.5% higher mole

fraction than predictions. For [HMIm][PF_6]/R-134a system, the experimental data of the mixture critical pressure is about 44 bar higher and the composition is about 8% mole higher due to the limitations of EoS as mentioned previously.

5.3.5 The anion effect on R-134a solubility, volume expansion and molar volume

The ionic liquids investigated have the same cation, [HMIm]. Therefore, the effects of the anion can be compared for [Tf_2N], [BF_4], and [PF_6]. Figure 5.15 illustrates the experimental solubility and modeling of each IL at 25°C. As shown, the solubility of R-134a in [HMIm][Tf_2N] at a particular pressure is remarkably higher than that of [HMIm][PF_6] and [HMIm][BF_4]. The solubility of R-134a in [HMIm][PF_6] is slightly higher than that in [HMIm][BF_4]. The trend is consistent with the measured LCEP temperature of these system which are in the order of [Tf_2N]>[PF_6]>[BF_4] [18]. Aki *et al.* [30] measured the solubility of CO_2 in [BMIm] cation based imidazolium ILs, the solubility increases in the following order: [NO_3] < [DCA] < [BF_4] ~ [PF_6] < [TfO] < [Tf_2N] <[methide]. Shiflett and Yokozeki [2] measured the solubility of R-32 in [BMIm][PF_6] and [BMIm][BF_4], and [PF_6] shows higher solubility than [BF_4], which is consistent with this work. This trend seems to scale with the diameter of the anion or charge density as larger anions can have more disperse negative charge. Ions with more disperse charge can more readily be solvated by some of the polar hydrofluorocarbons, and thus become miscible at lower temperatures and pressures.

The volume expansion and the molar volume of the ionic liquid phase were measured for each of the ionic liquids. Figure 5.16 illustrates the volume expansion

for all three ionic liquids at 50°C and is plotted with the mole fraction composition of R-134a rather than pressure. Figure 5.16 demonstrates relatively large volume expansion in these systems. For instance at 50°C and 11.9 bar (~76.4% R-134a), the volume expansion of [HMIm][Tf_2N] approaches approximately 79% from the initial volume with no R-134a dissolved. This is significantly more than the volume expansion experienced at the same concentration of dissolved CO_2 and the same temperature, which is approximately 35% expansion [35]. At the same composition of R-134a, the volume expansion increases in the order of [Tf_2N]< [PF_6]< [BF_4], which is the reverse of the solubility at constant pressure.

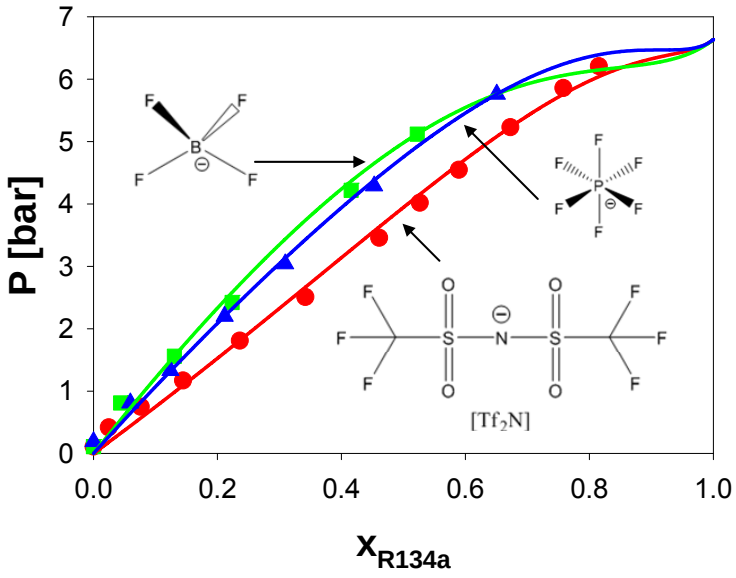

Figure 5.15 Anion effects of experimental vapor liquid equilibrium data and modeling results for [HMIm][Tf_2N],[HMIm][BF_4],[HMIm][PF_6] and R-134a at 25°C. Legend: ●:[HMIm][Tf_2N]; ■:[HMIm][BF_4];▲: [HMIm][PF_6]; Solid lines are modeling VLE.

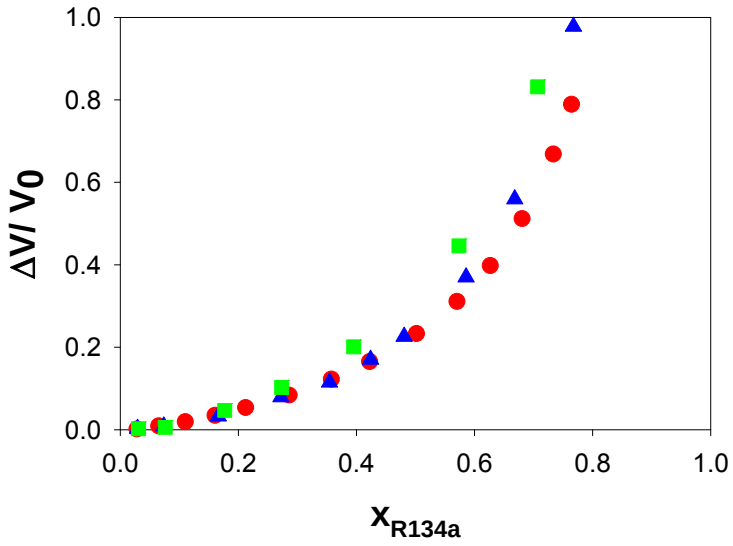

Figure 5.16 Anion effects of experimental volume expansion for [HMIm][Tf_2N], [HMIm][BF_4], [HMIm][PF_6] and R-134a at 50°C. Legend: ●:[HMIm][Tf_2N]; ■:[HMIm][BF_4];▲: [HMIm][PF_6].

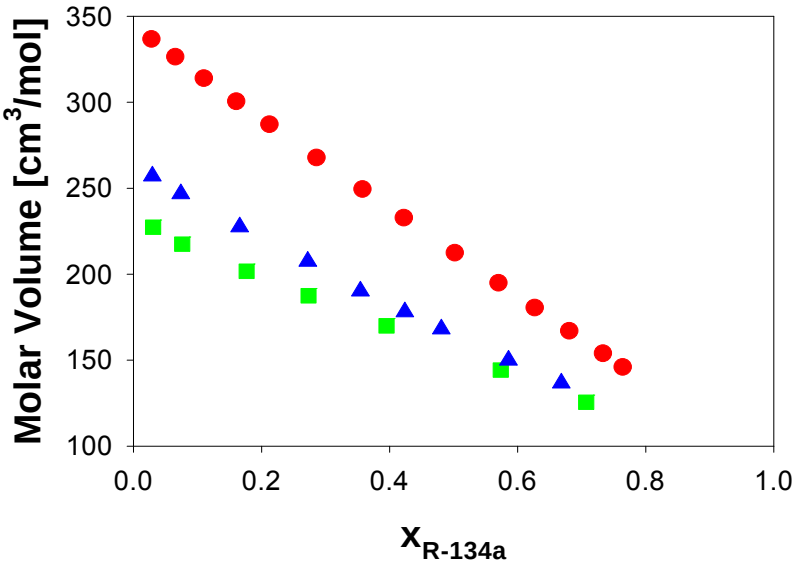

Figure 5.17 Anion effects of experimental molar volume for [HMIm][Tf_2N], [HMIm][BF_4],[HMIm][PF_6] and R-134a at 50°C. Legend: ●:[HMIm][Tf_2N]; ■:[HMIm][BF_4];▲: [HMIm][PF_6].

Figure 5.17 illustrates the molar volume for all three of the ionic liquids at 50°C and again plotted with composition. The molar volume of the ionic liquids decreases almost linearly with increasing concentration of the R-134. For a given ionic liquid with hydrofluorocarbons, Shiflett and Yokozeki [36] have demonstrated that the *molar volume* changes normalized to their pure component molar volume, i.e. $(\underline{V}_m - \underline{V}_0)/\underline{V}_0$, yield nearly the same line with composition for all isotherms. The molar volume accounts for effects of both volume and moles of liquid in the mixture. With pressure the solubility of gas in ionic liquids increase, thus the molar volume decrease with pressure or mole fraction of gases, which shows different trend with the absolute volume difference. Similar results were observed for these results. For these three ionic liquids, the molar volume at the same composition increases in the order of $[BF_4]<[PF_6]<[Tf_2N]$.

5.3.6 Conclusions

The phase equilibria of 1,1,1,2-tetrafluorethane (R-134a) with $[EMIm][Tf_2N]$, $[HMIm][Tf_2N]$, $[HMIm][PF_6]$, and $[HMIm][BF_4]$ were measured at 25°C, 50°C, and 75°C and pressures up to 143 bar. As these systems are Type V by the classification scheme of Scott and van Konynenburg,[29] regions of multiphase equilibria exist at the higher temperatures, *viz.* VLE, LLE, and VLLE. The anion has a more pronounced effect on the solubility of R-134a in the ILs increasing in the order of $[BF_4]<[PF_6]<<[Tf_2N]$. The mixture critical point at 75°C was the lowest in $[Tf_2N]$. Comparing $[HMIm][Tf_2N]$ with $[EMIm][Tf_2N]$, the solubility increases slightly with

the increase in the length of the alkyl- group on the cation. Significant volume expansion was observed in these systems with R-134a. The equilibria data were correlated using the PR EoS model with the van der Waals 2-parameter mixing rule (PR-vdW2) with predicted EoS parameters for the ionic liquids. The bubble-point data demonstrates an excellent agreement with the model. However, the predicted compositions of the VLLE transition to LLE were only satisfactorily predicted for all systems using the interaction parameters regressed from the VLE data alone. The mixture critical point pressures systematically under-predicted, although they are close to the experimental value of R-134a/[HMIm][Tf_2N].

5.4 High-Pressure Phase Equilibria of Carbon Dioxide (CO_2) + n-Alkyl-Imidazolium Bis(trifluoromethylsulfonyl)amide Ionic Liquids

The global phase behavior of ILs and CO_2 is illustrated in Chapter 4. This section describes the vapor-liquid, vapor-liquid-liquid and liquid-liquid equilibrium of 1-n-Alkyl-3-methyl-imidazolium bis(trifluoromethylsulfonyl)amide ionic liquids with alkyl groups of Ethyl-, n-Hexyl-, and n-Decyl- (see Figure 5.18) and compressed CO_2 were measured at 25 °C, 50 °C, 70 °C and pressures up to 250 bar. 1-Ethyl-3-methyl-imidazolium bis(trifluoromethylsulfonyl)amide ([EMIm][Tf_2N]), 1-Hexyl-3-methyl-imidazolium bis(trifluoromethylsulfonyl)amide ([HMIm][Tf_2N]) and 1-decyl-3-methyl-imidazolium bis(trifluoromethylsulfonyl) amide([DMIm][Tf_2N]) were chosen for study. Chapter 2 describes the synthesis procedure and analysis

results. The effect of alkyl chain length of the imidazolium cation on the VLE was quantified. PR-vdW2 EoS was used to correlate data with predicted critical properties.

5.4.1 Results and discussions

The VLE, VLLE of CO_2 and the ILs, [EMIm][Tf_2N], [HMIm][Tf_2N], and [DMIm][Tf_2N] were measured at 25°C, 50°C, and 70°C and pressures up to 250 bar. The volume expansion and the liquid molar volume were also measured for each IL at each isotherm. The PR-vdW2 EoS was employed to correlate the data to predict the VLE, VLLE, and mixture critical points. The details are given in Chapter 3. The results are discussed here. The physical critical points cannot be obtained experimentally due to decomposition at high temperature, The physical properties of ILs used in equation of state model in Table 5.6 were calculated from group contribution methods [37]. The binary interaction parameters with deviations between the predicted and experimental data are listed in Table 5.7.

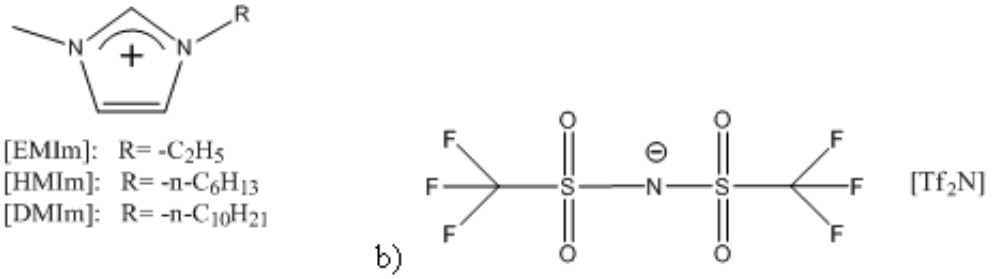

Figure 5.18 Ionic liquid cations and anions used in this study: a) IL cation structures; b) [Tf_2N] anion.

Table 5.6 lists the physical properties of ionic liquids and CO_2. The experimental VLE and LLE data of IL/CO_2 were correlated by PR-vdW2 using the

predicted critical point properties of the ionic liquids. The binary interaction parameters and modeling results are given in Table 5.7. The VLE, VLLE and LLE, volume expansion and molar volume (density) of carbon dioxide (CO_2) and the ionic liquids [EMIm][Tf_2N], [HMIm][Tf_2N], [DMIm][Tf_2N] were measured at 25 °C, 50 °C, and 70 °C and pressures up to 250 bar. The results are listed in Tables 5.8, 5.10 and 5.12.

Table 5.8 The physical property table of ionic liquids and CO_2

Component	Formula	Molecular Weight [g/mol]	Critical Temp. [K]	Critical Pressure [Bar]	Accentric Factor
[EMIm][Tf_2N]	$C_8H_{11}N_3F_6S_2O_4$	391.30	1244.9	32.6	0.1818
[HMIm][Tf_2N]	$C_{12}H_{19}N_3F_6S_2O_4$	447.41	1287.3	23.9	0.3539
[DMIm][Tf_2N]	$C_{16}H_{27}N_3F_6S_2O_4$	504.00	1345.1	18.7	0.5741
CO_2	CO_2	44.01	304.25	73.8	0.2280
Note:IL properties from Ref. [26,27]; The property data of CO_2 from Ref. [28]					

5.4.2 Phase equilibria of [HMIm][Tf_2N]/CO_2

The ionic liquid [HMIm][Tf_2N] has been chosen by IUPAC (Committee on the Thermodynamics of Ionic Liquids, Ionic Liquid Mixtures, and the Development of Standardized Systems) to be a reference IL for worldwide study [38]. The global phase behavior study in Chapter 4 shows that [Tf_2N] type ionic liquid and CO_2 belong to type III system according to the classification of Scott and van Konynenburg. [29] The VLE (bubble point) data for [HMIm][Tf_2N] and CO_2 was measured at 25 °C, 50 °C, and 70 °C and pressures up to 250 bar (shown in Figure 5.21). The isotherms at

50 °C and 70 °C are above the critical point of pure CO_2 and represent VLE throughout the pressure range measured. However as 25 °C is below the critical point of CO_2, a region of VLE exists at low pressures followed by a pressure at which VLLE exists. Here, the ionic liquid-rich phase is in equilibrium with a CO_2-liquid phase and a CO_2-vapor phase. Above the VLLE pressure is a region of liquid-liquid equilibrium (LLE). Aki *et al.* [30] and Shifflet and Yokozeki [39] also measured the CO_2 solubility at 25 °C in various pressure ranges as plotted in Figure 5.15. It can be observed that our data seems to smoothly connect the low pressure data of Shifflet and Yokozeki [39] with the medium-pressure VLE data of Aki *et al.* [30] to our higher pressure LLE data.

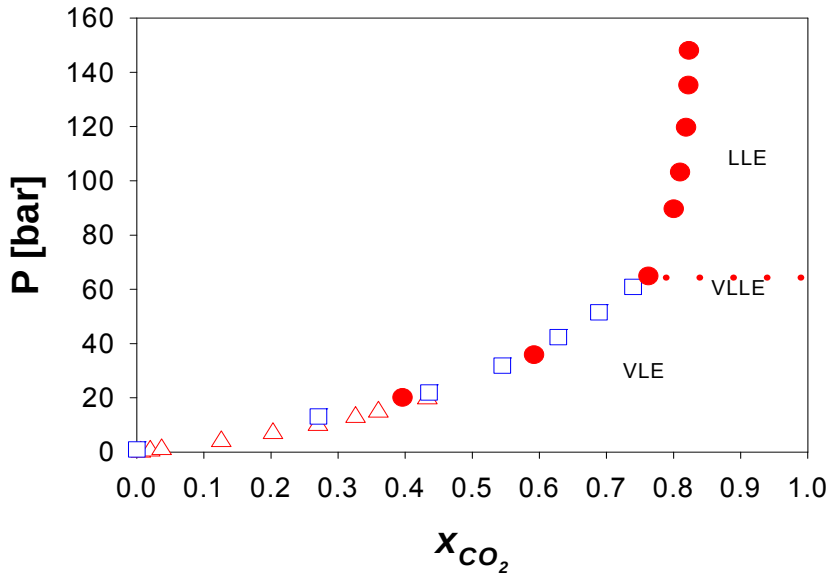

Figure 5.19 Comparison between the experimental phase equilibrium data and literature for [HMIm][Tf_2N] and CO_2 at 25 °C. Legend: □: Aki *et al.* [30]; Δ: Shifflet and Yokozeki [39]; ●: VLE and LLE data from this work.

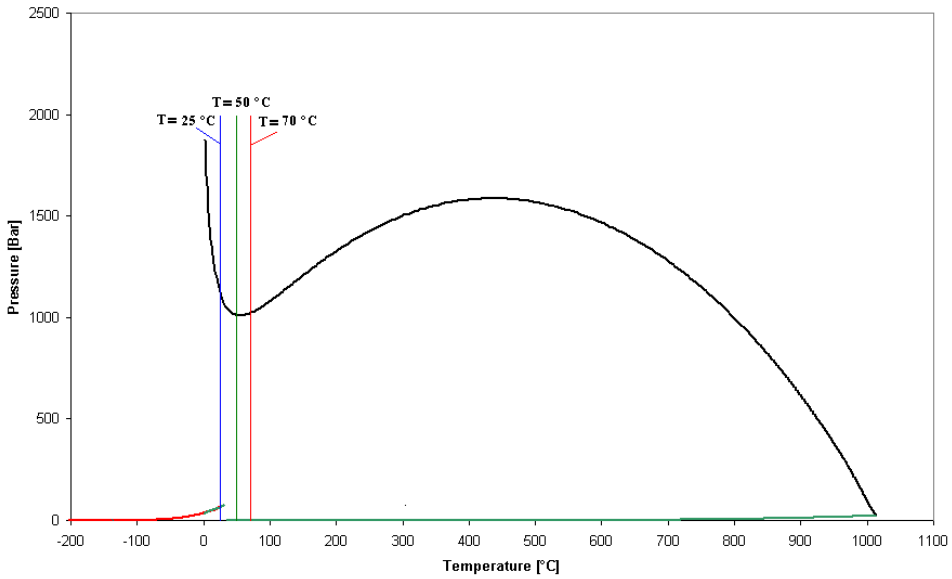

Figure 5.20 Global phase behavior for [HMIm][Tf_2N] and CO_2

Figure 5.20 illustrates the global phase behavior of [HMIm][Tf_2N] and CO_2 with three isothermals as predicted by the GPEC software using Peng-Robinson model and van der Waals mixing rules. The model details refer to Chapter 3. The interaction parameters used were obtained by correlating the vapor liquid equilibrium data. The details are given below. As shown, there are regions of 1-, 2-, and 3-phase equilibrium. At temperatures lower than UCEP (31.1°C), such as 25°C, four different equilibria are possible depending on the pressure. VLE exists at the pressures much lower than vapor pressure of CO_2, and VLLE exists near or at the pure CO_2 vapor pressure. At pressures above VLLE, liquid-liquid (LLE) equilibrium exists till the mixture critical point, beyond which the system becomes critical/miscible. The mixture critical points were predicted above 1000 bar, but the prediction may be low, as a similar ionic liquid, [BMIm][PF_6] does not become critical with CO_2 even to

3100 bar [40]. At temperatures higher than UCEP, such as 50°C and 70°C, vapor-liquid equilibrium exists until the system reaches the mixture critical curve at hyperbaric conditions, where the system becomes critical/miscible.

Table 5.9 The binary interaction parameters and modeling results for [HMIm][Tf_2N]and CO_2

ILs + CO_2	T [°C]	Number Data Points	Interaction Parameters		AARD%
			k_{12}	l_{12}	
[HMIm][Tf_2N]	25	7	0.0579	0.0826	6.17
	50	10	0.0299	0.0316	2.25
	75	8	0.0329	0.0054	5.93

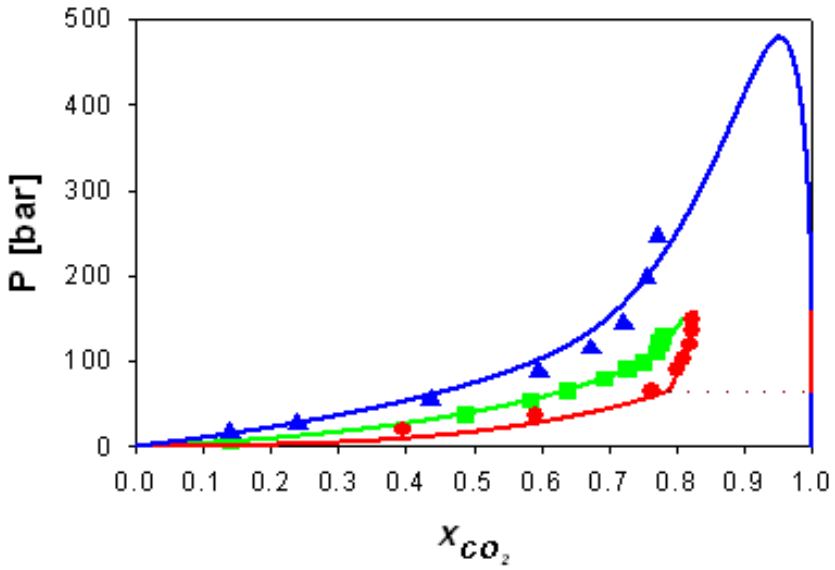

Figure 5.21 Experimental vapor-liquid, vapor-liquid-liquid and liquid-liquid equilibrium data and modeling results for [HMIm][Tf_2N] and CO_2. Legend: ●: 25 °C; ■: 50 °C; ▲: 70 °C; Solid lines are modeling and the dashed line is the predicted VLLE.

Figure 5.21 illustrates the experimental data and modeling results for all three isotherms. The binary interaction parameters and modeling results for [HMIm][Tf_2N]and CO_2 are given in Table 5.9. At 25 °C, the pressure of the VLLE transition is within experimental accuracy equal to the vapor pressure of pure CO_2 (64 bar [41]). This indicates that the solubility of the IL in the CO_2-rich liquid phase is very small. Shifflett and Yokozeki [42] measured the VLLE for ILs and compressed hydrofluorocarbon (HFC) gases and found nearly no IL in this polar liquid HFC. Technically, these systems may have a VLE region above the VLLE pressure at very high loadings of CO_2, but this was not experimentally confirmed. While not investigated here, the solubility of the ionic liquid into the vapor, liquid or supercritical CO_2-phases (dew, VLLE, or LLE points) is immeasurably small ($<<1\times10^{-7}$) as confirmed in the literature [43]. Han and coworkers [44] reported that approximately 30% mole of a polar co-solvent, *viz.* acetone, in supercritical CO_2 was required to obtain appreciable amounts of the IL in the CO_2 phase.

The VLE data and LLE at 298.15K were correlated using the PR-vdW2. The interaction parameters and modeling performance are listed in Table 5.10. As seen in Figure 5.21, the model has an excellent correlation of both the VLE and LLE at 25 °C and the VLE at 50 °C. The pressure of the VLLE transition is accurately correlated within 0.58 bar, and the predicted CO_2 composition in the IL-rich phase is approximately 0.03% mole higher than the experimental value at 25 °C. At 70 °C, the model adequately correlates the VLE data below 100 bar, but has more difficulties between 100 and 250 bar. The model also predicts finite dew points and IL solubility

in liquid CO_2 (see Figure 5.21); for example at 70 °C and 174 bar, the mole fraction of IL in the CO_2 phase is predicted to be 0.13 %. This is at least 4 orders of magnitude higher than the precision of most estimates ($>10^{-7}$) [43] and thus not physically realistic. In addition, the model predicts a mixture critical point at approximately 479 bar at 70 °C and 5% [HMIm][Tf_2N]. This result is qualitatively incorrect as ILs have no known critical points with CO_2. Brennecke and coworkers [40] observed no critical point in the [BMIm][PF_6]/CO_2 system to 3100 bar at 40 °C .

This predicted mixture critical point is believed to be an artifact of the EoS model and the predicted critical properties of the IL. Overall, the model provides a good correlation for the bubble-point data in the pressure range of the measurements (<250 bar), but predicts physically unrealistic dew-points, IL in liquid CO_2 solubility, and mixture critical point data. Extrapolation of the model beyond the data pressure region, in which the interaction parameters were fit, is not recommended. As such, these types of model predictions will be omitted from subsequent models of the other systems measured.

The liquid molar volume and the volume expansion were measured for this system at the three isotherms (Table 5.10). As shown in Figure 5.23, Ionic liquids have relatively little volume expansion with dissolved CO_2 compared with CO_2-expanded organic liquids [45] and the maximum volume expansion compared to the ambient pressure volume was 50% at 25 °C and approximately 150 bar.

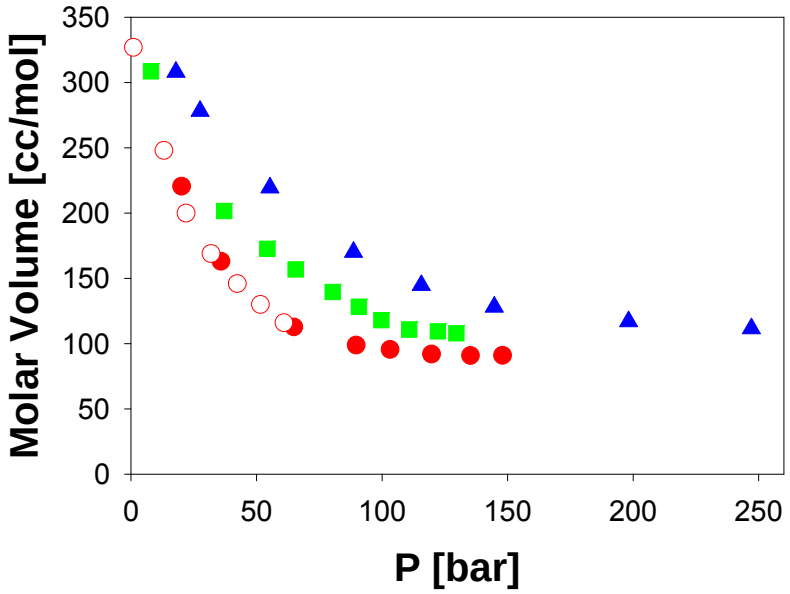

Figure 5.22 Molar volume for [HMIm][Tf_2N] and CO_2 at 25 °C (●); 50 °C (■); 70 °C (▲). Data from Aki et al. [28] at 298.15 K (○).

Figure 5.22 illustrates significant decrease in liquid molar volume with pressure (CO_2 composition) at the three isotherms. Aki *et al.* [30] also measured the liquid molar volumes for this system at 25 °C and their data is shown for comparison. The molar volume data of this study demonstrate an excellent agreement with those of the literature.

Table 5.10 Vapor-liquid, vapor-liquid-liquid, liquid-liquid equilibrium, volume expansion and molar volume of CO_2 and ILs experimental data

T [°C]	P [bar]	x_{CO2}	$\Delta V/V_0$ [a]	V_L [cm^3/mol]
[HMIm][Tf_2N]				
25	20.15	0.396±0.001	0.0673±0.0005	220.54±0.07
	35.86	0.592±0.001	0.1680±0.0005	163.03±0.04
	64.89[vll]	0.762±0.002	0.3870±0.0005	112.72±0.03
	89.67[ll]	0.800±0.001	0.4461±0.0006	98.83±0.02
	103.21[ll]	0.810±0.001	0.4676±0.0006	95.56±0.02
	119.69[ll]	0.819±0.001	0.4833±0.0006	91.98±0.02
	135.25[ll]	0.822±0.002	0.4926±0.0006	90.84±0.02
	148.04[ll]	0.823±0.002	0.5009±0.0006	90.95±0.02
50	8.00	0.139±0.001	0.0156±0.0004	308.25±0.09
	37.16	0.487±0.002	0.1131±0.0005	201.35±0.05
	54.30	0.583±0.002	0.1718±0.0005	172.49±0.04
	65.60	0.637±0.002	0.2253±0.0005	156.76±0.04
	80.39	0.692±0.002	0.2858±0.0005	139.52±0.03
	90.78	0.726±0.002	0.3252±0.0005	128.23±0.03
	99.69	0.751±0.002	0.3449±0.0005	118.03±0.03
	110.81	0.769±0.002	0.3611±0.0005	110.77±0.02
	122.24	0.774±0.002	0.3736±0.0005	109.43±0.02
	129.59	0.779±0.002	0.3855±0.0005	107.93±0.02
70	17.93	0.140±0.001	0.0316±0.0004	308.08±0.08
	27.54	0.239±0.001	0.0525±0.0004	278.17±0.07
	55.37	0.436±0.001	0.1204±0.0004	219.42±0.06
	88.61	0.596±0.002	0.2122±0.0004	170.13±0.04
	115.60	0.673±0.003	0.2760±0.0005	144.75±0.03
	144.69	0.721±0.002	0.3253±0.0005	128.16±0.03
	198.18	0.755±0.001	0.3753±0.0005	116.91±0.02
	247.08	0.771±0.001	0.4032±0.0005	111.52±0.02

[a] Volume expansion: $\frac{\Delta V}{V_0} = \frac{V^L(T,P) - V_0(T,P=1bar)}{V_0(T,P=1bar)}$; [ll]= liquid-liquid equilibrium points for the IL-rich phase; [vll] = vapor-liquid-liquid equilibrium point with composition for IL-rich liquid phase.

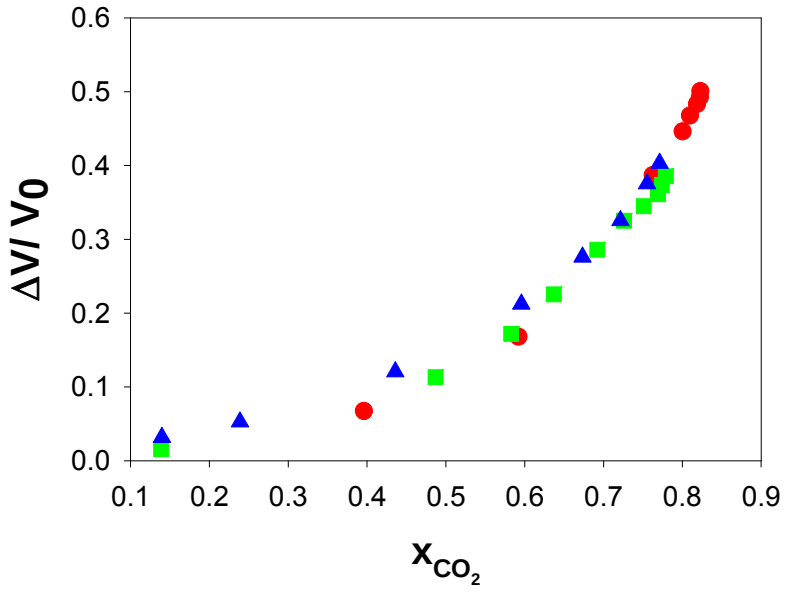

Figure 5.23 Volume expansion for [HMIm][Tf_2N] and CO_2 at 25 °C (●); 50 °C (■); 70 °C (▲).

5.4.3 Phase equilibria of [EMIm][Tf_2N]/CO_2

The vapor-liquid equilibrium data for [EMIm][Tf_2N] and CO_2 were measured to investigate the effect of a short alkyl chain-methyl-imidazolium cation on CO_2 solubility. The data with three isotherms are given in Table 5.11. Carvalho *et al.* [1] and Schilderman *et al.* [15] have investigated several points of the same system. The data comparison at 70 °C is shown in Figure 5.24. The data show a good agreement to approximately 80 bar and then the data of Carvalho *et al.* [1] seems to have a slightly lower CO_2 solubility at the highest pressure.

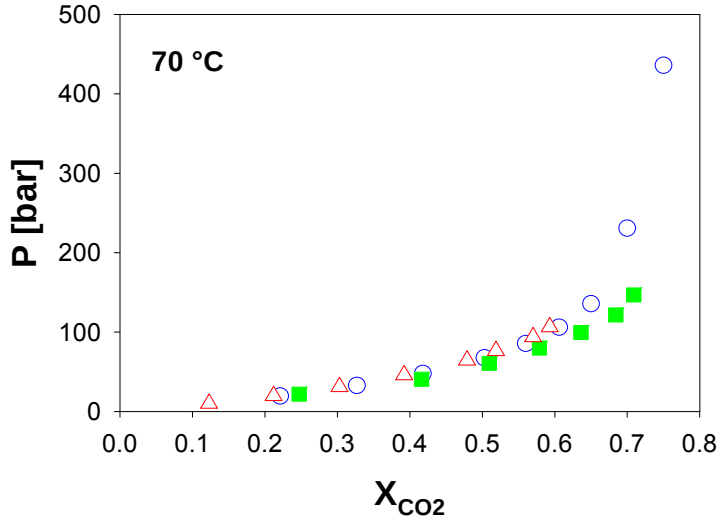

Figure 5.24 Comparisons between our experimental vapor liquid equilibrium data and literature data for [EMIm][Tf_2N] and CO_2 at 70°C.Legend: ○: Carvalho et al. [1]. Δ: Schilderman et al. [6, 15]■: data from this work.

The experimental data of [EMIm][Tf_2N]/CO_2 were correlated by the PR-vdW2 model. As shown in Figure 5.24 and Table 5.11, a good agreement is obtained between the model and the experimental data at all isotherms and pressures investigated for the VLE, LLE and also the VLLE. In addition, the model predicts a mixture critical point at approximately 408 bar at 70 °C and 7% [EMIm][Tf_2N], which is much smaller than reported experimental data.

Figure 5.26 illustrates liquid molar volume with pressure (CO_2 composition) at the three isotherms for [EMIm][Tf_2N] and CO_2. The molar volume data and volume expansion data display similar trends as the [HMIm][Tf_2N]/CO_2 system.

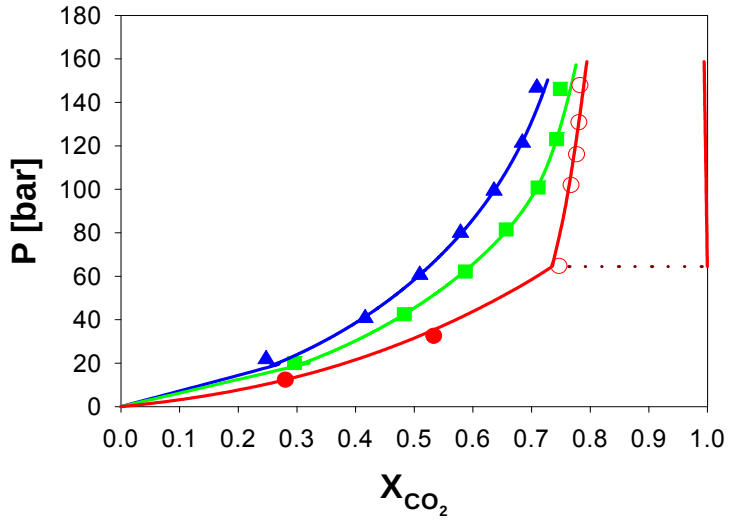

Figure 5.25 Experimental vapor liquid, liquid liquid equilibrium data and modeling results for [EMIm][Tf_2N] and CO_2.Legend: ●:25°C; ■:50°C ▲:70°C, ○:LLE data at 25°C. Solid lines are modeling VLE and LLE, dash line is VLLE.

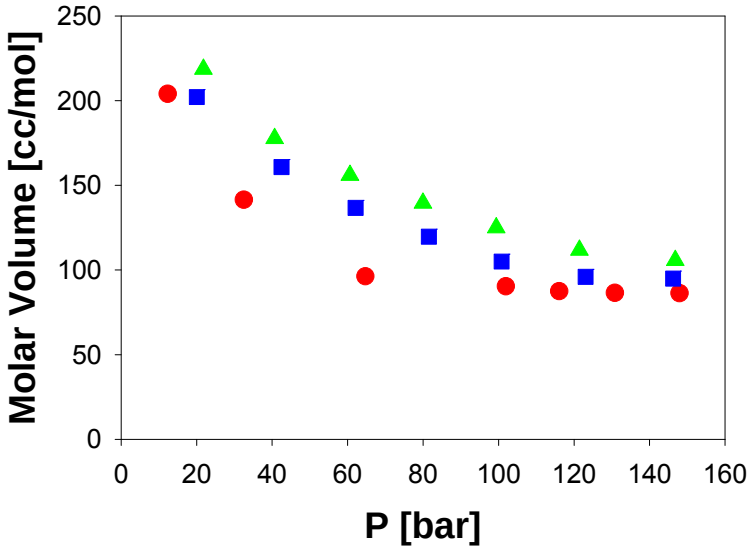

Figure 5.26 Molar volume data for [EMIm][Tf_2N] and CO_2 at 25°C, 50°C, 70°C. Legend: ●:25°C; ■:50°C ▲:70°C

Table 5.11 The binary interaction parameters and modeling results of [EMIm][Tf_2N] and CO_2

ILs + CO_2	T [°C]	Number Data Points	Interaction Parameters		AARD%
			k_{12}	l_{12}	
[EMIm][Tf_2N]	25	8	0.0571	0.0363	1.49
	50	7	0.0418	0.0409	1.42
	75	7	0.0288	0.0432	1.94

5.4.4 Phase equilibria of [DMIm][Tf_2N]/CO_2

The vapor-liquid equilibrium, liquid-liquid equilibrium, volume expansion and molar volume for the [DMIm][Tf_2N] and CO_2 system were measured at 25 °C, 50 °C, 70 °C. The data are given in Table 5.13. This is the first high-pressure VLE measurement of this IL with CO_2. This IL will help determine the effects of a long alkyl chain-methyl-imidazolium cation on CO_2 solubility.

The experimental data of [DMIm][Tf_2N]/CO_2 were correlated by the PR-vdW2 model. The binary interaction parameters and modeling results are given in Table 5.13. Figure 5.27 and Table 5.13 reveal a good agreement between the model and the experimental data at all isotherms and pressures investigated for the VLE, LLE and also the VLLE. In addition, the model predicted a mixture critical point at approximately 343 bar at 70 °C and 3% [DMIm][Tf_2N]. Similar to [HMIm][Tf_2N] and [EMIm][Tf_2N], this prediction does not match the reported experimental data.

Table 5.12 Vapor-liquid, vapor-liquid-liquid, liquid-liquid equilibrium, volume expansion and molar volume of CO_2 and ILs experimental data

T [°C]	P [bar]	x_{CO2}	$\Delta V/V_0$ [a]	V_L [cm3/mol]
[EMIm][Tf_2N]				
25	12.35	0.280±0.001	0.0533±0.0005	204.04±0.06
	32.54	0.533±0.001	0.1265±0.0005	141.50±0.04
	64.71[VII]	0.747±0.001	0.4108±0.0006	96.22±0.02
	101.94[II]	0.767±0.002	0.4424±0.0006	90.34±0.02
	116.08[II]	0.777±0.002	0.4554±0.0006	87.47±0.02
	130.84[II]	0.781±0.002	0.4643±0.0006	86.46±0.02
	147.94[II]	0.782±0.002	0.4725±0.0006	86.25±0.02
50	20.05	0.302±0.002	0.0573±0.0005	202.11±0.07
	42.50	0.483±0.002	0.1352±0.0005	160.73±0.05
	62.13	0.587±0.002	0.2084±0.0006	136.68±0.04
	81.56	0.657±0.002	0.2727±0.0006	119.67±0.03
	100.81	0.711±0.002	0.3254±0.0006	104.93±0.03
	123.07	0.743±0.002	0.3618±0.0006	95.97±0.02
	146.25	0.749±0.003	0.3797±0.0006	94.92±0.02
70	21.82	0.247±0.002	0.0394±0.0004	218.63±0.07
	40.70	0.416±0.002	0.0890±0.0005	177.66±0.05
	60.63	0.509±0.002	0.1371±0.0005	155.89±0.04
	79.99	0.579±0.002	0.1843±0.0005	139.43±0.04
	99.38	0.636±0.002	0.2279±0.0005	124.91±0.03
	121.43	0.684±0.003	0.2654±0.0005	111.69±0.03
	146.82	0.709±0.003	0.2986±0.0005	105.59±0.02

[a] Volume expansion: $\frac{\Delta V}{V_0} = \frac{V^L(T,P) - V_0(T, P = 1bar)}{V_0(T, P = 1bar)}$; [II]= liquid-liquid equilibrium points for the IL-rich phase; [vll] = vapor-liquid-liquid equilibrium point with composition for IL-rich liquid phase.

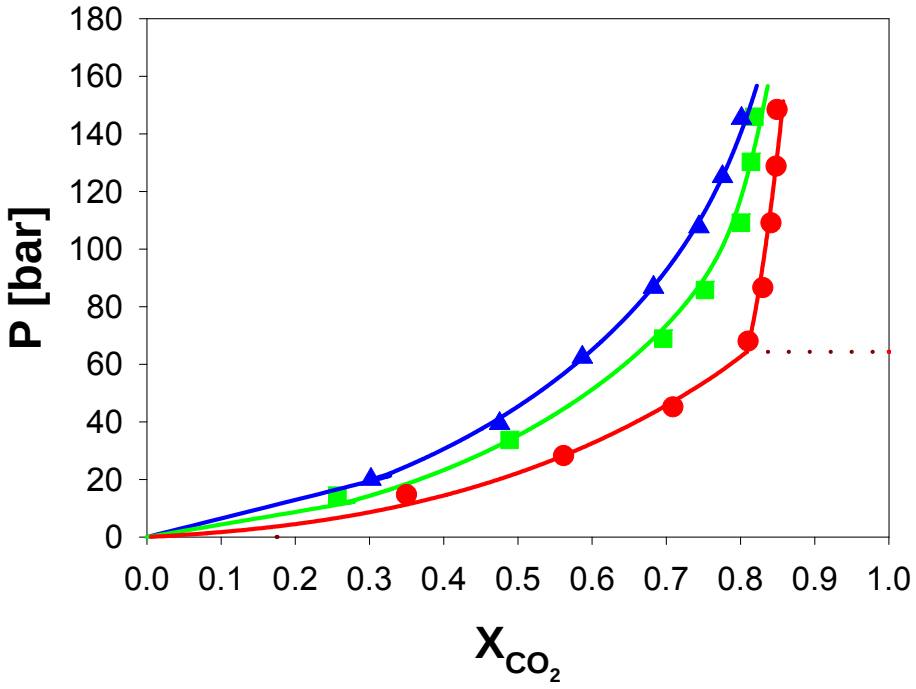

Figure 5.27 Experimental vapor-liquid, vapor-liquid-liquid, liquid-liquid equilibrium data and modeling results for [DMIm][Tf_2N] and CO_2.Legend: ●: 25 °C; ■: 50 °C; ▲: 70 °C ; Solid lines are modeling VLE and LLE, dash line is predicted VLLE.

Table 5.13 The binary interaction parameters and modeling results of [DMIm][Tf_2N] and CO_2

ILs + CO_2	T [°C]	Number Data Points	Interaction Parameters		AARD%
			k_{12}	l_{12}	
[DMIm][Tf_2N]	25	7	0.0328	0.0336	2.67
	50	7	0.0177	0.0293	3.34
	75	7	0.0078	0.0248	1.04

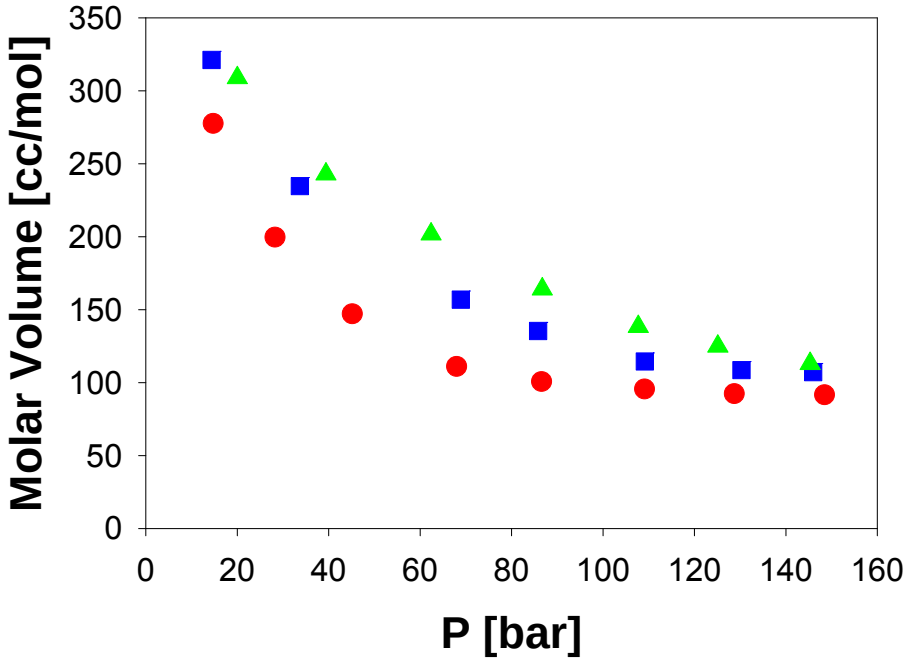

Figure 5.28 Molar volume for [DMIm][Tf_2N] and CO_2 at 25°C, 50°C, 70°C.

Legend: ●:25°C; ■:50°C ▲:70°C

Figure 5.28 shows the liquid molar volume of mixture with pressure (CO_2 composition) decreases at 25°C, 50°C, 70°C for [DMIm][Tf_2N] and CO_2. The molar volume data and volume expansion data display similar trends as the [HMIm][Tf_2N], [EMIm][Tf_2N] and CO_2 system at different temperature and CO_2 pressure.

Table 5.14 Vapor-liquid, vapor-liquid-liquid, liquid-liquid equilibrium, volume expansion and molar volume of CO_2 and ILs experimental data

T [°C]	P [bar]	x_{CO2}	$\Delta V/V_0$ [a]	V_L [cm^3/mol]
[DMIm][Tf_2N]				
25	14.74	0.350±0.002	0.0369±0.0005	277.51±0.10
	28.28	0.562±0.001	0.1070±0.0006	199.69±0.07
	45.16	0.709±0.001	0.2267±0.0006	147.04±0.04
	67.99[ll]	0.810±0.002	0.4206±0.0008	111.06±0.03
	86.59[ll]	0.830±0.001	0.4393±0.0007	100.63±0.03
	109.09[ll]	0.841±0.001	0.4604±0.0007	95.56±0.02
	128.73[ll]	0.848±0.001	0.4739±0.0007	92.35±0.02
	148.47[ll]	0.849±0.002	0.4776±0.0007	91.69±0.02
50	14.39	0.257±0.002	0.0332±0.0004	321.16±0.09
	33.71	0.489±0.002	0.0978±0.0004	234.66±0.06
	68.91	0.696±0.001	0.2337±0.0005	156.90±0.04
	85.81	0.752±0.001	0.3055±0.0005	135.36±0.03
	109.17	0.800±0.001	0.3715±0.0005	114.48±0.02
	130.30	0.814±0.002	0.3957±0.0005	108.56±0.02
	145.96	0.819±0.002	0.4126±0.0005	107.14±0.02
70	20.03	0.302±0.002	0.0371±0.0005	308.87±0.11
	39.41	0.475±0.003	0.0843±0.0005	242.81±0.08
	62.42	0.587±0.003	0.1443±0.0006	201.74±0.06
	86.74	0.683±0.003	0.2114±0.0006	164.04±0.05
	107.73	0.744±0.003	0.2667±0.0006	138.36±0.04
	125.15	0.776±0.003	0.3048±0.0006	124.89±0.03
	145.34	0.801±0.003	0.3322±0.0006	112.96±0.03

[a] Volume expansion: $\frac{\Delta V}{V_0} = \frac{V^L(T,P) - V_0(T,P=1bar)}{V_0(T,P=1bar)}$; [ll]= liquid-liquid equilibrium points for the IL-rich phase; [vll] = vapor-liquid-liquid equilibrium point with composition for IL-rich liquid phase.

5.4.5 Effect of n-Alkyl chain length

With the same anion [Tf_2N], the effect of the length of the cation alkyl- group on the CO_2 solubility is compared at 50 °C. As shown in Figure 5.29, the solubility of CO_2 is only slightly increased with the increase alkyl length, from [EMIm] to [HMIm] to [DMIm]. Therefore, it appears from this and other literature [30, 46] that the anion has a larger impact on solubility than the alkyl length of the cation. The alkyl- group increases the dispersion forces of the cation for better interaction with CO_2. Similar findings were discussed by Aki *et al.* [30]. In the Section 5.2 the solubility of R-134a in n-alkyl-3-methyl-imidazolium [Tf_2N] ionic liquids was measured. The results also demonstrate a solubility increase with increasing alkyl chain length.

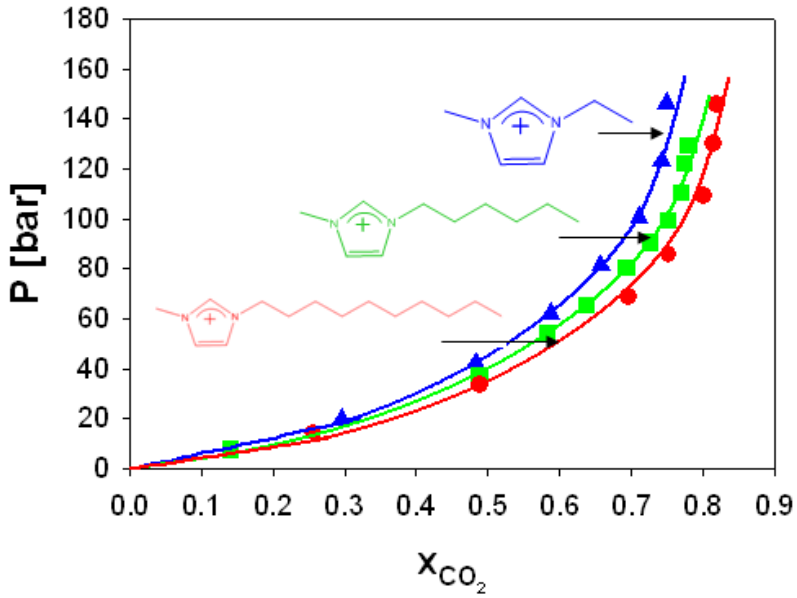

Figure 5.29 Experimental vapor liquid equilibrium data and modeling results for [Tf_2N] ILs and CO_2 at 50 °C. Legend: ●:DMIm; ■:HMIm ▲:EMIm Solid lines are modeling.

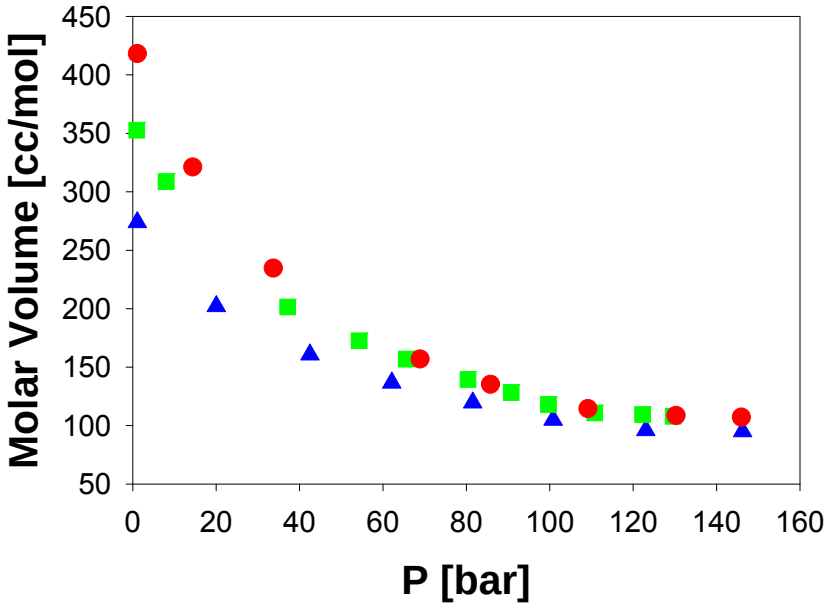

Figure 5.30 Molar volume for [EMIm][Tf_2N] (▲), [HMIm][Tf_2N] (■), [DMIm][Tf_2N] (●) and CO_2 at 50 °C.

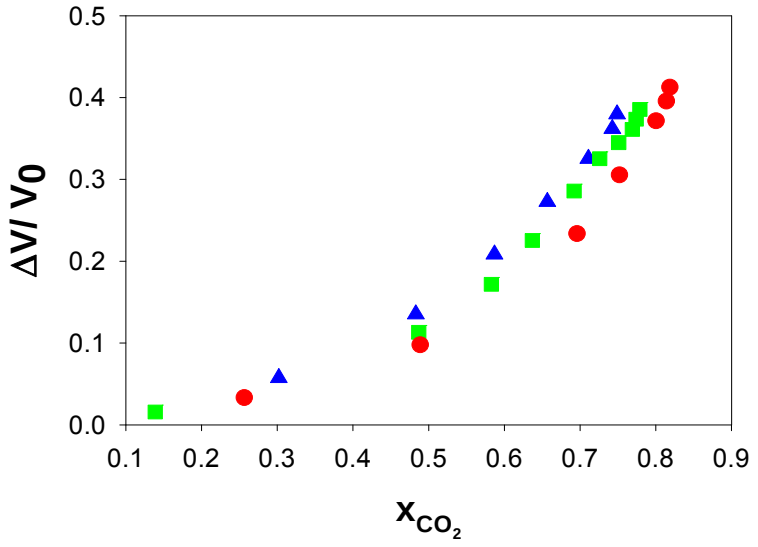

Figure 5.31 Volume expansion for [EMIm][Tf_2N] (▲), [HMIm][Tf_2N] (■), [DMIm][Tf_2N] (●) and CO_2 at 50 °C.

The ambient pressure molar volume increases with an increasing chain length. However, as shown in Figure 5.30, this effect diminishes with higher amounts of dissolved CO_2. Above 140 bar and the molar volumes of each IL becomes very similar. At these pressures, the IL consists of greater than 70% mole of CO_2 and thus the properties are better correlated with CO_2 than the ambient pressure IL properties.

The volume expansion of [EMIm][Tf_2N], [HMIm][Tf_2N], [DMIm][Tf_2N] and CO_2 at 50 °C were shown in Figure 5.31. At the same volume expansion, the solubility of CO_2 is highest in [DMIm][Tf_2N], lowest in [EMIm][Tf_2N]. At the same solubility, CO_2 expands [EMIm][Tf_2N] more than other two ILs. At lower pressure, the volume is expanded more than higher pressure due to the solubility difference of CO_2 in ionic liquid phase.

5.4.6 Effects of anion

Choosing different cation and anion affects CO_2 solubility in ILs. However, anions play a key role on CO_2 solubility. Brennecke's group has studied CO_2 solubility in ionic liquids with different structure [30, 46]. They studied CO_2 solubility for 1-Butyl-3-methylimidazolium ([BMIm]) based ILs at 60 °C and found increased in the order nitrate ([NO_3]) < [BF_4] < dicyanamide ([DCA]) ~ hexafluorophosphate ([PF_6]) ~ trifluoromethanesulfonate ([TfO]) < [Tf_2N] < tris(trifluoromethylsulfonyl)methide([methide]). They also reported that anions containing fluoroalkyl groups had some of the highest CO_2 solubilities, and as the quantity of fluoroalkyl groups increased, the CO_2 solubility also increased. [46]

Regarding environmental concerns of fluorinated components, researchers have explored the use of nonfluorinated molecules to maximize the CO_2 solubility. Carbonyl groups are known to be very good CO_2-philes, having a low level of self-interaction but the ability to take part in Lewis acid-Lewis base interactions [47-48]. Nonfluorinated ILs containing ether linkages and flexible alkyl chains to increase free volume can be designed to have a high affinity for CO_2 [46].

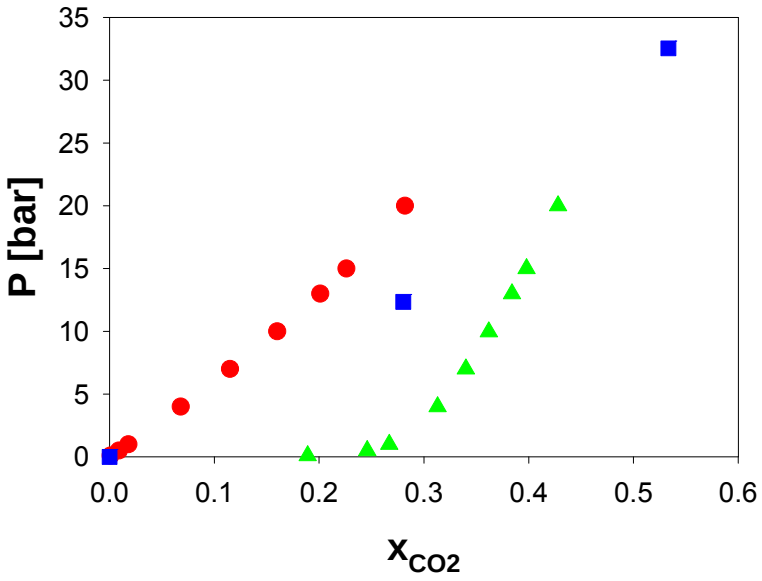

Figure 5.32 CO_2 solubility in [EMIm][TFA], [EMIm][Tf_2N] and [EMIm][AC] at 25°C. Legend: ●:[EMIm][TFA]; ■:[EMIm][Tf_2N]; ▲: [EMIm][AC] **.** The data of [EMIm][TFA] and [EMIm][AC] are from Shiflett and Yokozeki [49]

Shiflett and Yokozeki [49] Measured CO_2 solubility in 1-Ethyl-3-methylimidazolium acetate [EMIm][Ac] and 1-Ethyl-3-methylimidazolium trifluoroacetate [EMIm][TFA]. [A_C] shows much larger solubility than [Tf_2N]. The strong absorption is believed to form a reversible complex of AB_2 (A=CO_2 and B =

[EMIm][Ac] due to Lewis acid-base reaction. However, when the methyl group ($X=CH_3$) on the acetate anion (X-COO-) is replaced with the fluorinated methyl group ($X=CF_3$), the attraction is dramatically reduced as shown in Figure 5.32. Ionic liquids can be designed to have higher or lower CO_2 solubility for different applications. However, other factors, such as viscosity, cost, stability, environmental effort, etc. have to be considered.

5.4.7 Conclusions

The phase equilibria of carbon dioxide (CO_2) with [EMIm][Tf_2N], [HMIm][Tf_2N], [DMIm][Tf_2N] were measured at 25 °C, 50 °C, and 70 °C and pressures up to 250 bar. Multiphase equilibria exist at 25 °C, *viz.* VLE, LLE, and VLLE. The phase equilibrium data here show an excellent agreement with the limited literature reports. The PR vdW-2 EOS correlated well with these ILs and with CO_2 using simply predicted critical properties. However, the model does predict a mixture critical point at pressures above 400 bar which is not qualitatively correct. The CO_2 solubility in ionic liquids slightly increases with increasing alkyl chain length.

5.5 References

1. Carvalho, P.J., V.H. Álvarez, J.J.B. Machado, J. Pauly, J.-L. Daridon, I.M. Marrucho, M. Aznar, and J.A.P. Coutinho, *High pressure phase behavior of carbon dioxide in 1-alkyl-3-methylimidazolium*

bis(trifluoromethylsulfonyl)imide ionic liquids J. Supercrit. Fluids, 2008. **48**(2): p. 99-107.

2. Shiflett, M.B. and A. Yokozeki, *Solubility and diffusivity of hydrofluorocarbons in room-temperature ionic liquids.* AIChE Journal, 2006. **52**(3): p. 1205-1219.
3. Shiflett, M.B. and A. Yokozeki, *Vapor-Liquid-Liquid Equilibria of Hydrofluorocarbons + 1-Butyl-3-methylimidazolium Hexafluorophosphate.* . Journal of Chemical & Engineering Data, 2006. **51**(5): p. 1931-1939.
4. Shiflett, M.B. and A. Yokozeki, *Solubilities and diffusivities of carbon dioxide in ionic liquids: [BMIm][PF_6] and [BMIm][BF_4]*. Industrial & Engineering Chemistry Research, 2005. **44**(12): p. 4453-4464.
5. Shiflett, M.B. and A. Yokozeki, *Vapor-liquid-liquid equilibria of pentafluoroethane and ionic liquid [BMIm][PF_6] mixtures studied with the volumetric method.* J. Phys. Chem. B, 2006. **110**(29): p. 14436-14443.
6. Shiflett, M.B. and A. Yokozeki, *Solubility Differences of Halocarbon Isomers in Ionic Liquid [EMIm][Tf_2N]*. J. Chem. Eng. Data, 2007. **52**: p. 2007-2015.
7. Shiflett, M.B. and A. Yokozeki, *Liquid-liquid equilibria of hydrofluoroethers and ionic liquid 1-ethyl-3-methylimidazolium bis(trifluoromethylsulfonyl)imide.* J. Chem. Eng. Data, 2007. **52**(6): p. 2413-2418.
8. Shiflett, M.B. and A. Yokozeki, *Solubility of CO_2 in room temperature ionic liquid [HMIm][Tf_2N]*. J. Phys. Chem. B, 2007. **111**(8): p. 2070-2074.

9. Shiflett, M.B. and A. Yokozeki, *Binary Vapor–Liquid and Vapor–Liquid–Liquid Equilibria of Hydrofluorocarbons (HFC-125 and HFC-143a) and Hydrofluoroethers (HFE-125 and HFE-143a) with Ionic Liquid [EMIm][Tf$_2$N]*. J. Chem. Eng. Data, 2008. **53**: p. 492–497.

10. Shiflett, M.B. and A.M.S. Niehaus, *Liquid-Liquid Equilibria in Binary Mixtures Containing Substituted Benzenes with Ionic Liquid 1-Ethyl-3-methylimidazolium Bis(trifluoromethylsulfonyl)imide.* J. Chem. Eng. Data, 2009: p. Article ASAP.

11. Shiflett, M.B., A.M.S. Niehaus, and A. Yokozeki, *Liquid-Liquid Equilibria in Binary Mixtures Containing Chlorobenzene, Bromobenzene, and Iodobenzene with Ionic Liquid 1-Ethyl-3-methylimidazolim Bis(trifluoromethylsulfonyl)imide.* J. Chem. Eng. Data 2009, 2009. **54**: p. 2090–2094.

12. Shiflett, M.B. and A. Yokozeki, *Solubility and diffusivity of hydrofluorocarbons in room-temperature ionic liquids.* AIChE J., 2006. **52**(3): p. 1205-1219.

13. Shiflett, M.B. and A. Yokozeki, *Phase Equilibria of Hydrofluorocarbon-4310mee Mixtures with Ionic Liquids:Miscibility of threo- and erythro-Diastereomers in Ionic Liquids.* Ind. Eng. Chem. Res. , 2008. **47**: p. 926-934.

14. Shiflett, M.B. and A. Yokozeki, *Liquid-Liquid Equilibria in Binary Mixtures Containing Fluorinated Benzenes and Ionic Liquid 1-Ethyl-3-*

methylimidazolium Bis(trifluoromethylsulfonyl)imide. J. Chem. Eng. Data, 2008. **53**: p. 2683–269.

15. Yokozeki, A. and M.B. Shiflett, *Binary and Ternary Phase Diagrams of Benzene, Hexafluorobenzene, and Ionic Liquid [EMIm][Tf_2N] Using Equations of State.* Ind. Eng. Chem. Res., 2008. **47**: p. 8389–8395.
16. Schilderman, A.M., S. Raeissi, and C.J. Peters, *Solubility of carbon dioxide in the ionic liquid 1-ethyl-3-methylimidazolium bis(trifluoromethylsulfonyl)imide* Fluid Phase Equilibria, 2007. **260**(1): p. 19-22.
17. Yokozeki, A. and M.B. Shiflett, *Ammonia Solubilities in Room-Temperature Ionic Liquids.* Industrial & Engineering Chemistry Research 2007. **46**(5): p. 1605-1610.
18. Ren, W., A.M. Scurto, M.B. Shiflett, and A. Yokozeki, *Phase Behavior and Equilibria of Ionic Liquids and Refrigerants: 1-Ethyl-3-methyl-imidazolium bis(trifluoromethylsulfonyl)imide ([EMIm][Tf_2N]) and R-134a*, in *Gas Expanded Liquids and Near-Critical Media: Green Chemistry and Engineering* K.W. Hutchenson, A.M. Scurto, and B. Subramaniam, Editors. 2008, ACS Symposium Series 1006: Washington, D.C. p. 112-128.
19. Ren, W. and A.M. Scurto, *Global phase behavior of imidazolium ionic liquids and compressed 1,1,1,2-tetrafluoroethane (R-134a).* AIChE Journal, 2009. **55**(2): p. 486-493.
20. Ren, W., A.M. Scurto, M.B. Shiflett, and A. Yokozeki, *Phase Behavior and Equilibria of Ionic Liquids and Refrigerants: 1-Ethyl-3-methyl-imidazolium*

bis(trifluoromethylsulfonyl)imide ([EMIm][Tf_2N]) and R-134a, in *Gas Expanded Liquids and Near-Critical Media: Green Chemistry and Engineering*, K.W. Hutchenson, A.M. Scurto, and B. Subramaniam, Editors. 2008, ACS Symposium Series 1006: Washington, D.C. p. 112-128.

21. Kim, K.-S., B.-K. Shin, H. Lee, and F. Ziegler, *Refractive index and heat capacity of 1-butyl-3-methylimidazolium bromide and 1-butyl-3-methylimidazolium tetrafluoroborate, and vapor pressure of binary systems for 1-butyl-3-methylimidazolium bromide + trifluoroethanol and 1-butyl-3-methylimidazolium tetrafluoroborate + trifluoroethanol.* Fluid Phase Equilibria, 2004. **218**: p. 215-220.

22. Kim, K.-S., S.-Y. Park, S. Choi, and H. Lee, *Vapor Pressures of the 1-Butyl-3-methylimidazolium Bromide +Water, 1-Butyl-3-methylimidazolium Tetrafluoroborate + Water, and 1-(2-Hydroxyethyl)-3-methylimidazolium Tetrafluoroborate + Water Systems.* J. Chem. Eng. Data 2004. **49**: p. 1550-1553.

23. Karakatsani, E.K., I.G. Economou, M.C. Kroon, C.J. Peters, and G.-J. Witkamp, *tPC-PSAFT Modeling of Gas Solubility in Imidazolium-Based Ionic Liquids.* J. Phys. Chem. C, 2007. **111**(43): p. 15487–15492.

24. Kroon, M.C., E.K. Karakatsani, I.G. Economou, G.-J. Witkamp, and C.J. Peters, *Modeling of the Carbon Dioxide Solubility in Imidazolium-Based Ionic Liquids with the tPC-PSAFT Equation of State.* J. Phys. Chem. B, 2006. **110**(18): p. 9262–9269.

25. Kumelan, J., A.P. Kamps, D. Tuma, A. Yokozeki, M.B. Shiflett, and G. Maurer, *Solubility of Tetrafluoromethane in the Ionic Liquid [HMIm][Tf_2N]*. J. Phys. Chem.B., 2008. **112**: p. 3040-3047.

26. Shiflett, M.B. and A. Yokozeki, *Liquid-Liquid Equilibria of Hydrofluoroethers and Ionic Liquid 1-Ethyl-3-methylimidazolium Bis(trifluoromethylsulfonyl) imide.* J. Chem. Eng. Data, 2007. **52**: p. 2413-2418.

27. Castier, M. and S.I. Sandler, *Critical points with the Wong-Sandler mixing rule--II. Calculations with a modified Peng-Robinson equation of state.* Chem. Eng. Sci., 1997. **52**(20): p. 3579-3588.

28. Valderrama, J.O., W.W. Sanga, and J.A. Lazzus, *Critical Properties, Normal Boiling Temperature, and Acentric Factor of Another 200 Ionic Liquids.* . Industrial & Engineering Chemistry Research 2008. **47**(4): p. 1318-1330.

29. Pfohl, O., S. Petkov, and G. Brunner, *PE 2000 – A Powerful Tool to Correlate Phase Equilibria*. 2000, München: Herbert Utz Verlag.

30. Van Konynenburg, P.H. and R.L. Scott, *Critical lines and phase equilibriums in binary van der waals mixtures.* Philos. Trans. R. Soc. London, Ser. A, 1980. **298**: p. 495-540.

31. Aki, S.N.V.K., B.R. Mellein, E.M. Saurer, and J.F. Brennecke, *High-Pressure Phase Behavior of Carbon Dioxide with Imidazolium-Based Ionic Liquids.* J. Phys. Chem. B, 2004. **108**(52): p. 20355–20365.

32. Florusse, L.J., S. Raeissi, and C.J. Peters, *High-Pressure Phase Behavior of Ethane with 1-Hexyl-3-methylimidazolium Bis(trifluoromethylsulfonyl)imide.* J. Chem. Eng. Data, 2008. **53**(6): p. 1283–1285.

33. Kumelan, J., A.P.-S. Kamps, D. Tuma, and G. Mauer, *Solubility of H_2 in the ionic liquid [HMIm][Tf_2N]*. J. Chem. Eng. Data, 2006. **51**: p. 1364-1367.

34. Kumelan, J., A. Perez-Salado Kamps, D. Tuma, and G. Maurer, *Solubility of the single gases methane and xenon in the ionic liquid [HMIm][Tf_2N]*. Ind. Eng. Chem. Res., 2007. **46**(24): p. 8236-8240.

35. Scurto, A.M., C.M. Lubbers, G. Xu, and J.F. Brennecke, *Experimental measurement and modeling of the vapor-liquid equilibrium of carbon dioxide + chloroform.* Fluid Phase Equil., 2001. **190**(1-2): p. 135-147.

36. Ren, W., B. Sensenich, and A.M. Scurto, *High-Pressure Phase Equilibria of Carbon Dioxide (CO2) + n-Alkyl-Imidazolium Bis(trifluoromethylsulfonyl)amide Ionic Liquids.* Submitted, 2009.

37. Lemmon, E.W., M. L. Huber, *et al.* (2007). NIST Reference Fluid Thermodynamic and Transport Properties - REFPROP. Version 8.0. Gaithersburg, Maryland.

38. Valderrama, J.O. and P.A. Robles, *Critical Properties, Normal Boiling Temperatures, and Acentric Factors of Fifty Ionic Liquids.* . Industrial & Engineering Chemistry Research, 2007. **46**(4): p. 1338-1344.

39. Anon., *Thermodynamics of Ionic Liquids, Ionic Liquid Mixtures, and the Development of Standardized Systems.* Chem. Int., 2005. **27**(5): p. 22-23.

40. Shiflett, M.B. and A. Yokozeki, *Solubility of CO_2 in Room Temperature Ionic Liquid [HMIm][Tf_2N]*. . Journal of Physical Chemistry B 2007. **111**(8): p. 2070-2074.

41. Blanchard, L.A., Z. Gu, and J.F. Brennecke, *High-Pressure Phase Behavior of Ionic Liquid/CO_2 Systems.* Journal of Physical Chemistry B, 2001. **105**(12): p. 2437-2444.

42. Lemmon, E.W., M.L. Huber, and M.O. McLinden, *NIST Reference Fluid Thermodynamic and Transport Properties - REFPROP*, in *Version 8.0*. 2007: Gaithersburg, Maryland.

43. Shiflett, M.B. and A. Yokozeki, *Vapor-Liquid-Liquid Equilibria of Pentafluoroethane and Ionic Liquid [BMIm][PF_6] Mixtures Studied with the Volumetric Method.* Journal of Physical Chemistry B, 2006. **110**(29): p. 14436-14443.

44. Scurto, A.M., S.N.V.K. Aki, and J.F. Brennecke, *CO_2 as a Separation Switch for Ionic Liquid/Organic Mixtures.* J. Am. Chem. Soc., 2002. **124**: p. 10276-10277.

45. Weize;, W., Z. Jianmin;, H. Buxing;, C. Jiawei;, L. Zhimin;, J. Tao;, H. Jun;, and L. Wenjing, *Solubility of room-temperature ionic liquid in supercritical CO_2 with and without organic compounds.* Chem. Comm., 2003(12): p. 1412-1413.

47. Muldoon, M.J., S.N.V.K. Aki, J.L. Anderson, J.K. Dixon, and J.F. Brennecke, *Improving Carbon Dioxide Solubility in Ionic Liquids.* Journal of Physical Chemistry B 2007. **111**(30): p. 9001-9009.

48. Beckman, E.J., *A challenge for green chemistry: designing molecules that readily dissolve in carbon dioxide.* . Chemical Communications 2004. **17**: p. 1885-1888.

49. Kazarian, S.G., M.F. Vincent, F.V. Bright, C.L. Liotta, and C.A. Eckert, *Specific Intermolecular Interaction of Carbon-Dioxide with Polymers*. J. Am. Chem. Soc., 1996. **118**: p. 1729-1736.

50. Shiflett, M.B. and A. Yokozeki, *Phase Behavior of Carbon Dioxide in Ionic Liquids: [EMIm][Acetate], [EMIm][Trifluoroacetate], and [EMIm][Acetate] + [EMIm][Trifluoroacetate] Mixtures.* Journal of Chemical & Engineering Data 2009. **54**(1): p. 108-114.

Chapter 6 Feasibility of Absorption Air Conditioning Using Ionic Liquids and Compressed Gases as Working Fluids on Mobile Vihicle Application

6.1 Introduction

The traditional and dominate vehicle air-conditioning system is the vapor compression system, where a gas compressor either shaft or belt is driven by vehicle's engine. The main problem for this air-conditioning system is that it uses a portion of the engine duty, which significantly increases fuel consumption, lower gas mileage and increases emissions to the environment. Automobile air conditioners can affect the environment from the increased refrigerants used. In addition, vehicle air conditioners consume more energy than any other auxiliary vehicle equipment. For instance, the energy of a typical gasoline internal combustion engine can be split into three parts [1](see Figure 6.1): 30% goes to engine duty (work), 30% goes to the coolant as heat, and 40% as waste heat goes to the exhaust gas. Thus, most of fuel is wasted as heat in the exhaust and coolant. According to Environmental Protection Agency (EPA) report, in the United States alone, vehicle air conditioners consume over 7 billion gallons of gasoline every year, and emit over 58 million metric tons of carbon dioxide [2].

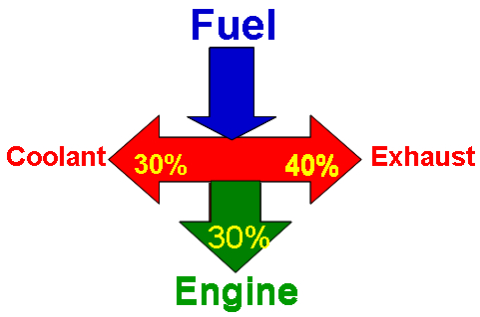

Figure 6.1 Energy splits in a typical gasoline internal combustion engine

To address these problems, one potential solution is absorption refrigeration technology. The vapor compression air conditioning system comsume more fuel due to power consumption, while absorption refrigeration system can save the fuel because of the waste heat recovery and decrease on the refrigeration leakage. If the fuel used by vehicle air conditioners can be reduced by 30% and refrigerant emissions is cut into half, this would reduce overall 9 million metric tons of carbon equivalent greenhouse gas emissions and save 2.1 billion gallons of gasoline for each year [3].

6.1.1 Absorption and the vapor-compression air conditioning systems

The principal difference between the absorption and the vapor-compression cycles is the mechanism for generating the high-pressure refrigerant gas. The vapor compressor, employed in the vapor-compression cycle, is replaced in the absorption cycle by an absorber and a generator or boiler. The energy input required by the vapor-compression cycle is supplied to the compressor in the form of mechanical work. However, in the absorption cycle, the energy input is mostly in the form of heat supplied to the generator. Most importantly, absorption systems, in general, can

be driven by lower quality energies, such as waste energy, solar energy, geothermal energy, etc. In the present vehicle case, heat source can be from the coolant or the exhaust of an internal combustion vehicle engine.

6.1.2 Absorption refrigeration

The general absorption refrigeration cycle is shown in Figure 6.2. It includes a vapor absorber, a generator, a condenser, an evaporator, a heat exchanger, a solution liquid pump and expansion valve to reduce the pressure. The refrigeration solution consists of refrigerant and absorbent. R-134a and CO_2 were chosen as refrigerants, ionic liquid, [HMIm][Tf_2N], was chosen as absorbent here. The "weak solution" (a term from the absorption refrigeration industry) contains a higher concentration of the refrigerant and less absorbent (therefore "weak"). The "strong solution" contains a lower concentration of the refrigerant and more absorbent.

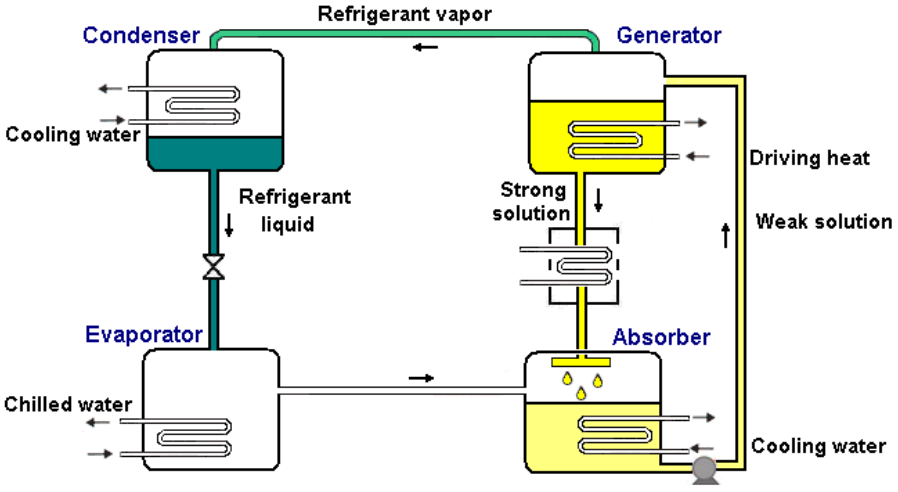

Figure 6.2 Idealized absorption refrigeration cycle

In the absorber, the solvent absorbs the refrigerant gas, forming the "weak solution." Then the weak solution is pumped to the generator. In the generator, the weak IL - refrigerant solution is heated, which drives the refrigerant vapor out of the solution. The "strong solution" is produced and flows back to the absorber for reuse. The refrigerant vapor leaves the generator and goes into the condenser as in the vapor-compression system. In the condenser, the refrigerant vapor condenses isobarically to a liquid as heat is removed. Then the refrigerant liquid passes through a throttling valve before entering the evaporator, where the pressure and temperature of the refrigerant are reduced. In the evaporator, the refrigerant evaporates, again forming a vapor. This evaporation of the refrigerant draws heat from a heat load and creates the cooling effect of a refrigerator or air conditioner. The refrigerant vapor returns to the absorber to finish a cycle.

Overall, the refrigerant path follows absorber → generator → condenser → evaporator → absorber. The path of the absorbent and refrigerant mixtures follows absorber → generator → absorber.

6.1.3 Challenges of conventional absorption systems

The most common absorption systems use ammonia/water and water/LiBr as working fluids. Ammonia/water system uses ammonia as the refrigerant and water as absorbent. Water and ammonia have a great affinity, thus a large amount of ammonia vapor can dissolve in water phase. Both air-cooled and water-cooled systems were developed. The major disadvantage of the ammonia/water system is that water is a relatively volatile absorbent so that water evaporates with the ammonia refrigerant in

the generator. Therefore, to obtain pure refrigerant vapors for proper operation of the system, a large rectifier must be placed between the generator and condenser to purify the ammonia vapor, which increases process complexity and costs. The rectifier is a distillation column that removes the absorbent (solvent) and purifies the refrigerant. While the amount of solvent in the high pressure refrigerant gas coming from the generator is often low, it may have a large effect on the cooling process. For instance, just 100ppm of H_2O in the refrigerant gas in the ammonia/water system discussed above reduces efficiency (COP) by 5% [4]. As there is a great need for a sizable rectifier, these systems are mostly used in large industrial operations. Additionally, handling and storing of pressurized ammonia demand prevention and protection measures, due to its volatility, toxicity and flammability [5-6]. Because of safety limitations and the large equipment size, this type of refrigeration cannot be used for refrigeration in motorized vehicles. For water/LiBr working fluid pair, water is now the refrigerant and LiBr is the absorbent. Lithium Bromide is better than water as an absorbent since it is not volatile. Consequently, the rectifier is not necessary for the cycle design. However, Lithium Bromide is corrosive [5-7] and the solution tends to crystallization at high concentrations, which usually limits its operation to above 0° C. Water-LiBr solutions are very viscous, therefore operation of the absorbent in the system requires more energy of pumping [6].

To overcome these challenges and issues, ionic liquids with refrigerant gases are proposed as a potential replacement. The ILs have no measurable vapor pressure, which may eliminate the need for a rectifier; are non-corrosive; and can have very

low freezing points. Thus, ionic liquids may be the perfect replacement of absorbents for absorption refrigeration systems for even small size applications.

6.1.4 Ionic liquids-excellent absorbent alternatives

ILs have unique properties, which are favorable for being absorbents. ILs are non-flammability and have non-measurable vapor pressure, which means an environmentally benign absorbent and no rectifier needed in the design of absorption systems. Many ionic liquids are liquid in a wide temperature range, from melting points well below 0°C to decomposition temperatures up to 400+°C. ILs can have high heat capacity (>2000 $Jkg^{-1} K^{-1}$ at 25°C) compared with water (1600 $Jkg^{-1}K^{-1}$ at 100°C) ([8-10]), high density, high thermal conductivity and chemical stability. The decomposition temperature of ILs is commonly greater than 300 °C, which is much greater than many sources of heat to be used in absorption refrigeration. A wide range of materials including inorganic, organic and even polymeric materials are soluble in ionic liquids. Furthermore, the solubility of gas (especially hydrofluorocarbons and CO_2) is high in ILs, which makes them to be good candidates. Preliminary toxicology studies of ILs indicate low to moderate toxicity on average [11-14]. Recent studies [15-17] indicate that most materials show very good corrosion resistance in the presence of ILs. Even the most reactive metals, such as Al-alloy, show extreme low corrosion rate at <0.1 mm y^{-1}, which indicates almost no corrosion problems on containers and pipes. ILs are "designer absorbents". It has been estimated that there are nearly 10^{14}different combinations of cation-anion possible [18]. Physical and chemical properties of ILs can be adjusted by the choice

of alkyl chain length, the presence of additional alkyl substitutions on the cation and the choice of anion [19-21]. For example, replacing the [PF_6] anion of the 1-alkyl-3-alkylimadazolium cation by [BF_4] dramatically increases the miscibility of the ionic liquid in water; however, the replacement by [Tf_2N] ion decreases the water miscibility. The change of the length of the alkyl chain can tune the miscibility of ionic liquid in water [20]. Therefore, ILs provide a great number of opportunities to find appropriate absorbents for pairing particular refrigerants.

6.1.5 Phase behavior and equilibria of IL and compressed gases as working fluids

To evaluate and choose novel working fluids, the physical and chemical properties of the working fluid are extremely important especially for designing thermodynamic systems. The favorable properties for working fluids are keys to determine the absorption cycle performance, efficiency and operating cost, such as, no solid phase, lower toxicity and high affinity between refrigerants and absorbents. To investigate if ionic liquids and compressed gases are feasible to be working fluids, the phase behavior and phase equilibrium data are necessary.

Chapter 4 gives the global phase behavior study for ionic liquids and compressed gases. Most ionic liquids and R-134a belong to type V systems which means that regions where vapor-liquid equilibrium, vapor-liquid-liquid equilibrium, liquid-liquid equilibrium exist. The global phase behavior is very important to determine the operating conditions. In the operating condition range, solids do not exist, but single phase mixtures exist at certain temperature and pressure, which

should be avoided in the operation. The global behavior of ionic liquid and CO_2 belong to type III, therefore, VLE exists in most cases and all regions of pressure and temperature can be used. Because of lower critical temperature of CO_2, the condenser (gas cooler) may operate in supercritical status. Chapter 5 reports the phase equilibrium of ionic liquids and compressed gases. The solubility of both R-134a and CO_2 decreases with increasing temperature and increases with the pressure. Therefore, the absorber should operate at lower temperature to dissolve more gases in the absorbent, while the generator operates at high temperature to release the gases out of absorbent. The solubility also changes with alkyl chain and anions, here, [HMIm][Tf_2N] was chosen as a model ionic liquid. Ionic liquid structure should be considered if ionic liquid optimization is performed.

In this chapter, the feasibility of absorption air conditioning system based on thermodynamic modeling will be performed.

6.2 Absorption Cycle Modeling and Simulation

A schematic diagram for a typical absorption refrigeration cycle in this study is shown in Figure 6.3.

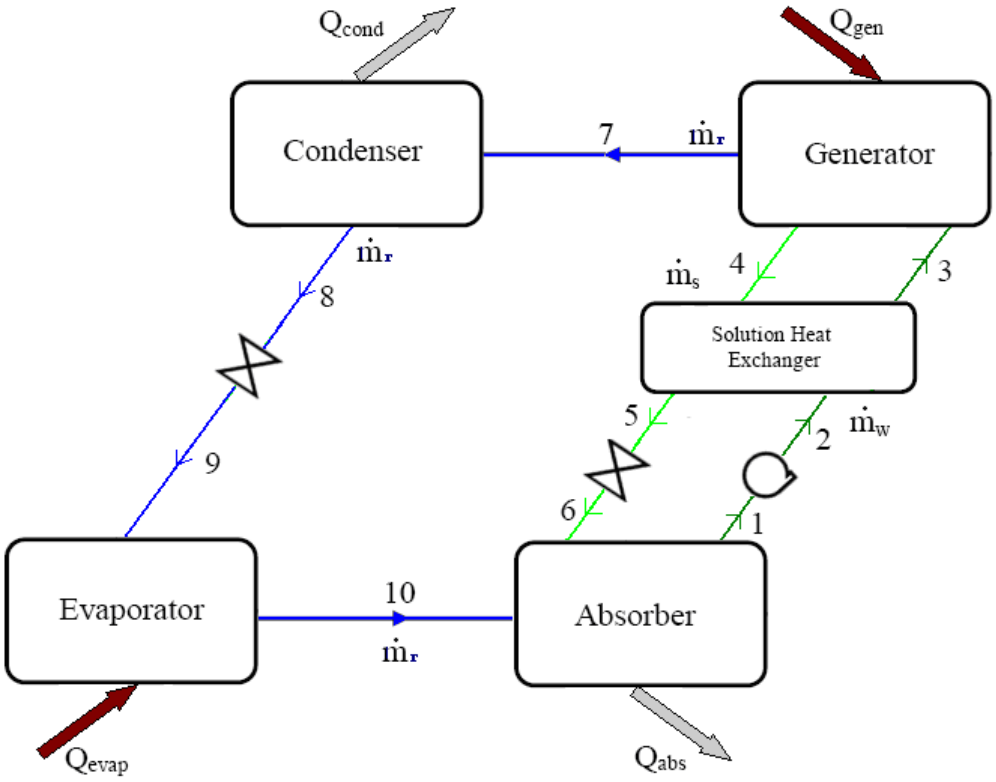

Figure 6.3 A schematic diagram of an absorption refrigeration cycle

The mass balance, energy balance, and theoretical cycle performance are modeled as follows: $\dot{m}$ represents the mass flowrate of fluids; $\dot{Q}$ represents the heat flowrate entering or leaving each unit; $\dot{W}$ is the work for the pump.

According to the first law of thermodynamics, the energy balance can relate the flows of heat, work, and mass through the enthalpy. The second law identifies where the real inefficiencies are in a system through entropy. Entropy generation is very common in all types of heat-transfer processes. The second law analysis is very important to perform the process optimizations. However, a 1st Law analysis can help determine the feasibility and general operating conditions of an absorption

refrigeration system and will be used here. The mass and energy balances for each of the unit operations in Figure 6.3 are given below, where $\hat{H}$ is the specific enthalpy of each stream.

Absorber:

Mass balance:

$$\dot{m}_{10} + \dot{m}_6 = \dot{m}_1 \tag{6.1}$$

$$\dot{m}_6 x_6 + \dot{m}_{10} x_{10} = \dot{m}_1 x_1 \tag{6.2}$$

Energy balance:

$$\dot{m}_6 \hat{H}_6 + \dot{m}_{10} \hat{H}_{10} = \dot{m}_1 \hat{H}_1 + \dot{Q}_{abs} \tag{6.3}$$

Generator:

Mass balance:

$$\dot{m}_3 = \dot{m}_4 + \dot{m}_7 \tag{6.4}$$

$$\dot{m}_3 x_3 = \dot{m}_4 x_4 + \dot{m}_7 x_7 \tag{6.5}$$

Energy balance:

$$\dot{m}_3 \hat{H}_3 + \dot{Q}_{gen} = \dot{m}_4 \hat{H}_4 + \dot{m}_7 \hat{H}_7 \tag{6.6}$$

Condenser:

Mass balance:

$$\dot{m}_7 = \dot{m}_8 \tag{6.7}$$

Energy balance:

$$\dot{m}_7 \hat{H}_7 = \dot{Q}_{cond} + \dot{m}_8 \hat{H}_8 \tag{6.8}$$

Evaporator:

Mass balance:

$$\dot{m}_9 = \dot{m}_{10} \tag{6.9}$$

Energy balance:

$$\dot{m}_9 \widehat{H}_9 + \dot{Q}_{evap} = \dot{m}_{10} \widehat{H}_{10} \tag{6.10}$$

Pump:

Mass balance:

$$\dot{m}_1 = \dot{m}_2 \tag{6.11}$$

$$x_1 = x_2 \tag{6.12}$$

Energy balance:

$$\dot{W}_p = \dot{m}_s (\widehat{H}_1 - \widehat{H}_2) \tag{6.13}$$

Solution expansion valve:

Mass balance:

$$\dot{m}_5 = \dot{m}_6 \tag{6.14}$$

$$x_5 = x_6 \tag{6.15}$$

Energy balance:

$$\widehat{H}_5 = \widehat{H}_6 \tag{6.16}$$

Solution heat exchanger:

Mass balance:

$$\dot{m}_2 = \dot{m}_3 \tag{6.17}$$

$$x_2 = x_3 \tag{6.18}$$

$$\dot{m}_4 = \dot{m}_5 \tag{6.19}$$

$$x_4 = x_5 \tag{6.20}$$

Energy balance:

$$\dot{m}_s(\widehat{H}_2 - \widehat{H}_3) = \dot{m}_w(\widehat{H}_5 - \widehat{H}_4) \tag{6.21}$$

Refrigerant expansion valve:

Mass balance:

$$\dot{m}_8 = \dot{m}_9 \tag{6.22}$$

Energy balance:

$$\widehat{H}_8 = \widehat{H}_9 \tag{6.23}$$

Where:

$$\dot{m}_s = \dot{m}_1 = \dot{m}_2 = \dot{m}_3 \tag{6.24}$$

$$\dot{m}_w = \dot{m}_4 = \dot{m}_5 = \dot{m}_6 \tag{6.25}$$

$$\dot{m}_f = \dot{m}_7 = \dot{m}_8 = \dot{m}_9 = \dot{m}_{10} \tag{6.26}$$

The circulation ratio (*f*) is expressed by weak solution mass flow rate and the refrigerant mass flow rate, which can be determined by mass balance of the generator.

$$f = \frac{\dot{m}_w}{\dot{m}_f} = \frac{\dot{m}_3}{\dot{m}_7} = \frac{(x_7 - x_4)}{(x_3 - x_4)} \tag{6.27}$$

The overall energy balance is:

$$\dot{Q}_{cond} + \dot{Q}_{abs} = \dot{Q}_{gen} + \dot{Q}_{evp} + \dot{W}_p \tag{6.28}$$

The coefficient of performance (COP), is expressed as

$$COP = \frac{\dot{Q}_{evap}}{\dot{Q}_{gen}} \tag{6.29}$$

To perform a thermodynamic analysis, an absorption refrigeration system is modeled based on mass and energy conservation, the feasibility simulation was implemented in MATLAB software. Peng-Robinson Equation of state (PR EoS) [22] was chosen to optimize the binary interaction parameters (discussed in Chapter 5), find the solubility at different operating conditions (temperature and pressure), located the density of liquid mixture. The pure gas properties corresponding to temperature and pressure were read from REFPROP dynamic link library, which allows incorporation with MATLAB. REFPROP has higher accuracies typically 0.1 % to 0.5 % in density, 1 % to 3 % in liquid heat capacities and sound speeds. [23]

PR EoS was also chosen to as thermodynamic model to calculate the phase equilibrium and residue enthalpy. An enthalpy can be calculated by the following equation [24].

$$\Delta \underline{H}^{r} = \underline{H}_{m} - \underline{H}^{IGM} \tag{6.30}$$

$$\underline{H}^{IGM} = \sum x_i \underline{H}_i^{IG} \tag{6.31}$$

$$\Delta \underline{H}^{r} = \underline{H}_{m} - \sum x_i \underline{H}_i^{IG} \tag{6.32}$$

$$\underline{H}_{m} = \Delta \underline{H}^{r} + \sum x_i \underline{H}_i^{IG} \tag{6.33}$$

where, $\Delta\underline{H}^{r}$ is the residual molar enthalpy or enthalpy departure function.

$\underline{H}^{IGM}$ is expressed as:

$$\underline{H}^{IGM} = \sum_{i=1}^{N} x_i \int C_{pi}^{0}(T) dT \tag{6.34}$$

Heat capacities of ionic liquids as a function of temperature were measured by Ge *et al.* [25] The relation between heat capacity and temperature for [HMIm][Tf_2N] is expressed as:

$$C_{p\_IL}(\text{J mol}^{-1}\text{K}^{-1}) = 0.389 \times T(K) + 549.33 \tag{6.35}$$

For R134a and CO_2, the idea gas heat capacity can be decided by REFPROP software.

The derivation of ΔH^r from equation of state is given by Lewis et. al [26-27]:

$$\Delta \underline{H}^r = RT(Z-1) - \int_V^\infty \left\{ T\left(\frac{\partial P}{\partial T}\right)_V - P \right\} dV \tag{6.36}$$

Combining with the PR EoS, we obtain:

For pure component *i*:

$$\Delta \underline{H}^r = RT\left\{ (Z_i - 1) - \left(\frac{T\left(\frac{\partial a_i}{\partial T}\right) - a_i}{2\sqrt{2}b_i RT} \right) \ln\left(\frac{Z_i + 2.414B_i}{Z_i - 0.414B_i} \right) \right\} \tag{6.37}$$

where,

$$B_i = \frac{b_i P}{RT} \tag{6.38}$$

$$\frac{\partial a_i}{\partial T} = -\frac{a_{ci} m_i}{\sqrt{T T_{ci} \alpha_i}} \tag{6.39}$$

$$\alpha_i = \left[1 + m_i\left(1 - \sqrt{T_{ri}}\right)\right]^2 \tag{6.40}$$

$$m_i = 0.37464 + 1.54226\omega_i - 0.26992\omega_i^2 \tag{6.41}$$

For a mixture:

$$\Delta \underline{H}^{r} = RT\left\{(Z-1) - \left(\frac{T\left(\frac{\partial a}{\partial T}\right) - a}{2\sqrt{2}bRT}\right)\ln\left(\frac{Z+2.414B}{Z-0.414B}\right)\right\} \tag{6.42}$$

where,

$$B = \frac{bP}{RT} \tag{6.43}$$

$$\frac{\partial a}{\partial T} = -\frac{1}{2}\sum_{i=1}^{N}\sum_{j=1}^{N} x_i x_j (1-k_{ij})\left[m_i\sqrt{\left(\frac{a_{ci}a_j}{T_{ci}T}\right)} + m_j\sqrt{\left(\frac{a_{cj}a_j}{T_{cj}T}\right)}\right] \tag{6.44}$$

The following assumptions are made for the simulations; the effectiveness of heat transfer is assumed to be 70%. The absorber and generator are operated in saturated status at its temperature. The pressure of evaporator is the same as absorber pressure. The generator pressure equals the condenser pressure. The pressure drops in the pipes are neglected. The expansion valve is working at constant enthalpy. The whole system is operated under steady-state conditions.

The physical properties of [HMIm]Tf_2N], R134a and CO_2 used in the modeling are given in Table 6.1. ILs properties are predicted [28]. The property data of R-134a and CO_2 are from the PE2000 database [29]. The binary interaction parameters were correlated in Chapter 5 and summarized here along with modeling results in Table 6.2.

Table 6.1 The physical property table of ILs, R-134a and CO_2

Component	Formula	Molecular Weight [g/mol]	Boiling Point [K]	Critical Temp. [K]	Critical Pressure [Bar]	Critical Volume (cm^3/mol)	Acentric Factor
[HMIm][Tf_2N]	$C_{12}H_{19}N_3F_6S_2O_4$	447.41	897.6	1287.3	23.9	1121.3	0.3539
R-134a	$C_2H_2F_4$	102.03	246.85	374.25	40.6	0.2	0.3268
Carbon Dioxide	CO_2	44.01	194.7	304.25	73.8	94	0.2280
Note: ILs properties are predicted as they decompose well before the boiling and critical points;[26] The property data of R-134a and CO_2 are from the PE2000 database[27]							

Table 6.2 The binary interaction parameters and modeling results

System	T [°C]	Number Data Points	Interaction Parameters		AARD%
			k_{12}	l_{12}	
[HMIm][Tf_2N] + CO2	25	7	0.0579	0.0826	6.17
	50	10	0.0299	0.0316	2.25
	70	8	0.0329	0.0054	5.93
[HMIm][Tf_2N]+ R134a	25	10	0.0062	0.0025	6.75
	50	14	0.0029	0.0070	3.37
	75	5	-0.0224	0.0057	0.39

6.3 Results and Discussions

6.3.1 Waste heat available from an Automobile

In order to evaluate the amount of waste heat of an automobile in the coolant and exhaust gas, Boatto *et al.* [1, 30] performed experimental work on a four-cylinder spark-ignition engine that was usually mounted in a passenger car. The engine speed and fuel, coolant and exhaust heat duty on engine were studied. Given a specific

engine speed, the fuel duty equals the sum of engine duty, exhaust duty and coolant duty. Table 6.3 gives the experimental results at engine speed 1300 rpm, 1500 rpm and 2000 rpm. For instance, when the speed of the motor is at 1300 rpm, the fuel duty is 30kW, while engine duty, exhaust duty, coolant duty are 10kW, 5kW and 15kW respectively. When the engine speed is increased to 1500 rpm, the fuel duty is 45kW. Engine duty, exhaust duty, coolant duty are increased to 14kW, 8 kW, and 23kW. Similarly, for 2000 rpm engine speed (cruise status), they are 70kW, 24kW, 17kW, 29kW. Therefore, if the waste heat can be used and recovered from the exhaust system, the available heat is from 5 kW to 17 kW, when the motor engine runs from 1300 rpm to 2000 rpm.

Table 6.3 Experimental data from the work of Boatto *et al.* [1]

Engine Speed (RPM)	Fuel duty (kW)	Engine duty (kW)	Exhaust duty (kW)	Coolant duty (kW)
1300	30	10	5	15
1500	45	14	8	23
2000	70	24	17	29

6.3.2 Vapor compression refrigeration performance

Table 6.4 lists the experimental results for the vapor compression system using R-134a as refrigerant at both idle and cruise conditions, which were done by Boatto et. al. [1, 30] The results show that at idle conditions, the mid-size car can provide the cooling capacity of 3.1 kW, the COP is 2.8, but needs the input work of 1.1kW. At cruise conditions, the cooling capacity is 6.21kW, and at the same COP,

the input work is 2.2kW. These are approximately 9.2 % of the total work available by the engine at 2000 RPM.

Table 6.4 Experimental results of a vapor compression system at both idle and cruise conditions by Boatto *et al.* [1]

P_{con} [kpa]	P_{eva} [kpa]	T_{con} [° C]	T_{evp} [° C]	RPM	$\dot{m}_{ref}$ [kg/s]	$\dot{W}_{com}$ [kW]	$\dot{Q}_{con}$ [kW]	$\dot{Q}_{eva}$ [kW]	COP
1574	314	57	0	1000	1.37×10^{-4}	1.1	4.21	3.1	2.8
1574	314	57	0	2000	1.37×10^{-4}	2.2	8.42	6.21	2.8

6.3.3 Use R134a and [HMIm][Tf_2N] as working fluids for vehicle air conditioning

6.3.3.1 Model system at typical conditions

In order to compare the vapor compression system and absorption system for potential use in automotive air conditioning, the absorption cycle simulation is performed to achieve the same level of cooling (Q_{eva}) at the found in the vapor compression system described above (Table 6.4). Table 6.5 gives the operating conditions for a vehicle air-conditioning system by using [HMIm][Tf_2N] and R134a as working fluids that is needed to produce identical cooling capacity (6.2kW) as the vapor compression system at 2000RPMs. The condenser and evaporator temperature are kept as the same as for the vapor compression system described above.

To compare the performance of absorption air conditioning system with vapor compression system, the operating conditions, including the condenser temperature (T_{con}), the evaporator temperature (T_{evp}) are chosen the same as in Table 6.4. T_{con}, 57 °C, is the actual condenser temperature of the fluid for a heat exchanger operating at 70% efficiency and an ambient (outdoor) temperature of 40°C. The temperature of the evaporator is usually set as low as possible, but often in most automobiles around 0 °C. The absorber temperature (T_{abs}) is generally set from 5°C – 35 °C, and 25 °C is chosen here for milder conditions. For given condenser and absorber temperatures, there is a minimum temperature of the generator (T_{gen}), below which the absorption cycle can not function. For this case, 118 °C is minimum generator temperature to make the mole fraction of refrigerant in strong solution to be less than that in weak solution. Thus, 120 °C is chosen here for generator temperature. The heat rate of the evaporator (Q_{eva}) represents the cooling capacity, which is 6.2 kW as the same as vapor compressor air conditioning system.

The results are shown in Table 6.6. To reach the cooling capacity as 6.2kW, the low pressure in the evaporator and the absorber is 292.8 kPa. The high pressure in the condenser and generator is 1565.6 kPa. The mass flowrate for refrigerant, strong solution and weak solution are 0.05 kg/s, 1.30 kg/s, 1.35 kg/s respectively. The heat input for the generator is 15.14 kW. The work for the pump is 0.45 kW, and the COP is 0.41. Compared with vapor compression system, the COP of absorption system is less than the vapor compression cycle. The COP of the vapor compression cycle is the ratio of cooling effect over work input, while the COP of the absorption is ratio of

cooling effect over heat input, which can be waste heat. Thus, only comparing COPs from each of the systems may be misleading, as mechanical energy is a higher quality (more expensive) form of energy compared with heat. The absorption air conditioning system does contain a small re-circulating pump between the absorber and generator. Pumps are much more thermodynamically efficient than compressors. At cruise conditions, the vapor compression system needs about 2.2 kW of mechanical work, while the absorption system needs only 0.45kW, which is about 80 % lower. The input heat for the generator is about 15.14 kW, which can be provided by the exhaust duty of 17kW and/or coolant duty of 29kW at cruise condition. Thus, the waste heat from either the exhaust or the coolant or some combination is enough to this absorption refrigeration system. It should be noted that these results are using just the model ionic liquid/R-134a system. With further molecular optimization of the ionic liquid, these results will improve.

6.3.3.2 Performance of the IL/R-134a system at different conditions

The ambient and process conditions listed in Tables 6.5 and 6.6, represent typical or average conditions. However, in different parts of the world (different climates), the ambient temperatures will change. This typically modifies the temperature at the condenser and absorber. Different vehicles will produce different temperatures in the coolant and exhaust, thus different potential temperatures to the generator. The heat exchangers to transfer this waste energy to the generator will have different capabilities. The changing parameters will be addressed in following sections.

Table 6.5 Operating conditions for vehicle air-conditioning system by using [HMIm][Tf_2N] and R134a as working fluids

T_{abs} [° C]	T_{con} [° C]	T_{eva} [° C]	T_{gen} [° C]	Q_{eva} [kW]
25	57	0	120	6.2

Table 6.6 Simulation results for vehicle air-conditioning system by using [HMIm][Tf_2N] and R134a as working fluids

P_{con} [kpa]	P_{eva} [kpa]	$\dot{m}_{ref}$ [kg/s]	$\dot{m}_{strong}$ [kg/s]	$\dot{m}_{weak}$ [kg/s]	$\dot{Q}_{con}$ [kW]	$\dot{Q}_{gen}$ [kW]	$\dot{W}_{pump}$ [kW]	COP
1565.6	292.8	0.05	1.30	1.35	11.54	15.14	0.45	0.41

6.3.3.3 Performance of the IL/R-134a system at a lower generator and condenser temperature

In the previous case, the condenser was operated in 57 °C, and the generator was operated in 120 °C. Most coolant temperatures are maintained below 100 °C for the safety and performance of the engine. So, if only the coolant is desired to be used to heat the generator, then a lower generator temperature is needed. The simulation was performed at milder conditions, i.e. the condenser at 40 °C and the generator at 90 °C. The results are given in Tables 6.7 and 6.8. The heat input for the generator, to achieve the same cooling effect, decreases to 12.25 kW. The pump only needs 0.24 kW. With the same cooling capacity, the COP increases to 0.51.

Table 6.7 Operating conditions for vehicle air-conditioning system by using [HMIm][Tf_2N] and R134a as working fluids

T_{abs} [° C]	T_{con} [° C]	T_{eva} [° C]	T_{gen} [° C]	Q_{eva} [kW]
25	40	0	90	6.2

Table 6.8 Simulation results for vehicle air-conditioning system by using [HMIm][Tf_2N] and R134a as working fluids

P_{con} [kpa]	P_{eva} [kpa]	$\dot{m}_{ref}$ [kg/s]	$\dot{m}_{strong}$ [kg/s]	$\dot{m}_{weak}$ [kg/s]	$\dot{Q}_{con}$ [kW]	$\dot{Q}_{gen}$ [kW]	$\dot{W}_{pump}$ [kW]	COP
1016.6	292.8	0.04	1.24	1.28	9.43	12.25	0.24	0.51

6.3.3.4 Effect of generator duty on performance

When the engine speed is increased from 1300rpm to 2000rpm, the available exhaust duty has a range from 5kW to 17kw (Table 6.3). In addition, different vehicles will have different heat transfer equipment and performance. The effects of different generator heat inputs on the rest of the system are investigated. The temperature of all of the units are kept the same as 6.4.3.3. As shown in Figure 6.4, the duties of all units increase with the increased heat input to generator. As shown the cooling effect (Q_{evap}) increases. However, this also requires that the condenser and absorber must increase. The cooling capacity (evaporator heat rate) increases from 2.32 kW to 7.87 kW. At idle conditions, the vapor compression system can provide 3.1kW cooling capacity. For the absorption system to provide 3.1 kW

cooling, the heat input for the generator has to be 6.69 kW, which can be provided by exhaust gases At cruise conditions, 12.25 kW can be sent to the generator to provide 6.2 kW cooling capacity, which is same as the vapor compressor system. At a generator input of 17kW, 7.87 kW of cooling can be obtained, which is even larger than vapor compressor system.

6.3.3.5 The effects of the generator and absorber temperature on performance

In this case , the heat input for the generator is kept constant as 12.25 kW, but the temperature of the generator is changed from 50 °C to 110 °C and the temperatures of evaporator, condenser and absorber are kept as same as in Table 6.5. The effects of the generator temperature on the circulating ratio of refrigerant are shown in Figure 6.5. The circulating ratio, defined as ratio of weak solution mass flow rate and the refrigerant mass flow rate, decreases with increasing generator temperature. At lower generator temperatures, less refrigerant vapor comes from solution, but the difference of refrigerant concentration in the weak and strong solution is relatively small. However, the circulation ratio becomes much higher at the lower generator temperatures. In this case, a relatively large solution pump would be required, which would decrease the efficiency of the process. When the generator temperature is increased, the refrigerant concentration will increase, and lower circulating ratios will be required.

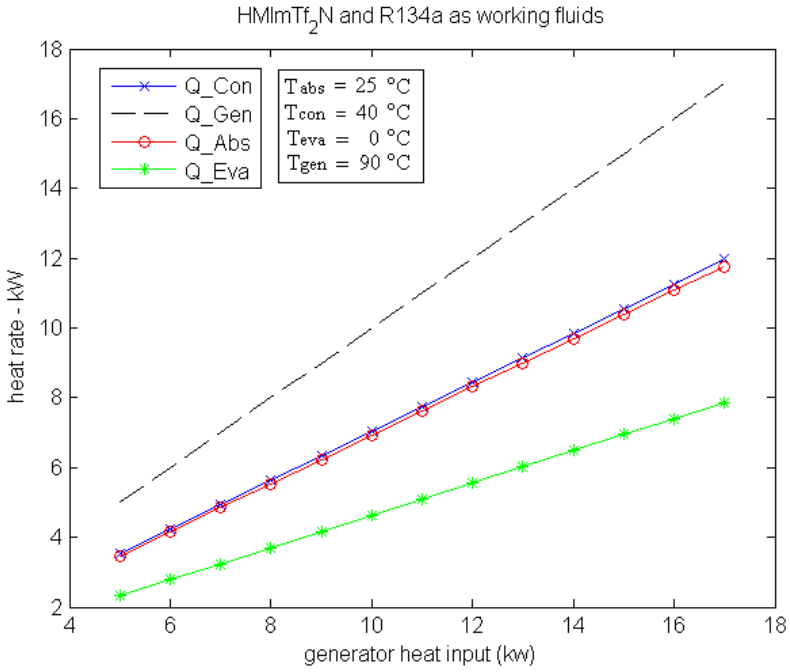

Figure 6.4 Heat duties can be provided with available waste heat for generator.

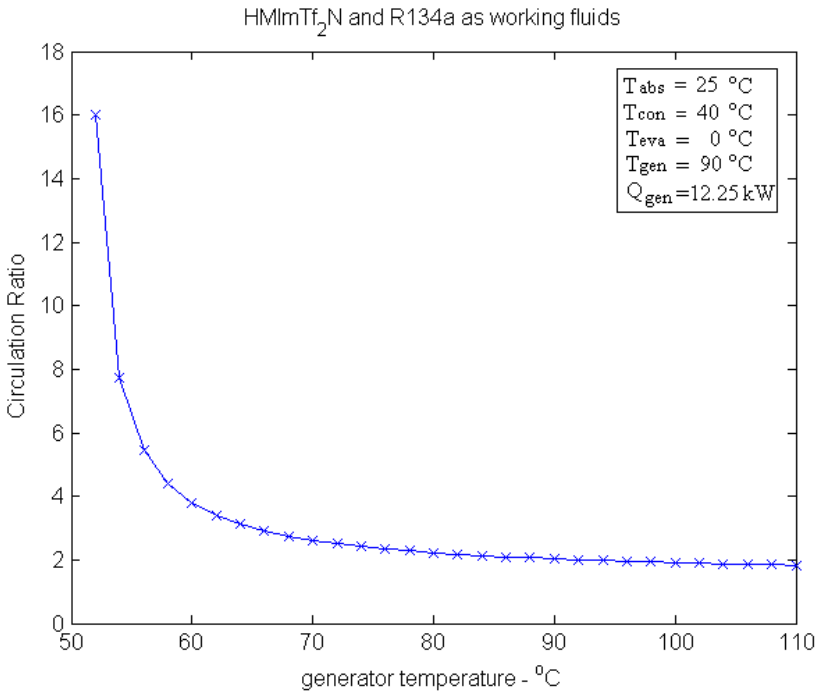

Figure 6.5 Effect of generator temperature on refrigerant circulation ratio

The effect of absorber temperature on circulations ratio and performance were also investigated. If the absorber temperature varies as 5 °C, 15 °C and 25 °C and the evaporator and condenser temperature are kept the same as 0 °C and 40 °C respectively, the effect of generator temperature on circulation ratio changes. As shown in Figure 6.6, the higher absorber temperature results in the higher the circulation ratio at the same generator temperature. At the higher absorber temperature, less refrigerant is absorbed. Therefore, a higher circulation ratio is needed to maintain the same level of cooling at the evaporator. The generator temperature has a greater effect on the circulation ratio at a higher absorber temperature. For the case study of an absorber temperature of 25 °C, the circulation ratio is 29.5 at a generator temperature of 90 °C, which is about 4 times the circulation ratio at 110 °C (7.5). At 15 °C in the absorber, the circulation ratio changes from 5.0 at 90°C in generator to 3.6 at 110°C in generator. At 5 °C in the absorber, the circulation ratio is 1.9 at a generator temperature 90 °C, which is similar to that at 110 °C, 1.8. Both absorber and generator temperatures are design parameters for absorption refrigeration systems.

As discussed above, the lower absorber temperature results in higher refrigerant solubility in the IL solvent, which results in a lower circulation ratio. Figure 6.7 shows the effect of the generator and absorber temperature on COP with fixed heat input. At 25 °C, an optimum generator temperature exists around 100 °C. Below it, COP increases with generator temperature. The trend reverses when the generator temperature is higher than 100 °C. For absorber temperatures at 5 °C and

15 °C, the optimum generator temperatures are 58 °C and 82 °C respectively. In general, COP increases with the generator temperature until a maximum value and then decreases. Since at lower generator temperatures, the solution in the generator will release a less mount of vapor to the condenser. However, when the saturation condition of solution is reached, no more vapor is generated even in higher generator temperature. Therefore, COP reduces with increasing generator temperature after reaching the maximum. Sathyabhama *et al.* [31] showed the similar effect of generator temperature on COP and circulation ratio for ammonia-water absorption system. Bourouis *et al.* [32] investigated the performance of air–cooled absorption air-conditioning systems working with water – (LiBr + LiI + $LiNO_3$ + LiCl). They report trends of generator temperature on COP similar to this work.

6.3.3.6 The effects of the condenser temperature on heat duty and COP

This case study investigates the effects of changing condenser temperature from 30 °C to 50 °C under the following operating conditions: the heat input to the generator is maintained at 12.25kW, the evaporator temperature is 0 °C, the generator temperature is 105 °C and the absorber temperature is 25 °C. The condenser temperature is related to environmental or ambient temperature. Thus, the condenser temperature set point is equal to ambient temperature plus the condenser offset temperature, i.e. heat exchanger efficiency. The efficiency has been assumed to be 70% for these calculations but can vary from 3.3-13.9°C difference. If the offset temperature is set as 6 °C, and ambient temperature is from 25°C to 44°C, the condenser temperature is set from 30°C to 50°C.

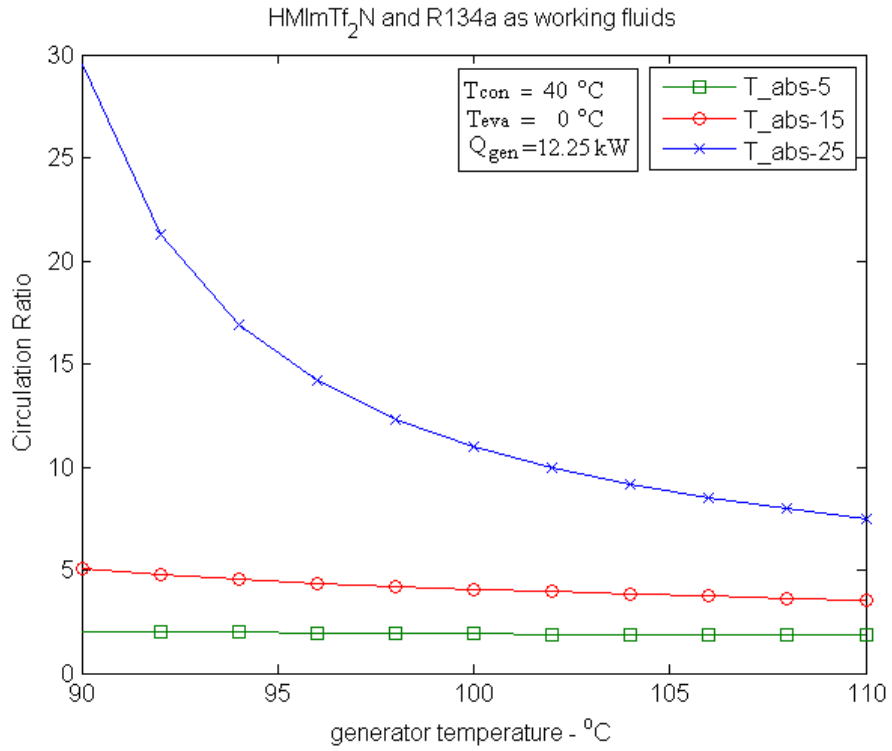

Figure 6.6 Effect of absorber temperature on refrigerant circulation ratio

As shown in Figure 6.8, the heat rates of the absorber, condenser and evaporator decrease with the condenser temperature given the same heat input to the generator. The evaporator provides 5.88 kW cooling capacity at the condenser temperature of 30 °C and decreases to 4.07 kW at 50°C. It means that the air conditioning system could provide sufficient cooling capacity at idle condition even in a hot season. If the heat input is kept at 12.25 kW, the cooling capacity (4.07kW) is not sufficient at cruise conditions. Since, the waste heat provided increases with RPM, higher RPM can generate more waste heat. If the heat input of the generator is increased to 16 kW, the cooling capacity of evaporator is from 7.68kW at 30 °C to

6.2 kW at 46 °C and decreases to 5.31 kW at 50°C. If the heat input is increased to 18.7 kW, the system can provide 6.2 kW cooling capacity even at 50 °C condenser temperature. It should be noted that the waste heat can be provided by both exhaust and coolant, and they both increase with engine speed (Table 6.3). It is thus feasible to utilize the energy from waste heat to reach enough cooling capacity for a car. The COP versus condenser temperature is plotted in Figure 6.9, which shows that the COP decreases with condenser temperature.

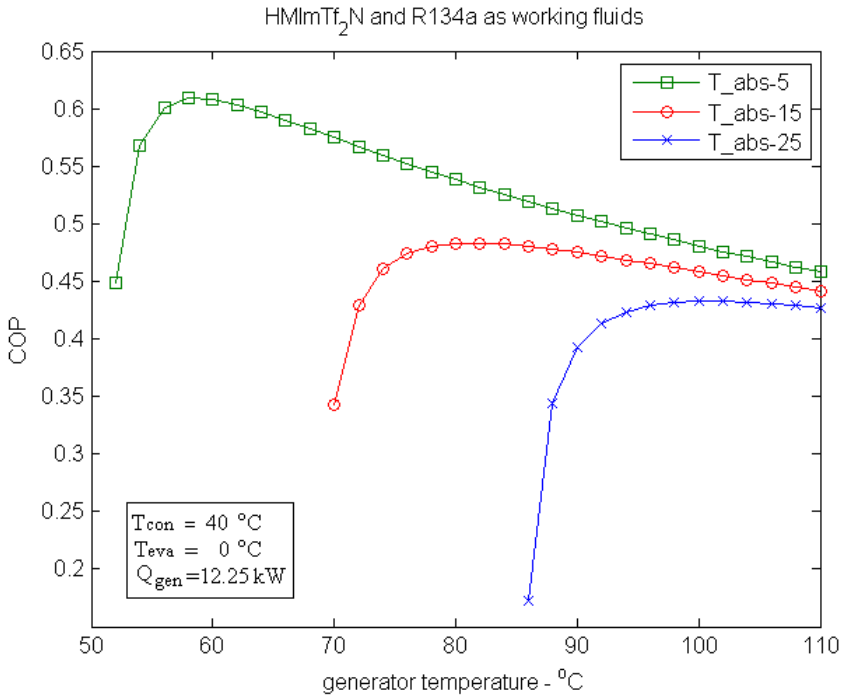

Figure 6.7 Effect of generator temperature on COP

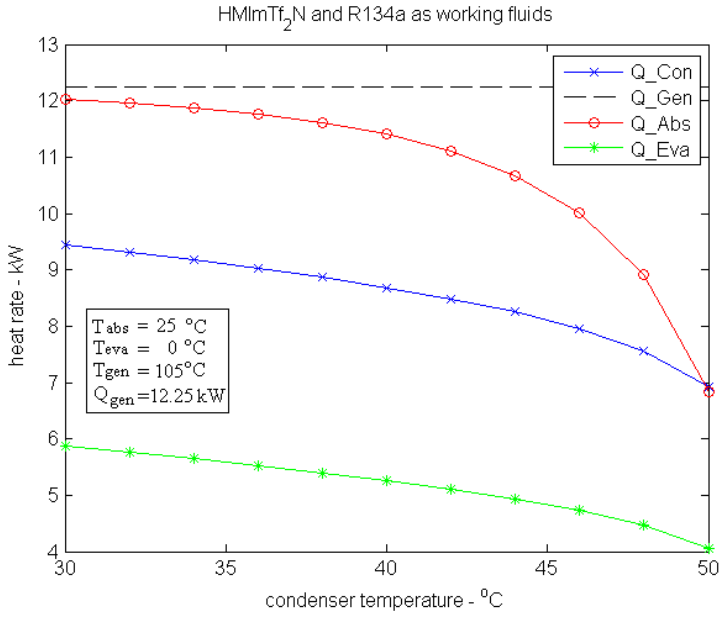

Figure 6.8 Effect of condenser temperature on heat rate

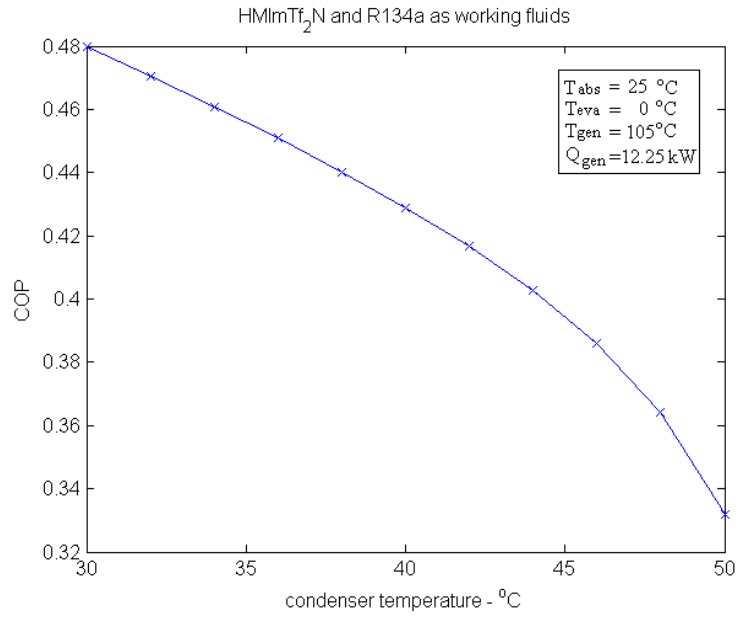

Figure 6.9 Effect of condenser temperature on COP

6.3.4 Use CO_2 and [HMIm][Tf_2N] as working fluids

The use of CO_2 as a refrigerant has gained renewed interest in the air conditioning and refrigeration markets due to the negative environmental impacts of the current use of HCFC and HFC refrigerants. Since R-134a has a global warming potential (GWP) of 1300, in EU it will be restricted from 2011 in all new cars and totally phase out by 2017. CO_2, known as refrigerant R744, has been a natural refrigerant for over one century. It is neither flammable nor toxic like NH_3, HFCs and HCFC. CO_2 is also cheap and ecologically clean (ODP = 0, GWP= 1) substance. The cost of carbon dioxide is about 100~120 times lower than that of R134a. As an alternative refrigerant of R-134a, CO_2 offers the following advantages: low price, simple servicing and compatibility with mineral oils. The following case studies are not specific to automobile applications, but for general industrial or home air conditioning systems using CO_2 as refrigerant.

6.3.4.1 Vapor compression and absorption systems

Officine Mario Dorin S.p.A. has published data on TCS CO_2 compressor model [33]. The TCS model is a single stage compressor that is able to operate in transcritical conditions and commercial refrigeration for medium-low evaporating temperature. The TCS 340 compressor does not have a common condenser, but a gas cooler, which is used to cool down the compressed CO_2. Thus, the global efficiency of the system is strongly dependent on how efficiently the heat exchange inside the gas cooler is. Table 6.9 [33] lists the parameters of a TCS compressor. The

evaporator is operated at -10 °C, the condenser temperature is at 15 °C, the duty input for the compressor is 3.3 kW. The cooling capacity is 9.5 kW, and the COP is 2.88.

Table 6.9 Parameters of a TCS range compressors using CO_2 as refrigerant [31].

Model	P_{con} [bar]	P_{evp} [bar]	T_{con} [° C]	T_{eva} [° C]	Q_{eva} [kW]	W_{comp} [kW]	COP
TCS 340	20.65	75	15	-10	9.5	3.3	2.88

The case study investigate an absorption system with model [HMIm][Tf_2N] and CO_2 as working fluids. Table 6.10 lists the operating parameters. The condenser (gas cooler) and evaporator temperatures are kept the same as the vapor compression system. The absorber temperature is set as 20 °C and the generator temperature is 110 °C. The simulation results are given in Table 6.11.

To reach the same cooling capacity of the evaporator of 9.5 kW, COP of absorption cycle is 1.29, while for the vapor compression system, it is 2.88. As discussed in IL and R134a absorption system, these COPs are not comparable. Moreover, the work of pump in the absorption system is 0.82 kW, which is about 25% of the duty needed for the compressor, 3.3kW. The heat input for the generator is 7.36kW. These results were obtained for just the model IL/CO_2 system. Further molecular optimization of the IL would result in even better performance.

Table 6.10 Operating conditions for absorption air-conditioning system by using [HMIm][Tf_2N] and CO_2 as working fluids

T_{abs} [° C]	T_{con} [° C]	T_{eva} [° C]	T_{gen} [° C]	Q_{eva} [kW]
20	15	-10	110	9.5

Table 6.11 Simulation results for absorption air-conditioning system by using [HMIm][Tf_2N] and CO_2 as working fluids

Pcon [bar]	Peva [bar]	$\dot{m}_{ref}$ [kg/s]	$\dot{m}_{strong}$ [kg/s]	$\dot{m}_{weak}$ [kg/s]	$\dot{Q}_{con}$ [kW]	$\dot{Q}_{gen}$ [kW]	$\dot{W}_{pump}$ [kW]	COP
50.87	26.49	0.05	1.34	1.39	15.20	7.36	0.82	1.29

6.3.4.2 Effects of generator heat input on cool capacity of the absorption system

This case study investigates the effects of the heat input of generator which varies from 5 kW to 17 kW and can be probably obtained from the waste heat. As shown in Figure 6.10, the heat rates of all units increase with the heat rate of the generator. The cooling capacity of the evaporator increases from 6.4 to 21.95 kW. When the heat input is 7.46 kW, the potential cooling capacity is 9.5 kW. If the 17kW heat is input into generator, the cooling capacity can even reach 21.95 kW, which is about 130% higher than the vapor compression system.

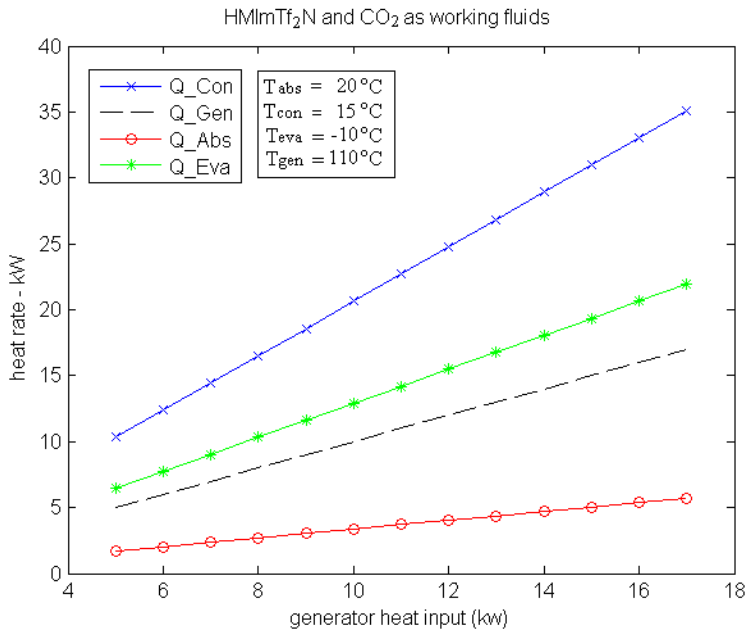

Figure 6.10 Heat capacity can be provided with available waste heat for generator

6.3.4.3 Effects of generator and absorber temperature on circulation ratio and COP

This case is to investigate the effect of the generator and absorber temperature on circulation ratio and COP. The condenser and evaporator temperature are kept the same as previous case, which are 15 °C and -10 °C, while the heat input of the generator is set as 7.36 kW. When the generator temperature is changed from 110 °C to 130 °C, the concentration of refrigerant in the strong solution is increased; more refrigerant leaves the generator and enters the refrigeration circuit, resulting in a decreased circulation ratio as shown in Figure 6.11. Similar to the case study of [HMIm][Tf_2N] and R-134a, a larger pump is needed at a low circulation ratio. The effect of the absorber temperature on circulation ratio is shown in Figure 6.12. With higher temperatures in the absorber, the refrigerant concentration in weak solution is lower, which results in a higher circulation ratio.

As shown in Figure 6.12 when the absorber temperature is 20 °C, the circulation ratio is 28.55 at generator temperature of 110 °C, which is about 2.1 times that of 130 °C, 13.67. At the absorber temperature of 10 °C, the circulation ratio changes from11.18 to 7.97. At 5 °C, the circulation ratio is 8.27 at generator temperature 110°C, which is about 1.29 times that of 130 °C, 6.43. Figure 6.13 reveals that the COP decreases with the generator temperature. Since both the absorber temperature and generator temperature affect the system performance significantly, these are two important parameters to be optimized. In the range of investigation here, higher absorber temperature with lower generator temperature results in high circulation ratio and better performance.

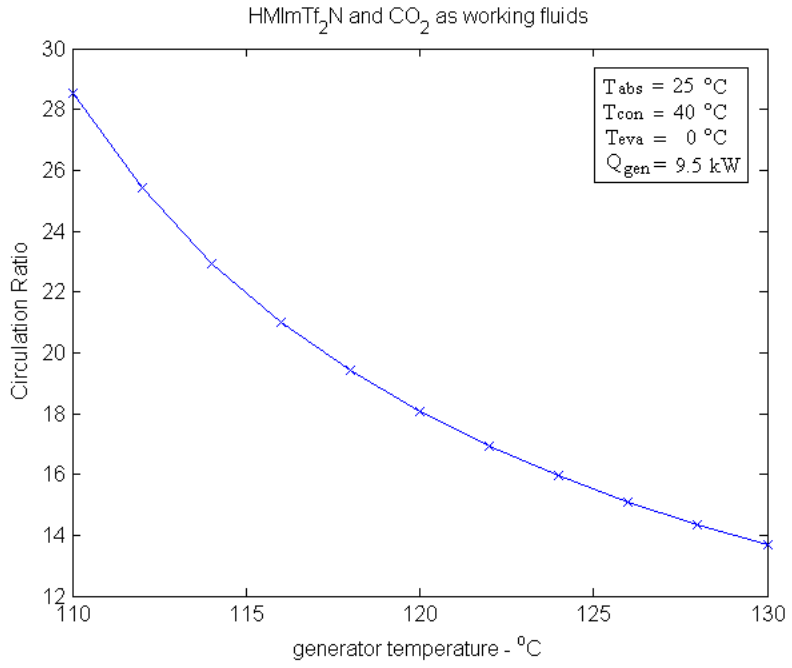

Figure 6.11 Effect of generator temperature on refrigerant circulation ratio

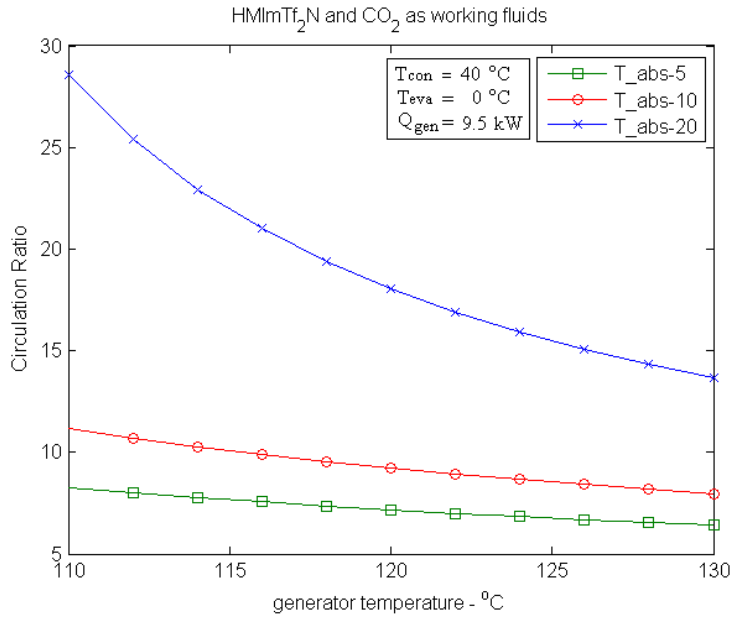

Figure 6.12 Effect of absorber temperature on refrigerant circulation ratio

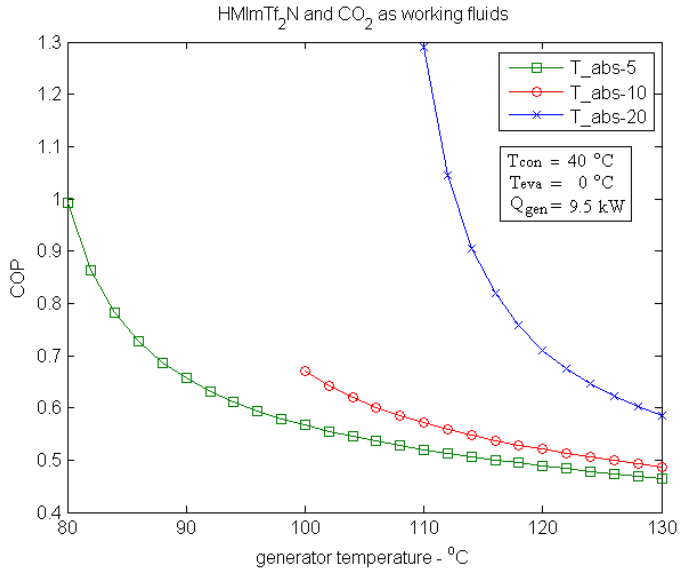

Figure 6.13 Effect of generator temperature on COP

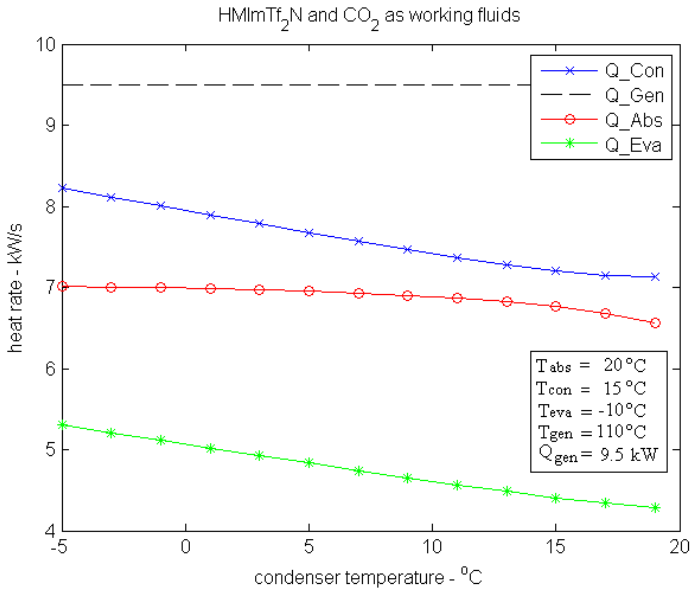

Figure 6.14 Effect of condenser temperature on heat rates

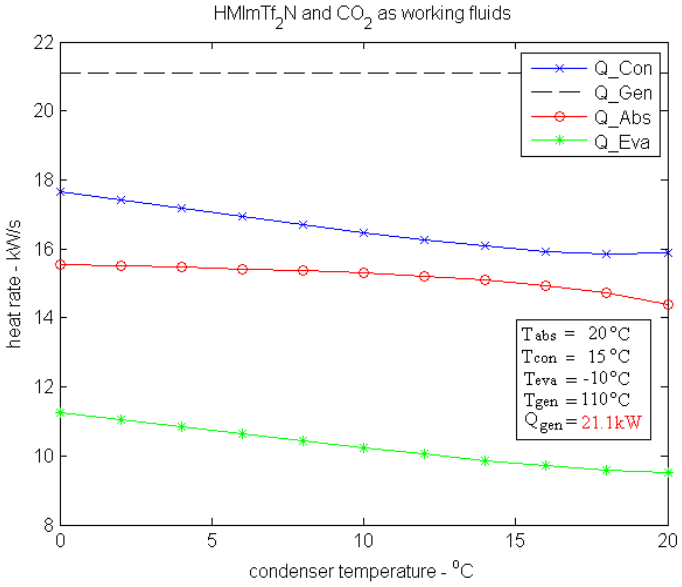

Figure 6.15 Effect of condenser temperature on the heat rates with larger heat input to the generator

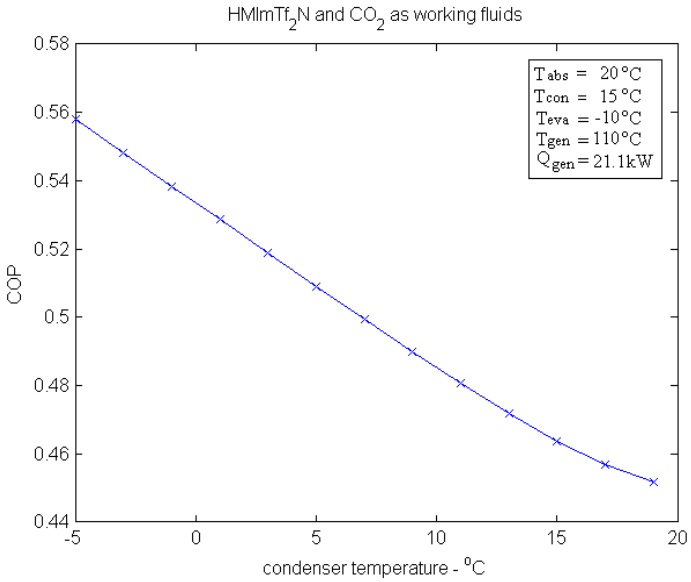

Figure 6.16 Effect of condenser temperature on COP

6.3.4.4 Effects of the condenser temperature on circulation ratio and performance

This case study investigates the effects of the condenser temperature on the performance of the absorption system. With CO_2 refrigerant, the condenser is a gas cooler and the global efficiency of the system strongly depends on the heat exchange efficiency inside the gas cooler. Thus, higher refrigerating capacities are found for lower gas cooler outlet temperatures. The parameters of this case study are: the heat input to the generator is 9.5 kW, the evaporator temperature is 0 °C, the generator temperature is 110 °C, the absorber temperature is 20 °C, and the condenser temperature changes from -5°C to 20°C. As shown in Figure 6.14, heat rates of absorber, condenser and evaporator all decrease with the condenser temperature. The

evaporator provides 5.30 kW cooling capacity at -5 °C. The cooling capacity decreases to 4.29 kW at 20°C. . If the heat input of generator is increased to 21.1 kW, (see Figure 6.15), the system can provide 11.28 kW cooling capacity at 0°C and 9.51 kW cooling capacity even at 20 °C. Figure 6.16 reveals that COP decreases with condenser temperature.

6.4 Conclusions

The simulation studies reveal that the absorption refrigeration system using ionic liquids are viable alternatives to traditional vapor compression ones. Simulation studies reveal that an absorption refrigeration system with [HMIm][Tf_2N] and R-134a as working fluid is feasible for automobile applications. The system can be operated by the waste heat from exhaust gases and the engine coolant system, thus reducing fuel consumption and air pollution. As ionic liquids have no vapor pressure, an absorption system would have no need for a bulky rectifier. With appropriate operating conditions, the working fluids using [HMIm][Tf_2N] and R-134a, [HMIm][Tf_2N] and CO_2 can be operated with only waste heat to produce comparable cooling capacity as vapor compression system. The optimal operating conditions and ionic liquid/refrigerant pairs are needed to be investigated in the future.

6.5 References

1. Boatto, P., C. Boccaletti, G. Cerri, and C. Malvicino, *Internal combustion engine waste heat potential for an automotive absorption system of air conditioning Part 1: tests on the exhaust system of a spark-ignition engine.* Proceedings of the Institute of Mechanical Engineers, 2000. **214**(8): p. 979-982.
2. John Rugh, a. Hovland, and S. Andersen. *Significant Fuel Savings and Emission Reductions by Improving Vehicle Air Conditioning*. 2004, Available from: http://www.nrel.gov/vehiclesandfuels/ancillary_loads/publications.html.
3. U.S. Envionmental protection agency, *Mobile Air Conditioning*. 2009 [cited 2009 October 22]; Available from: http://www.epa.gov/cppd/mac/
4. Bogart, M., *Ammonia Absorption Refrigeration in Industrial Processes*. illustrated ed. 1981: Gulf Pub. Co., Book Division,.
5. Kurem, E. and I. Horuz, *A comparison between ammonia-water and water-lithium bromide solutions in absorption heat transformers.* International Communications in Heat and Mass Transfer, 2001. **28**(3): p. 427-438.
6. Horuz, I., *A comparison between ammonia-water and water-lithium bromide solutions in vapor absorption refrigeration systems.* International Communications in Heat and Mass Transfer, 1998. **25**(5): p. 711-721.
7. Herold, K.E., R. Radermacher, and S.A. Klein, *Absorption Chillers and Heat Pumps*, ed. C. Oress. 1996.

8. Van Valkenburg, M.E., R.L. Vaughn, M. Williams, and J.S. Wilkes, *Thermochemistry of ionic liquid heat-transfer fluids.* Thermochimica Acta, 2005. **425**: p. 181-188.

9. Jacquemin, J., M.F. Costa Gomes, P. Husson, and V. Majer, *Solubility of carbon dioxide, ethane, methane, oxygen, nitrogen, hydrogen, argon, and carbon monoxide in 1-butyl-3-methylimidazolium tetrafluoroborate between temperatures 283 K and 343 K and at pressures close to atmospheric.* Journal of Chemical Thermodynamics, 2006. **38**(4): p. 490-502.

10. Crosthwaite, J.M., M.J. Muldoon, J.K. Dixon, J.L. Anderson, and J.F. Brennecke, *Phase transition and decomposition temperatures, heat capacities and viscosities of pyridinium ionic liquids.* Journal of Chemical Thermodynamics 2005. **37**(6): p. 559-568.

11. Bernot, R.B., M.; Evans-White, M.; Lamberti, G.,, *Acute and chronic toxicity of imidazolium-based ionic liquids on daphnia magna.* Environ. Toxicol. Chem. , 2005. **24**(1): p. 87-92.

12. Gathergood, N., M. Garcia, and P. Scammells, *Biodegradable ionic liquids: Part I. Concept, preliminary targets and evaluation.* Green Chemistry 2004. **6**(2): p. 166 -175.

13. Jastorff, B., R. Stoermann, J. Ranke, K. Moelter, F. Stock, B. Oberheitmann, W. Hoffmann, J. Hoffmann, M. Nuechter, B. Ondruschka, and J. Filser, *how hazardous are ionic liquids? Structure-activity relationships and biological*

testing as important elements for sustainability evaluation. Green Chemistry, 2003. **5**(2): p. 136-142.

14. Stepnowski, P., A. Skladanowski, A. Ludwiczak, and E. Laczynska, *Evaluating the cytotoxicity of ionic liquids using human cell line hela.* . Hum. Exp. Toxicol., 2004. **23**(11): p. 513-517.

15. Uerdingen, M., C. Treber, M. Balser, G. Schmitt, and C. Werner, *Corrosion behaviour of ionic liquids.* Green Chemistry 2005. **7**(5): p. 321-325.

16. Howlett, P.C., D.R. MacFarlane, and A.F. Hollenkamp, *High Lithium Metal Cycling Efficiency in a Room-Temperature Ionic Liquid.* Electrochemical and Solid-State Letters 2004. **7**(5): p. A97-A101.

17. Howlett, P.C., N. Brack, A.F. Hollenkamp, M. Forsyth, and D.R. MacFarlane, *Characterization of the Lithium Surface in N-Methyl-N-alkylpyrrolidinium Bis(trifluoromethanesulfonyl)amide Room-Temperature Ionic Liquid Electrolytes.* . Journal of the Electrochemical Society 2006. **153**(3): p. A595-A606. .

18. Holbrey, J.D. and K.R. Seddon, *Ionic liquids.* Clean Prod. Proc., 1999. **1**(4): p. 223-236.

19. Jain, N., A. Kumar, S. Chauhan, and S.M.S. Chauhan, *Chemical and biochemical transformations in ionic liquids.* Tetrahedron Letters, 2005. **61**(5): p. 1015-1060.

20. Marsh, K.N., J.A. Boxall, and R. Lichtenthaler, *Room temperature ionic liquids and their mixtures-a review.* Fluid Phase Equilibria, 2004. **219**(1): p. 93-98.

21. Huddleston, J.G., A.E. Visser, W.M. Reichert, H.D. Willauer, G.A. Broker, and R.D. Rogers, *Characterization and comparison of hydrophilic and hydrophobic room temperature ionic liquids incorporating the imidazolium cation.* Green Chemistry, 2001. **3**(4): p. 156-164.

22. Peng, D.Y. and D.B. Robinson, *A New Two-Constant Equation of State.* Industrial and Engineering Chemistry: Fundamentals, 1976. **15**: p. 59-64.

23. Lemmon, E.W., M.L. Huber, and M.O. McLinden, *NIST Reference Fluid Thermodynamic and Transport Properties - REFPROP Version 8.0*. 2007: Gaithersburg, Maryland.

24. Dai, W., K. Ochi, and K. Kolima, *Excess enthalpy data in binary system containing a supercritical fluid and their correlation.* J.Chem. Eng. Data, 1998. **43**: p. 687-694.

25. Ge, R., C. Hardacre, J. Jacquemin, P. Nancarrow, and D.W. Rooney, *Heat Capacities of Ionic Liquids as a Function of Temperature at 0.1 MPa. Measurement and Prediction.* J. Chem. Eng. Data, 2008. **53**(9): p. 2148–2153.

26. Lewis, K.L., S.E. Mosedale, and C.J. Wormald, *The enthalpies of mixing of methane + argon, methane + nitrogen, and methane + hydrogen in the gaseous and two-phase regions.* J. Chem. Thermodyn., 1977. **9**(2): p. 121-31.

27. Walas, S., *Phase equilibria in chemical engineering*. 1985.

28. Castier, M. and S.I. Sandler, *Critical points with the Wong-Sandler mixing rule--II. Calculations with a modified Peng-Robinson equation of state.* Chemical Engineering Science, 1997. **52**(20): p. 3579-3588.

29. Pfohl, O., S. Petkov, and G. Brunner, *PE 2000 – A Powerful Tool to Correlate Phase Equilibria*. 2000, München: Herbert Utz Verlag.

30. Boatto, P., C. Boccaletti, G. Cerri, and C. Malvicino, *Internal combustion engine waste heat potential for an automotive absorption system of air conditioning Part 2: the automotive absorption system.* Proceedings of the Institute of Mechanical Engineers, 2000. **214**(8): p. 983-989.

31. Sathyabhama, A. and T.P.A. Babu, *thermodynamic simulation of ammonia-water absorption refrigeration system.* thermal science, 2008. **3**: p. 45-53.

32. Bourouis, M.V., M. Medrano, and A. Coronas. , *Performance of air -cooled absorption air-conditioning systems working with water - (LiBr + LiI + $LiNO_3$ + LiCl).* Proceedings of the Institution of Mechanical Engineers, Part E: Journal of Process Mechanical Engineering, 2005. **219**(2): p. 205-213.

33. Officine Mario Dorin S.p.A, 2009 [cited 2009 October 15th]; Available from: http://www.dorin.com/documents/News/4/CO2_ctg_1207A.pdf.

Chapter 7 Phase Equilibrium Study of the Hydroformylation/Hydrogenation Reaction Using Ionic liquids/CO_2 Biphasic System as Reaction Media

Gas-liquid catalyzed reactions are very typical in the chemical industry, including hydrogenation, hydroformylation, and oxidation and so on. The choice of solvent can dramatically affect the reaction kinetics and the final separations. In order to fully understand the reaction with alternative solvents, complete fundamental investigations are necessary, such as thermodynamic, kinetic and mass transport properties, polarity, etc. To develop these reactions, the knowledge of the phase behavior of a reaction system is very important, as it helps to understand and explain the reaction kinetics results, which is also pre-requirement to plan and design the experiments and determine the operating conditions (temperature, pressure and concentration, etc).

In this Chapter, the phase behavior of hydroformylation and hydrogenation using ionic liquid and CO_2 as reaction media were investigated and analyzed. The effects of phase equilibrium on the catalytic reaction rate are discussed.

7.1 Introduction

7.1.1 Advantages of biphasic ionic liquids/CO_2

Biphasic reaction system is one system which has two phases. Generally, a biphasic system for homogeneous catalysts include lower phase with catalyst and reactants, and upper phase can carry the reactant in and phase the product out, but the

lower phase and catalyst do not dissolve in upper phase. The biphasic reaction media have been applied into a broad variety of reactions and solvents, including water and organic solvents,[1-6] fluorinated solvents,[7] ionic liquids and supercritical solvents like supercritical carbon dioxide [8-9]. The unique phase properties of IL/CO_2 make it a favorable biphasic solvent system. The CO_2 (upper phase) can deliver reactants and separate product from IL (lower phase), whereas CO_2 can be recompressed and recycled, IL phase with catalyst with catalyst can be reused. Therefore, the process is environmental benign. Moreover, if the product does not need further purification, the economical benefit will be a plus. In a commercial chemical process, the separation and purification units account for about >50% investment costs.

A biphasic ionic liquid/CO_2 system draws on the advantages of each of the respective technologies and helps overcome their challenges. Combining ionic liquid/CO_2 as reaction media forms a biphasic system, where catalyst and reactants dissolve in solvents and stay in one phase, the product, but catalyst will be extracted to the other phase after reaction. The catalyst left over in solvent phase can be recycled. Moreover, the attracting of the biphasic system is CO_2 can dramatically decrease the viscosity of ILs to that of common solvents, which results in increase the diffusivity of components in IL. In concurrent studies in Scurto lab, the viscosity of the IL, [HMIm][Tf_2N] was measured [8, 10]. The viscosity decreases approximately 80+% with up to 60 bar of CO_2 at 40°C. This decrease in viscosity has been used to predict the diffusivity in the ionic liquid with approximately a 3 fold improvement over the same pressure range.

The advantages of combining ionic liquids and CO_2 rather than using them individually have been reported by some groups. Several examples are chosen here. Scurto *et al.* [11-12] have demonstrated CO_2 can be a switch to separate ILs from organics, where CO_2 pressure/composition induces phase splitting into an IL-rich phase and an organic (or aqueous) phase. For gas reaction, Leitner and coworkers found that CO_2 pressure can increase the solubility of reaction gases into the IL-phase [13-14]. Another important finding which was reported by Scurto and Leitner [15-16], who demonstrated that CO_2 can dramatically decrease the melting point of many ionic solids, even lower the melting point over 100°C than their normal melting points. This greatly expands the numbers of compounds and functional groups of potential ionic liquids to be used as liquids in a process for various applications. We can also design ionic liquids in a variety of structures, and choose one that preferentially dissolves the homogeneous catalyst and reactants as solvent for a variety of catalytic reactions.

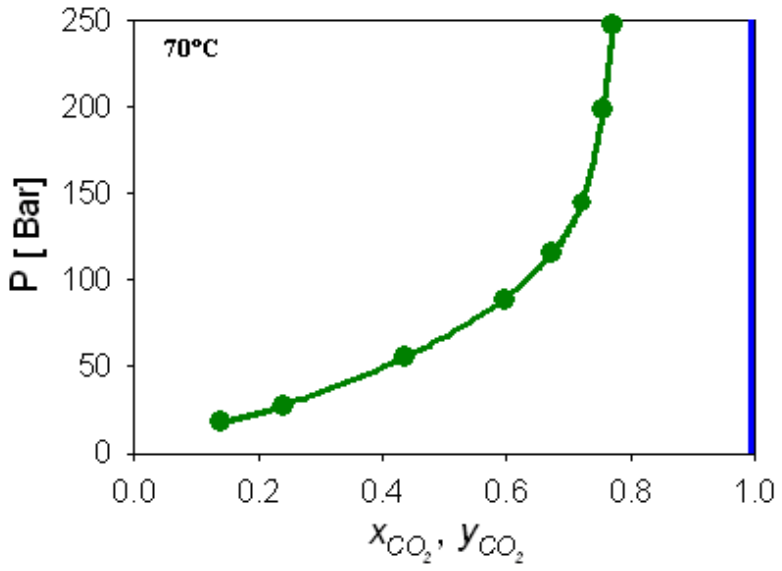

Figure 7.1 Phase behavior of the IL, [HMIm][Tf_2N] and CO_2 at 70°C. The solid line is smoothed data.

The global phase behavior of ionic liquid and CO_2 is discussed in Chapter 4. The phase behavior of [HMIm][Tf_2N] and CO_2 at 70°C were measured and illustrated in Figure 7.1. CO_2 is very soluble in the ionic liquid and reaches approximately 40% mole CO_2 at 50 bar and 65% mole at 100 bar. Below 100 bar, the solubility increases with pressure is approximately linear. Above 100 bar, the increase in pressure results in only marginal increase in solubility. Above 250 bar, the solubility increases slowly. In contrast, the ionic liquid in CO_2 phase is immeasurably insoluble, they does not become miscible (critical) for [BMIm][PF_6] and CO_2 even at hyperbaric pressures, e.g. 3100 bar at 40°C [17], which is unlike CO_2 with most organic solvents (CXLs), which become miscible (critical; one phase)

at moderate pressures (100-200bar)[18-19]. In Chapter 4 and 5, differences of phase behavior between ionic liquid/CO_2 and ionic liquid/ refrigerant gases were discussed, ionic liquid/ refrigerant system can be critical at moderate pressure. For instance, as shown in Chapter 4, we have measured [BMIm][PF_6] with R-134a becoming critical at approximately 110 bar at 50°C.

Therefore, the combination of compressed CO_2 and ionic liquids offers a number of benefits for catalyzed reactions, such as: ionic liquid phase sequesters the organometallic catalyst, the CO_2 phase becomes the mobile phase for reactants and products, the product can partition freely between IL phase and CO_2 phase, etc.

7.1.2 Literature survey of phase behavior of IL/organic component/CO_2 multicompoenent systems

Despite all the interests in ionic liquids/CO_2 as reaction media, phase behavior studies are still scarce in the literature, especially for multicomponent phase equilibria for reaction systems. Up to the date, investigations mostly focus on the binary reaction system. For Ionic liquid –organic component –CO_2 ternary system, Scurto *et al.* [11] used carbon dioxide to separate an organic compound–ionic liquid homogeneous mixture. Aki *et al.* [20] presented phase equilibria of different ionic liquid + organic +CO_2 mixtures and the factors to control the vapor-liquid-liquid equilibrium in ternary systems at 40 ºC: choice of organic, the type of IL, and the concentration of IL in the organic component.

Fu *et al.* [21] measured phase equilibrium of the ternary system "CO_2 + [BMIm][PF_6] + naphthalene" and found naphthalene concentration in CO_2-rich phase decreased

regularly with decreasing naphthalene molality in the liquid phase. Qi *et al.* [22] presented phase equilibrium data of CO_2/chloroaluminate ionic liquid/benzene ternary system at 60ºC and pressure ranging from 30 to 100 bar. Two- or three-phase region exists based on different initial molar ratios of composition. Pressure influences the equilibrium composition greatly in benzene rich phase. Zhang *et al.* [23] studied the phase behavior of CO_2 – water - [BMIm][BF_4]. At a fixed temperature or pressure, there can exist four phases. Compositions of the phases in three-phase region (ionic liquid-rich phase, water-rich phase, CO_2-rich phase) were measured and the distribution coefficients of [BMIm][BF_4] between IL-rich phase and water-rich phase were calculated. Zhang *et al.* [24] also measured the high-pressure phase behavior of CO_2/[BMIm][PF_6]/acetone and of CO_2/[BMIm][PF_6]/methonal system [25]. The distribution coefficients of the components between different phases were calculated based on the phase equilibrium data.

Nadjanovic-Visak *et al.* [26] also observed CO_2 pressure split the phases in systems with an ionic liquid. Water was shown to be a very good co-solvent. If a small amount of water is present in the [BMIm][Tf_2N]/1-butanol system, it will decrease the UCST as much as 1.5 K per mol% of water added to butanol.

All of these investigations provide a solid basis for separating the solute from ionic liquid phase using CO_2. There are only a few phase behavior study for reaction system. Kuehne *et al.* [27] investigated the liquid–vapor equilibrium for the ternary system [BMIm][BF_4] + 4-isobutylacetophenone + CO_2 of an intermediary hydrogenation reaction in the production of ibuprofen. This ternary system showed a

liquid–vapor equilibrium and a liquid–liquid equilibrium at 60 mol % CO_2 in the mixture under their experimental conditions,. Zhang *et al.* [28] showed the effect of CO_2 on the phase behavior of the reaction system and equilibrium conversion for esterification of acetic acid and ethanol in 1-butyl-3-methylimidazolium hydrogen sulfate([BMIm][HSO_4]) at 60.0 ºC up to 150 bar. The reaction system starts as one in the absence of CO_2, and then underwent two-phase→three-phase→two-phase transitions with increasing pressure. The pressure of CO_2 or the phase behavior of the system affected the equilibrium conversion of the reaction. The total equilibrium conversion was 64% without CO_2 and could be as high as 80% with 90 bar CO_2 pressure.

7.2 Motivation

Based on the literature survey, however, the role of CO_2 and its effect on the reaction is often reported conflicting, especially in terms of reaction rate/activity. Some of them think CO_2 will speed up the reactions, while the other believe it will reduce the reaction rate. Phase Equilibrium knowledge is vital to understand the contradictory trends in the literature and do the reaction engineering of an actual process. Therefore, in this chapter, the complete phase behavior of CO_2, ionic liquid and reaction system were investigated for hydrogenation and hydroformylation reactions. The effects of CO_2 pressure on phase behavior and reaction rate are discussed, and kinetics results are explained by phase equilibrium data.

7.3 Hydroformylation Reaction

The hydroformylation reaction is the addition of synthesis gas (CO and H_2) to alkenes to form aldehydes. A model system of hydroformylation of 1-octene to produce nonanal was chosen here, which is catalyzed by rhodium and a simple triphenylphosphine ligand. [HMIm][Tf_2N], was chosen here, the details of ionic liquid synthesis procedure and analysis results are given in Chapter 2. All of materials used are listed in Chapter 2. In order to understand the reaction kinetics by using a tunable IL/CO_2 biphasic system as reaction media and to engineer efficient reactions and separations, the complete phase behavior for reaction were measured. The vapor-liquid phase equilibrium, liquid - liquid phase equilibrium, mixture critical points were measured in this Chapter. The details of the apparatus set up and experimental procedure are described in detail in Chapter 2. The thermodynamic data also help to explain the different trends reported in the literature of the contribution of CO_2 to reaction system. The reaction mechanism is shown in Figure 7.2. The ratio between synthesis gas H_2 and CO was kept as 1:1.

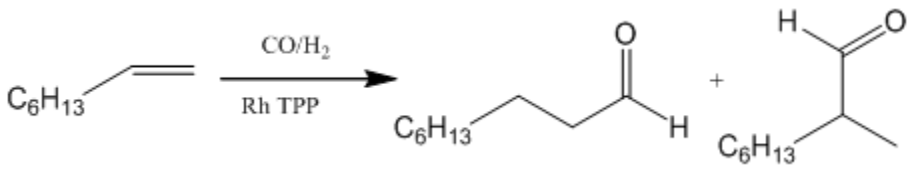

Figure 7.2 Hydroformylation mechanism of 1-octene with syngas (H_2:CO= 1:1 by mole) to n-nonanal (preferred) and the branched 1-methyl-octanal**.**

7.3.1 Phase equilibria of IL, CO_2 and reactants/products for hydroformylation reaction

The phase behavior of the reactants, product, CO_2, and the ionic liquid was fully investigated in this chapter. The various phase equilibria will be presented. A separation method by CO_2 pressure was also studied. The effects of CO_2 pressure on reaction rate are connected to the operating conditions, and the kinetics results are explained by phase equilibrium knowledge.

7.3.1.1 Volume expansion of the ionic liquid

As shown in Figure 7.1, CO_2 is highly soluble in ionic liquids, [HMIm][Tf_2N], at 70°C. With pressure, CO_2 begins to dissolve into the IL phase and slightly expands the liquid mixture volume. Thus, the total volume of the liquid mixture will increase, which will affect the molarity of the reactant in the reaction in biphasic IL/CO_2 systems. At 70°C, the volume expansion of the [HMIm][Tf_2N] with CO_2 and with a mixture of CO_2 and syngas (H_2:CO =1:1 by mole) have been measured. The data is given in Table 7.1 and shown in Figure 7.3. The volume expansion with the IL was also measured with different pressures of syngas (CO/H_2), which is a quaternary system of a mixture of syngas (H_2,CO), IL, and CO_2. As a multi-component system, it technically requires the specifications of the initial and final loading of all components, such as, concentrations or molar ratios, according to the Gibbs phase rule, to adequately characterize the thermodynamic properties (including volume expansion). For instance, syngas loaded into a reaction cell could be fixed at 6.11 bar, but without knowledge of the amount of IL and the amount in the vapor phase, it would hard to know the loaded amount (moles) of syngas. However, as the solubility

of the syngas is relatively low, the vapor-phase mole fraction will not change appreciably. Since the solubility of syngas is much lower than CO_2, the gas mixture with syngas can not expand the liquid volume as much as pure CO_2 pressure. The volume expansion with the mixed gases should change little whether loaded at a given pressure with a syngas to IL ratio of 0.5 or 1, for instance. The majority of the loaded syngas will stay in the CO_2 rich gas phase. Thus, the volume expansion at other conditions will be nearly similar.

With 119.8 bar pure CO_2 pressure, the IL rich liquid phase can be expanded by approximately 25%. However, with initial syngas pressure, the liquid volume expansion will decrease compared to the cases with only CO_2 pressure. For instance, at a given pressure, the volume expansion decreases about 33% with an initial pressure of approximately 6.11 bar of syngas over that of just pure CO_2. The volume expansion difference is expected due to lower solubility of H_2 and CO compared to CO_2 [30-33]. The introduction of syngas to the system reduces the partial pressure or, more appropriately, increase the fugacity of CO_2 in the vapor phase. Therefore, the solubility of CO_2 at a given pressure in the liquid phase will be lower. If the volume expansion of the $CO_2/H_2/CO$ mixture were linearly related to the partial pressure of the CO_2 in the vapor phase, the volume expansion of the mixture would not change for the case of the total pressure in the pure CO_2 equals to the partial pressure in the mixed gas case. However, based on the experimental data, the volume expansion with 30 bar initially of syngas is equal to the pure CO_2 case at approximately 22 bar lower, not 30 bar lower as given by the partial pressures. Therefore, one cannot

predict, the exact volume expansion with the gaseous mixture of interest for reactions by simply knowing the volume expansion at a certain pressure of pure CO_2.

7.3.1.2 Phase behavior of the reactants/product and CO_2

The knowledge of phase behavior of the reactants and products with CO_2 (without the IL) lead to valuable insights on the effect of pressure on the biphasic IL/CO_2 reaction system. Organic reactants and products, such as 1-octene and n-nonanal, can become miscible with CO_2 at certain conditions (temperature, pressure, and composition) above the bubble point or beyond the mixture critical point. The phase behavior and equilibrium of1-octene, n-nonanal, 1-octene/n-nonanal mixture and CO_2 are discussed in detail in Chapter 8. Here are only the results. At a given temperature, the mixture critical point is the highest pressure and composition where a vapor and liquid phase can coexist. The hydroformylation reaction system involves syngas, CO_2, 1-octene and n-nonanal, which is a 5-component system. For a mixture with two or more components, the mixture critical points can change with initial composition. As the ionic liquid is immeasurably insoluble in the CO_2 phase under the conditions studied here, the ionic liquid and CO_2 can not become critical. The unique phase behavior of ionic liquid and CO_2 results in a biphasic IL/CO_2 system. The fluid phase is directly tied to the phase behavior of the reactants, product and CO_2. This will be further discussed below.

Table 7.1 Volume expansion[a] of [HMIm][Tf_2N] with CO_2 and CO_2 & syngas (CO/H_2) at 70°C

Pure CO_2		CO_2 with initially 6.11 bar[b] CO/H_2(1:1)		CO_2 with initially 30.06 bar[c] CO/H_2(1:1)	
P [bar]	$\Delta V/V^0$ [%]	P [bar]	$\Delta V/V^0$ [%]	P [bar]	$\Delta V/V^0$ [%]
16.86	1.74	16.27	1.16	60.59	6.61
28.44	3.86	39.76	5.20	95.98	12.79
39.97	6.44	59.88	10.26	117.91	18.72
58.44	10.91	79.57	15.03	153.96	25.85
70.80	13.92	94.24	18.97	195.55	31.08
94.65	19.64	107.59	21.92		
119.78	24.95	120.70	24.17		

[a] $\%\Delta V/V_0$= [V(P)- V(P=1 bar)]/ V(P=1 bar)×100; [b] molar ratio of syngas:IL in the system is 0.293 [c] syngas:IL = 0.809

Figure 7.4 illustrates the mixture critical pressure at 70°C as the proportion of 1-octene to n-nonanal is varied between pure 1-octene and pure n-nonanal (on a CO_2-free basis). Above the mixture critical point line, a one phase mixture exists, and below the line, two-phase vapor-liquid equilibrium exists. The change in concentration corresponds to the conversion for the hydroformylation reaction. As shown in Figure 7.4, the mixture critical pressure increases from pure reactant (0% conversion), to pure product (100% conversion). Thus the phase behavior throughout

the entire composition (conversion) range must be known before running and maintaining reaction in a single phase throughout the reaction. For reactions in supercritical fluids, a single phase is usually desired, but simply choosing a pressure just above the critical point of the reactant (1-octene)/CO_2 system at beginning will yield two phases during the reaction. Similar conclusions were reached by Han, Poliakoff and coworkers[34], when studying the effect of the mixture critical point on reactions in initially single-phase supercritical fluids. The addition of syngas increases the mixture critical point, as shown in Figure 7.4. It also demonstrates that mixture critical pressure increased is beyond the initial syngas pressure (i.e. 30 bar). This is in an analogous manner to the volume expansion differences as discussed above. With an initial loading of 30 bar of syngas, the mixture critical pressure increases from 32 to 51 bar over the pure CO_2 conditions from starting to completing the reaction.

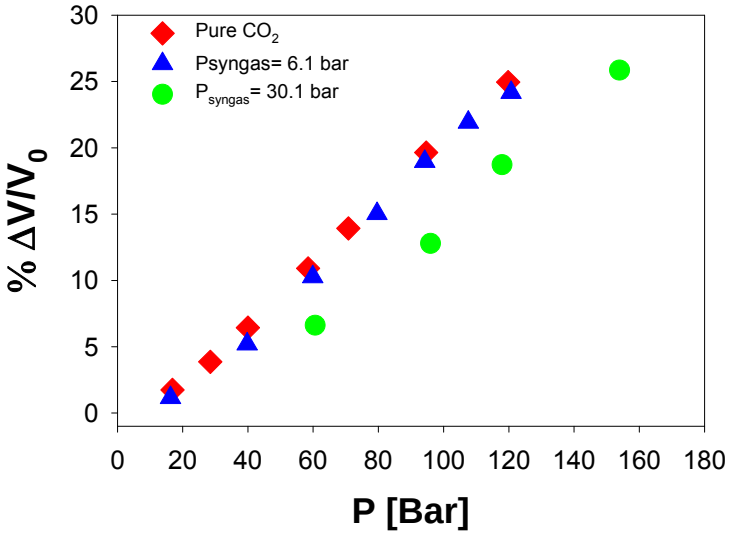

Figure 7.3 Volume expansion ($\%\Delta V/V_0 = (V-V_0)/V_0 \times 100$; pure IL volume, V_0) of [HMIm][Tf_2N] with CO_2 pressure with/without H_2 at 70°C; molar ratio of syngas:IL in the system is 0.3 at P_{syngas} = 6 bar and at 30 bar, 0.8.

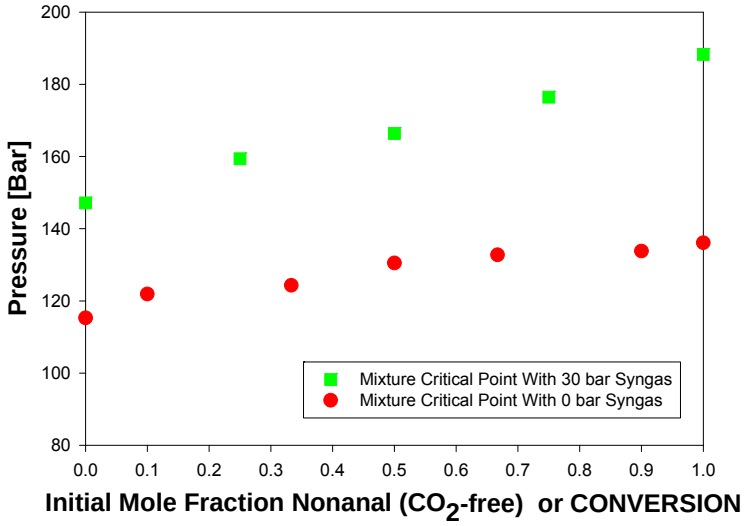

Figure 7.4 Phase behavior of 1-octene and n-nonanal and CO_2 as percent of initial amount of nonanal (CO_2-free basis); or can be read as phase behavior as a function of the conversion.

7.3.1.3 Phase behavior of the H_2/CO in IL with CO_2

It has been reported in the literature that the presence of CO_2 may enhance the solubility of permanent gases, such as CO, H_2, O_2, CH_4, in ionic liquids over the pure gases as similar pressures. Brennecke and coworkers [35] presented moderate to no enhancement for O_2 and CH_4. However, Solinas *et al.* [36-37] reported significant enhancement of H_2 in ionic liquids as observed from proton NMR. This phenomenon has been well-established for the CO_2-enhanced solubility of gases in organic solvents [14, 38-39].

Table 7.2 Mixture critical points of different initial ratios of 1-octene and n-nonanal with CO_2 and with CO_2 & CO/H_2 at 70 ºC

CO_2		CO_2 with Initial 30 bar CO/H_2 Pressures [c]	
Mole Fraction of n-nonanal [a]	Critical Pressure [bar]	Mole Fraction of n-nonanal [b]	Critical Pressure [bar]
0.00	115.30	0.00	147.13
0.10	121.90	0.25	159.41
0.33	124.31	0.50	166.39
0.50	130.50	0.75	176.46
0.67	132.75	1.00	188.30
0.90	133.80		
1.00	136.10		

[a] CO_2-free basis; [b] CO_2/syngas free basis;
[c] initial molar ratio of syngas : IL = 0.81:1

7.3.2 Effects of phase equilibrium on the catalytic reaction rate

The phase behavior with the pressure/composition effect on the reaction system was shown in Figure 7.5. The volume expansion data were also measured and given in Figure 7.3 and Table 7.1. The reaction results, which were done by Azita Ahosseini in the Scurto group, show that the apparent lower reaction rate with increasing CO_2 pressures. Before about 115 bar, the reaction rate slightly decreases with CO_2 pressure. However, after 115 bar, the reaction rate is affected by CO_2 pressure dramatically. How to explain the reaction results and kinetics using the phase equilibrium data is the main objective here.

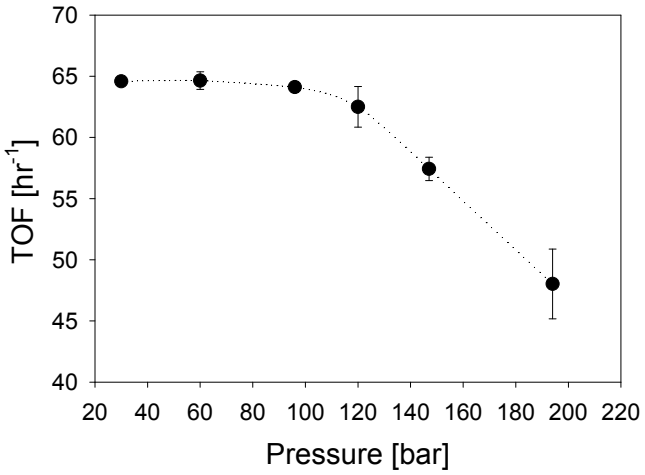

Figure 7.5 Reaction of the hydroformylation of 1-octene with total pressure CO_2. Line is of smoothed data.

It is obvious from Figure 7.5 that the reaction rate deceases apparently with CO_2 pressure. Firstly, when the reaction is operated at a relatively low pressure range (<115 bar), the system is below the mixture critical pressure of 1-octene and CO_2. In this regime, 1-octene can be assumed to be found mostly in the IL phase, and, thus,

the total moles of 1-octene are constant. However, as CO_2 pressure increases, CO_2 dissolves in the liquid phase and the volume of the liquid phase (ionic liquid rich phase) will continually expand. With constant moles and increasing volume, molarity of the reactant decreases as shown in Figure 7.6. Therefore, CO_2 pressure results in the dilution of reactants. For example, the concentration of 1-octene in the IL phase is initially about 45 mM without CO_2 pressure for the actual reaction. When the system is added about 130 bar CO_2 and 30 bar syngas, the liquid volume is expanded about 30% based on the volume expansion data in Table 7.1. Thus the concentration of 1-octene is decreased about 25% to approximately 34 mM. CO_2 pressure results in the dilution of reactants, which will decrease the overall reaction rate which is approximately 1st order in 1-octene.

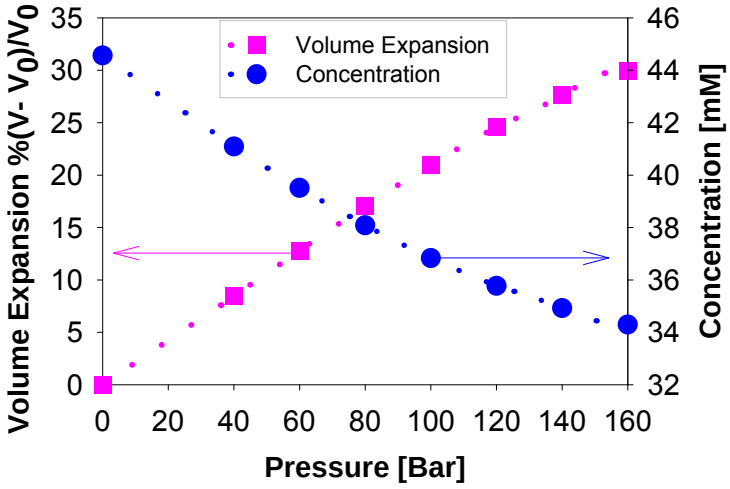

Figure 7.6 Volume expansion and molarity of 1-octene in the IL phase vs CO_2 pressure.

Secondly, when the reaction is operated at relatively high pressure (>115bar), for instance, CO_2 pressure equals or is higher than the mixture critical pressure of the binary system of 1-octene and CO_2, and 1-octene will be completely miscible with CO_2. In the multi-component IL/CO_2 biphasic system, the reactant, 1-octene will partition from the catalytic IL phase to CO_2 phase. As shown in Table 7.2, this mixture critical point of CO_2, the reactant and product with the IL changes with temperature and pressure. ILs are not soluble in the CO_2-phase and the CO_2/IL mixture cannot become critical. With the organic/ionic liquid mixture, increasing CO_2 pressure will partition the organic component out of catalytic ionic liquid phase. Therefore, at high pressure, especially after binary mixture critical points, the reaction rate decreased dramatically (see Figure 7.5). A similar reaction run at 120 bar helium pressure instead of CO_2 confirms this analysis, since the kinetic rate is similar to the CO_2-free condition. Compared with CO_2, the solubility of helium in ionic liquid is orders of magnitude lower. The mixture critical point of helium and organic component is not reported, but expected to be orders of magnitude higher than with CO_2.

Combined the reaction kinetics results with the phase behavior study; it was found that the pressure of about 115 bar defines two regions. The pressure draws a boundary for regions having different effects (Figure 7.7). As given in Table 7.2, 115 bar pressure is the mixture critical point of 1-octene and CO_2, which means that 1-octene become totally miscible with CO_2 after 115 bar for the binary system. For the ternary system with the IL, this means that the 1-octene would preferentially partition into the CO_2 phase.

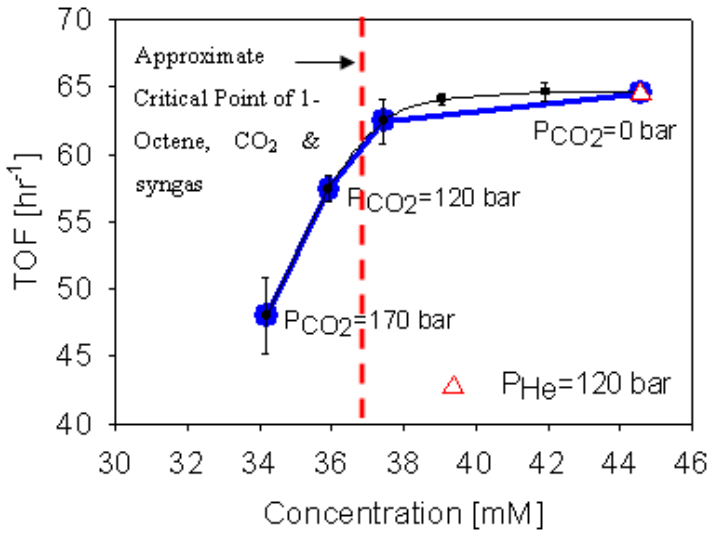

Figure 7.7 Hydroformylation reaction results based on nominal concentration [molarity] [8].

Another potential factor leading to a reaction rate decrease due to high CO_2 pressure may be partitioning of catalyst out of IL phase to CO_2 phase. It is reported by Shimoyama *et al.* [40] that both TPP and Rh complex can dissolve to some extent in supercritical CO_2. The solubility is about 8.7×10^{-4} for TPP and 5.8×10^{-7} for Rh mole fractions with 15 bar CO_2 pressure at 60 ºC. Wagner *et al.* [41] measured TPP solubility measurement in CO_2 and found similar solubility. While the ligand is three orders of magnitude more soluble than the Rh complex in supercritical CO_2, both have very low solubility in supercritical CO_2. Thus, compared with reactant partitioning, catalyst partitioning is not believed to have marked effect in the biphasic IL/CO_2 reaction system.

Thus, the reaction rate trend decrease with the increasing CO_2 pressure, which can be divided into two regions (dash line in Figure 7.9): dilution of reactant dominates at relatively lower pressure (<115 bar) and reactant partitioning (extraction) from the catalytic IL-rich phase to CO_2-rich phase dominates at relatively higher pressure (>115bar). This behavior explains the findings of other researchers in the literature that report similar decreases in reaction rate with increased CO_2 pressure. The actual concentration of reactants, including 1-octene, H_2 and CO, determined by accurate phase equilibrium measurement, plays an important role to determine the intrinsic kinetic constants for a given rate mechanism. The phase behavior equilibrium data of reactant and product with CO_2 were measured and given in Chapter 8. Understanding on phase behavior and kinetics are necessary and important for the properly design of the reaction system and process. This investigation here provides the whole picture to achieve high throughput for a biphasic reaction system using IL/CO_2 as reaction media.

7.3.3 Product separation: phase behavior of the reactant/product, IL, and CO_2

In addition, the phase behavior of the ionic liquid, reactant, product and CO_2 can yield insight in the reaction phenomena as well as illustrate potential advanced separation techniques. Scurto *et al.* [11-12] and other researchers [24, 26, 42-44] have indicated that CO_2 at certain conditions can be used to induce phase splitting and separation into an IL-rich phase and an organic-rich phase. The ambient pressure phase behavior of 1-octene, n-nonanal and [HMIm][Tf_2N] is illustrated in Figure 7.8. As shown, the product is miscible with the IL phase, but the reactant, 1-octene, is

only partially miscible. Thus, as conversion increases, the reaction could proceed from a two-phase region to a single miscible phase depending on the initial concentration of 1-octene. From a separations perspective, immiscible products would be preferred, as they would naturally separate. However, with CO_2 there are other possibilities and regions of behavior that must be understood for efficient reactions and separations of the biphasic IL/CO_2 reactions.

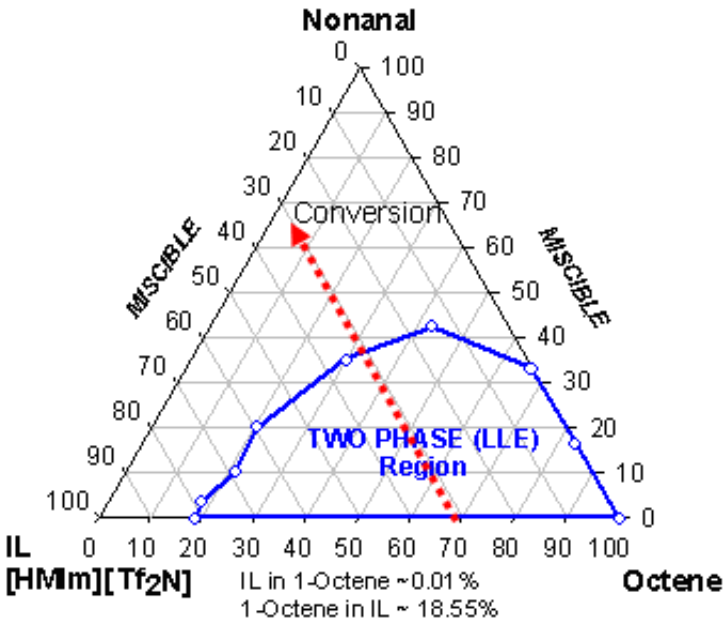

Figure 7.8 Ambient pressure phase behavior of 1-octene, n-nonanal, and [HMIm][Tf_2N] at 22°C.

With CO_2 pressure the organic liquids (reactant and product) may be induced to separate from the IL mixture. Figures 7.9 and 7.10 illustrate the qualitative phase behavior of loading of <30% of [HMIm][Tf_2N] with the product n-nonanal or mixtures with 1-octene. As shown, the mixture is homogeneous at ambient conditions. When CO_2 pressure is applied, the transition from VLE to vapor-liquid-

liquid equilibrium (VLLE) (V-L → V-L_1-L_2) is encountered, which is the first instance of liquid instability leading to two liquid phases in equilibrium with a vapor phase (VLLE). As pressure is increased, the relative volume of the organic-rich phase increases until it reaches the "K-point" where the organic-rich phase and CO_2 phase become critical and miscible to each other leaving an IL-rich phase and a vapor (fluid) phase. Above the "K-point" pressure, more of the remaining amount of organic in the IL phases partitions to the upper fluid phase, similar to supercritical fluid extraction from ionic liquids [45]. The K-point pressures have been observed to be identical within experimental accuracy to the mixture critical points of the binary organic and CO_2 system without the IL. This is due to the lack of IL in the CO_2 vapor phase and in the middle organic-rich phase near the K-point as confirmed in similar systems by Aki *et al.*[42].

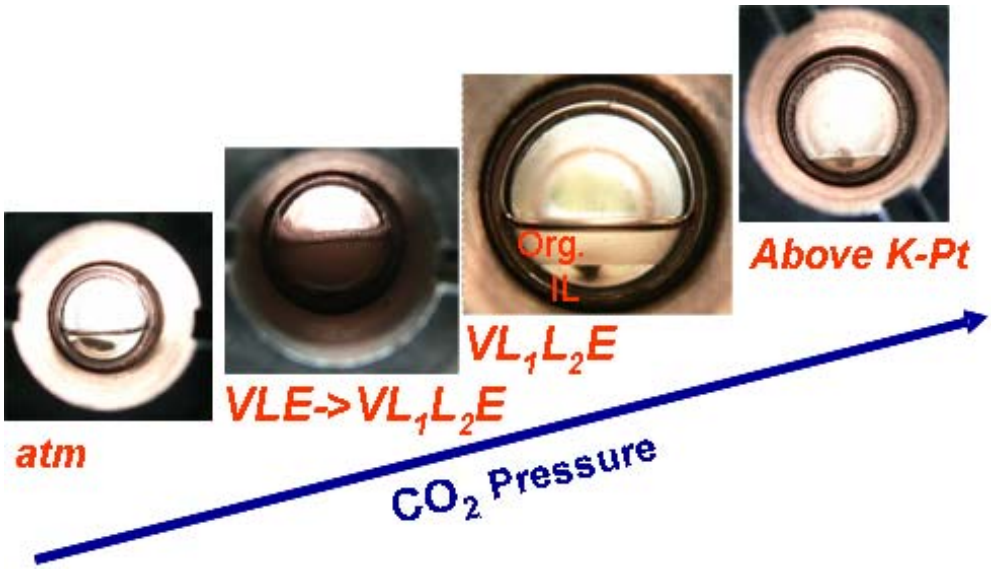

Figure 7.9 Pictures of the phase behavior in the autoclaves with increasing temperature and pressure

Often multiphase situations are avoided in reactions systems due to the interfacial mass transfer limitations. However, as the dissolved CO_2 significantly increases the mass transport properties of the IL phase, multiphase scenarios may not necessarily lead to mass-transport limited reaction kinetics.

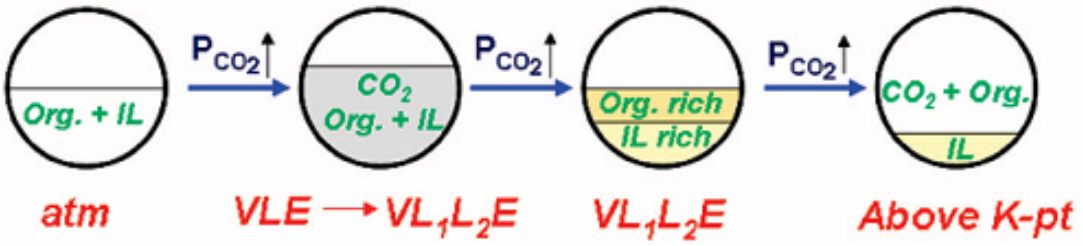

Figure 7.10 Diagram of the phase behavior in the autoclaves with increasing temperature and pressure for mixtures of the organic reactants/products with the IL and CO_2 pressure.

The pressure of the transition to VLLE (V-L→V-L_1-L_2) and back to VLE behavior (K-point) for mixtures of the IL with the product n-nonanal with CO_2 are illustrated in Figure 7.10. As shown, the mixture splits into two liquid phases at approximately 117 bar of pressure with an initial concentration of IL of 10% mole and 124 bar at 25% mole of the IL. The K-point of these two mixtures was nearly identical at 136 bar. When the concentration of the IL was further increased in the initial mixture, phase splitting did not occur. However, under these conditions, the nonanal would partition between the CO_2 phase and the IL phase, with a rapid increase in the partition occurring in the regime near the binary nonanal/CO_2 mixture critical point conditions of pressure 136 bar (see above).

Table 7.3 Phase transition of n-nonanal, [HMIm][Tf_2N], with CO_2 at 70°C.

Initial loading IL[a] [mole %]	VLE to VLLE **(**V-L→V-L_1-L_2**)** Phase Split Pressure [Bar]	K-point (L-L=V) [Bar]
0	--	136.1
10	117.3	136.2
25	124.2	136.3
31	No Split	--
50	No Split	--
[a] CO_2-free basis		

For the case of incomplete conversion, mixtures of 1-octene and n-nonanal will exist and this will change the condition of the transition (V-L→V-L_1-L_2) and K-point. Various ratios of 1-octene to n-nonanal were mixed with 10% mole of the IL. The VLE to VLLE transition and K-points are compared in Table 7.3. As large loadings of 1-octene are only partially miscible with the IL, two phases occur at ambient pressures to the K-point. The mixture critical point without the ionic liquid (in parentheses in the table) is within experimental accuracy of the case with the IL. The mixtures of equal portions of 1-octene and n-nonanal (45%:45%) with 10% IL are initially miscible and form the two liquid phase condition at relatively low pressure (32 bar). With higher proportion of n-nonanal, the VLE to VLLE transition pressure increases.

These results would have significant effect in the design of high-throughput reactions in biphasic IL/CO_2 systems. The catalytic results presented above are performed below the concentrations where phase splitting occurs. However, for higher loadings needed for realistic applications, the LLV and K-points must be known for proper engineering.

Table 7.4 Phase behavior of mixtures of 1-octene and n-nonanal with 10% mole [HMIm][Tf_2N] with CO_2 at 70°C

Initial loading of 1-octene [mole %][a]	VLE to VLLE (V-L→V-L_1-L_2) [Bar]	K-point (L-L=V) [Bar] [b]
Octene (90%)	LLE @ 1 bar	115.5 (115.3)
Nonanal(30%)+Octene(60%)	LLE @ 1 bar	124.1 (124.3)
Nonanal(45%)+Octene(45%)	32.0	131.0 (130.5)
Nonanal(60%)+Octene(30%)	87.4	132.5 (132.8)
Nonanal (90%)	117.3	136.2 (136.1)
[a] with 10% IL; [b] critical pressure without IL in parentheses.		

7.3.4 Conclusions for the hydroformylation reaction

The hydroformylation reaction of 1-octene using ionic liquid/CO_2 as reaction media was investigated, where [HMIm][Tf_2N] was chosen as model IL. Complete phase behavior studies were performed for the reactant, product, CO_2 and ionic liquid including volume expansion of liquid phase with CO_2 pressure. The reaction rate trend can be divided into two regions with different primary phenomena: dilution effect and reactant partitioning. With these phenomena understood, high-efficiency reaction engineering may be performed. A biphasic reaction system with IL/CO_2 for homogeneously catalyzed reactions provides a highly tunable, flexible and economical platform for reaction and separations. Detailed phase behavior and equilibrium are very important for fully understanding the kinetics results, determining the operating conditions, choosing appropriate separation process and properly designing an optimal reaction system.

7.4 Hydrogenation Reaction

The hydrogenation reaction is widely used in industry. Here, the hydrogenation of 1-octene catalyzed by rhodium-triphenylphosphine was used as a model reaction to investigate the effects of CO_2 pressure on reaction kinetics in the Scurto group. A biphasic ionic liquid/CO_2 system was chosen as reaction media, in which a model ionic liquid, 1-hexyl-3-methyl-imidazolium bis(trifluormethanesulfonyl)amide ([HMIm][Tf_2N]), was used, since it has been chosen as a model IL by International Union of Pure and Applied Chemistry(IUPAC). The reaction is shown in Figure 7.11.

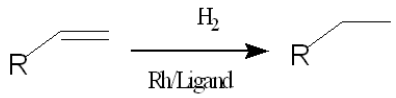

Figure 7.11 Reaction mechanism of hydrogenation reaction

7.4.1 Phase behavior of the reactant/product/CO_2

Even the simplest chemical reaction is likely to involve three components, e.g. reactant, product, and solvent, and most reactions generally involve more. Therefore, any study of reaction chemistry necessarily involves the phase equilibrium of multicomponent mixtures. In this work, the phase behavior of the reactants (1-octene, H_2) and products (octane) with CO_2 (without the IL) were measured, which also yields valuable insight into the reaction mixture phenomena. As will be discussed in Chapter 8, organic liquids, such as 1-octene and octane, can become miscible with CO_2 at certain conditions (temperature, pressure, and composition) above the bubble

point (solubility of the CO_2 in the liquid phase) or at conditions beyond the mixture critical point. The mixture's critical point (CP) is defined as the point where the two phases are identical. The mixture critical pressure is defined as the highest pressure and composition at a given temperature where a vapor and liquid phase can coexist. For liquid mixtures with multiple components, the mixture critical points can change with composition.

Figure 7.12 illustrates the mixture critical pressure at 70°C with conversion between pure 1-octene and pure octane on a CO_2-free basis. The proportion of 1-octene to octane is varied between as ratio of 3:1, 1:1, 1:3. Since the mixture critical point defines a boundary for different phase equilibria. Above mixture critical point line, only one phase exists, but below the line, two -phase vapor-liquid equilibrium exists. This change in concentration corresponds to conversions of 0% (pure 1-octene), 25%, 50%, 75% conversion, and 100% conversion (pure octane) for the actual hydrogenation reaction. As seen in Figure 7.12, both the binary mixture critical points of the organics with CO_2 and their mixture of the organics have similar critical pressures. This is believed to be due to similar physical and critical point properties of 1-octene and octane. If the reaction is operated at the conditions above the mixture critical point, the system will remain in one phase regardless of the level of conversion. Otherwise, it will be a biphasic system. The Figure 7.12 also demonstrates that the mixture critical pressure increases with the addition of initial pressures of H_2. This is in an analogous manner to the volume expansion differences as discussed above in hydroformylation reaction. The mixture critical pressure

increases by approximately 12 bar over the pure CO_2 conditions with an initial loading of 10 bar of H_2. With an initial loading of 50 bar of H_2, the mixture critical pressure increases about 57 bar compared with the pure CO_2 conditions.

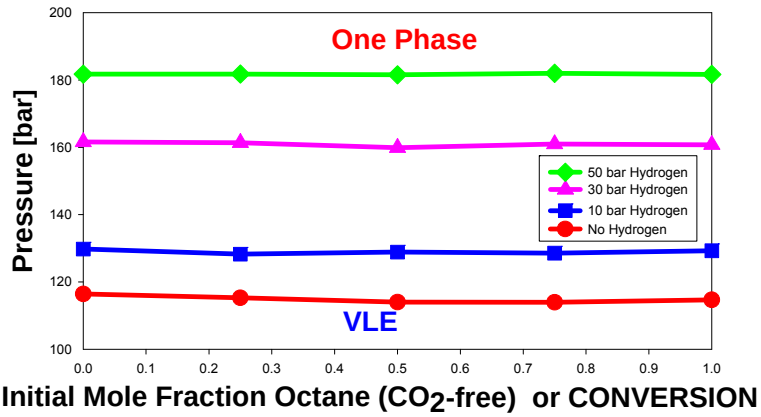

Figure 7.12 Phase behavior of 1-Octene and Octane and CO_2 as percent of initial amount of octane (CO_2-free basis) or the conversion.

Table 7.5 Mixture critical points of 1-octene, octane and CO_2 with H_2 at 70 °C

	Mixture Critical Points			
		CO_2 with Initial Pressures of H_2		
Mole Fraction Octane (CO_2-free Basis)	Pure CO_2	10 bar	30 bar	50 bar
0	116.45	129.79	161.62	181.74
0.25	115.29	128.27	161.36	181.76
0.5	114.03	128.90	159.90	181.55
0.75	113.95	128.56	160.98	182.00
1	114.69	129.28	160.77	181.65

7.4.2 Volume expansion of the ionic liquid

As discussed in Chapter 5, CO_2 is highly soluble in ionic liquids. When CO_2 begins to dissolve into the IL phase, it expands the liquid and increases the total volume of the mixture. However, the volume expansion of ionic liquids is much smaller than organic liquids at similar pressure. For instance, with CO_2 pressure, methanol volume can be expanded to 200% at approximately 69.73 bar and 35°C, 686.15% at 72.63 bar [46]. The volume expansion of the [HMIm][Tf_2N] with CO_2 pressure with or without hydrogen have been measured at 70°C. The volume expansion data of [HMIm][Tf_2N] with CO_2 are shown in Chapter 7.3, it is given here again to compared with volume expansion data with hydrogen pressure.

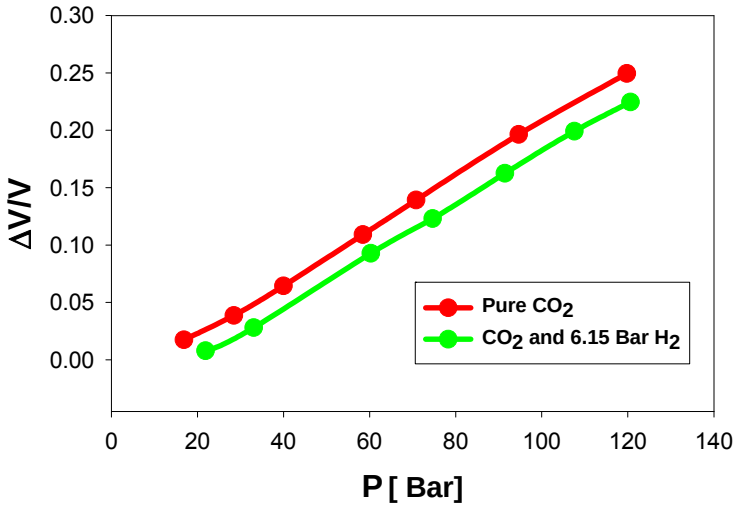

Figure 7.13 Volume expansion of [HMIm][Tf_2N] with CO_2 pressure with/without H_2 at 70°C.

As seen in Figure 7.13, the IL phase expands by approximately 25% over the volume at a CO_2 pressure range of 120 bar. With an initial pressure of approximately

6 bar of H_2, at a given pressure, the volume expansion decreases compared to pure CO_2. When the volume expansion is the same, the pressure difference is not just the initial 6 bar as of H_2 initially loading, but approximately 8-10 bar higher than the pure CO_2 case.

Table 7.6 Volume expansion of [HMIm][Tf_2N] with CO_2 and CO_2 with H_2 pressure at 70 °C

Pure CO_2		CO_2 with initially 6.15 bar H_2	
P [bar]	$\Delta V/V^0$	P [bar]	$\Delta V/V^0$
16.86	0.0174	21.87	0.0078
28.44	0.0386	33.06	0.0280
39.97	0.0644	60.29	0.0928
58.44	0.1091	74.66	0.1230
70.8	0.1392	91.43	0.1625
94.65	0.1964	107.58	0.1992
119.78	0.2495	120.62	0.2247
[a] $\Delta V/V^0 = [V(P_{CO_2}) - V(P_{CO_2}=1 \text{ bar})]/ V(P_{CO_2}=1 \text{ bar})$			

7.4.3. Effects of phase equilibrium on the catalytic reaction rate

The effect of CO_2 pressure on the reaction rate was investigated and given in Figure 7.14. The kinetics study was done by my colleague, Azita Ahosseini [9]. The motivation of the study is based on inconsistent literature reports. Some report that CO_2 pressure increases the reaction rate, but others say that it decreases the rate. Kinetics results in Figure 7.14 show that increasing CO_2 pressure seems to decrease the reaction rate. How does the presence of CO_2 affect the reaction rate? In this session, phase equilibrium knowledge is used to explain how the mechanism dominates phenomena by elevated CO_2 pressure.

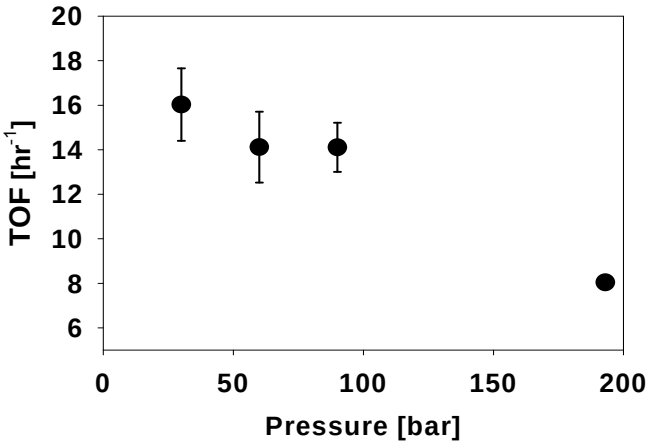

Figure 7.14 Reaction of the hydrogenation of 1-octene with total pressure CO_2. Reaction conditions: P_{H2} = 30 bar, 70°C; 3 hours catalyzed by Rh-TPP (1:4) [46]

The phase behavior study indicates that a boundary of reactant, 1-octene, product, octane, and reactant gas, H_2, is normally completely soluble/miscible in the CO_2 phase above the critical point (Figure 7.12). Above these approximate pressures, the reaction results (Figure 7.14) show lower reaction rate with an increase of CO_2 pressure. At the pressure above its mixture critical point with the CO_2 and/or CO_2/H_2 mixture, reactant 1-octene partitions favorably into the CO_2-phase from the IL phase. As 1-octene partitions away from the catalytic ionic liquid phase to non-catalytic CO_2 phase, it is obvious to see the reaction rate decrease as the corresponding molarity of the reactant decreasing. Thus, the more dramatic drop in reaction rate at the higher pressures can be due to the decrease in solubility or concentration of the 1-octene reactant as seen in Figure 7.14.

However, at lower pressures of CO_2, 1-octene will stay the catalytic phase-ionic liquid phase. Partitioning between two phases will not be the dominant factor,

but dilution. Here, dilution is a dominate factor that affects the reaction rate. The concentration of a reactant in the IL phase is affected by CO_2 pressure, which is apparent by the volume expansion study. The volume expansion data, given in Figure 7.13 and Table 7.6, indicate that the reaction mixture is expanded with the increasing CO_2 pressure, so that the volume of the reaction mixtures will increase accordingly. While keeping mass or moles of the reactant in the initial IL constant, the addition of CO_2 will decrease the molarity of the reactant due to the accompanying volume expansion. For instance, if the concentration of 1-octene in the IL is 1M at atmosphere pressure, then when CO_2 pressure is increased to 120 bar, the concentration of 1-octene would be reduced by 20% to 0.8 M. This concentration reduction results in dilution before the reaction occurs. In the real reaction scenario, the reaction rate is determined by the order of the kinetic rate expression. Concentration dilution will decrease the reaction rate.

Therefore, the combination of phase behavior study and volume expansion data, the reaction rate will be affected by both the partitioning of the reactant and the reactants dilution. With complete measurement and thorough characterization of the phase equilibrium, the reactant concentration and molarity, including 1-octene and H_2, can be determined with volume expansion data. Then reaction rate can be determined by intrinsic kinetic constants from kinetic rate expression for a given rate mechanism. From the discussion above, it is obvious that the reaction rate decreases with CO_2 pressure, although the effect of CO_2 concentration on the intrinsic kinetics is not clear.

7.4.4 Conclusions for the hydrogenation reaction

The biphasic ionic liquid/CO_2 system was proposed as alternative solvent for hydrogenation reaction of 1-octene. The combination of reaction media overcome the challenges of using ionic liquid and CO_2 individually as solvent for catalytic reaction and the benefits are explained and listed. The phase behavior and volume expansion with CO_2 pressure were studied. The kinetics results and observations are reasonable explained by phase equilibrium data. Reactants partitioning and dilution with CO_2 pressure affect the reaction rate apparently, and show a negative effect. However, a biphasic IL/CO_2 system represents a highly tunable and flexible platform for homogeneously catalyzed reactions. Detailed phase equilibrium is needed to properly understand and engineer these reactions.

7.5 References

1. Gröger, H., W. Hummel, C. Rollmann, F. Chamouleau, H. Hüsken, H. Werner, C. Wunderlich, K. Abokitse, K. Drauz, and S. Buchholz, *Preparative asymmetric reduction of ketones in a biphasic medium with an (S)-alcohol dehydrogenase under in situ-cofactor-recycling with a formate dehydrogenase.* Tetrahedron, 2004. **60**: p. 633-640.
2. Filho, M.V., T. Stillger, M. Müller, A. Liese, and C. Wandrey, *Is log P a Convenient Criterion to Guide the Choice of Solvents for Biphasic Enzymatic Reactions.* angew. chem. int. ed., 2003. **42**: p. 2993-2996.

3. Klein, H., R. Jackstell, and M. Beller, *Synthesis of linear aldehydes from internal olefins in water.* Chem. Commun., 2005: p. 2283-2285.

4. Hernandez-Justiz, O., R. Fernandez-Lafuente, M. Terreni, and J.M. Guisan, *Use of aqueous two-phase systems for in situ extraction of water soluble antibiotics during their synthesis by enzymes immobilized on porous supports.* Biotechnology and Bioengineering, 1998. **59**: p. 73-79.

5. Bauer, M., H. Griengl, and W. Steiner, *Parameters influencing stability and activity of a S-hydroxynitrile lyase from Hevea brasiliensis in two-phase systems.* Enzyme and Microbial Technology 1999. **24**: p. 514-522.

6. Sandford, V., M. Breuer, B. Hauer, P. Rogers, and B. Rosche, *(R)-phenylacetylcarbinol production in aqueous/organic two-phase systems using partially purified pyruvate decarboxylase from Candida utilis.* Biotechnology and Bioengineering, 2005. **91**: p. 190-198.

7. Adams, D.J., D.J. Cole-Hamilton, E.G. Hope, P.J. Pogorzelec, and A.M. Stuart, *Hydroformylation in fluorous solvents.* Organomet. Chem., 2004. **689**: p. 1413-1417.

8. Ahosseini, A., W. Ren, and A.M. Scurto, *Hydrogenation in biphasic ionic liquid/CO_2 systems in Gas Expanded Liquids and Near-Critical Media: Green Chemistry and Engineering*, K.S. Hutchenson, A.M.; Subramaniam, B., Editor. 2009. p. 218-234.

9. Ahosseini, A., E. Ortega, B. Sensenich, and A.M. Scurto, *Viscosity of n-alkyl-3-methyl-imidazolium bis(trifluoromethylsulfonyl)amide ionic liquids saturated with compressed CO_2.* Fluid Phase Equilibria, 2009. **286**: p. 62-68.

10. Ahosseini, A., W. Ren, and A.M. Scurto, *Understanding Biphasic Ionic Liquid/CO2 Systems for Homogeneous Catalysis: Hydroformylation.* Ind. Eng. Chem. Res., 2009. **48**: p. 4254-4265.

11. Scurto, A.M., S.N.V.K. Aki, and J.F. Brennecke, *CO_2 as a Separation Switch for Ionic Liquid/Organic Mixtures.* J. Am. Chem. Soc., 2002. **124**: p. 10276-10277.

12. Scurto, A.M., S.N.V.K. Aki, and J.F. Brennecke, *Carbon Dioxide induced separation of ionic liquids and water.* Chem. Comm., 2003: p. 572-573.

13. Hert, D.G., J.L. Anderson, S.N.V.K. Aki, and J.F. Brennecke, *Enhancement of oxygen and methane solubility in 1-hexyl-3-methylimidaxolium bis(trifluoromethylsulfonyl)imide using carbon dioxide.* Chem. Comm., 2005.

14. Lopez-Castillo, Z.K., S.N.V.K. Aki, M.A. Stadtherr, and J.F. Brennecke, *Enhanced Solubility of Oxygen and Carbon Monoxide in CO_2-Expanded Liquids* Ind. Eng. Chem. Res., 2006. **45**(15).

15. Scurto, A.M. and W. Leitner, *Expanding the useful range of ionic liquids: melting point depression of organic salts with carbon dioxide for biphasic catalytic reactions.* Chem. Comm., 2006(35): p. 3681-3683.

16. Scurto, A.M., E. Newton, R.R. Weikel, L. Draucker, J. Hallett, C.L. Liotta, W. Leitner, and C.A. Eckert, *Melting Point Depression of Ionic Liquids with CO_2: Phase Equilibria.* Ind. Eng. Chem. Res., 2008(47): p. 493-501.

17. Blanchard, L., Z. Gu, and J. Brennecke, *High-pressure phase behavior of ionic liquid/CO_2 systems.* JOURNAL OF PHYSICAL CHEMISTRY B, 2001. **105**(12): p. 2437-2444.

18. Jessop, P.G. and B. Subramaniam, *Gas-Expanded Liquids.* Chemical Reviews, 2007. **107**(6): p. 2666-2694.

19. Scurto, A.M., B. Subramaniam, and K. Hutchenson, *Gas-Expanded Liquids (GXLs): Fundamentals and Applications*, in *Gas Expanded Liquids and Near-Critical Media: Green Chemistry and Engineering*, K. Hutchenson, A.M. Scurto, and B. Subramaniam, Editors. 2008, ACS Symp. Ser. 1006: Washington, D.C.

20. Aki, S.N.V.K., A.M. Scurto, and J.F. Brennecke, *Ternary Phase Behavior of Ionic Liquid (IL)-Organic- CO_2 Systems.* Ind. Eng. Chem. Res., 2006. **45**: p. 5574-5585.

21. Fu, D., X. Sun, Y. Qiu, X. Jiang, and S. Zhao, *High-pressure phase behavior of the ternary system CO_2 + ionic liquid [BMIm][PF_6] + naphthalene.* Fluid Phase Equilibria, 2007. **251**: p. 114-120.

22. Qi, G.-p., X.-w. Sun, S.-q. Zhao, and J.-y. Fu, *Phase behavior of the CO_2/chloroaluminate ionic liquid/benzene ternary system.* Gaoxiao Huaxue Gongcheng Xuebao, 2009. **23**: p. 1-6.

23. Zhang, Z., W. Wu, H. Gao, B. Han, B. Wang, and Y. Huang, *Tri-phase behavior of ionic liquid- water - CO_2 system at elevated pressures.* Physical Chemistry Chemical Physics, 2004. **6**: p. 5051-5055.

24. Zhang, Z., W. Wu, B. Wang, J. Chen, D. Shen, and B. Han, *High-pressure phase behavior of CO_2/acetone/ionic liquid system.* J. Supercrit. Fluids, 2007. **40**: p. 1–6.

25. Zhang, Z., W. Wu, Z. Liu, B. Han, H. Gao, and T. Jiang, *A study of tri-phasic behavior of ionic liquid-methanol-CO_2 systems at elevated pressures.* Physical Chemistry Chemical Physics, 2004. **6**: p. 2352-2357.

26. Najdanovic-Visak, V., L.P.N. Rebelo, and M. Nunes da Ponte, *Liquid-liquid behaviour of ionic liquid-1-butanol-water and high pressure CO_2 - induced phase changes.* Green Chem., 2005. **7**(6): p. 443-450.

27. Kuehne, E., E. Perez, G.J. Witkamp, and C.J. Peters, *Solute influence on the high-pressure phase equilibrium of ternary systems with carbon dioxide and an ionic liquid.* J. Supercrit. Fluids, 2008. **45**: p. 27-31.

28. Zhaofu, Z., W. Weze, H. Buxing, J. Tao, W. Bo, and L. Zhimin, *Phase separation of the reaction system induced by CO_2 and conversion enhancement for the esterification of acetic acid with ethanol in ionic liquid.* The journal of physical chemistry. B, 2005. **109**: p. 16176-9.

29. Ren, W. and A.M. Scurto, *High-pressure phase equilibria with compressed gases.* Review of Scientific Instruments, 2007. **78**(12): p. 125104-7.

30. Kumelan, J., Á. Kamps, D. Tuma, and G. Maurer, *Solubility of CO in the ionic liquid [BMIm][PF_6]*. Fluid Phase Equilibria, 2005. **228**: p. 207-211.

31. Kumelan, J., A. Perez-Salado Kamps, D. Tuma, and G. Maurer, *Solubility of H_2 in the ionic liquid [BMIm][PF_6]*. J. Chem. Eng. Data, 2006. **51**(1): p. 11-14.

32. Kumelan, J., Á. Pérez-Salado Kamps, D. Tuma, and G. Maurer, *Solubility of CO_2 in the ionic liquid [HMIm][Tf_2N]*. The Journal of Chemical Thermodynamics, 2006. **38**(11): p. 1396-1401.

33. Kumelan, J., Á. Pérez-Salado Kamps, D. Tuma, and G. Maurer, *Solubility of the single gases H_2 and CO in the ionic liquid [BMIm][CH_3SO_4]*. Fluid Phase Equilibria, 2007. **260**(1): p. 3-8.

34. Ke, J., B. Han, M.W. George, H. Yan, and M. Poliakoff, *How Does the Critical Point Change during a Chemical Reaction in Supercritical Fluids? A Study of the Hydroformylation of Propene in Supercritical CO_2* J. Am. Chem. Soc., 2001. **123** (16): p. 3661-3670.

35. Hert, D.G., J.L. Anderson, S. Aki, and J.F. Brennecke, *Enhancement of oxygen and methane solubility in 1-hexyl-3-methylimidazolium bis (trifluoromethylsulfonyl) imide using carbon dioxide.* Chemical Communications, 2005. **2005**(20): p. 2603-2605.

36. Solinas, M., A. Pfaltz, P.G. Cozzi, and W. Leitner, *Enantioselective Hydrogenation of Imines in Ionic Liquid / Carbon Dioxide Media.* Journal of the American Chemical Society, 2004. **126**: p. 16142-16147.

37. Solinas, M., P. Wasserscheid, W. Leitner, A. Pfaltz, R. Chemie, I. Kamps, I.J. Xia, and I.G. Maurer, *Enantioselective Hydrogenation of Imines in Ionic Liquid/Carbon Dioxide media.* Chemie Ingenieur Technik, 2003. **75**(8): p. 1153-1153.

38. Bezanehtak, K., F. Dehghani, and N.R. Foster, *Vapor-Liquid Equilibrium for the Carbon Dioxide + Hydrogen + Methanol Ternary System.* J. Chem. Eng. Data, 2004. **49**(3): p. 430-434.

39. Jin, H., B. Subramaniam, A. Ghosh, and J. Tunge, *Intensification of catalytic olefin hydroformylation in CO_2-expanded media.* AIChE J., 2003. **52**(7): p. 2575-2591.

40. Shimoyama, Y., M. Sonoda, K. Miyazaki, H. Higashi, Y. Iwai, and Y. Arai, *Measurement of solubilities for rhodium complexes and ligands in supercritical carbon dioxide.* J. Supercrit. Fluids, 2008. **44**: p. 266-272.

41. Wagner, K.-D., N. Dahmen, and E. Dinjus, *Solubility of Triphenylphosphine, Tris(p-fluorophenyl)phosphine, Tris(pentafluorophenyl)phosphine, and Tris(p-trifluoromethylphenyl)phosphine in Liquid and Supercritical Carbon Dioxide.* J. Chem. Eng. Data, 2000. **45**: p. 672-677.

42. Aki, S.N.V.K., A.M. Scurto, and J.F. Brennecke, *Ternary Phase Behavior of Ionic Liquid (IL)-Organic-CO_2 Systems.* . Ind. Eng. Chem. Res., 2006. **45** (16): p. 5574-5585.

43. Mellein, B.R. and J.F. Brennecke, *Characterization of the Ability of CO_2 To Act as an Antisolvent for Ionic Liquid / Organic Mixtures.* J. Phys. Chem. B, 2007. **111**(18): p. 4837-4843.

44. Zhang, Z., W. Wu, H. Gao, B. Han, B. Wang, and Y. Huang, *Tri-phase behavior of ionic liquid - water - CO_2 system at elevated pressures.* PCCP, 2004. **6** (21): p. 5051-5055.

45. Blanchard, L.A. and J.F. Brennecke, *Recovery of organic products from ionic liquids using supercritical carbon dioxide.* Industrial & Engineering Chemistry Research, 2001. **40**(1): p. 287-292.

46. Bezanehtak, K., G.B. Combes, F. Dehghani, N.R. Foster, and D.L. Tomasko, *Vapor-Liquid Equilibrium for Binary Systems of Carbon Dioxide + Methanol, Hydrogen + Methanol, and Hydrogen + Carbon Dioxide at High Pressure.* Journal of Chemical and Engineering Data, 2002. **47**(2): p. 161-168.

Chapter 8 High-Pressure Phase Equilibrium for the Hydroformylation of 1-Octene to Nonanal in Compressed CO_2

8.1 Introduction

Chapter 7 presents the high pressure phase equilibrium study of the hydroformylation reaction using ionic liquid/CO_2 as reaction media. In this chapter, the high pressure phase behavior of hydroformylation reaction in compressed CO_2 is investigated. The hydroformylation reaction converting olefins to aldehydes with synthesis gas CO/H_2 is one of the largest homogeneously-catalyzed reactions in industry [1-2]. The reaction media has mostly used organic solvents, water, or solvent-free conditions. In recent years, CO_2-expanded liquids (CXLs) gained increasing attentions due to lower pressure over supercritical systems, reduced solvent use and enhanced catalytic performance [3-5]. The reaction has been investigated in both CXLs [4, 6] and supercritical carbon dioxide [7-10]. For the hydroformylation reaction, it was also investigated in CO_2-expanded ionic liquids (biphasic IL/CO_2 systems) [11-14]. The phase equilibrium study for biphasic IL/CO_2 systems is given in Chapter 7.3. Accurate knowledge of the phase equilibria of the hydroformylation reaction mixtures is necessary to properly understand and design these reactions. In addition, accurate equation of state modeling is needed to predict the phase equilibrium at operating conditions and optimize the reaction system.

Several groups have investigated hydroformylation reactions in supercritical CO_2 [4, 6, 15-18]. However, to properly explain the effect of operating conditions,

such as temperature, pressure and composition, on the reaction kinetics results in both the CXL and supercritical regimes, complete phase equilibria studies are needed.

Guha *et al.* [19] presented a detailed reactor model incorporating reaction kinetics, mass transfer rates and estimated phase equilibria to systematically investigate the effects of mass transfer and catalyst activation on induction period in 1-octene hydroformylation in CXLs. This report predicted all of the phase equilibrium using an equation of state. Jiang *et al.* [20] studied the phase behavior of the system CO_2, CO, H_2, 1-hexene, and heptanal with conversion 0 to 1 at different temperatures. It is demonstrated that the phase behavior and mixture critical points of reaction system involving 5 components change with conversion of 1-hexene, temperature and pressure. Ke *et al.* [6, 21] reported the change in mixture critical points with conversion for the hydroformylation of propene in supercritical CO_2. Fujita *et al.* [15-16] investigated effects of fluorinated phosphine ligand/rhodium complexes and reaction conditions on the hydroformylation of 1-hexene and 1,5-hexadiene in supercritical carbon dioxide and in toluene. They observed phase changes with conversion and found that the yield changes with CO_2 pressure. However, they did not study the complete phase behavior to explain the reaction results. Recently, Pereda *et al.* [22] reviewed the effects of phase equilibrium on reactions and reaction engineering in supercritical fluids involving hydrogenation and Fisher–Tropsch.

This Chapter reports the investigations of the vapor-liquid phase equilibrium, volume expansion, liquid molar volume and mixture critical points for binary systems

of 1-octene/CO_2 and nonanal/CO_2, and the ternary mixture of 1-octene/nonanal/CO_2 at various initial ratios of the 1-octene:nonanal. The volume expansion and mixture critical points are also measured for the system with all reactants and products of 1-octene/nonanal/CO_2/CO/H_2. The mixture critical points define the boundary for different phase equilibria. One can choose the operating conditions (temperature, pressure) for reaction based the phase behavior measured here. Volume expansion data are particularly important to calculate the molarity of reaction mixtures at different amounts of CO_2 present as kinetic rates are often based upon molarity. Reaction kinetics study can follow the molarity with conversion and pressure by volume expansion data here [23]. The equilibria are measured at 60°C (a common reaction temperature) and pressures to approximately 120 bar with reaction conversion as 0%, 25%, 50%, 75%, 100%.

The phase equilibrium study of binary system between 1-octene and CO_2, nonanal and CO_2 were predicted by using PR EOS, which shows excellent correlation with experimental data. During reaction, multi-components exist in the system. The ternary system phase equilibria of 1-octene, nonanal and CO_2 are also predicted. The ternary equilibria are predicted only based on the interaction coefficients of 1-octene and CO_2, nonanal and CO_2. Details are given in results and discussions session.

8.2 Results and Discussions

The solubility, volume expansion and molar volume of CO_2 in 1-octene, nonanal and mixtures are measured at 60 °C and up to 120 bar in a in a static equilibrium apparatus. Details of the apparatus and materials used are described in Chapter 2. For

the mixtures, the initial molar ratios of 1-octene and nonanal were 3:1, 1:1, and 1:3. In real reaction systems, the ratios would correspond to conversion of 25%, 50%, 75%. The pure 1-octene and nonanal correspond to the conversion of 0 and 100%. Therefore, all of data provide the whole scenario for the reaction. In addition, the critical points of 1-octene, nonanal and CO_2 are measured to determine the maximum pressure that a biphasic system would exist, which helps to determine the operating conditions if one wants to run the reaction in supercritical status at one phase, or gas-liquid biphasic system. The effects of CO/H_2 on the mixture critical pressure are also considered.

Table 8.1 Physical properties and equation of state parameters

Components	Formula	MW [g/mol]	T_b [K]	T_c [K]	P_c [bar]	Ω
1-octene	C_8H_{16}	112.21	395.00	566.55	26.8	0.282
Nonanal	$C_9H_{18}O$	142.24	464.20	637.67	24.8	0.605
Carbon Dioxide	CO_2	44.01	194.70	304.25	73.80	0.228
Note: parameters are from PE2000 database[24]						

8.2.1 Binary vapor-liquid equilibrium systems

8.2.1.1 Vapor-liquid equilibrium of CO_2 in pure 1-octene

The vapor-liquid equilibrium of CO_2 in pure 1-octene is measured at 60 °C and pressure up to 98 bar. The bubble-point (solubility) data are plotted in Figure 8.1.

Relatively high CO_2 solubility in 1-octene is observed especially at elevated pressures. The mixture reaches the critical point at approximately 102 bar with 96% mole of CO_2. The PR EOS with van der Waals 2-parameter mixing rule is chosen to correlate the data. Modeling results are shown in Figure 8.2 and the interaction parameters between 1-octene and CO_2, nonanal and CO_2 are given Table 8.2. For ternary equilibrium prediction, the model performed simulation without 1-octene and nonanal interaction parameter. The model accurately correlates the CO_2 solubility data except in the near critical regime (>100 bar). The predicted critical point appears at approximately 99 bar, which is 3.4% lower than the experimental point. The predicted critical composition is 1.7% lower. The poorer performance of the near critical region is observed commonly for cubic equations of state modeling of bubble-point data, which are also reported in [19, 20].

Table 8.2 EoS interaction parameters and results

System	T [°C]	Exp. Data Points	Interaction Parameters						
			k_{12}	l_{12}	k_{13}	l_{13}	k_{23}	l_{23}	AARD (%)
1-octene (1) +CO_2 (3)	60	10			0.0807	-0.0035	-	-	3.71
Nonanal (2) +CO_2 (3)	60	10			-	-	0.0196	-0.0118	0.76
1-octene (1) + nonanal (2) + CO_2 (3)	60	15			0.0807	-0.0035	0.0196	-0.0118	4.69
1-octene (1)/ nonanal (2) (1:1) + CO_2 (3)	60	6			0.0807	-0.0035	0.0196	-0.0118	3.62

8.2.1.2 Vapor-liquid equilibrium of CO_2 and nonanal

The solubility of CO_2 in pure nonanal (product of the hydroformylation reaction) is measured at 60 °C and pressure up to 117 bar. The data are given in Table 8.2 and plotted in Figure 8.2. At 116.6 bar, the mixture of nonanal and CO_2 becomes critical and one phase with 97.1% mole of CO_2. As shown in Table 8.2 and Figure 8.2, the modeling results of solubility of CO_2 in nonanal correlate excellently with the experimental solubility data. The composition of critical point is also very well predicted (0.5% error), but the pressure is a slightly over-predicted by about 0.6%.

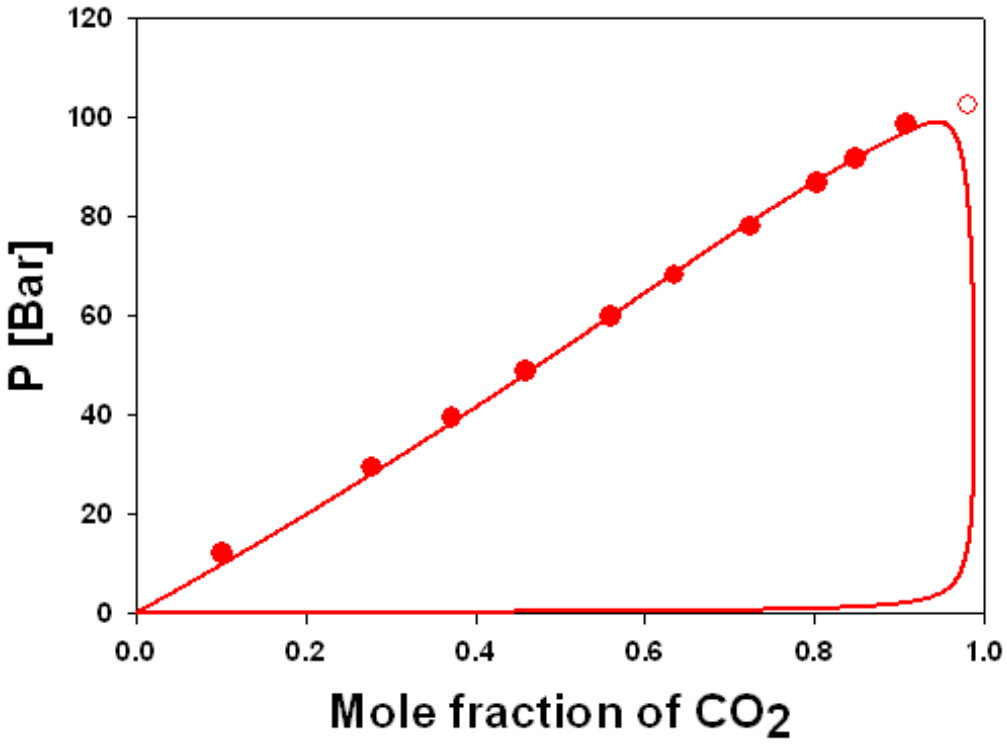

Figure 8.1 Experimental bubble-points and mixture critical point of 1-octene/CO_2 at 60°C. ●: bubble points.○: critical points. Solid line: modeling correlation

8.2.1.3 Vapor-liquid equilibrium of CO_2/ Octene and CO_2/nonanal

When the system pressure is below the mixture critical point, the reaction is operated in biphasic system. The solubility of CO_2 is different in reactant and product. As shown in Figure 8.3, the solubility of CO_2 is higher in product of nonanal than 1-octene at lower pressures. At approximately 65 bar, the solubility is equal. Above 65 bar, the solubility of CO_2 then becomes higher in 1-octene. This may have ramifications for reactions in a biphasic CXLs.

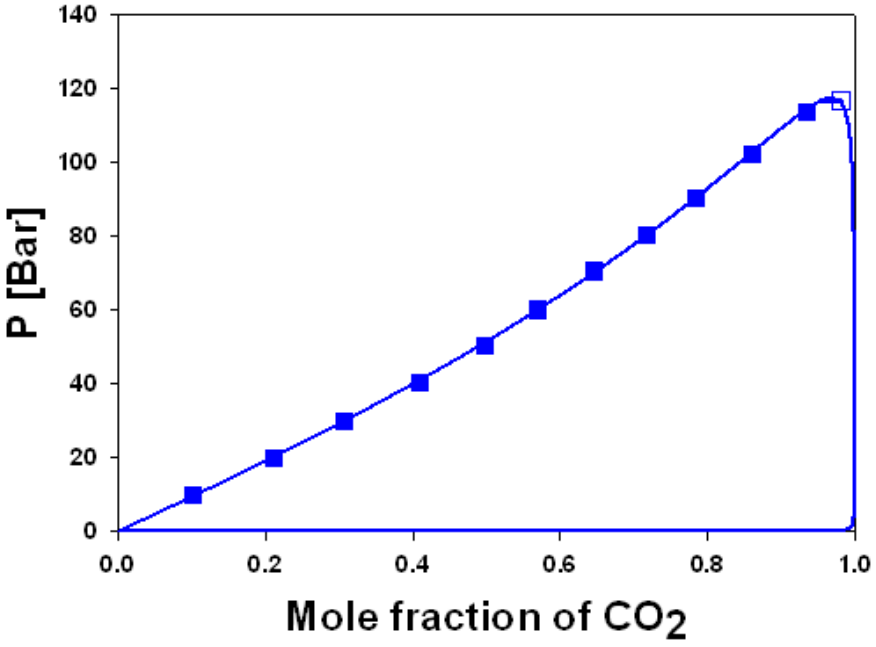

Figure 8.2 Experimental bubble-points and mixture critical point of nonanal/CO_2 at 60°C. ■: bubble points.□: critical points. Solid line: modeling correlation.

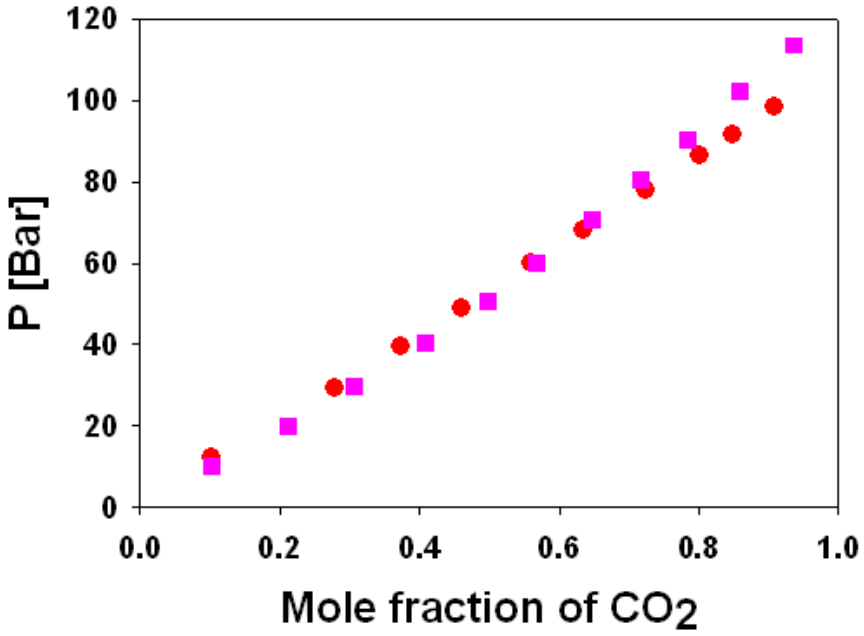

Figure 8.3 Experimental bubble-points of 1-octene/CO_2 and nonanal/CO_2 at 60°C. ●: 1-octene; ■: nonanal

For reactions conducted below this cross-over pressure in a batch mode, the pressure may decrease as the mixture converts from a lower solubility reactant to a higher solubility product. However, above this pressure, the pressure may actually increase throughout the reaction. If these pressure changes are large enough, both the solubility and volume expansion (discussed below) may change the concentrations in the reacting mixture.

Table 8.3 Vapor-liquid equilibrium data of 1-octene/CO_2 and nonanal/CO_2 systems at 60 °C

System	P [bar]	x_{CO2}	ΔV/V0	V_L [cm^3/mol]
1-octene+CO_2	12.17	0.1019 ± 0.0033	0.033 ± 0.001	141.55 ± 0.14
	29.52	0.2778 ± 0.0041	0.130 ± 0.001	124.55 ± 0.11
	39.45	0.3725 ± 0.0040	0.212 ± 0.002	116.08 ± 0.10
	48.98	0.4599 ± 0.0038	0.309 ± 0.002	107.89 ± 0.08
	59.85	0.5591 ± 0.0032	0.464 ± 0.002	98.49 ± 0.07
	68.16	0.6348 ± 0.0026	0.640 ± 0.002	91.41 ± 0.06
	77.95	0.7235 ± 0.0018	0.974 ± 0.002	83.32 ± 0.04
	86.61	0.8021 ± 0.0011	1.575 ± 0.003	77.76 ± 0.03
	91.67	0.8475 ± 0.0007	2.220 ± 0.004	74.91 ± 0.02
	98.46	0.9078 ± 0.0003	4.528 ± 0.006	77.81 ± 0.01
CP	102.39	0.9607±0.0002		84.26 ± 0.01
nonanal+CO_2	10.08	0.1019 ± 0.0034	0.016 ± 0.002	167.64 ± 0.19
	20.04	0.2108 ± 0.0028	0.062 ± 0.002	154.04 ± 0.17
	29.9	0.3067 ± 0.0023	0.123 ± 0.002	143.05 ± 0.15
	40.25	0.4085 ± 0.0019	0.185 ± 0.002	128.81 ± 0.13
	50.49	0.4968 ± 0.0016	0.282 ± 0.002	118.49 ± 0.11
	60.02	0.5683 ± 0.0014	0.386 ± 0.002	109.90 ± 0.09
	70.53	0.6463 ± 0.0012	0.540 ± 0.002	100.10 ± 0.08
	80.32	0.7174 ± 0.0010	0.732 ± 0.002	89.93 ± 0.06
	90.18	0.7831 ± 0.0008	1.023 ± 0.003	80.62 ± 0.05
	102.04	0.8597 ± 0.0005	1.697 ± 0.003	69.52 ± 0.03
CP	116.55	0.9706 ± 0.0001		69.60 ± 0.01

Volume expansion: $\frac{\Delta V}{V_0} = \frac{V^L(T,P) - V_0(T, P = 1bar)}{V_0(T, P = 1bar)}$

CP: Mixture critical point

8.2.2 Multi-component vapor-liquid equilibrium systems

8.2.2.1 Ternary VLE systems

The solubility of CO_2 in mixtures of 1-octene and nonanal are measured at 60°C with initial ratios of 3:1 (25% nonanal), 1:1 (50% nonanal), and 1:3 (75% nonanal). The results are listed in Table 8.4 and presented in Figure 8.3 by choosing and grouping the data approximately at pressures of 10 bar, 30 bar, 50 bar, 70 bar and 90 bar. At lower pressure the solubility of CO_2 appears to change linearly in both pure 1-octene and in nonanal. However, at higher pressure and intermediate 1-octene/nonanal concentrations, the CO_2 solubility decreases slightly. In order to predict the ternary equilibrium, 3 sets of binary interaction parameters are needed: k_{13} and l_{13} of CO_2/1-octene, k_{23} and l_{23} of CO_2/nonanal, and k_{12} and l_{12} of 1-octene/nonanal. The first two can be obtained from correlating the binary experimental data. However, no low-pressure vapor-liquid equilibrium data are known for the 1-octene/nonanal system and their interactions, so that k_{12} and l_{12} are set to zero.

The results in Figure 8.4 reveal that the model predicts the ternary data quite well, despite no 1-octene-nonanal interaction parameters. At lower pressure (< about 65 bar), the solubility in nonanal is higher than 1-octene. When pressure is higher than 65 bar, CO_2 is more soluble in 1-octene than nonanal. When running the reaction at certain pressure, the pressure may change with the conversion. In order to see this clearly on the model prediction, the data are plotted at an initial ratio of 1-octene/nonanal of 1:1 in Figure 8.5, which again shows an excellent prediction.

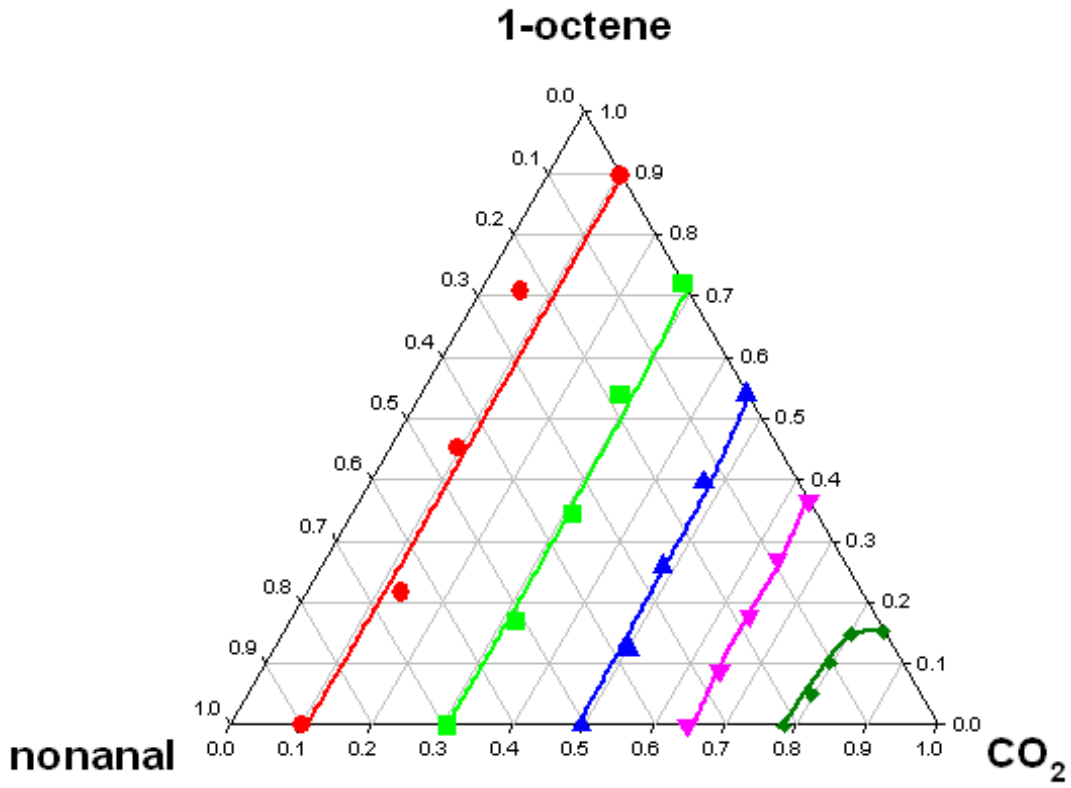

Figure 8.4 Ternary diagram of 1-octene (1), nonanal (2) and CO_2 (3). ●:~10bar; ■:~30bar; ▲:~50bar; ▼:~70bar; ♦:~90bar. Modeling prediction using only binary interaction parameters and k_{12}, $l_{12} = 0$.

Table 8.4 Ternary vapor-liquid equilibrium data of 1-octene/nonanal/CO_2 systems at 60 °C.

System	***P*** ***[bar]***	x_{CO2}	$\Delta V/V_0$	$\underline{V}^L$ ***[cm³/mol]***
1-octene/nonanal (1:1) +CO_2	9.81	0.0963 ± 0.0034	0.023 ± 0.002	148.88 ± 0.19
	20.45	0.2121 ± 0.0028	0.076 ± 0.002	136.55 ± 0.17
	30.33	0.3111 ± 0.0023	0.143 ± 0.002	126.80 ± 0.15
	40.30	0.4009 ± 0.0019	0.223 ± 0.002	117.97 ± 0.13
	49.80	0.4817 ± 0.0016	0.318 ± 0.002	110.01 ± 0.11
	60.18	0.5623 ± 0.0014	0.447 ± 0.002	102.01 ± 0.09
	70.58	0.6453 ± 0.0012	0.630 ± 0.002	93.10 ± 0.07
	80.66	0.7230 ± 0.0009	0.893 ± 0.003	84.47 ± 0.06
	90.33	0.7956 ± 0.0006	1.309 ± 0.003	76.02 ± 0.04
	100.57	0.8699 ± 0.0004	2.276 ± 0.004	68.65 ± 0.03
CP	108.39	0.9697 ± 0.0001		76.67 ± 0.01
1-octene/nonanal (3:1) +CO_2	9.80	0.0568 ± 0.0043	0.033 ± 0.002	153.13 ± 0.19
	20.53	0.1863 ± 0.0048	0.079 ± 0.002	138.07 ± 0.16
	31.29	0.2814 ± 0.0054	0.148 ± 0.002	129.66 ± 0.14
	40.70	0.3753 ± 0.0053	0.221 ± 0.002	119.92 ± 0.12
	50.66	0.4714 ± 0.0049	0.315 ± 0.002	109.25 ± 0.11
	60.08	0.5484 ± 0.0043	0.438 ± 0.002	102.07 ± 0.09
	70.53	0.6387 ± 0.0034	0.618 ± 0.002	91.88 ± 0.07
	80.61	0.7204 ± 0.0025	0.892 ± 0.003	83.14 ± 0.06
	90.79	0.8032 ± 0.0015	1.401 ± 0.003	74.29 ± 0.04
	100.42	0.8796 ± 0.0007	2.623 ± 0.005	68.53 ± 0.02
	105.34	0.9221 ± 0.0003	4.936 ± 0.008	72.66 ± 0.02

CP	105.92	0.9645 ± 0.0001		79.25 ± 0.01
1-octene/nonanal (1:3) +CO_2	11.66	0.1335 ± 0.0042	0.021 ± 0.002	145.41 ± 0.19
	20.69	0.2267 ± 0.0047	0.058 ± 0.002	134.45 ± 0.17
	30.36	0.3185±0.0051	0.105 ± 0.002	123.78 ± 0.15
	39.92	0.3983±0.0052	0.177 ± 0.002	116.48 ± 0.13
	51.51	0.5018±0.0047	0.287 ± 0.002	105.46 ± 0.11
	60.71	0.5762±0.0041	0.396 ± 0.002	97.25 ± 0.09
	69.86	0.6484±0.0034	0.549 ± 0.002	89.53 ± 0.08
	80.00	0.7258±0.0025	0.799 ± 0.003	81.12 ± 0.06
	89.47	0.7965±0.0017	1.183 ± 0.003	73.04 ± 0.04
	98.87	0.8652±0.0009	1.986 ± 0.004	66.19 ± 0.03
	107.83	0.9352±0.0002	5.648 ± 0.009	70.85 ± 0.01
CP	114.41	0.9697±0.0001		72.01 ± 0.01
Volume expansion: $\frac{\Delta V}{V_0} = \frac{V^L(T,P) - V_0(T,P=1bar)}{V_0(T,P=1bar)}$; CP: Mixture critical point				

Table 8.5 Critical point data of 1-octene/nonanal/CO_2 systems without CO/H_2 pressure at 60 °C

Conversion	**P [Bar]**	X_{CO2}	$X_{1\text{-}octene}$	$X_{nonanal}$
0	102.39	0.9607	0.0393	0.0000
0.25	105.92	0.9645	0.0266	0.0089
0.5	108.39	0.9697	0.0151	0.0151
0.75	114.41	0.9697	0.0076	0.0227
1	116.55	0.9705	0.0000	0.0295

The mixture critical points for each initial ratio of reactants and products are measured and listed in Table 8.5. The mixture critical points increase with

conversion. The CO_2/nonanal mixture critical point is approximately 14.2 bar higher than that of CO_2/1-octene at 60°C. The critical points increase almost linearly with increasing amount of the nonanal as shown in Figure 8.6.

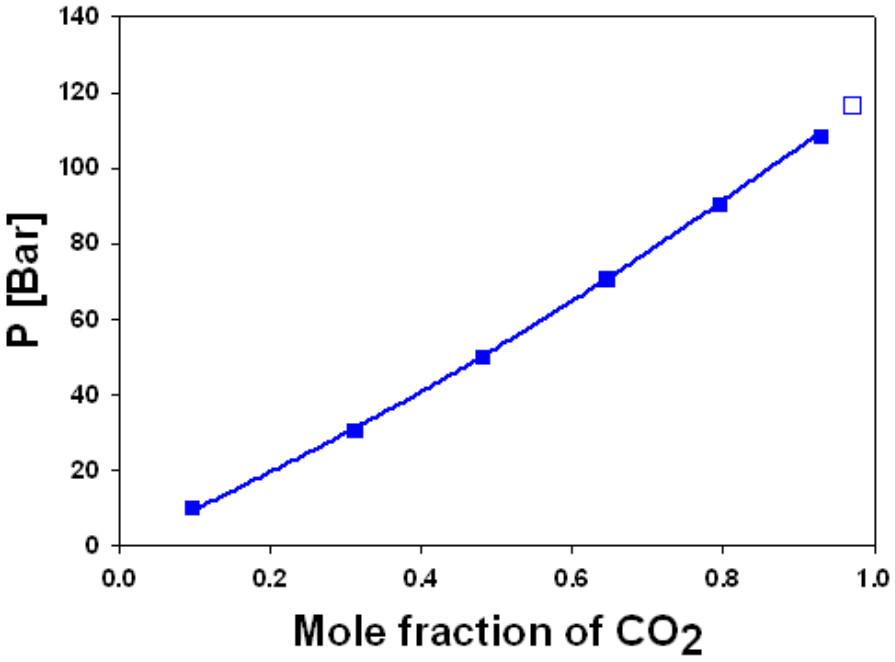

Figure 8.5 Experimental bubble-points and mixture critical point of an initially 1:1 mixture of 1-octene/nonanal with CO_2 at 60°C ■: bubble points; □: critical point.

The mixture critical points of these mixtures define the boundary between a biphasic CXL reaction and a reaction in a single supercritical phase, which determines the reaction conditions. There are potential advantages in either mode [21], but due to the large potential change in the mixture critical point as the reaction

proceeds from 100% 1-octene (0% conversion) to 100% nonanal (100% conversion). If a reaction runs just above the mixture critical point of 1-octene/CO_2, a phase change would occur during the reaction. If the reaction runs in a closed reactor without window, it is hard to monitor and keep the system in one phase during the whole reaction. Without the knowledge of the phase behavior and anomalous kinetics results, it is impossible for rational reactor design.

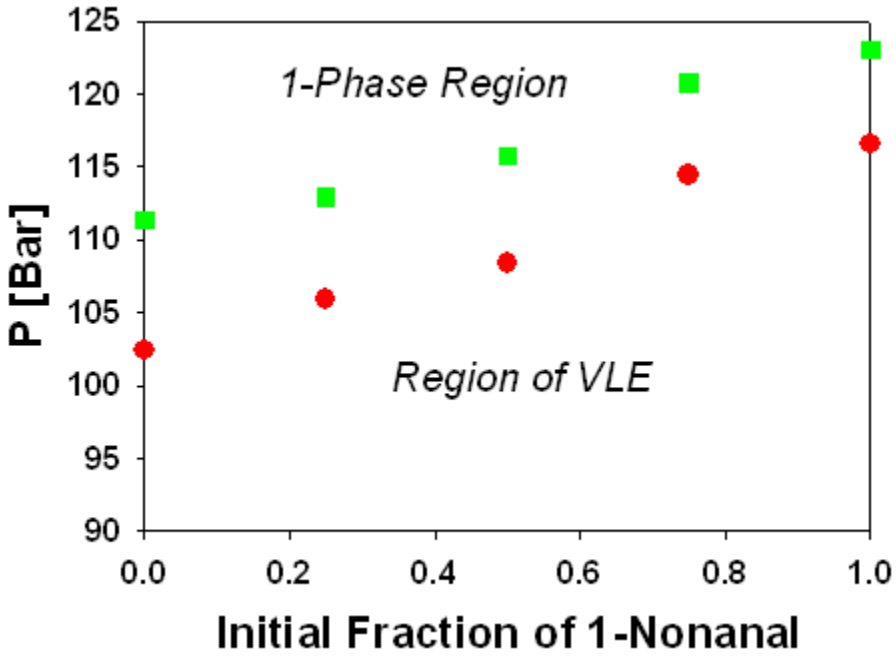

Figure 8.6 Experimental mixture critical points of mixtures of 1-octene and nonanal (initial gas-free basis), and CO_2 with (■) and without (●) 6 bar initially of CO/H_2.

8.2.2.2 Mixture critical points of the 5-component Mixture: 1-Octene/Nonanal/CO_2/CO/H_2

The mixture critical points with the presence of syngas (CO/H_2 1:1 by mole) is measured at an initial loading of 6 bar of syngas corresponding to a global loading of approximately 36% by mole with the initial amount of 1-octene and or nonanal; exact

initial concentrations are listed in Table 8.6. The critical pressure and composition with various initial fractions of nonanal, 0, 0.25, 0.5, 0.75, 1 (on a CO_2 and syngas free basis), are measured at 60°C. The mixture critical points increase with the conversion. The critical points of the 5-component mixture are compared with the syngas-free case in Table 8.5. As shown, the mixture critical points occur at higher pressures than the syngas-free case. Moreover, despite adding only 6 bar of syngas to the mixture, the 5-component mixture critical pressures are 8 bar (sometimes more) higher than that of the syngas-free. Therefore, simply knowing the ternary mixture critical points and adding 6 bar to obtain the multi-component critical point do not lead to a quantitative prediction for the actual mixture.

Table 8.6 Critical point data of 1-octene/nonanal/CO_2 Systems with CO/H_2 pressure at 60 °C

		Initial syngas	**Mixture Critical Point Compositions**		
Initial Fraction nonanal[a]	***P [Bar]***	x_{CO/H_2}	x_{CO/H_2}	x_{CO_2}	$x_{organics}$
0	111.36	0.3561	0.0203	0.9430	0.0367
0.25	112.95	0.3681	0.0196	0.9469	0.0336
0.5	115.76	0.3730	0.0193	0.9483	0.0324
0.75	120.78	0.3753	0.0178	0.9527	0.0296
1	123.04	0.3762	0.0172	0.9542	0.0286
[a] CO_2 and CO/H_2 free basis					

8.2.3 Volume expansion

The volume expansions of the binary, ternary system with syngas pressure, up to 5-component systems are measured at 60°C and pressure approaching the mixture critical points. The data are listed in Tables 8.3, 8.4 and 8.7 and shown in Figures 8.7 and 8.8. The volume expansion is calculated by the ratio of the volume change with CO_2 pressure and initial liquid volume. The volume change accounts for the volume difference between the volume of CO_2 expanded liquid and the initial liquid volume without CO_2 pressure. The volume expansion of the mixture expanded with CO_2 is an important parameter for reactions and can be used to explain the reaction kinetics results. Kinetic rate equations are most often functions of concentration (moles reactants per volume). When the CO_2 pressure is increased, CO_2 dissolves in the liquid phase and expands the volume of the liquid mixture. If the moles of reactant are kept as constant, this volume expansion would lower the concentration, CO_2 pressure dilutes the reactant. Thus from the reaction view point, the CO_2 pressure results in a huge dilution in the reaction system. If this were not taken into consideration, the apparent reaction rate would appear to drop with additional CO_2 pressure. However, the actual kinetic rate may be constant, decrease or even increase. The volume expansion of pure 1-octene and nonanal are plotted in Figure 8.7.

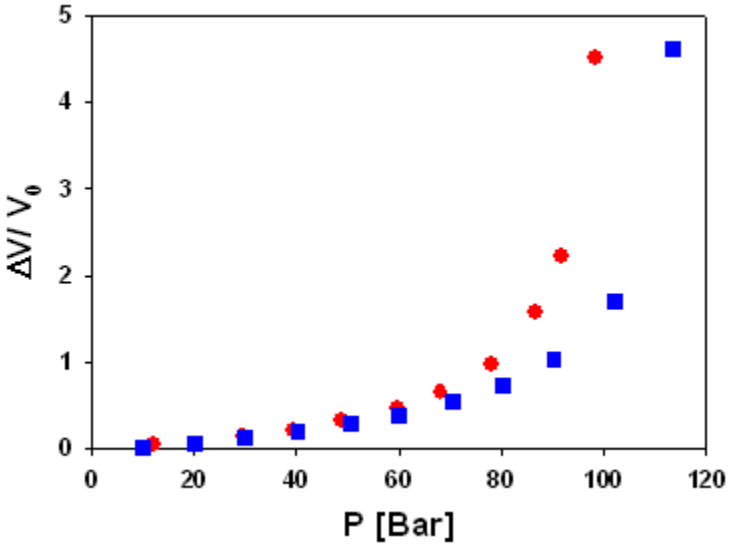

Figure 8.7 Volume expansion of 1-octene/CO_2 and nonanal/ CO_2. ●: 1-octene. ■: nonanal

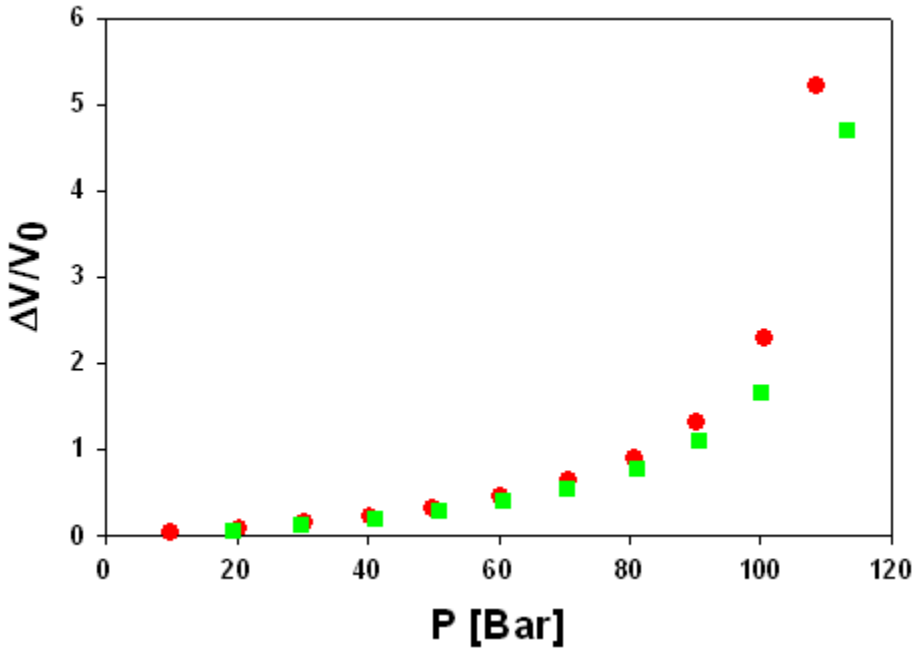

Figure 8.8 Volume expansion of 1-octene/nonanal mixtures (1:1) and CO_2 with and without CO/H_2 pressure ●: without syngas pressure. ■: with syngas pressure.

Table 8.7 Volume expansion of 1-octene/nonanal/CO_2 with initially 6 bar of CO/H_2 pressure [a] at 60 °C

1-octene+CO_2		**1-octene /nonanal (3:1)+CO_2**		**1-octene /nonanal (1:1)+CO_2**		**1-octene /nonanal (1:3)+CO_2**		**nonanal+CO_2**	
***P* [bar]**	$\Delta V/V_0$	***P* [bar]**	$\Delta V/V_0$	***P* [bar]**	$\Delta V/V_0$	***P* [bar]**	$\Delta V/V_0$	***P* [bar]**	$\Delta V/V_0$
20.36	0.056 ±0.002	19.9	0.063 ±0.002	10.27	0.066±0.002	19.78	0.062±0.002	20.21	0.074±0.002
29.99	0.119 ±0.002	29.98	0.124 ±0.002	22.00	0.136±0.002	30.01	0.117±0.002	30.08	0.131±0.002
40.32	0.187 ±0.002	40.43	0.198 ±0.002	29.88	0.185±0.002	40.42	0.188±0.002	40.52	0.202±0.002
50.06	0.274 ±0.002	50.03	0.279 ±0.002	39.05	0.256±0.002	50.24	0.267±0.002	50.19	0.276±0.002
60.14	0.408 ±0.002	59.98	0.380 ±0.002	50.40	0.369±0.002	60.82	0.382±0.002	60.60	0.378±0.002
70.33	0.578 ±0.002	70.76	0.549 ±0.002	61.25	0.528±0.002	70.70	0.498±0.002	70.53	0.504±0.002
80.39	0.839 ±0.003	80.52	0.770 ±0.003	71.13	0.716±0.002	80.15	0.682±0.002	80.28	0.670±0.002
90.51	1.312 ±0.003	90.73	1.157 ±0.003	80.44	0.993±0.003	90.54	0.947±0.003	90.27	0.894±0.003
100.21	2.413 ±0.004	100.79	1.962 ±0.004	90.43	1.499±0.003	99.97	1.379±0.003	100.27	1.263±0.003
106.14	4.799 ±0.007	110.68	5.129 ±0.008	100.21	2.708±0.005	116.41	4.292±0.006	109.87	1.897±0.004
				105.65	5.067±0.007			120.30	4.025±0.006

[a] 6 bar of syngas with current experimental configuration results in an initial percent of syngas to organic ~37% by mole

Volume expansion: $\frac{\Delta V}{V_0} = \frac{V^L(T,P) - V_0(T,P=1bar)}{V_0(T,P=1bar)}$

At pressures below 50 bar, the volume expansions of each of the components are very similar. Between 50 bar and the respective mixture critical pressures, the volume expansion of 1-octene becomes significantly greater than nonanal due to higher solubility in 1-octene than nonanal. Moreover, as nonanal is slightly polar, the nonanal-nonanal interactions in the CO_2 expanded fluid become stronger than mostly dispersive forces found in the 1-octene/CO_2 mixture.

The volume expansion data with CO/H_2 pressure are measured at 60°C and up to 120 bar pressure; the data are summarized in Table 8.7. The volume expansion of CO_2 with an initial CO/H_2 pressure is very similar to that of CO_2 without CO/H_2 pressure. The volume expansion of a 1:1 mixture of 1-octene and nonanal is illustrated in Figure 8.7 until approximately 60 bar of pressure. Above 60 bar, the volume expansion with only CO_2 pressure becomes moderately different and greatest near the mixture critical point. With an initial pressure of approximately 6 bar of syngas, the volume expansion decreases at a given pressure over that of a similar pressure of pure CO_2. This would be expected as the solubility of H_2 and CO is much less than CO_2 [25-27]. By reducing the partial pressure or, more appropriately, increasing the fugacity of CO_2 in the vapor phase, the solubility of CO_2 at a given pressure in the liquid phase will be lower, therefore, the volume expansion without CO/H_2 pressure is higher than runs with CO/H_2 pressure.

8.2.4 Molar volume

The volume expansions of the binary, ternary systems are measured at 60°C and pressure approaching the mixture critical points. The data are listed in Tables 8.3 and

8.4. The molar volume decreases with CO_2 pressure until it is close to critical status, where the volume expansion is increased dramatically to make the molar volume slightly higher than minimum. For instance, the mixture of 1-octene and CO_2 is 141.55 mol/ml at 12.17 bar, 77.81mol/ml at 98.46 bar, which decreases about 45%. Figure 8.9 shows that the molar volume of 1-octene and nonanal decreases linearly at lower pressure and reaches the minimum when the pressure is close to mixture critical points. The molar volume data is very important for kinetics result explanations and also important for viscosity correlation.

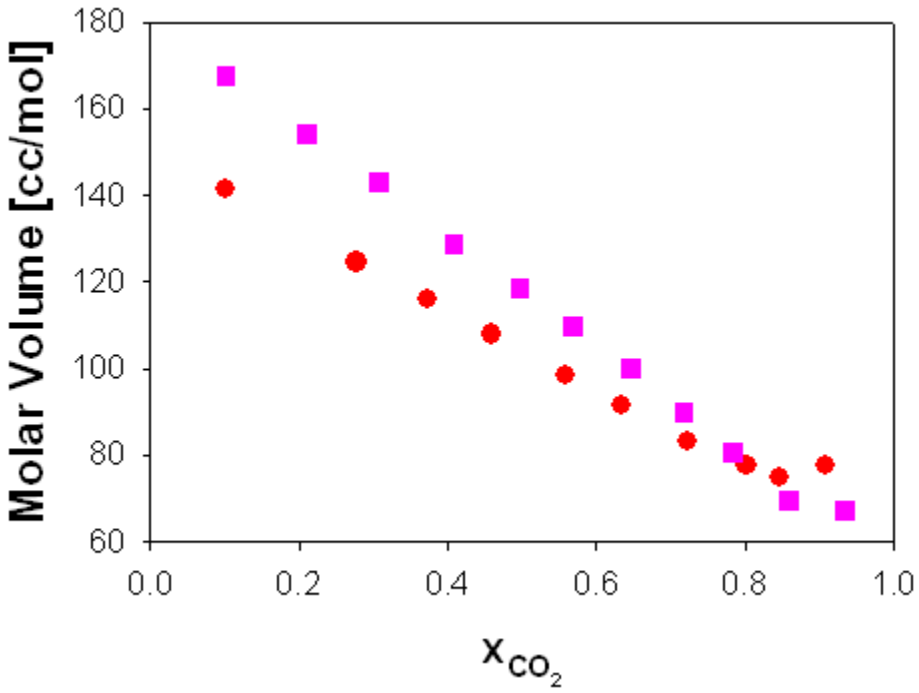

Figure 8.9 Molar volume of 1-octene/CO_2 and nonanal/ CO_2. ●: 1-octene. ■: nonanal

8.3 Conclusions

To understand the phase behavior and phase equilibrium of the hydroformylation of 1-octene in CO_2-expanded liquids, the vapor-liquid equilibrium of CO_2 with 1-octene, nonanal, and syngas (CO/H_2) has been measured at 60°C and pressure up to 120 bar. The phase behavior data determine the operating conditions. The molar volume and volume expansion data are very useful to explain the kinetics results. The vapor-liquid equilibrium data is the basis for reaction and calculation of kinetics rate. As expected, the solubility and volume expansion increase with CO_2 pressure, which can be quite significant in the binary and multi-component mixtures. The Peng-Robinson equation of state with vdW-2 mixing rules was chosen for modeling, which correlates the binary experimental solubility data well. The model also provides an adequate prediction of the ternary results without interaction parameters for the 1-octene and nonanal especially at low to moderate pressures. For the ternary mixtures of the 1-octene and nonanal, the mixture critical points increase with initial nonanal composition (increasing conversion during a reaction) and increase in the presence of syngas (CO/H_2) pressure. These data will aid to understand the reaction kinetics and help reaction engineering for the Hydroformylation reaction in CO_2–expanded liquids and supercritical fluids.

8.4 References

1. Cornils, B. and W.A. Herrmann, eds. *Applied Homogeneous Catalysis with Organometallic Compounds*. 1996, Wiley-VCH: Weinheim.
2. Cornils, B. and W.A. Herrmann, eds. *Aqueous Phase Organometallic Catalysis*. 1998, Wiley-VCH: Weinheim.
3. Jessop, P.G. and B. Subramaniam, *Gas-Expanded Liquids.* Chemical Reviews, 2007. **107**(6): p. 2666-2694.
4. Jin, H., B. Subramaniam, A. Ghosh, and J. Tunge, *Intensification of catalytic olefin hydroformylation in CO_2-expanded media* AIChE Journal, 2006. **52**(7): p. 2575-2581.
5. Scurto, A.M., B. Subramaniam, and K. Hutchenson, *Gas-Expanded Liquids (GXLs): Fundamentals and Applications*, in *Gas Expanded Liquids and Near-Critical Media: Green Chemistry and Engineering*, K. Hutchenson, A.M. Scurto, and B. Subramaniam, Editors. 2008, ACS Symp. Ser. 1006: Washington, D.C.
6. Jin, H. and B. Subramaniam, *Homogeneous catalytic hydroformylation of 1-octene in CO_2-expanded solvent media.* Chemical Engineering Science, 2004. **59**(22-23): p. 4887-4893.
7. Franciò, G., K. Wittmann, and W. Leitner, *Highly efficient enantioselective catalysis in supercritical carbon dioxide using the perfluoroalkyl-substituted ligand (R,S)-3-H_2F_6-BINAPHOS.* Journal of Organometallic Chemistry, 2001. **621**(1-2): p. 130-142.

8. McCarthy, M., H. Stemmer, and W. Leitner, *Catalysis in inverted supercritical CO_2/aqueous biphasic media.* Green Chemistry, 2002. **4**(5): p. 501-504.

9. Palo, D.R. and C. Erkey, *Kinetics of the Homogeneous Catalytic Hydroformylation of 1-Octene in Supercritical Carbon Dioxide with $HRh(CO)[P(p\text{-}CF_3C_6H_4)_3]_3$.* Ind. Eng. Chem. Res., 1999. **38**: p. 3786-3792.

10. Koekena, A.C.J., S.J.M.d. Bakkera, H.M. Costerusa, L.J.P.v.d. Broekea, B.-J. Deelmanb, and J.T.F. Keurentjes, *Evaluation of pressure and correlation to reaction rates during homogeneously catalyzed hydroformylation in supercritical carbon dioxide* Journal of Supercritical Fluids, 2008. **46**(1): p. 47-56.

11. Ahosseini, A., W. Ren, and A.M. Scurto, *Understanding Biphasic Ionic Liquid/CO_2 Systems for Homogeneous Catalysis: Hydroformylation.* Ind. Eng. Chem. Res., 2009. **48**(9): p. 4254–4265.

12. Scurto, A.M. and W. Leitner, *Expanding the useful range of ionic liquids: melting point depression of organic salts with carbon dioxide for biphasic catalytic reactions.* Chem. Comm., 2006(35): p. 3681-3683.

13. Sellin, M.F., P.B. Webb, and D.J. Cole Hamilton, *Continuous flow homogeneous catalysis: hydroformylation of alkenes in supercritical fluid–ionic liquid biphasic mixtures.* Chemical Communications, 2001: p. 781-782.

14. Webb, P.B., T.E. Kunene, and D.J. Cole-Hamilton, *Continuous flow homogeneous hydroformylation of alkenes using supercritical fluids.* Green Chemistry, 2005. **7** p. 373-379.

15. Fujita, S.-I., S. Fujisawa, B.M. Bhanage, Y. Ikushima, and M. Arai, *Hydroformylation of 1-hexene catalyzed with rhodium fluorinated phosphine complexes in supercritical carbon dioxide and in conventional organic solvents: effects of ligands and pressures.* New J. Chem., 2002. **26**: p. 1479–1484.

16. Fujita, S.-I., S. Fujisawa, B.M. Bhanage, Y. Ikushima, and M. Arai, *Hydroformylation of 1,5-Hexadiene Catalyzed by Rhodium Complexes in Supercritical Carbon Dioxide and in Toluene: Effects of Fluorinated Phosphane Ligands and Reaction Conditions.* Eur. J. Org. Chem., 2004: p. 2881 - 2887.

17. Brennecke, J.F. and E.J. Maginn, *Ionic liquids: innovative fluids for chemical processing.* . AIChE Journal, 2001. **47**(11): p. 2384-2389.

18. Ren, W. and A.M. Scurto, *High-pressure phase equilibria with compressed gases.* Review of Scientific Instruments, 2007. **78**(12): p. 125104-7.

19. Guha, D., H. Jin, M.P. Dudukovic, P.A. Ramachandran, and B. Subramaniam, *Mass Transfer Effects during Homogeneous 1- Octene Hydroformylation in CO_2-expanded Solvent: Modeling and Experiments.* Chem. Eng. Sci., 2007. **62**: p. 4967-4975.

20. Jiang, T., Z. Hou, B. Han, L. Gao, Z. Liu, J. He, and G. Yang, *A study on the phase behavior of the system CO_2 + CO + H_2 + 1-hexene + heptanal.* Fluid Phase Equilibria 2004. **215**: p. 85-89.

21. Ke, J., B. Han, M.W. George, H. Yan, and M. Poliakoff, *How Does the Critical Point Change during a Chemical Reaction in Supercritical Fluids? A Study of the Hydroformylation of Propene in Supercritical CO_2* J. Am. Chem. Soc., 2001. **123** (16): p. 3661-3670.

22. Pereda, S., E.A. Brignole, and S.B. Bottini, *Advances in phase equilibrium engineering of supercritical reactors.* J. Supercrit. Fluids, 2009. **47** p. 336–343.

23. Ren, W., B. Rutz, and A.M. Scurto, *High-Pressure Phase Equilibrium for the Hydroformylation of 1-Octene to Nonanal in Compressed CO_2.* J. Supercrit. Fluids, 2009, 51(2) p. 142 - 147.

24. Pfohl, O., S. Petkov, and G. Brunner, *PE 2000 – A Powerful Tool to Correlate Phase Equilibria*. 2000, München: Herbert Utz Verlag.

25. Brunner, E., *Solubility of hydrogen in 10 organic solvents at 298.15, 323.15, and 373.15 K.* J. Chem. Eng. Data, , 1985. **30**(3): p. 269-273.

26. Katayama, T., K. Ohgahi, W. Maekawa, M. Goto, and T. Nagano, *Isothermal vapor-liquid equilibriums of acetone-carbon dioxide and methanol-carbon dioxide systems at high pressures.* Journal of Chemical Engineering of Japan, 1975. **8**(2): p. 89-92.

27. Purwanto, R.M. Deshpande, R.V. Chaudhari, and H. Delmas, *Solubility of Hydrogen, Carbon Monoxide, and 1-Octene in Various Solvents and Solvent Mixtures.* J. Chem. Eng. Data,, 1996. **41**(6): p. 1414-1417.

Chapter 9 Conclusions and Recommendations

The research presents the investigation of the global phase behaviors and equilibria of ionic liquids and compressed gases for chemical reactions and engineering applications. A biphasic IL/CO_2 reaction system is a promising alternative for hydrogenation and hydroformylation reactions. Experimental results and thermodynamic model studies reveal that ionic liquids and compressed gases are feasible to be used as working fluids for absorption air conditioning systems.

Binary mixtures of the refrigerant gas, R-134a, and ionic liquids of [EMIm][Tf_2N], [HMIm][Tf_2N], [HMIm][PF_6], [HMIm][BF_4], and [BMIm][PF_6] belong to a Type V system according to the classification of Scott and van Konynenburg, which includes vapor liquid equilibrium, vapor liquid liquid equilibrium, liquid liquid equlibirum, and reaches mixture critical points at certain temperature and pressure. R-134a and [HMIm][Br] is a type III system which also includes vapor liquid equilibrium, vapor liquid liquid equilibrium, liquid liquid equilibrium, multiple phase equilibrium, but cannot reach a mixture critical point at the studied conditions. The different phase behaviors between [HMIm][Br], [HMIm][Tf_2N] and R-134a provide a feasible purification method of synthesizing the IL by compressed fluids. The phase behavior of CO_2 and all ionic liquids indicate Type III systems. The global phase behavior of ionic liquids and compressed gases is predicted with Peng-Robinson equation of state (EoS). The model can quantitatively predict the global phase behavior by only using

the EoS parameters and binary interaction parameters correlated from vapor liquid equilibrium data.

The phase equilibrium data of imidazolium ionic liquids and CO_2/R-134a at three isotherm and pressure up to 250 bar reveal an excellent agreement with those reported in literature. The ionic liquid structure demonstrates significant influence on both the phase equilibrium data and the global phase behavior, such as solubility, molar volume, LCEP and mixture critical points. The solubility and LCEP temperature increase and the mixture critical pressures decrease with increasing the alkyl- group on the cation. The anion plays a more important role for a given cation class than changes to the cation itself. The solubility and the LCEP temperature increases and the mixture critical pressures decrease in the order of [BF_4], [PF_6], and [Tf_2N]. The phase equilibria data is well correlated by the PR-vdW2 EoS using predicted critical properties of ionic liquids. However, the model under predicts the mixture critical points. The EoS prediction of a mixture critical point for the CO_2/[HMIm][Tf_2N] system at pressures above 400 bar is not supported by any experimental data.

The feasibility of absorption refrigeration systems using ionic liquids and compressed gases in vehicles was investigated by thermodynamic modeling. Simulation studies reveal that the air conditioning system could be operated by the waste heat from the engine coolant and/or exhaust gases. This would reduce fuel consumption and lower environmental pollution. In addition, it is not necessary for an absorption system to have a bulky rectifier, needed for common absorption

refrigeration systems using solvents, since the ionic liquid has no vapor pressure. Modeling studies reveal that the working fluids of [HMIm][Tf_2N]/R-134a and [HMIm][Tf_2N]/CO_2 can produce comparable cooling capacity as standard vapor compression systems. Further optimization is also possible by varying operational conditions and molecular design of the ionic liquid.

Complete phase behavior study of the reactant, product, CO_2 and ionic liquids for hydrogenation and hydroformylation reactions of 1-octene were measured. Volume expansion of liquid phase with CO_2 pressure was determined simultaneously. CO_2 pressure shows two main effects on the reactants: dilution and reactant partitioning. The unique phase behavior of CO_2, the organic components and ionic liquid provide a feasible process to perform the reaction and separation of the product from the catalytic phase. With these phenomena understood, a biphasic reaction system with IL/CO_2 for homogeneously catalyzed reactions provides a highly tunable, flexible and possibly economical platform for reactions and separations. Complete phase behavior studies for reactions enable the understanding the kinetics results, determining the operating conditions and choosing appropriate separation process and properly designing an optimal reaction system.

In the future, designing and synthesizing an ionic liquid absorbent with high CO_2 and R134a solubility and capacity are recommended. Developing a preliminary process using ionic liquids/compressed gases in an absorption system is desired. More physical and chemical property data with different ionic liquids need to be measured to build a database. Models that provide the correlation between property and

structure would be highly useful for molecular design of novel ionic liquids. The absorption and desorption kinetics of ionic liquids and compressed gases should be measured for further process design. For alternative refrigerants of R-134a, the hydro-fluoro olefin, 2,3,3,3 tetrafluoropropene (HFO-1234yf) is a promising alternative in addition to CO_2. The atmospheric lifetime of HFO-1234yf is just 11 days, compared to 13 years for today's R-134a. The properties of HFC-134a and HFO-1234yf are very similar. The service equipment and service practices will also be similar for vapor compression systems. The phase behavior and equilibrium of ionic liquids and HFO-1234yf should be measured and simulation studies for absorption air conditioning systems in vehicles should be performed.

To better understand the association between ionic liquids and compressed gases, it is necessary to further explore the factors affecting the gas solubility. The solubility is not only affected by temperature and pressure, but also the molecular size and polarity. Moreover, three intermolecular forces play significant roles here: coulombic forces, dispersive forces, dipolar forces, and sometimes hydrogen bonds. Identifying and quantifying the dominant forces will help explain and relate the solubility with IL structure.

Appendix A: Mechanical Drawing of High Pressure Vapor-Liquid Equilibrium Cell

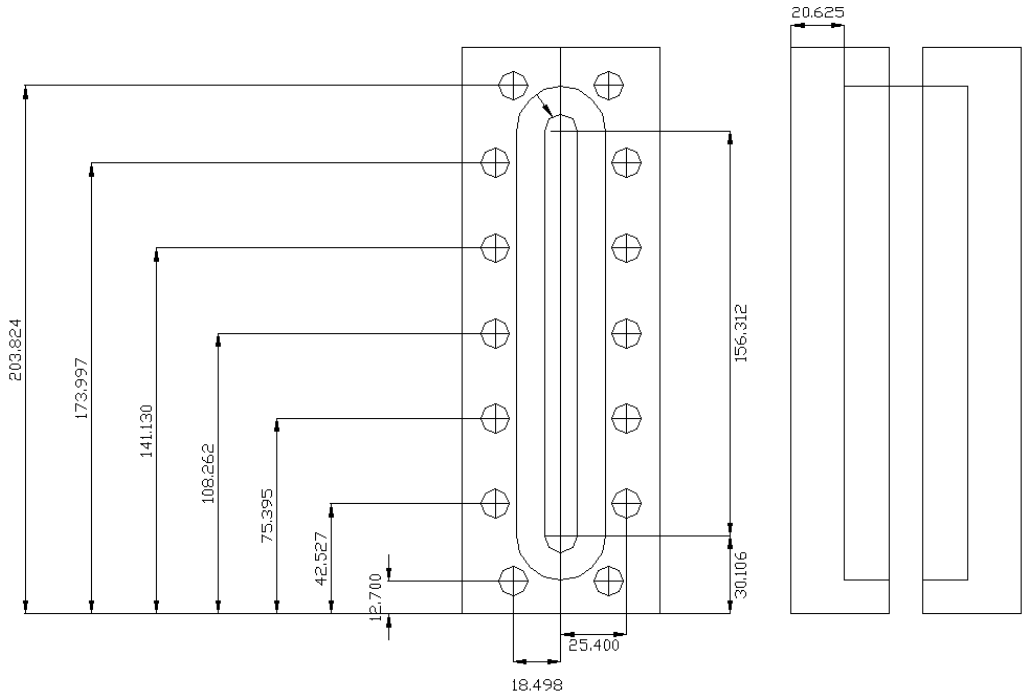

Figure A.1 Mechanical drawing of vapor-liquid equilibrium cell from front view.

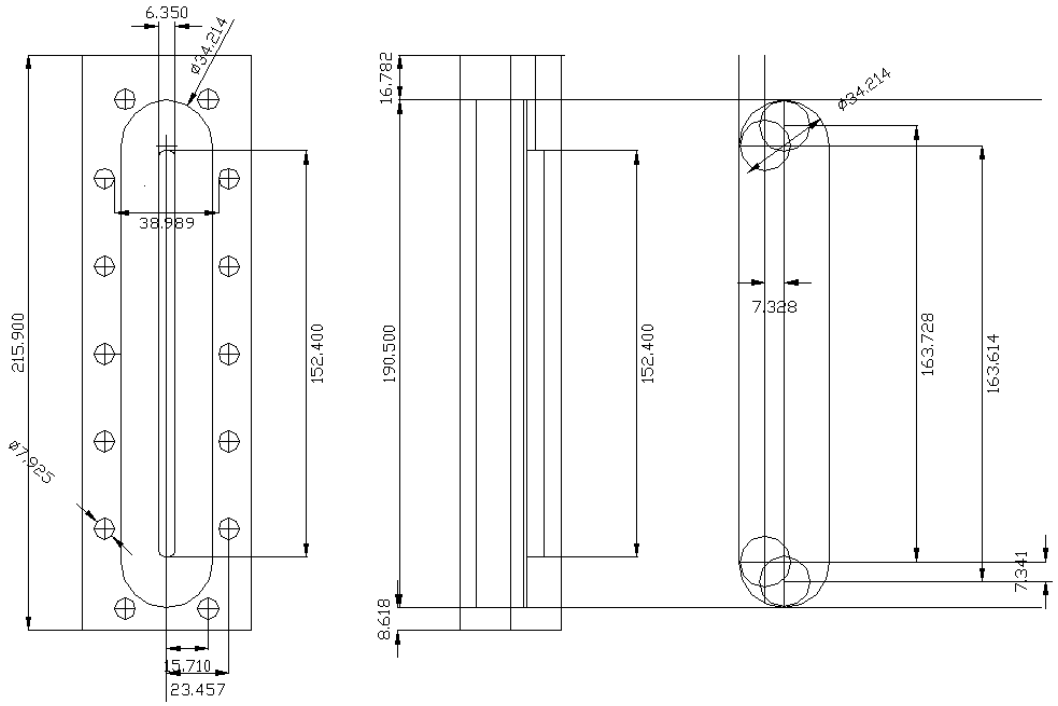

Figure A.2 Mechanical drawing of vapor-liquid equilibrium cell from side view.

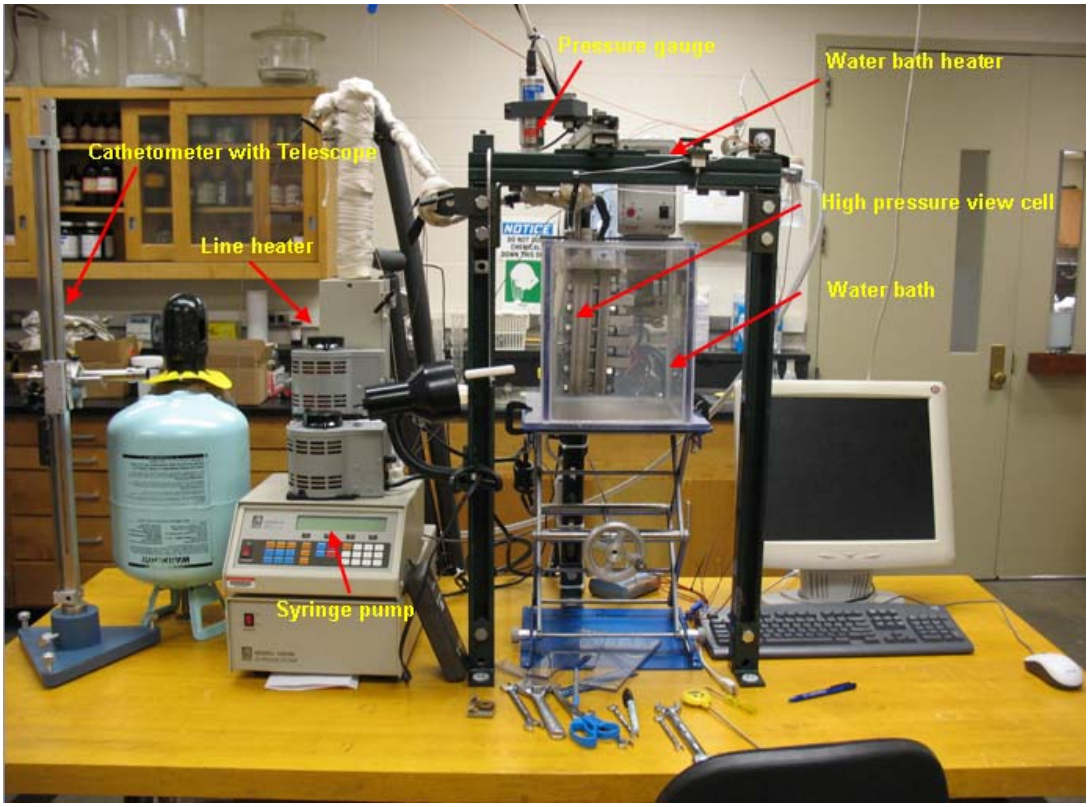

Figure A.3 Picture of experimental apparatus.

Appendix B: Error Analysis for Vapor-Liquid Equilibrium Calculations

Combined standard uncertainties represent the estimated standard deviation of the results, which can be used to evaluate the accuracy for the apparatus [1]. In order to provide the uncertainties, the error analysis is developed following the procedure given by Scurto[2].

Suppose f is a function that depends on more than one variable, f can be expressed as:

$$f = f(a_1, a_2, ..., a_n)$$

In general, the partial derivative df is defined to be:

$$df = \left(\frac{\partial f}{\partial a_1}\right) da_1 + \left(\frac{\partial f}{\partial a_2}\right) da_2 + ... + \left(\frac{\partial f}{\partial a_n}\right) da_n$$

Second-order partial derivatives are:

$$\frac{\partial^2 f}{\partial a_1^2}, \frac{\partial^2 f}{\partial a_2^2}, ..., \frac{\partial^2 f}{\partial a_n^2}$$

Second-order mixed derivatives are:

$$\frac{\partial^2 f}{\partial a_1 \partial a_2}, \frac{\partial^2 f}{\partial a_1 \partial a_3}, ..., \frac{\partial^2 f}{\partial a_1 \partial a_n}$$

....

$$\frac{\partial^2 f}{\partial a_n \partial a_1}, \frac{\partial^2 f}{\partial a_n \partial a_2}, ..., \frac{\partial^2 f}{\partial a_n \partial a_{n-1}}$$

To simplify the calculation for practical interest, the variables can be assumed to be uncorrelated. Then the second-order mixed derivatives are neglected. The combined standard uncertainty is:

$$d^2 f = \left(\frac{\partial^2 f}{\partial a_1^2}\right) d^2 a_1 + \left(\frac{\partial^2 f}{\partial a_2^2}\right) d^2 a_2 + ... + \left(\frac{\partial^2 f}{\partial a_n^2}\right) d^2 a_n$$

If the quantities of variables are very small, the second-order derivatives can be approximated to the corresponding variances, i.e. $d^2 a_1 \approx (\Delta a_1)^2$.

In the following equations, 1 represents the liquid property, 2 represents the gas property.

Error analysis of the mole faction of CO_2, x_2, is calculated as:

$$x_2 = f(n_1, n_2)$$

$$x_2 = \frac{n_2}{n_1 + n_2} = \frac{n_2}{n_t}$$

$$dx_2{}^2 = \left(\frac{\partial x_2}{\partial n_1}\right)^2 \partial n_1{}^2 + \left(\frac{\partial x_2}{\partial n_2}\right)^2 \partial n_2{}^2$$

$$\left(\frac{\partial x_2}{\partial n_1}\right) = \frac{-n_2}{(n_1 + n_2)^2} = \frac{-n_2}{n_t{}^2}$$

$$\left(\frac{\partial x_2}{\partial n_2}\right) = \frac{n_1 + n_2}{(n_1 + n_2)^2} + \frac{-n_2}{(n_1 + n_2)^2} = \frac{1}{n_t} - \frac{n_2}{n_t{}^2}$$

$$n_1 = \frac{m_1}{MW_1}$$

$$dn_1 = \frac{dm_1}{MW_1}$$

$$n_2 = n_{pump} - n_{lines} - n_{headspace} + (n_{lines}^0 + n_{headspace}^0)$$

$$n_{pump} = \frac{\Delta V_{pump} \times \rho(T_{pump}, P_{pump})}{MW_2}$$

$$n_{lines} = \frac{V_{lines} \times \rho(T_{line}, P)}{MW_2}$$

$$n_{headspace} = \frac{(V_{cell} - V^L(H)) \times \rho(T_{line}, P)}{MW_2}$$

$$dn_2{}^2 = \left(\frac{\partial n_2}{\partial n_{pump}}\right)^2 dn_{pump}{}^2 + (-1)^2\left(\frac{\partial n_2}{\partial n_{lines}}\right)^2 dn_{lines}{}^2 + (-1)^2\left(\frac{\partial n_2}{\partial n_{headspace}}\right)^2 dn_{headspance}{}^2$$
$$+\left(\frac{\partial n_2}{\partial n^0_{lines}}\right)^2 dn^0_{lines}{}^2 + \left(\frac{\partial n_2}{\partial n^0_{headspace}}\right)^2 dn^0_{headspace}{}^2$$

$$dn_2{}^2 = dn_{pump}{}^2 + dn_{lines}{}^2 + dn_{headspance}{}^2 + dn^0_{lines}{}^2 + dn^0_{headspace}{}^2$$

$$dn_{pump}{}^2 = \left(\frac{\partial n_{pump}}{\partial \Delta V_{pump}}\right)^2 d\Delta V_{pump}{}^2 + \left(\frac{\partial n_{pump}}{\partial \rho_{pump}}\right)^2\left(\frac{\partial \rho}{\partial T_{pump}}\right)^2 dT_{pump}{}^2 + \left(\frac{\partial n_{pump}}{\partial \rho_{pump}}\right)^2\left(\frac{\partial \rho}{\partial P_{pump}}\right)^2 dP_{pump}{}^2$$
$$= \left(\frac{\partial n_{pump}}{\partial \Delta V_{pump}}\right)^2 d\Delta V_{pump}{}^2 + \left(\frac{\partial n_{pump}}{\partial T_{pump}}\right)^2 dT_{pump}{}^2 + \left(\frac{\partial n_{pump}}{\partial P_{pump}}\right)^2 dP_{pump}{}^2$$

$$\left(\frac{\partial n_{pump}}{\partial \Delta V_{pump}}\right) = \frac{\rho\left(T_{pump}, P_{pump}\right)}{MW_2};$$

$$\left(\frac{\partial n_{pump}}{\partial T_{pump}}\right) = \frac{\Delta V_{pump}}{MW_2}\left(\frac{\partial \rho\left(T_{pump}, P_{pump}\right)}{\partial T_{pump}}\right)$$
$$= \frac{\Delta V_{pump}}{MW_2}\frac{\rho\left(P_{pump}, T_{pump} + \sigma_{T_{pump}}\right) - \rho\left(P_{pump}, T_{pump} - \sigma_{T_{pump}}\right)}{2\sigma_{T_{pump}}}$$

$$\left(\frac{\partial n_{pump}}{\partial P_{pump}}\right) = \frac{\Delta V_{pump}}{MW_2}\left(\frac{\partial \rho\left(T_{pump}, P_{pump}\right)}{\partial P_{pump}}\right)$$
$$= \frac{\Delta V_{pump}}{MW_2}\frac{\rho\left(P_{pump} + \sigma_{P_{pump}}, T_{pump}\right) - \rho\left(P_{pump} - \sigma_{P_{pump}}, T_{pump}\right)}{2\sigma_{P_{pump}}}$$

$$dn_{lines}{}^2 = \left(\frac{\partial n_{lines}}{\partial V_{lines}{}^2}\right)^2 dV_{lines}{}^2 + \left(\frac{\partial n_{lines}}{\partial \rho_{lines}}\right)^2 \left(\frac{\partial \rho}{\partial T_{lines}}\right)^2 dT_{lines}{}^2 + \left(\frac{\partial n_{pump}}{\partial \rho_{lines}}\right)^2 \left(\frac{\partial \rho}{\partial P}\right)^2 dP^2$$
$$= \left(\frac{\partial n_{lines}}{\partial V_{lines}}\right)^2 dV_{lines}{}^2 + \left(\frac{\partial n_{lines}}{\partial T_{lines}}\right)^2 dT_{lines}{}^2 + \left(\frac{\partial n_{lines}}{\partial P}\right)^2 dP^2$$

$$\left(\frac{\partial n_{lines}}{\partial V_{lines}}\right) = \frac{\rho\left(T_{lines,} P\right)}{MW_2}$$

$$\left(\frac{\partial n_{lines}}{\partial T_{lines}}\right) = \frac{V_{lines}}{MW_2}\left(\frac{\partial \rho\left(T_{lines}, P\right)}{\partial T_{lines}}\right) = \frac{V_{lines}}{MW_2}\frac{\rho\left(P, T_{lines} + \sigma_{T_{lines}}\right) - \rho\left(P, T_{lines} - \sigma_{T_{lines}}\right)}{2\sigma_{T_{lines}}}$$

$$\left(\frac{\partial n_{lines}}{\partial P}\right) = \frac{V_{lines}}{MW_2}\left(\frac{\partial \rho\left(T_{lines}, P\right)}{\partial P}\right) = \frac{V_{lines}}{MW_2}\frac{\rho\left(P + \sigma_P, T_{lines}\right) - \rho\left(P - \sigma_P, T_{lines}\right)}{2\sigma_P}$$

$$dn_{headspace}{}^2 = \left(\frac{\partial n_{headspace}}{\partial V_{cell}}\right)^2 dV_{cell}{}^2 + \left(\frac{\partial n_{headspace}}{\partial V_L}\right)^2 dV_L{}^2$$
$$+ \left(\frac{\partial n_{headspace}}{\partial \rho_{cell}}\right)^2 \left(\frac{\partial \rho_{cell}}{\partial T}\right)^2 dT^2 + \left(\frac{\partial n_{headspace}}{\partial \rho_{cell}}\right)^2 \left(\frac{\partial \rho_{cell}}{\partial P}\right)^2 dP^2$$
$$= \left(\frac{\partial n_{headspace}}{\partial V_{cell}}\right)^2 dV_{cell}{}^2 + \left(\frac{\partial n_{headspace}}{\partial V_L}\right)^2 dV_L{}^2 + \left(\frac{\partial n_{headspace}}{\partial T}\right)^2 dT^2 + \left(\frac{\partial n_{headspace}}{\partial P}\right)^2 dP^2$$

$$\left(\frac{\partial n_{headspace}}{\partial V_{cell}}\right) = \frac{\rho\left(T_{,} P\right)}{MW_2}$$

$$\left(\frac{\partial n_{headspace}}{\partial V_L}\right) = -\frac{\rho\left(T_{,} P\right)}{MW_2}$$

$$\left(\frac{\partial n_{headspace}}{\partial T_{cell}}\right) = \frac{\left(V_{cell} - V_L(H)\right)}{MW_2}\left(\frac{\partial \rho\left(T_{,} P\right)}{\partial T}\right) = \frac{\left(V_{cell} - V_L(H)\right)}{MW_2}\frac{\rho\left(P, T + \sigma_T\right) - \rho\left(P, T - \sigma_T\right)}{2\sigma_T}$$

$$\left(\frac{\partial n_{headspace}}{\partial P_{cell}}\right) = \frac{\left(V_{cell} - V_L(H)\right)}{MW_2}\left(\frac{\partial \rho(T,P)}{\partial P}\right) = \frac{\left(V_{cell} - V_L(H)\right)}{MW_2}\frac{\rho(P+\sigma_P,T) - \rho(P-\sigma_P,T)}{2\sigma_P}$$

Error analysis for liquid molar volume, $\underline{V}_L$, is computed as

$$V_L = C_1 H - C_0$$

$$dV_L{}^2 = \left(\frac{dV_L}{dH}\right)^2 dH^2 = (C_1)^2 dH^2$$

$$\underline{V}_L = \frac{V_L}{n_1 + n_2} = \frac{V_L}{n_t}$$

$$d\underline{V}_L{}^2 = \left(\frac{\partial \underline{V}_L}{\partial V_L}\right)^2 dV_L{}^2 + \left(\frac{\partial \underline{V}_L}{\partial n_1}\right)^2 dn_1{}^2 + \left(\frac{\partial \underline{V}_L}{\partial n_2}\right)^2 dn_2{}^2$$

$$\left(\frac{\partial \underline{V}_L}{\partial V_L}\right) = \frac{1}{n_1 + n_2} - \frac{V_L}{(n_1 + n_2)^2}\left(\frac{\partial n_1}{\partial V_L}\right)^2$$

$$\left(\frac{\partial n_1}{\partial V_L}\right) = -\left(\frac{\partial n_{headspace}}{\partial V_L}\right) = \frac{\rho(T,P)}{MW_2}$$

$$\left(\frac{\partial \underline{V}_L}{\partial V_L}\right) = \frac{1}{n_t} - \frac{V_L \rho(T,P)}{MW_2 \times (n_t)^2}$$

$$\left(\frac{\partial V_L}{\partial n_{1\,or\,2}}\right) = \frac{-V_L}{n_t^{\,2}}$$

Error analysis for density of the liquid solution, ρ, is computed as

$$\rho = \frac{m_L}{V_L} = \frac{m_1 + m_2}{V_L}$$

$$d\rho^2 = \left(\frac{\partial \rho}{\partial V_L}\right)^2 dV_L^{\,2} + \left(\frac{\partial \rho}{\partial m_1}\right)^2 dm_1^{\,2} + \left(\frac{\partial \rho}{\partial m_2}\right)^2 dm_2^{\,2}$$

$$\left(\frac{\partial \rho}{\partial V_L}\right) = \frac{-(m_1 + m_2)}{V_L}$$

$$\left(\frac{\partial \rho}{\partial m_{1\,or\,2}}\right) = \frac{1}{V_L}$$

Error analysis for the mass fraction of the gas, w, is calculated as

$$w_2 = f(m_1, m_2)$$

$$w_2 = \frac{m_2}{m_1 + m_2} = \frac{m_2}{m_t}$$

$$dw_2^{\,2} = \left(\frac{\partial w_2}{\partial m_1}\right)^2 \partial m_1^{\,2} + \left(\frac{\partial w_2}{\partial m_2}\right)^2 \partial m_2^{\,2}$$

$$\left(\frac{\partial w_2}{\partial m_1}\right) = \frac{-m_2}{(m_1 + m_2)^2} = \frac{-n_2 MW_2}{(n_1 MW_1 + n_2 MW_2)^2}$$

$$dm_1^2 = MW_1^2 dn_1^2$$

$$\left(\frac{\partial w_2}{\partial m_2}\right) = \frac{m_1 + m_2}{(m_1 + m_2)^2} + \frac{-m_2}{(m_1 + m_2)^2}$$

$$= \frac{1}{(m_1 + m_2)} + \frac{-m_2}{(m_1 + m_2)^2}$$

$$= \frac{1}{(n_1 MW_1 + n_2 MW_2)} + \frac{-n_2 MW_2}{(n_1 MW_1 + n_2 MW_2)^2}$$

$$dm_2^2 = MW_2^2 dn_2^2$$

Error analysis for the volume expansion, $\frac{\Delta V}{V_0}$, is computed as:

$$\Delta V = f(V, V_0)$$

$$\frac{\Delta V}{V_0} = \frac{V - V_0}{V_0} = \frac{V}{V_0} - 1$$

$$d\left(\frac{\Delta V}{V_0}\right)^2 = \left(\frac{\partial \Delta V}{\partial V}\right)^2 dV^2 + \left(\frac{\partial \Delta V}{\partial V_0}\right)^2 dV_0{}^2$$

$$\left(\frac{\partial \Delta V}{\partial V}\right) = \frac{1}{V_0}$$

$$\left(\frac{\partial \Delta V}{\partial V_0}\right) = \frac{-V}{V_0^2}$$

Error analysis for Molality , [m], is determined from the definition:

Molality = moles of CO_2/ mass of IL (kg),

Molality = n_2*1000/mass of IL (g)

$$[m] = \frac{1000 \times n_2}{m_1}$$

$$d[m]^2 = \left(\frac{\partial[m]}{\partial n_2}\right)^2 dn_2^2 + \left(\frac{\partial[m]}{\partial m_1}\right)^2 dm_1^2$$

$$\left(\frac{\partial[m]}{\partial n_2}\right) = \frac{1000}{m_1}$$

$$\left(\frac{\partial[m]}{\partial m_1}\right) = \frac{-1000 n_2}{m_1^2}$$

Error analysis for Molarity, M, is computed in the similar way with Molality.

Molarity = Moles of the gas/ Volume of the solution (liter)

Molarity = $1000*n_2/V_L$ (milliliter)

$$[M] = \frac{n_2}{1L} = \frac{1000 \times n_2}{V_L}$$

$$d[M]^2 = \left(\frac{\partial[M]}{\partial n_2}\right)^2 dn_2^2 + \left(\frac{\partial[M]}{\partial V_L}\right)^2 dV_L^2$$

$$\left(\frac{\partial[M]}{\partial n_2}\right) = \frac{1000}{V_L}$$

$$\left(\frac{\partial[M]}{\partial V_L}\right) = \frac{-1000 \times n_2}{V_L^2}$$

Table B.1 Nomenclature used in the error analysis

x_i	Mole fraction of component i
n_i	Moles of component i
n_t	Total mole of the liquid-gas mixture
$n_{pump,headspace,lines}$	Moles of the gas in the pump, headspace, lines
$n^0_{line,headspaces}$	Initial moles of the gas in the lines and headspace
m_i	Mass of component i
MW_i	Molecular weight of component i
C_1, C_0	Calibration coefficients from the liquid height H to the volume V_L

Table B.2 Measurement precision for the error analysis

dT_i $i = 1,2,3$	± 0.5 C
dT_{pump}	± 0.01 C
dP_{pump}	0.334 Bar
dT , $dT_{headspace}$	± 0.01 C
dP , dP_{lines}	0.0668 Bar
dV_{cell}	0.01438ml
dV_L	0.001ml
dH	0.01mm
dm_1	0.0001g

Reference:

1. Ren, W. and A.M. Scurto, *High-pressure phase equilibria with compressed gases.* The Review of scientific instruments, 2007. **78**(12).

2. Scurto, A.M., *HIGH-PRESSURE PHASE AND CHEMICAL EQUILIBRIA OF β–DIKETONE LIGANDS AND CHELATES WITH CARBON DIOXIDE*, in *Department of chemical engineering*. 2002, University of Notre Dame: Notre Dame, Inidiana. p. 323.

Appendix C: Mechanical Drawing of High Pressure High Pressure UV-vis Cell

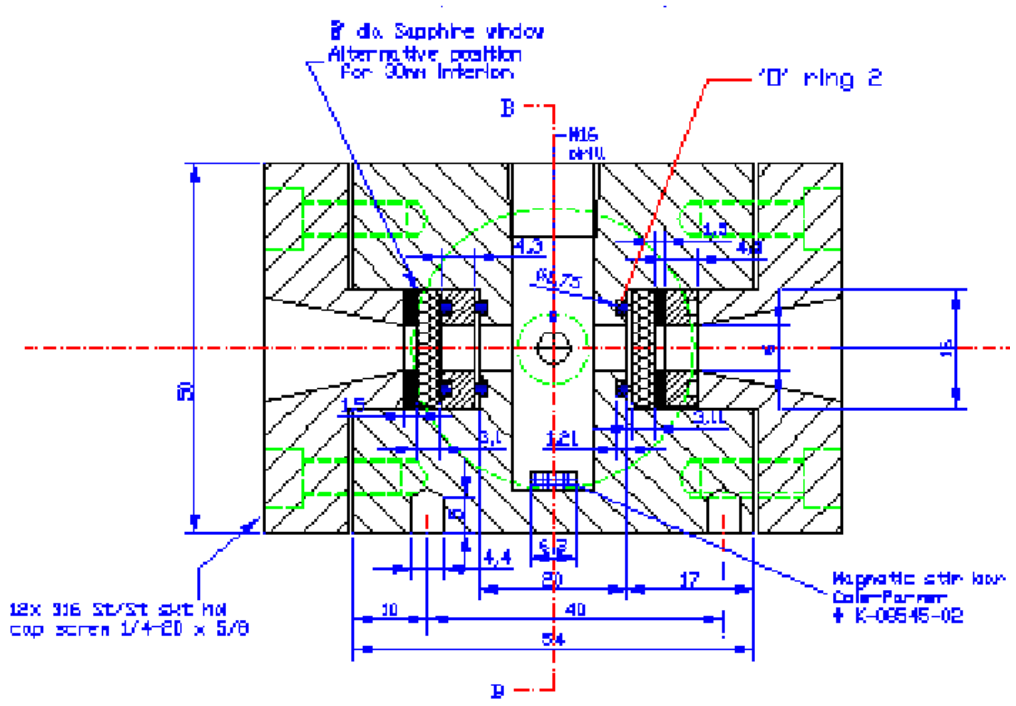

Figure C.1 Mechanical drawing of high pressure UV- vis cell.

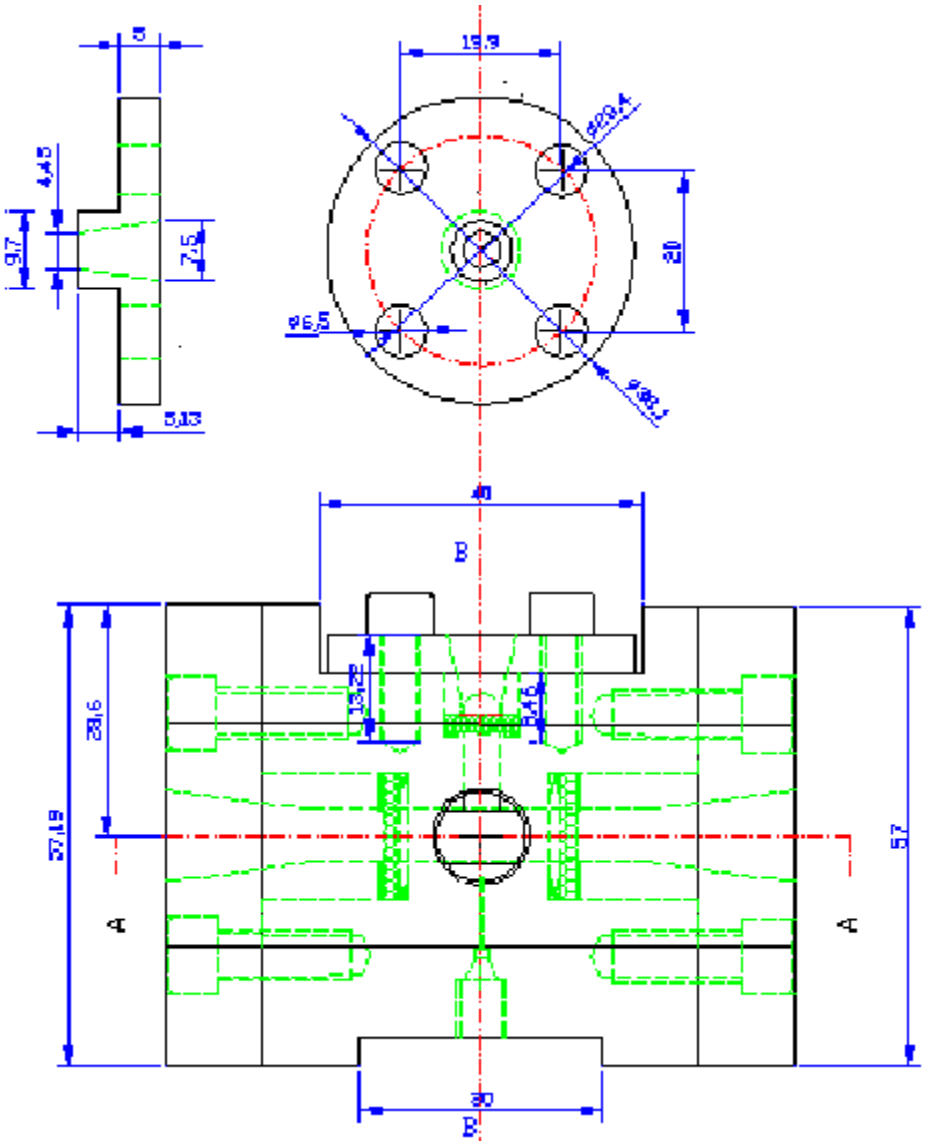

Figure C.2 Mechanical drawing of high pressure UV- vis cell from top view.

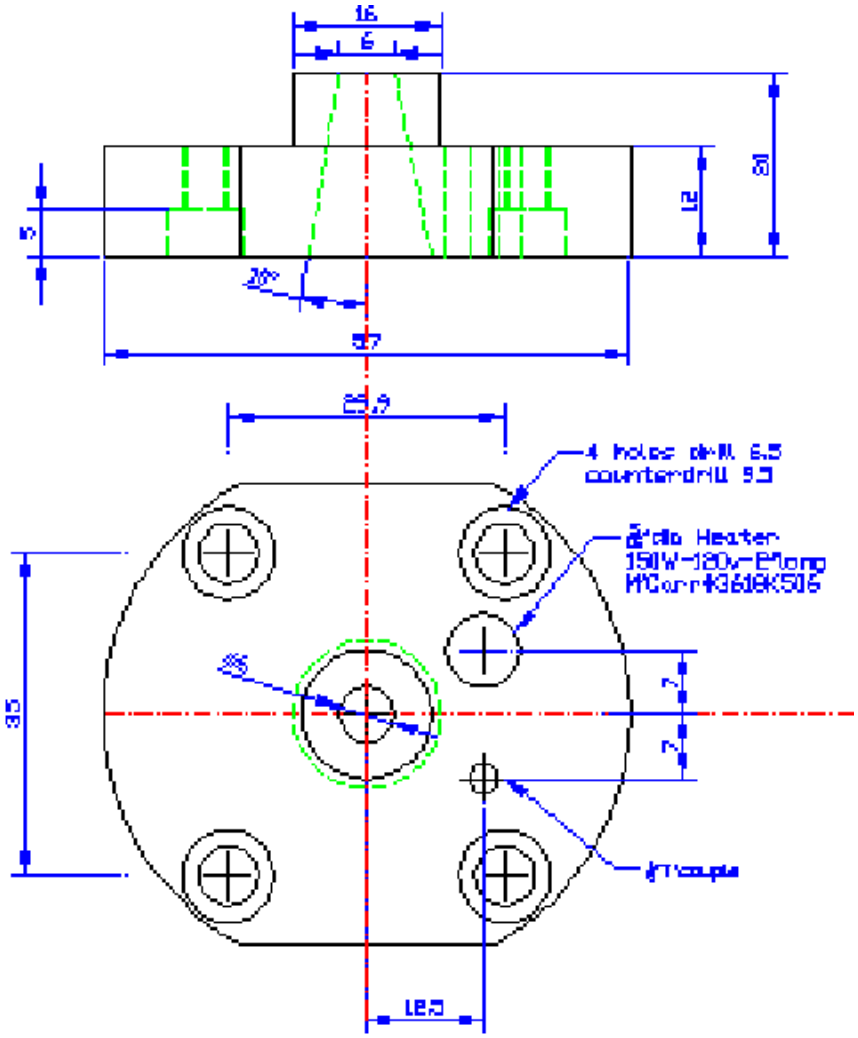

Figure C.3 Mechanical drawing of high pressure UV- vis cell from left side view.

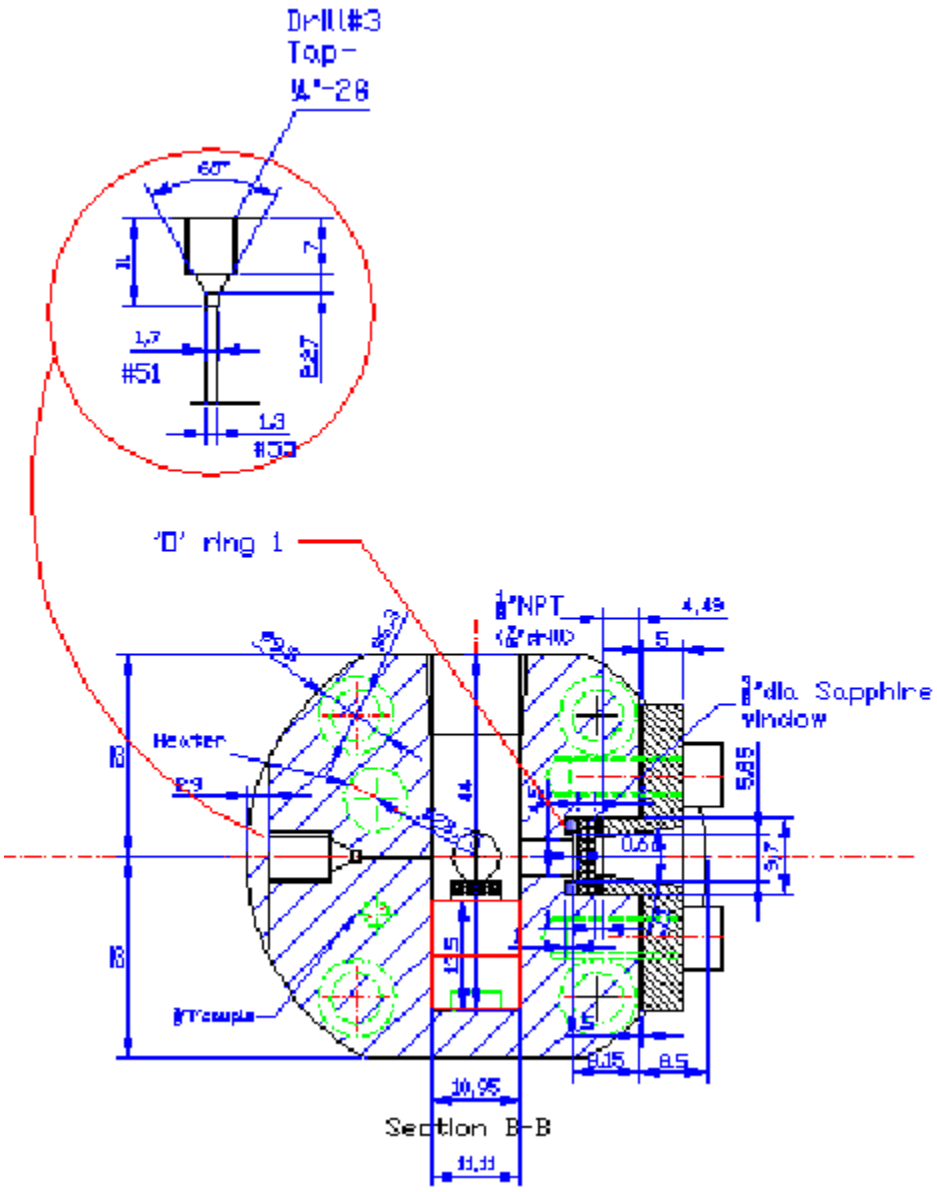

Figure C.4 Mechanical drawing of high pressure UV- vis cell from right side view.

Appendix D: Vapor-Liquid Equilibrium Data and Error Analysis for [HMIm][Tf_2N] and R134a System

INPUT

Date:	4/5/2007			Species MW		Cell Weights [g]							
				R134a	102.03	Gross	7.51578	2.5ml					
Run ID	R134a - Hmim-Tf2N			Hmim-Tf_2N	447.42	Tare	4.02016						
				-		Net:	3.49562	0.0078	moles				
Temperature	50					Water Cont.	98ppm	346.0279	cc/mol				
								1.2930	g/ml				
	P [Bar]	P [Bar]	T [°C]	Pump V_0 [ml]	V_f[ml]	ΔV [ml]	ρ [g/ml]	n [mol]					
1	100	100.98177	59.68	32.82844	32.80319	0.02525	1.13679	0.00028					
2	100	100.98177	59.68	32.80132	32.76628	0.03504	1.13679	0.00067					
3	100	100.98177	59.68	32.76601	32.72187	0.04414	1.13679	0.00116					
4	100	100.98177	59.68	32.71635	32.66175	0.05460	1.13679	0.00177					
5	100	100.98177	59.68	32.66068	32.59661	0.06407	1.13679	0.00249					
6	100	100.98177	59.68	32.59587	32.49106	0.10481	1.13679	0.00365					
7	100	100.98177	59.68	32.48703	32.36391	0.12312	1.13679	0.00503					
8	100	100.98177	59.68	32.36309	32.22908	0.13401	1.13679	0.00652					
9	100	100.98177	59.68	32.22835	32.02095	0.20740	1.13679	0.00883					
10	100	100.98177	59.68	32.01951	31.78689	0.23262	1.13679	0.01142					
11	100	100.98177	59.68	31.78598	31.53413	0.25185	1.13679	0.01423					
12	100	100.98177	59.68	31.53356	31.21834	0.31522	1.13679	0.01774					
13	100	100.98177	59.68	31.21821	30.79559	0.42262	1.13679	0.02245					
14	100	100.98177	59.68	30.79432	30.46278	0.33154	1.13679	0.02614					
15	100	100.98177	59.68	30.46215	30.15766	0.30449	1.13679	0.02953					

Ambient Conditions		Calculations 1:
T [C]	25.1	T in °C
P [bar]	0.98177	P in bar abs.
P_initial [Bar]	0.14	Vcell in abs. mL

			Line				
V [ml]	P [Bar]	T1 [°C]	T2 [°C]	T3 [°C]	ρ1 [g/ml]	ρ2 [g/ml]	ρ3 [g/ml]
0.84605	0.53	90.57	105.99	103.85	0.00180	0.00172	0.00173
0.84605	1.04	91.04	106.09	104.39	0.00354	0.00339	0.00341
0.84605	1.55	90.13	105.56	103.87	0.00532	0.00509	0.00511
0.84605	2.13	90.35	105.34	103.72	0.00734	0.00703	0.00707
0.84605	2.86	90.26	105.86	104.22	0.00994	0.00949	0.00953
0.84605	3.92	90.26	105.44	103.95	0.01378	0.01315	0.01321
0.84605	5.06	90.29	105.45	103.92	0.01800	0.01715	0.01723
0.84605	6.12	89.73	105.20	103.65	0.02207	0.02096	0.02107
0.84605	7.48	90.00	105.12	103.27	0.02738	0.02597	0.02613
0.84605	8.66	90.09	105.57	103.56	0.03214	0.03037	0.03058
0.84605	9.72	90.20	105.33	104.05	0.03653	0.03448	0.03465
0.84605	10.62	89.68	105.15	104.13	0.04046	0.03806	0.03820
0.84605	11.43	90.09	105.41	105.17	0.04394	0.04127	0.04131
0.84605	11.92	89.80	105.22	104.28	0.04618	0.04330	0.04346
0.84605	12.12	89.70	104.71	104.01	0.04710	0.04422	0.04434

Cell_headspace

P [Bar]	T [°C]	ρ [g/ml]	V_cell [ml]	h[mm]	Vliquid[ml]	ΔV [ml]
0.53	50	0.00203	5.71639	69.30	2.70744	3.00895
1.04	50	0.00401	5.71639	69.83	2.72853	2.98786
1.55	50	0.00603	5.71639	70.52	2.75600	2.96040
2.13	50	0.00836	5.71639	71.55	2.79699	2.91940
2.86	50	0.01136	5.71639	72.85	2.84873	2.86766
3.92	50	0.01585	5.71639	74.90	2.93032	2.78607
5.06	50	0.02089	5.71639	77.52	3.03460	2.68180
6.12	50	0.02578	5.71639	80.40	3.14922	2.56717
7.48	50	0.03239	5.71639	85.02	3.33310	2.38330
8.66	50	0.03848	5.71639	90.32	3.54404	2.17236
9.72	50	0.04429	5.71639	96.24	3.77965	1.93674
10.62	50	0.04951	5.71639	103.97	4.08731	1.62909
11.43	50	0.05447	5.71639	114.61	4.51078	1.20562
11.92	50	0.05761	5.71639	122.82	4.83754	0.87886
12.12	50	0.05893	5.71639	131.02	5.16390	0.55250

Line_initial

V [ml]	P [Bar]	T1 [°C]	T2 [°C]	T3 [°C]	ρ1 [g/ml]	ρ2 [g/ml]	ρ3 [g/ml]
0.84605	0.14	90.13	104.69	103.77	0.00047	0.00046	0.00046
0.84605	0.14	90.13	104.69	103.77	0.00047	0.00046	0.00046
0.84605	0.14	90.13	104.69	103.77	0.00047	0.00046	0.00046
0.84605	0.14	90.13	104.69	103.77	0.00047	0.00046	0.00046
0.84605	0.14	90.13	104.69	103.77	0.00047	0.00046	0.00046
0.84605	0.14	90.13	104.69	103.77	0.00047	0.00046	0.00046
0.84605	0.14	90.13	104.69	103.77	0.00047	0.00046	0.00046
0.84605	0.14	90.13	104.69	103.77	0.00047	0.00046	0.00046
0.84605	0.14	90.13	104.69	103.77	0.00047	0.00046	0.00046
0.84605	0.14	90.13	104.69	103.77	0.00047	0.00046	0.00046
0.84605	0.14	90.13	104.69	103.77	0.00047	0.00046	0.00046
0.84605	0.14	90.13	104.69	103.77	0.00047	0.00046	0.00046
0.84605	0.14	90.13	104.69	103.77	0.00047	0.00046	0.00046
0.84605	0.14	90.13	104.69	103.77	0.00047	0.00046	0.00046
0.84605	0.14	90.13	104.69	103.77	0.00047	0.00046	0.00046

Cell_headspace_initial

P [Bar]	T [°C]	ρ [g/ml]	V_cell [ml]	h[mm]	Vliquid[ml]	ΔV [ml]
0.14	50	0.00053	5.71639	69.2	2.70346	3.01293
0.14	50	0.00053	5.71639	69.2	2.70346	3.01293
0.14	50	0.00053	5.71639	69.2	2.70346	3.01293
0.14	50	0.00053	5.71639	69.2	2.70346	3.01293
0.14	50	0.00053	5.71639	69.2	2.70346	3.01293
0.14	50	0.00053	5.71639	69.2	2.70346	3.01293
0.14	50	0.00053	5.71639	69.2	2.70346	3.01293
0.14	50	0.00053	5.71639	69.2	2.70346	3.01293
0.14	50	0.00053	5.71639	69.2	2.70346	3.01293
0.14	50	0.00053	5.71639	69.2	2.70346	3.01293
0.14	50	0.00053	6.71639	69.2	2.70346	4.01293
0.14	50	0.00053	7.71639	69.2	2.70346	5.01293
0.14	50	0.00053	8.71639	69.2	2.70346	6.01293
0.14	50	0.00053	9.71639	69.2	2.70346	7.01293
0.14	50	0.00053	10.71639	69.2	2.70346	8.01293

Result	T	P	n [mol]		X		
	[C]	[bar]	R134a	Hmim-Tf_2N	R134a	Hmim-Tf_2N	+/-
1	50	0.53	0.0002	0.0078	0.0282	0.9718	0.0014
2	50	1.04	0.0005	0.0078	0.0652	0.9348	0.0013
3	50	1.55	0.0010	0.0078	0.1100	0.8900	0.0012
4	50	2.13	0.0015	0.0078	0.1604	0.8396	0.0011
5	50	2.86	0.0021	0.0078	0.2123	0.7877	0.0010
6	50	3.92	0.0031	0.0078	0.2860	0.7140	0.0008
7	50	5.06	0.0044	0.0078	0.3577	0.6423	0.0007
8	50	6.12	0.0057	0.0078	0.4223	0.5777	0.0006
9	50	7.48	0.0079	0.0078	0.5019	0.4981	0.0005
10	50	8.66	0.0104	0.0078	0.5702	0.4298	0.0004
11	50	9.72	0.0131	0.0078	0.6267	0.3733	0.0003
12	50	10.62	0.0167	0.0078	0.6807	0.3193	0.0003
13	50	11.43	0.0215	0.0078	0.7334	0.2666	0.0002
14	50	11.92	0.0253	0.0078	0.7642	0.2358	0.0002
15	50	12.12	0.0289	0.0078	0.7871	0.2129	0.0002

Molar Volume		Density		w (mass fract.)		
[cc/mol]	+/-	[g/cc]	+/-	R134a	Hmim-Tf_2N	+/-
336.77	0.12	1.300	0.001	0.0066	0.9934	0.0003
326.46	0.12	1.302	0.001	0.0157	0.9843	0.0003
313.96	0.11	1.304	0.001	0.0274	0.9726	0.0003
300.56	0.11	1.304	0.001	0.0418	0.9582	0.0003
287.21	0.10	1.303	0.001	0.0579	0.9421	0.0003
267.80	0.09	1.302	0.001	0.0837	0.9163	0.0003
249.48	0.08	1.298	0.001	0.1127	0.8873	0.0003
232.85	0.07	1.295	0.001	0.1429	0.8571	0.0003
212.50	0.06	1.290	0.001	0.1868	0.8132	0.0003
194.98	0.06	1.285	0.001	0.2322	0.7678	0.0003
180.57	0.05	1.279	0.001	0.2769	0.7231	0.0003
167.04	0.04	1.271	0.001	0.3271	0.6729	0.0003
153.94	0.03	1.261	0.001	0.3855	0.6145	0.0003
146.01	0.03	1.257	0.001	0.4250	0.5750	0.0002
140.71	0.03	1.248	0.001	0.4574	0.5426	0.0002

Volume Expansion ΔV/V	+/-	Molality [mol/kg]	+/-	Molarity [mol/l]	+/-
0.0015	0.0005	0.065	0.003	0.084	0.004
0.0093	0.0005	0.156	0.003	0.200	0.004
0.0194	0.0005	0.276	0.003	0.350	0.004
0.0346	0.0005	0.427	0.003	0.534	0.004
0.0537	0.0005	0.602	0.004	0.739	0.004
0.0839	0.0005	0.895	0.004	1.068	0.004
0.1225	0.0006	1.245	0.004	1.434	0.004
0.1649	0.0006	1.634	0.004	1.814	0.005
0.2329	0.0006	2.252	0.004	2.362	0.005
0.3109	0.0006	2.965	0.005	2.924	0.005
0.3981	0.0006	3.753	0.005	3.471	0.005
0.5119	0.0007	4.765	0.006	4.075	0.005
0.6685	0.0007	6.148	0.007	4.764	0.005
0.7894	0.0008	7.243	0.007	5.234	0.005
0.9101	0.0008	8.263	0.008	5.594	0.005

Error Analysis	dVpump [ml]	**0.0001**	dVlines	0.0359		1.08	1.1
	dVcell [ml]	0.0144	dTline [C]	**0.5**		7.1	7
	ΔTpump=dTpump [C]	**0.01**	dh [mm]	**0.01**			
	dTcell = dTspace [C]	**0.01**	dPpump	**0.334**	0.10%		
	dPcell=dPlines	**0.0668**	dm1[g]	0.0001			
	dVL [ml]	**0.001**	**0.000398**				

Pump

$dn/d(\Delta V_{pump})$	ΔV_{pump}	$T_{pump}+\Delta T$	$T_{pump}-\Delta T$	P_{pump}	density(P,T+ΔT)	density(P,T-ΔT)
0.01	0.03	59.69	59.67	100.98177	1.13675	1.13682
0.01	0.04	59.69	59.67	100.98177	1.13675	1.13682
0.01	0.04	59.69	59.67	100.98177	1.13675	1.13682
0.01	0.05	59.69	59.67	100.98177	1.13675	1.13682
0.01	0.06	59.69	59.67	100.98177	1.13675	1.13682
0.01	0.10	59.69	59.67	100.98177	1.13675	1.13682
0.01	0.12	59.69	59.67	100.98177	1.13675	1.13682
0.01	0.13	59.69	59.67	100.98177	1.13675	1.13682
0.01	0.21	59.69	59.67	100.98177	1.13675	1.13682
0.01	0.23	59.69	59.67	100.98177	1.13675	1.13682
0.01	0.25	59.69	59.67	100.98177	1.13675	1.13682
0.01	0.32	59.69	59.67	100.98177	1.13675	1.13682
0.01	0.42	59.69	59.67	100.98177	1.13675	1.13682
0.01	0.33	59.69	59.67	100.98177	1.13675	1.13682
0.01	0.30	59.69	59.67	100.98177	1.13675	1.13682

dn/dT	P+ΔP	P-ΔP	T	density(P+ΔP,T)	density(P-ΔP,T)	dn/dP	dn_{pump}^2
-9.11E-07	101.31577	100.64777	59.68	1.13702	1.13655	0.000000	1.24E-12
-1.26E-06	101.31577	100.64777	59.68	1.13702	1.13655	0.000000	1.25E-12
-1.59E-06	101.31577	100.64777	59.68	1.13702	1.13655	0.000000	1.25E-12
-1.97E-06	101.31577	100.64777	59.68	1.13702	1.13655	0.000000	1.26E-12
-2.31E-06	101.31577	100.64777	59.68	1.13702	1.13655	0.000000	1.26E-12
-3.78E-06	101.31577	100.64777	59.68	1.13702	1.13655	0.000001	1.3E-12
-4.44E-06	101.31577	100.64777	59.68	1.13702	1.13655	0.000001	1.32E-12
-4.83E-06	101.31577	100.64777	59.68	1.13702	1.13655	0.000001	1.34E-12
-7.48E-06	101.31577	100.64777	59.68	1.13702	1.13655	0.000001	1.47E-12
-8.39E-06	101.31577	100.64777	59.68	1.13702	1.13655	0.000002	1.53E-12
-9.08E-06	101.31577	100.64777	59.68	1.13702	1.13655	0.000002	1.59E-12
-1.14E-05	101.31577	100.64777	59.68	1.13702	1.13655	0.000002	1.78E-12
-1.52E-05	101.31577	100.64777	59.68	1.13702	1.13655	0.000003	2.21E-12
-1.20E-05	101.31577	100.64777	59.68	1.13702	1.13655	0.000002	1.84E-12
-1.10E-05	101.31577	100.64777	59.68	1.13702	1.13655	0.000002	1.74E-12

Lines

dn/dV_{lines}	dV_{lines}	$T_1+\Delta T$	$T_1-\Delta T$	P	density(P,T1+ΔT)	density(P,T1-ΔT)	dn/dT_1	P+ΔP	P-ΔP	T_1
0.00002	0.0359	91.07	90.07	0.53	0.00179	0.00180	-4.2E-08	0.5968	0.4632	90.57
0.00003	0.0359	91.54	90.54	1.04	0.00353	0.00355	-8.4E-08	1.1068	0.9732	91.04
0.00005	0.0359	90.63	89.63	1.55	0.00531	0.00532	-1.3E-07	1.6168	1.4832	90.13
0.00007	0.0359	90.85	89.85	2.13	0.00733	0.00736	-1.8E-07	2.1968	2.0632	90.35
0.00010	0.0359	90.76	89.76	2.86	0.00992	0.00995	-2.5E-07	2.9268	2.7932	90.26
0.00014	0.0359	90.76	89.76	3.92	0.01375	0.01380	-3.6E-07	3.9868	3.8532	90.26
0.00018	0.0359	90.79	89.79	5.06	0.01797	0.01803	-4.9E-07	5.1268	4.9932	90.29
0.00022	0.0359	90.23	89.23	6.12	0.02203	0.02211	-6.3E-07	6.1868	6.0532	89.73
0.00027	0.0359	90.5	89.5	7.48	0.02733	0.02743	-8.3E-07	7.5468	7.4132	90
0.00031	0.0359	90.59	89.59	8.66	0.03208	0.03220	-1E-06	8.7268	8.5932	90.09
0.00036	0.0359	90.7	89.7	9.72	0.03646	0.03660	-1.2E-06	9.7868	9.6532	90.2
0.00040	0.0359	90.18	89.18	10.62	0.04038	0.04055	-1.4E-06	10.6868	10.5532	89.68
0.00043	0.0359	90.59	89.59	11.43	0.04384	0.04403	-1.6E-06	11.4968	11.3632	90.09
0.00045	0.0359	90.3	89.3	11.92	0.04608	0.04628	-1.7E-06	11.9868	11.8532	89.8
0.00046	0.0359	90.2	89.2	12.12	0.04700	0.04721	-1.7E-06	12.1868	12.0532	89.7

density(P+ΔP,T1)	density(P-ΔP,T1)	dn/dP	du_{line1}^2	dn/dV_{lines}	dV_{lines}	$T_2+\Delta T$	$T_2-\Delta T$	P
0.002	0.002	2.83E-05	3.97E-12	1.69E-05	0.04	106.49	105.49	0.53
0.004	0.003	2.85E-05	5.18E-12	3.33E-05	0.04	106.59	105.59	1.04
0.006	0.005	2.89E-05	7.23E-12	4.99E-05	0.04	106.06	105.06	1.55
0.008	0.007	2.92E-05	1.05E-11	6.89E-05	0.04	105.84	104.84	2.13
0.010	0.010	2.97E-05	1.62E-11	9.3E-05	0.04	106.36	105.36	2.86
0.014	0.014	3.04E-05	2.76E-11	0.000129	0.04	105.94	104.94	3.92
0.018	0.018	3.11E-05	4.45E-11	0.000168	0.04	105.95	104.95	5.06
0.022	0.022	3.2E-05	6.5E-11	0.000205	0.04	105.7	104.7	6.12
0.028	0.027	3.3E-05	9.78E-11	0.000254	0.04	105.62	104.62	7.48
0.032	0.032	3.4E-05	1.33E-10	0.000298	0.04	106.07	105.07	8.66
0.037	0.036	3.5E-05	1.71E-10	0.000338	0.04	105.83	104.83	9.72
0.041	0.040	3.6E-05	2.09E-10	0.000373	0.04	105.65	104.65	10.62
0.044	0.044	3.67E-05	2.46E-10	0.000405	0.04	105.91	104.91	11.43
0.046	0.046	3.73E-05	2.71E-10	0.000424	0.04	105.72	104.72	11.92
0.047	0.047	3.76E-05	2.82E-10	0.000433	0.04	105.21	104.21	12.12

density(P,T2+ΔT)	density(P,T2-ΔT)	dn/dT_2	P+ΔP	P-ΔP	T_2	density(P+ΔP,T_2)	density(P-ΔP,T2)
0.002	0.002	-3.8E-08	0.6	0.5	106.0	0.002	0.002
0.003	0.003	-7.7E-08	1.1	1.0	106.1	0.004	0.003
0.005	0.005	-1.2E-07	1.6	1.5	105.6	0.005	0.005
0.007	0.007	-1.6E-07	2.2	2.1	105.3	0.007	0.007
0.009	0.010	-2.3E-07	2.9	2.8	105.9	0.010	0.009
0.013	0.013	-3.3E-07	4.0	3.9	105.4	0.013	0.013
0.017	0.017	-4.4E-07	5.1	5.0	105.5	0.017	0.017
0.021	0.021	-5.6E-07	6.2	6.1	105.2	0.021	0.021
0.026	0.026	-7.2E-07	7.5	7.4	105.1	0.026	0.026
0.030	0.030	-8.8E-07	8.7	8.6	105.6	0.031	0.030
0.034	0.035	-1E-06	9.8	9.7	105.3	0.035	0.034
0.038	0.038	-1.2E-06	10.7	10.6	105.2	0.038	0.038
0.041	0.041	-1.3E-06	11.5	11.4	105.4	0.042	0.041
0.043	0.043	-1.4E-06	12.0	11.9	105.2	0.044	0.043
0.044	0.044	-1.5E-06	12.2	12.1	104.7	0.044	0.044

dn/dP	dn_{line2}^2	dn/dV_{lines}	dV_{lines}	$T_3+\Delta T$	$T_3-\Delta T$	P	density(P,T3+ΔT)	density(P,T3-ΔT)
2.71E-05	3.64E-12	1.7E-05	0.0359	104.35	103.35	0.53	0.002	0.002
2.73E-05	4.76E-12	3.34E-05	0.0359	104.89	103.89	1.04	0.003	0.003
2.76E-05	6.61E-12	5.01E-05	0.0359	104.37	103.37	1.55	0.005	0.005
2.79E-05	9.6E-12	6.92E-05	0.0359	104.22	103.22	2.13	0.007	0.007
2.82E-05	1.47E-11	9.35E-05	0.0359	104.72	103.72	2.86	0.010	0.010
2.88E-05	2.51E-11	0.000129	0.0359	104.45	103.45	3.92	0.013	0.013
2.94E-05	4.03E-11	0.000169	0.0359	104.42	103.42	5.06	0.017	0.017
3.01E-05	5.85E-11	0.000206	0.0359	104.15	103.15	6.12	0.021	0.021
3.09E-05	8.79E-11	0.000256	0.0359	103.77	102.77	7.48	0.026	0.026
3.16E-05	1.19E-10	0.0003	0.0359	104.06	103.06	8.66	0.031	0.031
3.24E-05	1.52E-10	0.00034	0.0359	104.55	103.55	9.72	0.035	0.035
3.3E-05	1.85E-10	0.000374	0.0359	104.63	103.63	10.62	0.038	0.038
3.36E-05	2.16E-10	0.000405	0.0359	105.67	104.67	11.43	0.041	0.041
3.4E-05	2.38E-10	0.000426	0.0359	104.78	103.78	11.92	0.043	0.044
3.43E-05	2.48E-10	0.000435	0.0359	104.51	103.51	12.12	0.044	0.044

dn/dT_3	P+ΔP	P-ΔP	T_3	density(P+ΔP,T3)	density(P-ΔP,T3)	dn/dP	dn_{line3}^2	dn_{line}^2
-3.9E-08	0.5968	0.4632	103.85	0.002	0.002	9.69E-05	4.22E-11	1.66E-11
-7.7E-08	1.1068	0.9732	104.39	0.004	0.003	9.69E-05	4.33E-11	1.78E-11
-1.2E-07	1.6168	1.4832	103.87	0.005	0.005	9.7E-05	4.52E-11	1.97E-11
-1.7E-07	2.1968	2.0632	103.72	0.007	0.007	9.67E-05	4.79E-11	2.27E-11
-2.3E-07	2.9268	2.7932	104.22	0.010	0.009	9.61E-05	5.25E-11	2.78E-11
-3.3E-07	3.9868	3.8532	103.95	0.013	0.013	9.53E-05	6.21E-11	3.83E-11
-4.5E-07	5.1268	4.9932	103.92	0.017	0.017	9.38E-05	7.6E-11	5.36E-11
-5.6E-07	6.1868	6.0532	103.65	0.021	0.021	9.17E-05	9.26E-11	7.2E-11
-7.4E-07	7.5468	7.4132	103.27	0.026	0.026	8.77E-05	1.19E-10	1.02E-10
-9E-07	8.7268	8.5932	103.56	0.031	0.030	8.19E-05	1.46E-10	1.33E-10
-1.1E-06	9.7868	9.6532	104.05	0.035	0.034	7.45E-05	1.74E-10	1.66E-10
-1.2E-06	10.6868	10.5532	104.13	0.038	0.038	6.4E-05	1.99E-10	1.98E-10
-1.3E-06	11.4968	11.3632	105.17	0.042	0.041	4.8E-05	2.22E-10	2.28E-10
-1.4E-06	11.9868	11.8532	104.28	0.044	0.043	3.55E-05	2.4E-10	2.5E-10
-1.5E-06	12.1868	12.0532	104.01	0.045	0.044	2.25E-05	2.46E-10	2.59E-10

HeadSpace

$dn_{headspace}/dV_{cell}$	dVcell	$dn_{headspace}/dV_L$	dV_L	Tspacel+ΔT	Tspace-ΔT	P	**density(P,Tspace+ΔT)**	**density(P,Tspace-ΔT)**
0.00002	0.01438	-0.00002	0.001	50.01	49.99	0.53	0.002	0.002
0.00004	0.01438	-0.00004	0.001	50.01	49.99	1.04	0.004	0.004
0.00006	0.01438	-0.00006	0.001	50.01	49.99	1.55	0.006	0.006
0.00008	0.01438	-0.00008	0.001	50.01	49.99	2.13	0.008	0.008
0.00011	0.01438	-0.00011	0.001	50.01	49.99	2.86	0.011	0.011
0.00016	0.01438	-0.00016	0.001	50.01	49.99	3.92	0.016	0.016
0.00020	0.01438	-0.00020	0.001	50.01	49.99	5.06	0.021	0.021
0.00025	0.01438	-0.00025	0.001	50.01	49.99	6.12	0.026	0.026
0.00032	0.01438	-0.00032	0.001	50.01	49.99	7.48	0.032	0.032
0.00038	0.01438	-0.00038	0.001	50.01	49.99	8.66	0.038	0.038
0.00043	0.01438	-0.00043	0.001	50.01	49.99	9.72	0.044	0.044
0.00049	0.01438	-0.00049	0.001	50.01	49.99	10.62	0.050	0.050
0.00053	0.01438	-0.00053	0.001	50.01	49.99	11.43	0.054	0.054
0.00056	0.01438	-0.00056	0.001	50.01	49.99	11.92	0.058	0.058
0.00058	0.01438	-0.00058	0.001	50.01	49.99	12.12	0.059	0.059

dn/dTcell	Pspace+ΔP	Pspace-ΔP	Tspace	density(P+ΔP,T)	density(P-ΔP,T)	dn/dP	dn_{space}^2
-1.9E-07	0.5968	0.4632	50	0.002	0.002	0.00011	5.79E-11
-3.8E-07	1.1068	0.9732	50	0.004	0.004	0.00011	5.91E-11
-5.9E-07	1.6168	1.4832	50	0.006	0.006	0.00012	6.03E-11
-8.3E-07	2.1968	2.0632	50	0.009	0.008	0.00012	6.16E-11
-1.2E-06	2.9268	2.7932	50	0.012	0.011	0.00012	6.36E-11
-1.7E-06	3.9868	3.8532	50	0.016	0.016	0.00012	6.72E-11
-2.3E-06	5.1268	4.9932	50	0.021	0.021	0.00012	7.15E-11
-2.9E-06	6.1868	6.0532	50	0.026	0.025	0.00012	7.61E-11
-3.7E-06	7.5468	7.4132	50	0.033	0.032	0.00012	8.22E-11
-4.4E-06	8.7268	8.5932	50	0.039	0.038	0.00011	8.68E-11
-5E-06	9.7868	9.6532	50	0.045	0.044	0.00011	9.03E-11
-5.1E-06	10.6868	10.5532	50	0.050	0.049	0.00010	8.94E-11
-4.5E-06	11.4968	11.3632	50	0.055	0.054	0.00007	8.4E-11
-3.6E-06	11.9868	11.8532	50	0.058	0.057	0.00006	8.04E-11
-2.4E-06	12.1868	12.0532	50	0.059	0.058	0.00004	7.51E-11

Lines_initial

dn/dV_{lines}	dV_{lines}	$T_1+\Delta T$	$T_1-\Delta T$	P	**density(P,T1+ΔT)**	**density(P,T1-ΔT)**	**dn/dT_1**	$P+\Delta P$	$P-\Delta P$	T_1
4.64E-06	0.0359	90.63	89.63	0.14	0.0005	0.0005	-1.1E-08	0.21	0.07	90.13
4.64E-06	0.0359	90.63	89.63	0.14	0.0005	0.0005	-1.1E-08	0.21	0.07	90.13
4.64E-06	0.0359	90.63	89.63	0.14	0.0005	0.0005	-1.1E-08	0.21	0.07	90.13
4.64E-06	0.0359	90.63	89.63	0.14	0.0005	0.0005	-1.1E-08	0.21	0.07	90.13
4.64E-06	0.0359	90.63	89.63	0.14	0.0005	0.0005	-1.1E-08	0.21	0.07	90.13
4.64E-06	0.0359	90.63	89.63	0.14	0.0005	0.0005	-1.1E-08	0.21	0.07	90.13
4.64E-06	0.0359	90.63	89.63	0.14	0.0005	0.0005	-1.1E-08	0.21	0.07	90.13
4.64E-06	0.0359	90.63	89.63	0.14	0.0005	0.0005	-1.1E-08	0.21	0.07	90.13
4.64E-06	0.0359	90.63	89.63	0.14	0.0005	0.0005	-1.1E-08	0.21	0.07	90.13
4.64E-06	0.0359	90.63	89.63	0.14	0.0005	0.0005	-1.1E-08	0.21	0.07	90.13
4.64E-06	0.0359	90.63	89.63	0.14	0.0005	0.0005	-1.1E-08	0.21	0.07	90.13
4.64E-06	0.0359	90.63	89.63	0.14	0.0005	0.0005	-1.1E-08	0.21	0.07	90.13
4.64E-06	0.0359	90.63	89.63	0.14	0.0005	0.0005	-1.1E-08	0.21	0.07	90.13
4.64E-06	0.0359	90.63	89.63	0.14	0.0005	0.0005	-1.1E-08	0.21	0.07	90.13
4.64E-06	0.0359	90.63	89.63	0.14	0.0005	0.0005	-1.1E-08	0.21	0.07	90.13

density(P+ΔP,T1)	**density(P-ΔP,T1)**	**dn/dP**	**$dn_{final-initial}^2$**	dn/dV_{lines}	dV_{lines}	$T_2+\Delta T$	$T_2-\Delta T$	P
0.0007	0.0002	2.81E-05	3.55E-12	4.64E-06	0.0359	105.19	104.19	0.14
0.0007	0.0002	2.81E-05	3.55E-12	4.64E-06	0.0359	105.19	104.19	0.14
0.0007	0.0002	2.81E-05	3.55E-12	4.64E-06	0.0359	105.19	104.19	0.14
0.0007	0.0002	2.81E-05	3.55E-12	4.64E-06	0.0359	105.19	104.19	0.14
0.0007	0.0002	2.81E-05	3.55E-12	4.64E-06	0.0359	105.19	104.19	0.14
0.0007	0.0002	2.81E-05	3.55E-12	4.64E-06	0.0359	105.19	104.19	0.14
0.0007	0.0002	2.81E-05	3.55E-12	4.64E-06	0.0359	105.19	104.19	0.14
0.0007	0.0002	2.81E-05	3.55E-12	4.64E-06	0.0359	105.19	104.19	0.14
0.0007	0.0002	2.81E-05	3.55E-12	4.64E-06	0.0359	105.19	104.19	0.14
0.0007	0.0002	2.81E-05	3.55E-12	4.64E-06	0.0359	105.19	104.19	0.14
0.0007	0.0002	2.81E-05	3.55E-12	4.64E-06	0.0359	105.19	104.19	0.14
0.0007	0.0002	2.81E-05	3.55E-12	4.64E-06	0.0359	105.19	104.19	0.14
0.0007	0.0002	2.81E-05	3.55E-12	4.64E-06	0.0359	105.19	104.19	0.14
0.0007	0.0002	2.81E-05	3.55E-12	4.64E-06	0.0359	105.19	104.19	0.14
0.0007	0.0002	2.81E-05	3.55E-12	4.64E-06	0.0359	105.19	104.19	0.14

density(P,T2+ΔT)	density(P,T2-ΔT)	dn/dT_2	P+ΔP	P-ΔP	T_2	density(P+ΔP,T2)	density(P-ΔP,T2)	dn/dP
0.0005	0.0005	-1E-08	0.21	0.07	104.69	0.0007	0.0002	2.7E-05
0.0005	0.0005	-1E-08	0.21	0.07	104.69	0.0007	0.0002	2.7E-05
0.0005	0.0005	-1E-08	0.21	0.07	104.69	0.0007	0.0002	2.7E-05
0.0005	0.0005	-1E-08	0.21	0.07	104.69	0.0007	0.0002	2.7E-05
0.0005	0.0005	-1E-08	0.21	0.07	104.69	0.0007	0.0002	2.7E-05
0.0005	0.0005	-1E-08	0.21	0.07	104.69	0.0007	0.0002	2.7E-05
0.0005	0.0005	-1E-08	0.21	0.07	104.69	0.0007	0.0002	2.7E-05
0.0005	0.0005	-1E-08	0.21	0.07	104.69	0.0007	0.0002	2.7E-05
0.0005	0.0005	-1E-08	0.21	0.07	104.69	0.0007	0.0002	2.7E-05
0.0005	0.0005	-1E-08	0.21	0.07	104.69	0.0007	0.0002	2.7E-05
0.0005	0.0005	-1E-08	0.21	0.07	104.69	0.0007	0.0002	2.7E-05
0.0005	0.0005	-1E-08	0.21	0.07	104.69	0.0007	0.0002	2.7E-05
0.0005	0.0005	-1E-08	0.21	0.07	104.69	0.0007	0.0002	2.7E-05
0.0005	0.0005	-1E-08	0.21	0.07	104.69	0.0007	0.0002	2.7E-05
0.0005	0.0005	-1E-08	0.21	0.07	104.69	0.0007	0.0002	2.7E-05

$dn_{line2\text{-}initial}^2$	dn/dV_{lines}	dV_{lines}	$T_3+\Delta T$	$T_3-\Delta T$	P	**density(P,T3+ΔT)**	**density(P,T3-ΔT)**
3.28E-12	4.47E-06	0.0359	104.27	103.27	0.14	0.0005	0.0005
3.28E-12	4.47E-06	0.0359	104.27	103.27	0.14	0.0005	0.0005
3.28E-12	4.47E-06	0.0359	104.27	103.27	0.14	0.0005	0.0005
3.28E-12	4.47E-06	0.0359	104.27	103.27	0.14	0.0005	0.0005
3.28E-12	4.47E-06	0.0359	104.27	103.27	0.14	0.0005	0.0005
3.28E-12	4.47E-06	0.0359	104.27	103.27	0.14	0.0005	0.0005
3.28E-12	4.47E-06	0.0359	104.27	103.27	0.14	0.0005	0.0005
3.28E-12	4.47E-06	0.0359	104.27	103.27	0.14	0.0005	0.0005
3.28E-12	4.47E-06	0.0359	104.27	103.27	0.14	0.0005	0.0005
3.28E-12	4.47E-06	0.0359	104.27	103.27	0.14	0.0005	0.0005
3.28E-12	4.47E-06	0.0359	104.27	103.27	0.14	0.0005	0.0005
3.28E-12	4.47E-06	0.0359	104.27	103.27	0.14	0.0005	0.0005
3.28E-12	4.47E-06	0.0359	104.27	103.27	0.14	0.0005	0.0005
3.28E-12	4.47E-06	0.0359	104.27	103.27	0.14	0.0005	0.0005
3.28E-12	4.47E-06	0.0359	104.27	103.27	0.14	0.0005	0.0005

dn/dT_3	P+ΔP	P-ΔP	T_3	**density(P+ΔP,T3)**	**density(P-ΔP,T3)**	**dn/dP**	**$dn_{line3-initial}^2$**	**$dn_{line-initial}^2$**
-1E-08	0.21	0.07	103.77	0.0007	0.0002	2.71E-05	3.29368E-12	3.3738E-12
-1E-08	0.21	0.07	103.77	0.0007	0.0002	2.71E-05	3.29368E-12	3.3738E-12
-1E-08	0.21	0.07	103.77	0.0007	0.0002	2.71E-05	3.29368E-12	3.3738E-12
-1E-08	0.21	0.07	103.77	0.0007	0.0002	2.71E-05	3.29368E-12	3.3738E-12
-1E-08	0.21	0.07	103.77	0.0007	0.0002	2.71E-05	3.29368E-12	3.3738E-12
-1E-08	0.21	0.07	103.77	0.0007	0.0002	2.71E-05	3.29368E-12	3.3738E-12
-1E-08	0.21	0.07	103.77	0.0007	0.0002	2.71E-05	3.29368E-12	3.3738E-12
-1E-08	0.21	0.07	103.77	0.0007	0.0002	2.71E-05	3.29368E-12	3.3738E-12
-1E-08	0.21	0.07	103.77	0.0007	0.0002	2.71E-05	3.29368E-12	3.3738E-12
-1E-08	0.21	0.07	103.77	0.0007	0.0002	2.71E-05	3.29368E-12	3.3738E-12
-1E-08	0.21	0.07	103.77	0.0007	0.0002	2.71E-05	3.29368E-12	3.3738E-12
-1E-08	0.21	0.07	103.77	0.0007	0.0002	2.71E-05	3.29368E-12	3.3738E-12
-1E-08	0.21	0.07	103.77	0.0007	0.0002	2.71E-05	3.29368E-12	3.3738E-12
-1E-08	0.21	0.07	103.77	0.0007	0.0002	2.71E-05	3.29368E-12	3.3738E-12
-1E-08	0.21	0.07	103.77	0.0007	0.0002	2.71E-05	3.29368E-12	3.3738E-12

HeadSpace_Initial

$dn_{headspace}/dV_{cell}$	dV_{cell}	$dn_{headspace}/dV_L$	dV_L	$T_{space}+\Delta T$	Tspace-ΔT	P	**density(P,Tspace+ΔT)**	**density(P,Tspace-ΔT)**
5.22E-06	0.01438	-0.00053	0.001	50.01	49.99	0.14	0.0005	0.0005
5.22E-06	0.01438	-0.00053	0.001	50.01	49.99	0.14	0.0005	0.0005
5.22E-06	0.01438	-0.00053	0.001	50.01	49.99	0.14	0.0005	0.0005
5.22E-06	0.01438	-0.00053	0.001	50.01	49.99	0.14	0.0005	0.0005
5.22E-06	0.01438	-0.00053	0.001	50.01	49.99	0.14	0.0005	0.0005
5.22E-06	0.01438	-0.00053	0.001	50.01	49.99	0.14	0.0005	0.0005
5.22E-06	0.01438	-0.00053	0.001	50.01	49.99	0.14	0.0005	0.0005
5.22E-06	0.01438	-0.00053	0.001	50.01	49.99	0.14	0.0005	0.0005
5.22E-06	0.01438	-0.00053	0.001	50.01	49.99	0.14	0.0005	0.0005
5.22E-06	0.01438	-0.00053	0.001	50.01	49.99	0.14	0.0005	0.0005
5.22E-06	0.01438	-0.00053	0.001	50.01	49.99	0.14	0.0005	0.0005
5.22E-06	0.01438	-0.00053	0.001	50.01	49.99	0.14	0.0005	0.0005
5.22E-06	0.01438	-0.00053	0.001	50.01	49.99	0.14	0.0005	0.0005
5.22E-06	0.01438	-0.00053	0.001	50.01	49.99	0.14	0.0005	0.0005
5.22E-06	0.01438	-0.00053	0.001	50.01	49.99	0.14	0.0005	0.0005

dn/dT_{cell}	$P_{space}+\Delta P$	$P_{space}-\Delta P$	T_{space}	density(P+ΔP,T)	density(P-ΔP,T)	dn/dP	$dn_{space\text{-}initial}^2$	dn_2^2
-4.9E-08	0.2068	0.0732	50	0.0008	0.0003	0.0001	5.69E-11	1.36E-10
-4.9E-08	0.2068	0.0732	50	0.0008	0.0003	0.0001	5.69E-11	1.38E-10
-4.9E-08	0.2068	0.0732	50	0.0008	0.0003	0.0001	5.69E-11	1.42E-10
-4.9E-08	0.2068	0.0732	50	0.0008	0.0003	0.0001	5.69E-11	1.46E-10
-4.9E-08	0.2068	0.0732	50	0.0008	0.0003	0.0001	5.69E-11	1.53E-10
-4.9E-08	0.2068	0.0732	50	0.0008	0.0003	0.0001	5.69E-11	1.67E-10
-4.9E-08	0.2068	0.0732	50	0.0008	0.0003	0.0001	5.69E-11	1.87E-10
-4.9E-08	0.2068	0.0732	50	0.0008	0.0003	0.0001	5.69E-11	2.1E-10
-4.9E-08	0.2068	0.0732	50	0.0008	0.0003	0.0001	5.69E-11	2.45E-10
-4.9E-08	0.2068	0.0732	50	0.0008	0.0003	0.0001	5.69E-11	2.81E-10
-6.5E-08	0.2068	0.0732	50	0.0008	0.0003	0.0001	1.01E-10	3.62E-10
-8.2E-08	0.2068	0.0732	50	0.0008	0.0003	0.0002	1.57E-10	4.49E-10
-9.8E-08	0.2068	0.0732	50	0.0008	0.0003	0.0002	2.26E-10	5.43E-10
-1.1E-07	0.2068	0.0732	50	0.0008	0.0003	0.0003	3.07E-10	6.42E-10
-1.3E-07	0.2068	0.0732	50	0.0008	0.0003	0.0003	4.01E-10	7.39E-10

n_t	$(-n_2/n_t^2)^2$	dn_1^2	$(1/n_t-n_2/n_t^2)^2$	dn_2^2	dx_2^2	dx_2
0.0080	12.29	5E-14	14612.62	1.36E-10	1.99E-06	0.0014
0.0084	60.91	5E-14	12508.31	1.38E-10	1.73E-06	0.0013
0.0088	156.94	5E-14	10280.30	1.42E-10	1.45E-06	0.0012
0.0093	297.22	5E-14	8139.61	1.46E-10	1.19E-06	0.0011
0.0099	458.20	5E-14	6306.48	1.53E-10	9.64E-07	0.0010
0.0109	683.08	5E-14	4258.21	1.67E-10	7.11E-07	0.0008
0.0122	864.76	5E-14	2788.30	1.87E-10	5.21E-07	0.0007
0.0135	975.10	5E-14	1824.22	2.1E-10	3.83E-07	0.0006
0.0157	1023.88	5E-14	1008.44	2.45E-10	2.48E-07	0.0005
0.0182	983.97	5E-14	559.19	2.81E-10	1.57E-07	0.0004
0.0209	896.54	5E-14	317.97	3.62E-10	1.15E-07	0.0003
0.0245	773.91	5E-14	170.28	4.49E-10	7.65E-08	0.0003
0.0293	626.38	5E-14	82.79	5.43E-10	4.5E-08	0.0002
0.0331	532.01	5E-14	50.66	6.42E-10	3.26E-08	0.0002
0.0367	460.01	5E-14	33.65	7.39E-10	2.49E-08	0.0002

$d\underline{V}_L/dV_L$	dV_L	$d\underline{V}_L/dn_1$	dn_1^2	$d\underline{V}_L/dn_2$	dn_2^2	$d\underline{V}_L^2$	$d\underline{V}_L$
124.39	0.001	-41890.36	5E-14	-41890.36	1.36E-10	0.0155	0.12
119.65	0.001	-39058.88	5E-14	-39058.88	1.38E-10	0.0143	0.12
113.92	0.001	-35766.19	5E-14	-35766.19	1.42E-10	0.0130	0.11
107.46	0.001	-32298.62	5E-14	-32298.62	1.46E-10	0.0115	0.11
100.82	0.001	-28955.82	5E-14	-28955.82	1.53E-10	0.0102	0.10
91.39	0.001	-24474.84	5E-14	-24474.84	1.67E-10	0.0084	0.09
82.21	0.001	-20509.82	5E-14	-20509.82	1.87E-10	0.0068	0.08
73.94	0.001	-17216.03	5E-14	-17216.03	2.1E-10	0.0055	0.07
63.75	0.001	-13547.64	5E-14	-13547.64	2.45E-10	0.0041	0.06
55.01	0.001	-10726.77	5E-14	-10726.77	2.81E-10	0.0030	0.06
47.77	0.001	-8626.52	5E-14	-8626.52	3.62E-10	0.0023	0.05
40.87	0.001	-6826.71	5E-14	-6826.71	4.49E-10	0.0017	0.04
34.13	0.001	-5253.43	5E-14	-5253.43	5.43E-10	0.0012	0.03
30.18	0.001	-4407.06	5E-14	-4407.06	6.42E-10	0.0009	0.03
27.25	0.001	-3834.23	5E-14	-3834.23	7.39E-10	0.0007	0.03

m_1	m_2	V_L	$d\rho/dV_L$	dV_L	dm_1	dm_2	$d\rho^2$	$d\rho$
3.50	0.02	2.71	-1.30	0.001	0.0001	0.001	1.88E-06	0.001
3.50	0.06	2.73	-1.30	0.001	0.0001	0.001	1.89E-06	0.001
3.50	0.10	2.76	-1.30	0.001	0.0001	0.001	1.9E-06	0.001
3.50	0.15	2.80	-1.30	0.001	0.0001	0.001	1.9E-06	0.001
3.50	0.21	2.85	-1.30	0.001	0.0001	0.001	1.89E-06	0.001
3.50	0.32	2.93	-1.30	0.001	0.0001	0.001	1.9E-06	0.001
3.50	0.44	3.03	-1.30	0.001	0.0001	0.001	1.9E-06	0.001
3.50	0.58	3.15	-1.30	0.001	0.0001	0.001	1.9E-06	0.001
3.50	0.80	3.33	-1.29	0.001	0.0001	0.002	1.89E-06	0.001
3.50	1.06	3.54	-1.28	0.001	0.0001	0.002	1.88E-06	0.001
3.50	1.34	3.78	-1.28	0.001	0.0001	0.002	1.9E-06	0.001
3.50	1.70	4.09	-1.27	0.001	0.0001	0.002	1.9E-06	0.001
3.50	2.19	4.51	-1.26	0.001	0.0001	0.002	1.87E-06	0.001
3.50	2.58	4.84	-1.26	0.001	0.0001	0.003	1.87E-06	0.001
3.50	2.95	5.16	-1.25	0.001	0.0001	0.003	1.85E-06	0.001

;

n_1	n_2	MW_1	MW_2	dw_2/dm_1	dw_2/dm_2	dn_1^2	dn_2^2	dw_2^2	dw_2
0.008	0.0002	447.42	102.03	-0.002	0.28	5E-14	1.36E-10	1.13E-07	0.0003
0.008	0.0005	447.42	102.03	-0.004	0.28	5E-14	1.38E-10	1.11E-07	0.0003
0.008	0.0010	447.42	102.03	-0.008	0.27	5E-14	1.42E-10	1.08E-07	0.0003
0.008	0.0015	447.42	102.03	-0.011	0.26	5E-14	1.46E-10	1.05E-07	0.0003
0.008	0.0021	447.42	102.03	-0.016	0.25	5E-14	1.53E-10	1.03E-07	0.0003
0.008	0.0031	447.42	102.03	-0.022	0.24	5E-14	1.67E-10	1E-07	0.0003
0.008	0.0044	447.42	102.03	-0.029	0.23	5E-14	1.87E-10	9.86E-08	0.0003
0.008	0.0057	447.42	102.03	-0.035	0.21	5E-14	2.1E-10	9.64E-08	0.0003
0.008	0.0079	447.42	102.03	-0.043	0.19	5E-14	2.45E-10	9.14E-08	0.0003
0.008	0.0104	447.42	102.03	-0.051	0.17	5E-14	2.81E-10	8.33E-08	0.0003
0.008	0.0131	447.42	102.03	-0.057	0.15	5E-14	3.62E-10	8.43E-08	0.0003
0.008	0.0167	447.42	102.03	-0.063	0.13	5E-14	4.49E-10	7.85E-08	0.0003
0.008	0.0215	447.42	102.03	-0.068	0.11	5E-14	5.43E-10	6.6E-08	0.0003
0.008	0.0253	447.42	102.03	-0.070	0.09	5E-14	6.42E-10	5.99E-08	0.0002
0.008	0.0289	447.42	102.03	-0.071	0.08	5E-14	7.39E-10	5.46E-08	0.0002

$d\Delta V/dV$	dV	$d\Delta V/dV_0$	dV_0	$d\Delta V^2$	$d\Delta V$	m_1	dm_1^2	n_2	dn_2^2	dG^2	dG
0.4	0.001	-0.4	0.001	2.74E-07	0.0005	3.5	1E-08	0.0002	1.36E-10	1.11E-05	0.003
0.4	0.001	-0.4	0.001	2.76E-07	0.0005	3.5	1E-08	0.0005	1.38E-10	1.13E-05	0.003
0.4	0.001	-0.4	0.001	2.79E-07	0.0005	3.5	1E-08	0.0010	1.42E-10	1.16E-05	0.003
0.4	0.001	-0.4	0.001	2.83E-07	0.0005	3.5	1E-08	0.0015	1.46E-10	1.19E-05	0.003
0.4	0.001	-0.4	0.001	2.89E-07	0.0005	3.5	1E-08	0.0021	1.53E-10	1.25E-05	0.004
0.4	0.001	-0.4	0.001	2.98E-07	0.0005	3.5	1E-08	0.0031	1.67E-10	1.37E-05	0.004
0.4	0.001	-0.4	0.001	3.09E-07	0.0006	3.5	1E-08	0.0044	1.87E-10	1.53E-05	0.004
0.4	0.001	-0.4	0.001	3.22E-07	0.0006	3.5	1E-08	0.0057	2.1E-10	1.72E-05	0.004
0.4	0.001	-0.5	0.001	3.45E-07	0.0006	3.5	1E-08	0.0079	2.45E-10	2.01E-05	0.004
0.4	0.001	-0.5	0.001	3.72E-07	0.0006	3.5	1E-08	0.0104	2.81E-10	2.3E-05	0.005
0.4	0.001	-0.5	0.001	4.04E-07	0.0006	3.5	1E-08	0.0131	3.62E-10	2.96E-05	0.005
0.4	0.001	-0.6	0.001	4.5E-07	0.0007	3.5	1E-08	0.0167	4.49E-10	3.67E-05	0.006
0.4	0.001	-0.6	0.001	5.18E-07	0.0007	3.5	1E-08	0.0215	5.43E-10	4.44E-05	0.007
0.4	0.001	-0.7	0.001	5.75E-07	0.0008	3.5	1E-08	0.0253	6.42E-10	5.25E-05	0.007
0.4	0.001	-0.7	0.001	6.36E-07	0.0008	3.5	1E-08	0.0289	7.39E-10	6.05E-05	0.008

V_L	n_2	dV_L^2	dn_2^2	dM^2	dM
2.7	0.0002	0.000001	1.36E-10	1.85E-05	0.004
2.7	0.0005	0.000001	1.38E-10	1.85E-05	0.004
2.8	0.0010	0.000001	1.42E-10	1.85E-05	0.004
2.8	0.0015	0.000001	1.46E-10	1.84E-05	0.004
2.8	0.0021	0.000001	1.53E-10	1.86E-05	0.004
2.9	0.0031	0.000001	1.67E-10	1.91E-05	0.004
3.0	0.0044	0.000001	1.87E-10	1.98E-05	0.004
3.1	0.0057	0.000001	2.1E-10	2.06E-05	0.005
3.3	0.0079	0.000001	2.45E-10	2.14E-05	0.005
3.5	0.0104	0.000001	2.81E-10	2.16E-05	0.005
3.8	0.0131	0.000001	3.62E-10	2.44E-05	0.005
4.1	0.0167	0.000001	4.49E-10	2.59E-05	0.005
4.5	0.0215	0.000001	5.43E-10	2.56E-05	0.005
4.8	0.0253	0.000001	6.42E-10	2.64E-05	0.005
5.2	0.0289	0.000001	7.39E-10	2.66E-05	0.005

dn_{pump}^2	dn_{time}^2	dn_{space}^2	$dn_{time\text{-}initial}^2$	$dn_{space\text{-}initial}^2$	dn_2^2	dx_2^2	dx_2
4.41E-08	1.12E-07	5.79E-11	3.37E-12	5.69E-11	1.36E-10	1.99E-06	0.0014
2.74E-07	3.33E-07	5.91E-11	3.37E-12	5.69E-11	1.38E-10	1.73E-06	0.0013
3.15E-06	1.85E-06	6.03E-11	3.37E-12	5.69E-11	1.42E-10	1.45E-06	0.0012
8.70E-06	5.12E-06	6.16E-11	3.37E-12	5.69E-11	1.46E-10	1.19E-06	0.0011
1.64E-05	1.14E-05	6.36E-11	3.37E-12	5.69E-11	1.53E-10	9.64E-07	0.0010
2.30E-05	1.89E-05	6.72E-11	3.37E-12	5.69E-11	1.67E-10	7.11E-07	0.0008
2.30E-05	1.89E-05	7.15E-11	3.37E-12	5.69E-11	1.87E-10	5.21E-07	0.0007
2.30E-05	1.89E-05	7.61E-11	3.37E-12	5.69E-11	2.10E-10	3.83E-07	0.0006
2.30E-05	1.89E-05	8.22E-11	3.37E-12	5.69E-11	2.45E-10	2.48E-07	0.0005
2.30E-05	1.89E-05	8.68E-11	3.37E-12	5.69E-11	2.81E-10	1.57E-07	0.0004
2.30E-05	1.89E-05	9.03E-11	3.37E-12	1.01E-10	3.62E-10	1.15E-07	0.0003
2.30E-05	1.89E-05	8.94E-11	3.37E-12	1.57E-10	4.49E-10	7.65E-08	0.0003
2.30E-05	1.89E-05	8.40E-11	3.37E-12	2.26E-10	5.43E-10	4.50E-08	0.0002
2.30E-05	1.89E-05	8.04E-11	3.37E-12	3.07E-10	6.42E-10	3.26E-08	0.0002
2.30E-05	1.89E-05	7.51E-11	3.37E-12	4.01E-10	7.39E-10	2.49E-08	0.0002

$d\underline{V}_L^2$	$d\underline{V}_L$	$d\rho^2$	$d\rho$	dw_2^2	dw_2
0.0155	0.12	1.88E-06	0.001	1.13E-07	0.0003
0.0143	0.12	1.89E-06	0.001	1.11E-07	0.0003
0.0130	0.11	1.90E-06	0.001	1.08E-07	0.0003
0.0115	0.11	1.90E-06	0.001	1.05E-07	0.0003
0.0102	0.10	1.89E-06	0.001	1.03E-07	0.0003
0.0084	0.09	1.90E-06	0.001	1.00E-07	0.0003
0.0068	0.08	1.90E-06	0.001	9.86E-08	0.0003
0.0055	0.07	1.90E-06	0.001	9.64E-08	0.0003
0.0041	0.06	1.89E-06	0.001	9.14E-08	0.0003
0.0030	0.06	1.88E-06	0.001	8.33E-08	0.0003
0.0023	0.05	1.90E-06	0.001	8.43E-08	0.0003
0.0017	0.04	1.90E-06	0.001	7.85E-08	0.0003
0.0012	0.03	1.87E-06	0.001	6.60E-08	0.0003
0.0009	0.03	1.87E-06	0.001	5.99E-08	0.0002
0.0007	0.03	1.85E-06	0.001	5.46E-08	0.0002

$d\Delta V^2$	$d\Delta V$	dG^2	dG	dN^2	dN
2.74E-07	0.0005	1.11E-05	0.003	1.85E-05	0.004
2.76E-07	0.0005	1.13E-05	0.003	1.85E-05	0.004
2.79E-07	0.0005	1.16E-05	0.003	1.85E-05	0.004
2.83E-07	0.0005	1.19E-05	0.003	1.84E-05	0.004
2.89E-07	0.0005	1.25E-05	0.004	1.86E-05	0.004
2.98E-07	0.0005	1.37E-05	0.004	1.91E-05	0.004
3.09E-07	0.0006	1.53E-05	0.004	1.98E-05	0.004
3.22E-07	0.0006	1.72E-05	0.004	2.06E-05	0.005
3.45E-07	0.0006	2.01E-05	0.004	2.14E-05	0.005
3.72E-07	0.0006	2.30E-05	0.005	2.16E-05	0.005
4.04E-07	0.0006	2.96E-05	0.005	2.44E-05	0.005
4.50E-07	0.0007	3.67E-05	0.006	2.59E-05	0.005
5.18E-07	0.0007	4.44E-05	0.007	2.56E-05	0.005
5.75E-07	0.0008	5.25E-05	0.007	2.64E-05	0.005
6.36E-07	0.0008	6.05E-05	0.008	2.66E-05	0.005